DELIVERY OF PLANETARY EJECTA TO EARTH

A Dissertation
Presented to the Faculty of the Graduate School
of Cornell University
in Partial Fulfillment of the Requirements for the Degree of
Doctor of Philosophy

by
Brett James Gladman
August 1996

DELIVERY OF PLANETARY EJECTA TO EARTH

Brett James Gladman, Ph.D.
Cornell University 1996

Orbital histories of ejecta from the terrestrial planets are numerically integrated to study their transfer to Earth. The regularized mixed-variable symplectic integration code includes the effects of the planets from Mercury through Neptune. Particles are followed until they impact a planet, strike the Sun, or cross the orbit of Jupiter. The distribution of transit times for Earth-impacting objects is compared with the cosmic-ray exposure data for the lunar and martian meteorites. This comparison is consistent with a recurrent ejection of small meteoroids due to impacts on their parent bodies. Long-range gravitational effects, especially secular resonances, strongly influence the orbits of many meteoroids and can increase meteoroid collision rates with other planets and even the Sun. These effects, and collisional destruction in the asteroid belt, result in shortened time scales and higher fluxes than previously believed, especially for martian meteorites. A small flux of mercurian meteorites appears possible; recovery of ejecta from the Earth and Venus is less likely.

A model is presented which calculates the expected transfer-age spectrum in terms of the impactor flux onto the Moon and Mars. The non-zero, but finite, age of the Antarctic ice sheet is crucial in understanding the different distributions of transfer ages in the lunar and martian cases. To match the data, most recently-arrived lunar meteorites must have been launched by impactors of diameter $D <$ 100 m which struck the Moon in the last few hundred thousand years. In contrast, martian meteorites were launched by impactors several kilometers in diameter that struck Mars several million years ago. The number of meteoroids launched by each impact must scale as D^2 in the lunar case, but $\approx D^3$ for Mars. Different surface properties for the Moon and Mars may account for these differences.

Biographical Sketch

Most thesis biographies seem to begin with birth, which has an inescapable logic that one must conform to. Brett James Gladman was born on April 19th, 1966 as his poor parents were attempting to drive from northern Alberta to Calgary (he being in a rush, as usual). Because his father was in the Royal Canadian Air Force, Brett spent much of his youth moving around Canada from military base to military base, which gave him a trait of social independence which has been both a strength and a weakness. Travel was a constant thing in his life, for even when not changing towns or occupations, his parents were constantly going off camping, with Brett, his brother Brad (14 months junior), and a trailer, in tow. During the long drives, Brett read voraciously although this produced many beratings from his father, who didn't want him to miss the "beautiful scenery" (which consisted of perfectly level central Canadian plains punctuated by the occasional heroic grain elevator). His father encouraged an interest in arithmetic during these trips by naming long strings of operations to be performed on an initial number ("Take 3, multiply by 10, subtract 2, divide by 4, ..."); an activity which Brett would be willing to do until it drove everyone nutty.

At the start of his teenage years Brett had no real idea of what he wanted to do with his life, but knew it would probably be in a field ending in -ology or -onomy (paleontology, geology, and astronomy were high on the list, reflexology never appeared, and gastronomy was a later addition). As is the case for many children, he was fascinated by space and dinosaurs. He had an addiction to computers in high school, but decided that he wanted the machine to be a tool instead of being the center of a career.

Near the end of high school, Brett happened to see a magazine article biographing a relativist, Dr. Werner Israel, at the University of Alberta. Since Brett had always thought that black holes were 'cool', he wrote Dr. Israel a letter expressing an interest in the subject and asking for some further recommended readings. The reply included an invitation to visit the university. This visit, and the kind advice of Dr. Israel, convinced Brett to enroll in a physics program, which he completed in 1988, receiving a B.Sc. (Honours) degree. While at the U. of A., he was most heavily influenced by the astronomer Dr. Douglas Hube, under whose guidance Brett performed a term-project to compute the orbit of the asteroid Vesta, which was photographed from the observatory on the roof of the physics building. Although the success of this project left something to be desired, it whetted Brett's appetite for mechanics and dynamics. For a change, Brett worked during his undergraduate summers at a nuclear medicine department at the Foothills hospital in Calgary, Alberta. While there Brett obtained an appreciation for the difficulties of applied science (the human body is poorly approximated by a sphere).

After a brief foray for a summer into general relativity (which Brett found somewhat dry) Brett fortuitously chose to attend Queen's University in Kingston, Ontario. There he worked with Dr. Martin Duncan, who was also fleeing general relativity and had begun working on solar system dynamics. Brett's M.Sc. thesis 'Symplectic integrations of test particle orbits in the outer solar system' applied new numerical algorithms to show that there were no stable orbits between the outer planets where small bodies could survive for the lifetime of the solar system. The degree was completed in August 1990.

Brett drew a huge breath in the summer of 1990 and elected to take a year away from university before continuing his studies. For several months Brett worked as a 'swamper' back home in Calgary, unloading several tonnes of margarine each day from cargo trucks. This experience firmly reinforced in Brett's mind the value of an education, although the manual labour was a refreshing change from sitting in front of computer terminals. However, the highlight and main purpose of the year's 'sabbatic' was a three-month vacation in Europe. Brett spent two months in northern Italy soaking up its art treasures and eating like a king. He then visited Salzburg, Bavaria (where he finally developed a taste for beer), and central France.

Brett arrived at Cornell in September 1991 and began working with Dr. Joseph A. Burns. A term project turned into a paper on theoretical dynamics (B. Gladman 1993. Dynamics of systems of two close planets. *Icarus* **106**, 247-263). Brett was also fortunate to be able to conduct a series of observations to search for, and recover, Kuiper-Belt comets at the Mount Palomar 5-meter telescope. Another term project evolved into an extended collaboration, which eventually produced a paper on satellite spin dynamics (B. Gladman, D. Quinn, P. Nicholson, and R. Rand 1996. Synchronous locking of tidally evolving satellites. *Icarus*, in press). Although these were interesting and rewarding studies, Brett still did not have a thesis topic, nor did he yet feel like a Cornellian. The purchase of a pair of Birkenstocks quickly solved the latter problem, and put Brett in line with a distinguished string of Burns' graduate students (in fact, the resemblance to his advisor began to reach frightening proportions in the late stages of this thesis).

Brett's doctoral thesis is the end product of a gradual evolution of topics. Rabinowitz *et al.* (1993) discovered of belt of small Earth-approaching asteroids (SEAs) and postulated a lunar source for these objects. While studying this problem, it was determined that although some facets of the orbital distribution of the SEAs could be explained using the lunar source, the required number of large (≥ 10 m) meteoroids could not be launched without having the number of lunar meteorites be far larger than observed. It was then natural to study the delivery dynamics of these lunar meteorites, and then extend this to include the martian ones as well.

Brett accepted the offer of a Henri Poincaré fellowship to work at l'Observatoire de la Côte d'Azur in Nice, France, to begin Sept. 1, 1996. He will then begin a post-doctoral fellowship at the Canadian Institute of Theoretical Astrophysics in Toronto, Canada on Sept. 1 1997.

To my family, for their support,
to Sue Chamberlain, for making writing this less painful,
to George Wetherill, for whom I have the greatest respect,
and
to Joe Burns, for his guidance.

Acknowledgments

Joe Burns receives my utmost appreciation for the support he has given me throughout my time at Cornell. Joe allowed me free reign to pursue topics that attracted my interest, and was a source of sage advice in every case. His abilities as an editor are second to none, and I believe that my ability to concisely express scientific ideas has increased greatly under his tutelage. The opportunities he provided for travel to conferences allowed me to meet and collaborate with many scientists; I believe that this has helped my career immensely. I regret that we were never able to make the mythic journey to Palomar together.

I learned much from Phil Nicholson in the course of one class and many discussions. Phil encouraged me to be a better scientist by stressing the importance of having facts at one's fingertips so that ideas can be quickly checked for sanity. His thorough reading of this thesis has resulted in several improvements.

Martha Haynes, Terry Herter, Tyler Nordgren, Phil Nicholson, and Marco Scodeggio, were of great help in preparing for trips to Palomar. Greg Black, Tyler Nordgren, Marco Scodeggio, and Peter Wilson were receptive to hearing me attempt to explain some idea or another that I'd gotten into my head, and crucial in helping to get through those first-year electrodynamics and statistical mechanics problem sets during our weekend homework-crunching meetings. Dane Quinn and Richard Rand were a pleasure to work with on the satellite-spin problem, and I learned a great deal of non-linear dynamics from Richard and Philip Holmes (how much I remember off the top of my head is another story of course...).

Martin Duncan and Hal Levison were very kind in providing me with their numerical integration code (RMVS), without which this thesis would not have been possible. Joe Burns must be commended for allowing me talk him into purchasing a fast Hewlett Packard workstation, which made this study feasible.

George Wetherill and Paul Warren provided a wealth of creative ideas and thoughtful criticisms at various stages of this work. Many of the ideas behind this thesis follow directly from Paul's work. I have the utmost respect for George Wetherill, whom I view as the father of this whole field; I shall not soon forget his wisdom and his insight.

Sue Pakkala, Danielle O'Conner, Sandy Mack, and Elizabeth Bilson all helped me by taking care of the nitty-gritty details of everyday existence, and photocopying all those papers. I especially must express my gratitude to Cheryl Hall for her unwavering, smiling assistance in all manner of deeds relating to paper submissions, faxes, 4:59 PM Fed Exs, and mailing out preprint after preprint (but man, how I loved that 'printed matter' stamp!).

On the social front, I thank Matt Ashby for his priceless support as a friend through good times and bad; never have I felt that someone understood me so well. Amy Miran brightened many an hour with her good humor and her menagerie. I will remember fondly all the trips with Tyler Nordgren and Julie Rathbun to various watering holes. Marco Scodeggio and Anna Giuliani provided many an enjoyable get-together; unforgettable dinners were provided by Anna's skilled hands (one word: gnocchi!). I was fortunate enough to be graciously entertained in the sumptuous kitchen-by-the-lake of Joseph and Judy Burns on several occasions. Martha Haynes and Riccardo Giovanelli hosted memorable evenings at their house. Many a fine steak (rare, of course) was devoured at the secretive bi-annual meetings of the MEA (Meat-Eaters Anonymous, founded by myself, Tyler, and Riccardo). To this day I wonder: does Martha know?

Treasured memories of Ithaca include: Bound for Glory (a live Sunday night folk music broadcast), sailing on Cayuga Lake, a tasty beer or two at the Chapter house, those wonderful wine-tasting expeditions, gorge hiking, plays at the Hangar Theater, dancing with Donna the Buffalo, Sunday morning coffee on the Ithaca Commons with Matt and Tyler, picnic-table lunches at the Big Red Barn with the Space Sciences gang, night skiing at Greek Peak, yummy bagels at CTB, picnics in Stewart Park, the Ithaca Festival, the wine club, and of course those incredible autumn colors.

My parents have always stood behind me, and their continuous assistance was invaluable. Lastly, I am grateful to Susan Chamberlain for her help and support while this thesis was being written. Sue made every one of my last days here at Cornell enjoyable, even during the worst stress. My heartfelt thanks Sue.

Table of Contents

List of Tables

List of Figures

Chapter 1

Introduction

Rocks fell from the sky long before Chicken Little made her famed remark. In ancient times the fall of a meteorite was seen as the wrath of the gods, as a punishment for the evils of humanity. There even exist some Chinese accounts (Yau *et al.* 1994) of meteorites falling during the course of battles and affecting their outcome (the army on the receiving side of the barrage seldom emerging triumphant). Other meteorite falls could be beneficial since the purity of the metal contained in iron meteorites was vastly superior to unrefined Earth rocks; thus these meteorites were valuable for producing objects requiring high grade metal. To this day each new sultan of Java receives a dagger, called a *kris*, newly manufactured from a piece of a huge iron meteorite that fell in ancient times (Burke 1986). However, only recently have we really understood the origin, and perceived the importance of meteorites for our knowledge of the solar system.

1.1 Meteorite Terminology and Types

A *meteorite* is a recovered rock of extraterrestrial origin; that is, the rock has arrived here after a journey through outer space unassisted by humans (rocks returned via spacecraft are generally called 'samples'). On the other hand, a *meteoroid* is the name given to an object while in space. Asteroids are large meteoroids, and there is no firm distinction between these two, although the term meteoroid is usually meant to indicate objects that are of the size range to be the immediate pre-atmospheric precursors of the meteorites (centimeter to meter-sized). A *meteor* is the visible light display that accompanies the entry of a meteoroid into the Earth's atmosphere.

Depending on their chemical composition, meteorites are classified into one of three general types. *Irons* are almost pure chunks of nickel iron. *Stones* are basically pure silicate, and *stony-irons* are midway between these two classifications. Stones are subdivided into chondrites and achondrites, the former so named because they contain tiny (mm to cm) spherules of silicate named chondrules. An achondrite is simply any stone that is not a chondrite.

A meteorite is classified as either a *fall* (if the meteorite's instant of fall was directly experienced by a human) or a *find* (if the meteorite was just found on the ground by chance). As one can imagine, selection biases are of great importance in determining the mix of meteorite types that we have in our collections. Irons make up a huge percentage of finds since they are much more resistant to weathering than other meteorite types. However, chondrites account for more than 80% of falls. These selection effects can be seen in Table 1.1. Observe among the achondrites the shergottites, nakhlites, and chassignites. These are some of the martian meteorites, discussed in Sec. 1.3.1 (although they now number 12). The lunar breccia is ALH84001, the only one known in 1986, found in Antarctica.

Two important concepts also need to be defined. Upon entering the atmosphere many meteoroids fragment to varying degrees, and those which survive to reach the ground are distributed across the ground in a *strewn field* which may be many square kilometers in size. Because of this, it is possible to find *paired* meteorites, which are fragments of the same meteoroid that was incident on the top of the Earth's atmosphere. Such pairings can usually be established by isotopic and age similarities of the various fragments. Erosional effects can also split meteorites on the ground, producing more fragments and the potential for further pairings. For the lunar and martian meteorites the concept of *source-crater pairing* is also important, in which two meteoroids are launched by the same impact cratering event, but follow separate paths to the Earth.

1.2 Antarctic meteorites

Until 1969, the collection of meteorites was mostly a matter of luck, requiring us to wait for the rain of rocks, or to be lucky enough to happen across (and recognize) a find. For even though a freshly fallen meteorite will have a *fusion crust* produced by its passage through the atmosphere, this thin skin is quickly (perhaps in as little as a few years) worn away by the effects of weathering. Following this, the chances are small that a non-specialist would recognize the rock as anything out of the ordinary; iron meteorites, whose very high density distinguishes them, are an exception to this rule (as anyone who stubs a toe on one will attest). The chaotic mix of rocks on the Earth's surface camouflages the meteorites very effectively, and the fall rate of 1 kg or larger meteorites is estimated to be only of order 10 per km^2 per Myr in any case (Halliday *et al.* 1984). Luckily, there is now a much more efficient meteorite collection mechanism.

A Japanese team was measuring ice flow movement in the Yamato mountains of Antarctica in 1969 when they happened upon the first group of Antarctic meteorites (though isolated meteorites had been found in Antarctica before). In Antarctica meteorites can be found strewn over the ice in great abundance (Cassidi and Rancitelli 1982), where their contrast with the ice makes spotting them

Table 1.1 Statistics of meteorite finds and falls, summarized from Sears and Dodd (1988). The column for Antarctic finds (accurate as of 1986) is now very dated, but the proportions remain roughly correct. The chondrites and irons are sub-classified according to mineral content (*e.g.*, H chondrites have high iron contents); see Wasson (1985) for more details.

Class	Falls	Fall Frequency (%)	Finds	
			Non-Antarctic	Antarctic
Chondrites				
C	35	4.2	11	45
H	276	33.2	347	671
L	319	38.3	286	224
LL	66	7.9	21	42
E	13	1.6	7	7
other	3	0.4	3	3
Achondrites				
Eucrites	25	3.0	8	13
Howardites	18	2.2	3	4
Diogenites	9	1.1	0	9
Ureilites	4	0.5	6	9
Aubrites	9	1.1	1	17
Shergottites	2	0.2	0	2
Nakhlites	1	0.1	2	0
Chassignites	1	0.1	0	0
Lunar breccias	0	0.0	0	1
Stony-Irons				
Mesosiderites	6	0.7	22	2
Pallasites	3	0.4	34	1
Irons				
I	6	0.8	108	4
II	10	0.7	96	6
III	10	1.6	227	0
IV	3	0.4	64	1
other	13	1.3	175	0

an easier task. The dryness of the climate means that the ice stores the meteorites, protects them from erosion, and may (through the process of flowing glacial ice) concentrate them on what are known as 'meteorite stranding fields' (Cassidy and Whillans 1990). Antarctic meteorites are named after their collection site (*e.g.,* ALH for Allan Hills, and Y for the Yamato Mountains), followed by two digits indicating the field season of their collection, and then three or four digits giving the meteorite its unique number. So, for example MAC88104 was the 104th meteorite from the MacAlpine Hills numbered from the 1988-89 (Antarctic summer) recovery season. A discussion of the major collections sites is given by Cassidy *et al.* (1992). Roughly 20,000 meteorites have now been collected in Antarctica, to be compared with roughly 2,000 non-Antarctic meteorites collected in the world's museums (throughout all history, mind you). Antarctic and non-Antarctic meteorites differ in some important ways: Antarctic meteorites have smaller average masses, have proportionally different representation in the various meteorite classes, and (on average) have much longer Earth residence times (Koeberl and Cassidy 1990; Huss 1990).

This last difference is especially important for our purposes. Because of weathering effects, the amount of time a stony meteorite can spend on the Earth's surface before being destroyed is relatively short ($<3 \times 10^4$ yr); in contrast, Antarctic meteorites can often survive for an order of magnitude longer than this, and in some cases even up to 1 Myr (Nishiizumi *et al.* 1989). Therefore, the ice sheet 'integrates' for much longer than human history, which explains the great success of meteorite recovery there. The various ice fields of Antarctica have different mean residence times, which produce different average recovered masses due to weathering effects (Huss 1990).

The desirable Antarctic features of low weathering and relative absence of terrestrial surface rocks are also present in desert terrains. Searches in such areas of Australia have yielded many finds, including one lunar meteorite: Calcalong Creek (Hill *et al.* 1991).

1.3 The martian meteorites

It is perhaps somewhat ironic that sample return missions to Mars might not be necessary if all we wanted was to have some rocks from Mars. In fact, it seems that the Earth has been subject to a continuous hail of martian material throughout its history (H.G. Wells was right!).

1.3.1 The original SNCs

The meteorite Chassigny fell in France on October 3, 1815. (Except in Antarctica and the desert areas described above, meteorites are named after the nearest post office to which they fall.) Shergotty fell in 1865 in India, and Nakhla in

Alexandria, Egypt in 1911. These three large falls (Table 1.2) gave their names to three new classes of meteorites, collectively known by their acronym as the SNC meteorites. Chassigny was the lone member of its class. Outside of Antarctica, Shergotty was joined by Zagami (which fell in 1962 in Nigeria), and Nakla by Lafayette (found in Indiana, 1931) and Governador Valadares (found in Brazil, 1958). These meteorites were all linked by a distinctive oxygen isotopic signature, which proves their non-terrestrial origin, but have many petrologic signatures that distinguish them from other achondrites (Laul 1986). Most stunning of these is that crystallization ages (how long ago the rock cooled to a solid form, see Sec. 2.2) for all of these objects are less than 1.3 billion years. This fact alone suggested that these objects might be from Mars.

1.3.2 History of the SNC debate

I will not attempt to discuss all of the many arguments that establish, to a high degree of certainty, that the SNC meteorites are from Mars (see McSween 1995 for a comprehensive discussion). Instead I review some of the history of this debate and point out only the most compelling arguments.

Radioactive dating establishes most meteorites as being the same age as the solar system (4.5 Gyr). The <1.3 Gyr ages of the SNCs demonstrate that they came from a body that was geologically active recently (Chpt. 2). The most plausible source was Mars, as was suggested by several authors (McSween *et al.* 1979, Nyquist 1979, Walker *et al.* 1979, Wasson and Wetherill 1979). However, this suggestion was treated with skepticism because of one simple fact: there were no lunar meteorites. The Moon is vastly closer and has a lower escape velocity, and so one would perhaps expect a much greater flux of lunar material. The lack of such meteorites presented a major obstacle to an acceptance of the Mars-SNC link. Secondly, the NC meteorites (although not the shergottites) show at most weak shock levels (Treiman 1995), which was taken as evidence that they could not have been blasted off a large body at the escape velocity.

The recognition of the first lunar meteorite, ALH81005, in 1982 removed this obstacle. The meteorite was similar enough to returned Apollo samples that the community immediately accepted this identification. In fact, lunar meteorites had been collected in Antarctica before 1981 (Y791197 and Y793274), but these had been misclassified. The existence of these meteorites, and the fact that they also recorded low shock pressures, forced serious reconsideration of the hypothesis that the SNCs could be from Mars (Eugster 1989).

Perhaps the most compelling evidence linking the SNCs to Mars is due to trapped gas components in some of the shergottites. The isotopic composition of this trapped gas is almost identical to that of the martian atmosphere, as measured by the Viking landers (McSween 1995). Additional isotopic and petrologic evidence is consistent with what is known about Mars from other sources. To

Table 1.2 Masses of the martian and lunar meteorites. Martian objects also have their SNC classification listed; a * indicates the object is the source of the class name. The shergottites are subclassified as basaltic (b) or lherzolitic (l) petrologies.

Lunar Meteorite	mass (kg)	Martian Meteorite	mass (kg)	Class
ALH81005	0.031	ALH77005	0.48	S(l)
Asuka-881757	0.442	ALH84001	1.93	–
Calcalong Creek	0.019	Chassigny	4	C*
EET87521	0.031	EET79001	7.94	S(b)
MAC88104/5	0.724	Governador Valadares	0.16	N
QUE93069	0.021	Lafayette	0.80	N
QUE94269	0.0032	LEW88516	0.013	S(l)
QUE94281	0.0234	Nakhla	40	N*
Y-791197	0.052	Shergotty	4	S(b)*
Y-793169	0.0061	QUE94201	0.012	S(b)
Y-793274	0.0087	Y-793605	0.018	S(?)
Y-82192,3/86032	0.712	Zagami	18	S(b)

quote McSween: "If the SNC meteorites are not from Mars, but rather from an asteroid, then our understanding of small bodies is fundamentally flawed."

1.3.3 The current martian meteorite sample

At the time of writing, there are 12 martian meteorites. More than half are shergottites, which are subclassified, on the basis of their petrology, into basaltic and lherzolitic types (McSween 1995). The three original falls are still the only Nakhlites, and Chassigny remains the only member of its class. ALH84001 does not fit into the SNC classification and since other future meteorites from Mars may not fit either, I will abandon the usage of the term SNC as a synonym for 'martian meteorite', as has been suggested (Mittlefehldt 1994). ALH84001 is particularly special in that its crystallization age (see Sec. 2.2) is $\approx$4.5 Gyr (Jagoutz *et al.* 1994). This is incredibly old for a rock that has come from the martian crust (there are no Earth or Moon rocks this old), and yet the martian identification is felt to be fairly firm (Ash *et al.* 1996).

The martian meteorites all record overall shock pressures less than that originally thought necessary to have launched them ($\sim$100 Gpa = 1 Mbar). I defer the discussion of the implications of this fact to Sec. 6.1.3, pausing here only to note that the NCs have overall peak shock pressures of approximately 15 Gpa, the shergottites record 30-54 Gpa (Treiman 1995a), and ALH84001 shows evidence of several shock events (Treiman 1995b).

1.4 Lunar meteorites

The lunar meteorites, taking pairing into account, also number 12 at the time of writing, although the newly found QUE94269 is probably paired with QUE93069 (Nishiizumi and Caffee 1996a). Except for the finds of the 1994-95 season, these meteorites are comprehensively reviewed by Warren (1994). Most are regolith breccias, but two (Asuka 881757 and Y-793169) are pure mare basalts. Interestingly, the average mass of a lunar meteorite is 38 times less than the martian meteorites. The median mass is 27 times times less, reflecting the effect of the two very massive martian meteorites Nakhla and Zagami.

1.5 Goals of this work

The lunar and martian meteorites present several puzzles:

(1) the equal numbers of each group,

(2) the much larger average mass of the martian meteorites,

(3) the inferred shallow pre-launch depths of the lunar meteorites vs. the deep ones of the martian meteorites (Sec. 2.3.4),

(4) the prevalence of geologically young rocks amongst the SNCs (even though such terrain is relatively rare on Mars), and

(5) the 4π age spectrum (Sec. 2.3.2) of the martian objects terminates at $\sim$15 Myr (*i.e.,* we have no martian meteorites that took longer than this to arrive).

A complete model should explain these facts.

Chpt. 2 presents a summary of the techniques and the results of radioactive analyses that determine several important properties of the lunar and martian meteorites, most especially the amount of time that they spent in space as small bodies before reaching the Earth. These data, in conjunction with the dynamical simulations described in Chpts. 3–5, will constrain the modelling performed in Chpt. 6 which attempts to construct a self-consistent model of the launch and delivery of these objects.

Chpts. 3 and 4 examine the dynamics of the delivery of the lunar and meteorites, respectively. Chpt. 5 discusses the possibility of the Earth receiving meteorites from Mercury, Venus, and even the Earth. Chapter 6 then discusses a model which self-consistently resolves the above puzzles.

Chapter 2

Cosmogenic ages of meteorites

2.1 Introduction

It is probably fair to say that the study of meteorites has contributed more to our understanding of the formation of the solar system than any other pursuit (except the basics of celestial mechanics, of course). The amount of information that can be gleaned by the study of noble gases, radioactive isotopes, and their decay products is so great that it would be impossible to attempt to review the entire topic here. I shall concentrate on those studies which provide information that is relevant to the problem of the delivery of the lunar and martian meteorites, but even with this restriction, the body of literature is very large.

Radiometric studies of meteorites (Reedy *et al.* 1983, Vogt *et al.* 1990) allow several quantities to be determined: (1) the crystallization age, *i.e.,* the time at which the various isotopes were locked into a closed system (*e.g.,* the parent rock cools below its molten phase); (2) the 2π depth, which measures how far below the surface of the parent body the meteorite resided before launch; (3) the 2π age $t_{2\pi}$, which is the duration of this surface exposure; (4) the 4π age $t_{4\pi}$ measures the amount of time which the meteorite spent in space exposed to an isotropic flux of cosmic rays; and (5) the terrestrial age $t_{\oplus}$, which is the duration of residence on the Earth's surface before the meteorite was discovered. The terms 2π and 4π refer to the solid angle subtended by the flux of incoming particles that produce the isotopes of interest; objects sitting on the surface of a large body are only exposed to flux coming from 2π steradians. Knowledge of these quantities will allow us to constrain theories about the origin and transfer of the meteorites of interest. The last four of these quantities are dependent on the fact that objects in interplanetary space are exposed to a continuous flux of energetic cosmic rays, whereas the first is in some ways more straightforward. Therefore we will discuss isochron ages first, and cosmic ray exposure methods later.

2.2 Crystallization ages

At the instant that a rock cools and becomes isolated chemically from its surroundings, the radioactive system becomes closed. This results in isotopic ratios involving radionuclides to change with time. If this age can be determined, it is called the *crystallization age* of the object.

To be specific, suppose that a daughter nuclide D is produced in the radioactive decay of a parent nucleus P. Then the rate of change of the concentration (number of atoms per unit volume) of the parent nucleus is given by

$$\frac{dP}{dt} = -\lambda P \qquad \Longrightarrow \qquad P(t) = P_o\, e^{-\lambda t}, \tag{2.1}$$

where P_o is the parent's initial concentration and $\lambda = \ln 2/\tau$ with τ being the usual half-life. Since the daughter isotope may be present in some initial concentration D_o, we write

$$\begin{aligned} D(t) &= D_o + [P_o - P(t)] \\ &= D_o + P(t)\,[\frac{P_o}{P(t)} - 1] \\ &= D_o + P(t)\,[e^{\lambda t} - 1]. \end{aligned} \tag{2.2}$$

This is the fundamental equation of radioactive age determination for a closed system. Since the concentration of an element is difficult to measure, in practice the ratio of concentrations with a stable isotope (usually of the daughter nucleus) is observed, these ratios being determined by mass spectrometry (Wasson 1985). If D_r denotes the reference isotope, then we have

$$\frac{D}{D_r} = \left(\frac{D}{D_r}\right)_o + \frac{P}{D_r}(e^{\lambda t} - 1). \tag{2.3}$$

If different minerals of the same rock having different concentrations of the radioactive parent are sampled, then this equation predicts that the parent and daughter ratios should describe a straight line, called an isochron. The ordinate intercept $(D/D_r)_o$ gives the initial concentration of the daughter isotope, and the slope of this isochron can be used to calculate the time since the system was closed.

An example of this is shown in Fig. 2.1, for the case of the Nakhla meteorite. Here the isotopes used are the very important rubidium-strontium $^{87}\mathrm{Rb} \rightarrow {}^{87}\mathrm{Sr}$ pair, with a 49 Gyr half-life, and $^{86}\mathrm{Sr}$ is used as the stable reference isotope. This is the same method used to date the formation age of almost all of the chondrites at 4.57 ± 0.03 Gyr, which is generally accepted as the time of formation of the solar system. The intercept of this plot shows that (since this corresponds to no initial radioactive Rb present) the initial $^{87}\mathrm{Sr}\,/\,^{86}\mathrm{Sr}$ ratio was about 0.7. The

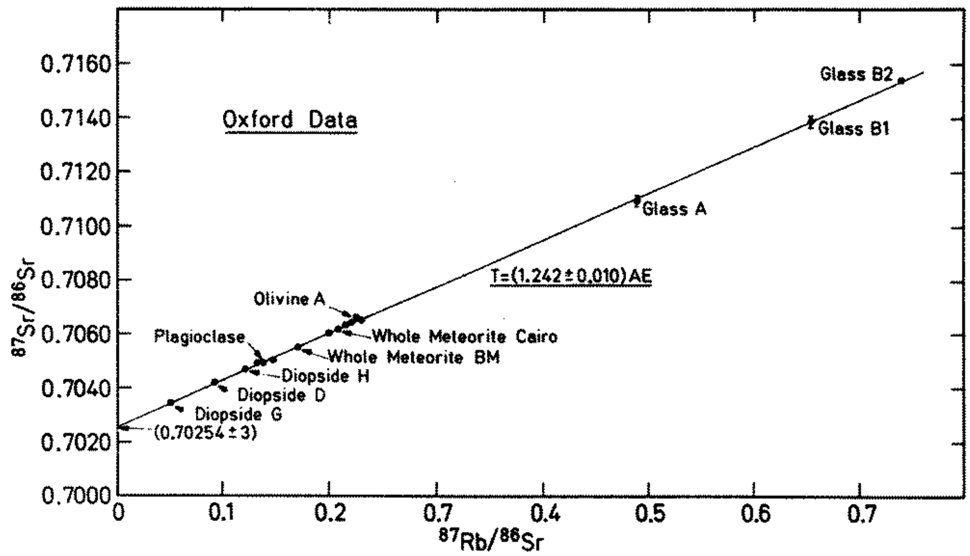

Figure 2.1 An internal isochron for the Nakhla meteorite, using Rb-Sr technique. The large spread in the ^{87}Rb / ^{86}Sr values available at various sites in the meteorite allows an isochron age of 1.24 Gyr to be determined. Figure from Kirsten (1978).

isochron age of Nakhla is 1.24 Gyr, which is surprisingly low, since it implies relatively recent geologic activity.

The crystallization ages of the most lunar meteorites are all very old, varying from 3.9 to 4.3 Gyr (Eugster and Niedermann 1988, Warren and Kallemeyn 1993). This is basically the same as the lunar crust, which remained active for approximately 1 Gyr. Mare basalts can be as young as 3.1 Gyr (Taylor *et al.* 1991); the two mare meteorities Asuka-881757 and Y-793169 have crystallization ages of 3.1 and 4.2 respectively, which is within the normal range although the latter is somewhat high (Eugster *et al.* 1996).

The martian meteorites have 3 groups of crystallization ages, determined from both Rb-Sr and Sm-Nd (Samarium-Neodymium) methods (Nyquist *et al.* 1995). The shergottites (Shergotty, Zagami, EET79001, ALH77005) are dated at $\sim$ 180 Myr, Chassigny and the Nakhlites (Nakhla, Lafayette, and Governador Valadares) at $\sim$ 1.3 Gyr, and ALH84001 at the surprisingly high age of $\sim$ 4.5 Gyr (Jagoutz *et al.* 1994). This last meteorite has caused considerable excitement since it would seem to represent a very ancient piece of the martian crust, in which evidence of a wet early phase for Mars is being sought. The very young crystallization ages of the shergottites may not be crystallization ages at all if a shock event is capable of resetting the Rb-Sr clock; it is possible that they also crystallized $\sim$ 1.3 Gyr ago, but this is in considerable debate (McSween 1995;

Treiman 1995).

The crystallization ages of the martian meteorites are young even for Mars; in fact, terrain younger than 1.3 Gyr probably comprises only 10-15% of the martian surface (Nyquist 1995). Why are 11 of the 12 martian meteorites apparently from this terrain that occupies such a small fraction of the surface? Warren (1994) suggests that the older highland terrain has been pervasively weathered so that almost no intact rocks remain in the upper region of the oldest martian crust. Thus impacts into highland terrain are unable to launch coherent meteoroids. Clearly the existence of ALH84001 must be allowed for if this model is correct.

2.3 Cosmic ray exposure ages

2.3.1 General considerations

The interplanetary flux of cosmic rays causes the production of cosmogenic nuclides (Reedy *et al.* 1983, Vogt *et al.* 1990) in objects that are not shielded by the equivalent of several meters of rock (we say 'equivalent' because, for example, the Earth's atmosphere is also sufficient to shield the surface, decreasing the production rates of radioisotopes by 2–3 orders of magnitude). The isotopes produced can be then studied to determine the duration of the exposure. The cosmic rays of interest for our purposes consist of two types: solar and galactic cosmic rays (SCRs and GCRs), the numbers of which drop off as approximately a power law in the energy E according to $dN/dE \propto E^{-\gamma}$ (Caffee 1988). Both types consist primarily of protons and some alpha particles, with $\simeq 1\%$ heavier nuclei. SCRs of energies about a few MeV can induce nuclear reactions, but only in the upper few mm of matter; the rarer 100 Mev SCRs can penetrate slightly deeper. The GCRs have typical energies of 0.1–10 Gev and can penetrate to a depth of several meters (the flux of primaries decreasing exponentially with depth in the target), causing nuclear reactions not only directly but also through a shower of secondary neutrons that is produced during their passage. Interestingly, nuclide production routes that depend on these secondary neutrons become *more* efficient with depth due to the lack of secondaries near the surface, at least until one gets deep enough in the target that the primaries are screened out (see Englert and Herr 1980 for an example).

The flux of cosmic particles produces the following effects: (1) the implantation of low energy SCRs in the upper 0.1 μm of the target, (2) damage to mineral lattices (mostly in the upper 100 μm) which can be detected under a microscope, and (3) nuclear reactions which transform atoms in the target into new ones (which are then known as cosmogenic nuclides). The most interesting of the created isotopes are noble gases and radioisotopes, both of which are detectable in the sample. Generally the longer the target was subjected to the cosmic ray flux, the greater the concentration of the isotope. Noble gas concentrations (determined as ratios) can be measured by heating samples of the meteorite and observing the escape of the gas (Pal *et al.* 1986, Ott 1988). Activities of radioisotopes can be measured directly (usually in units of disintegrations per minute per kilogram of the sample, denoted dpm/kg) in a nondestructive fashion. All these techniques were refined after the Apollo and Luna missions brought back immense numbers of lunar samples for study.

Clearly the utility of this method depends on knowing the cosmic ray flux over the period of interest, in particular whether or not the flux has been constant. The numbers of both SCRs and GCRs vary with solar activity due to changing SCR production and the fact that the solar magnetic field can shield the inner solar system from GCRs. Over the very short term, the 11-year solar cycle modulates CR activity by changing the rate of solar flares; higher solar magnetic activity prevents the less energetic GCR primaries from reaching the inner solar system. We are more interested in the flux averaged over longer time scales, and in general the data points to the flux being constant in time, although there is some evidence for higher SCR activity in the last hundred thousand years when compared to the last million years. (Reedy *et al.* 1983). This variation is not of great concern since the shallow SCR record is usually removed during the ablation of the meteorite during its atmospheric passage, leaving only the cosmogenic nuclides produced by GCRs available for study. Most cosmogenic nuclides are created by the more energetic GCRs in any case, the flux of which seems to have varied by less than 25–50% in the last few Myr (Reedy *et al.* 1983). A constant flux is assumed by almost all workers in the field.

Cosmogenic *radio*nuclides (as opposed to noble gases) do not continuously accumulate since they are simultaneously decaying. The equation governing the change in their number N (per kg) is $dN/dt = P - \lambda N$, where the first term P is the production rate (events/min/kg) and the second gives the number of decays. Since

$$N(t) = \frac{P}{\lambda}\left(1 - e^{-\lambda t}\right)$$

the activity $A(t)$ (in dpm/kg) that would be measured is

$$A(t) = \lambda N(t) = P(1 - e^{-\lambda t}). \tag{2.4}$$

This produces the expected behavior that, after several half-lives of the isotope, the rate of disintegrations will reach equilibrium with the production rate P, which is thus called the *saturation activity*.

The production rates of the various atomic species depend on the cosmic ray flux, and the composition of the target. In general, the formation rate of a given nuclide x at depth d inside a meteoroid of nominal radius R is given by (Vogt *et al.* 1990)

$$P_x(d, R) = \sum_j N_j \sum_k \int_0^\infty \sigma_{xjk}(E)\ \phi_k(E, d, R)\ dE\ , \tag{2.5}$$

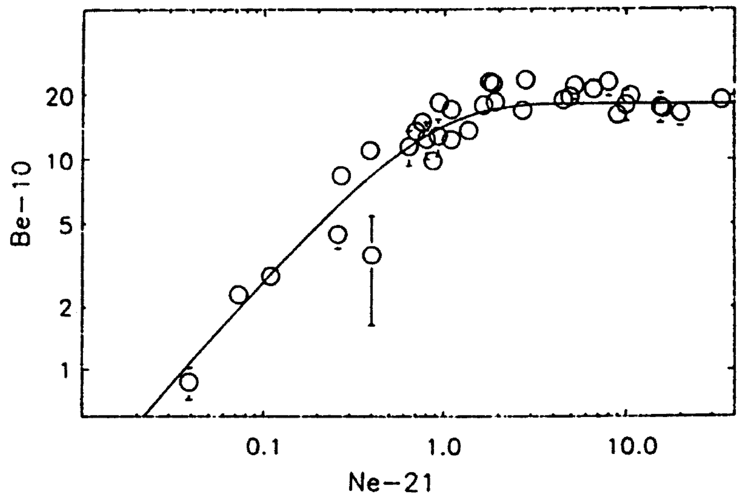

Figure 2.2 ^{10}Be activities (dpm/kg) versus ^{21}Ne content (volume per gram, measured in 10^{-8}cm^3 STP g^{-1}) for stony meteorites. From Vogt *et al.* (1990).

where N_j represents the concentration of target element j, σ_{xjk} is the cross section for the production of x from element j by particle type k at energy E, and ϕ is the flux of these particles. As can be imagined, determining these cross-sections experimentally is a time consuming task. The production rate's dependence on the target's composition produces formulae such as

$$P_{10} = 0.30\mathrm{O} + 0.26(\mathrm{Mg} + 0.8\mathrm{Al} + 0.65\mathrm{Si}) + 0.12\mathrm{S} + 0.10\mathrm{Ca} + 0.07(\mathrm{Fe} + \mathrm{Ni}) \qquad (2.6)$$

for the saturation activity of ^{10}Be in stones, where the elemental names refer to the fractional abundance (by weight) of that element in the sample (Pal *et al.* 1986).

If one wishes to confine one's attention to a particular meteorite type (so that the compositions are similar), then the production rate can be measured in a much simpler way. Consider that stable isotopes (such as noble gases) are also being produced at a rate P_s, but that the concentration S of these nuclides will increase linearly since they do not decay; that is:

$$S = P_s\, t\, . \qquad (2.7)$$

If the activity of radionuclide is plotted against the concentration of the stable isotope for a variety of meteorites of similar composition, then a plot like Fig. 2.2 results, where the ^{10}Be activity is plotted against the ^{21}Ne content (which thus serves as a clock) and shows the ^{10}Be activity reaching saturation. Since Eq. (2.7) can be used to eliminate the time in Eq. (2.4) to yield $^{10}\mathrm{Be} = P_{10}[1 - \exp(-\lambda\ ^{21}\mathrm{Ne}/P_{21})]$, a two parameter fit to the data yields *both* production rates.

The production rates obtained by a variety of methods agree within 10 or 20%. The rates used in analyses of the lunar and martian meteorites are typically those produced in stony meteorites (specifically chondrites), with minor modification

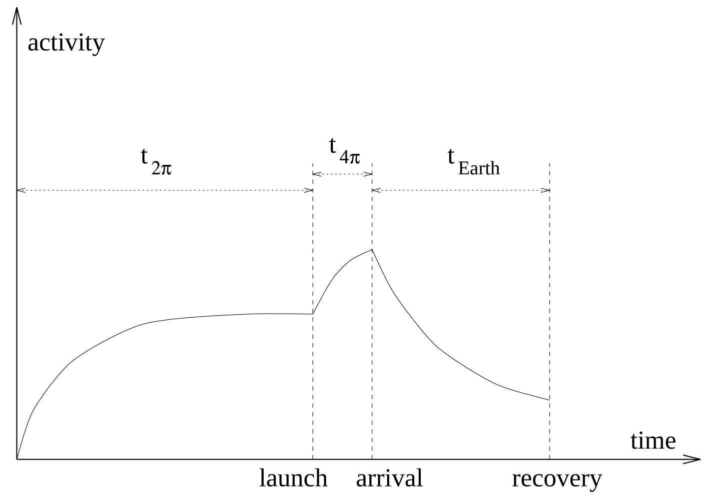

Figure 2.3 Schematic representation of the time evolution of the activity of a radionuclide. In this example the meteoroid is close enough to the surface for many half-lives so that the 2π saturation activity is reached. During the short transfer ($t_{4\pi}$) the new saturation level is not obtained, and then during Earth residence time ($t_{\text{Earth}} = t_{\oplus}$) the activity decays away continuously.

(Pal *et al.* 1986). A final correction needs to be done to allow for the effects of shielding within the meteorite itself. Measurement of the noble gas concentration ratio ^{3}He / ^{21}Ne (which is diagnostic of the shielding depth) combined with estimates of the pre-atmospheric size yield a corrected production rate which is then used in the age calculation.

The overall errors in the CRE ages, as judged by the results determined using different isotopes, appear to be roughly 10–30%. This accuracy should be sufficient for our purposes. The overall problem now becomes one of disentangling where, and for how long, the various irradiations and shieldings occurred. For the lunar and martian meteorites, this consists of three possible phases: (1) irradiation on the surface of the parent body for $t_{2\pi}$, where the depth of burial is important, (2) irradiation in space ($t_{4\pi}$), and (3) the Earth residence time $t_{\oplus}$, during which the meteorite is effectively shielded. A current measured activity A could unfortunately result from several different exposure histories, which satisfy

$$A = [\ P_{pb}(1 - e^{-\lambda t_{2\pi}})e^{-\lambda t_{4\pi}} + P_{4\pi}(1 - e^{-\lambda t_{4\pi}})\ ]\ e^{-\lambda t_{\oplus}}. \tag{2.8}$$

Here the production rate on the parent body P_{pb} accumulates for $t_{2\pi}$, and then this contribution will decay away while the meteoroid is in space for $t_{4\pi}$. However, the 4π production rate $P_{4\pi}$ is always greater and so the activity will increase until the object reaches the Earth, whereupon the final exponential factor in Eq. (2.8) indicates both contributions continue to decay on the Earth. This is illustrated schematically in Fig. 2.3, which is a reasonable representation of the history of a lunar meteorite. In contrast, martian meteorites have no surface exposure (Sec. 2.3.4), and so their activities would be zero at the moment of launch. Since there are five unknowns (if we include the production rates), many different histories could lead the same final activity. For example, in the figure the same final activity could result by having an instantaneous transfer ($t_{4\pi} = 0$) followed by a shorter Earth residence time. Fortunately, by measuring more than one isotope (ideally five), this ambiguity can be removed. It can be difficult to find enough radioisotopes with half-lives in the appropriate regimes; four is usually sufficient since $P_{4\pi}$ can be estimated (Nishiizumi *et al.* 1991). We now discuss results for these various portions of the exposure histories, best estimates of which are shown in Table 2.1.

2.3.2 4π exposure ages

The 4π ages will be our chief constraint since we are primarily interested in how much time elapsed between launch and Earth impact. It is apparent from an examination of Table 2.1 is that the average lunar meteorite was delivered to the Earth in a far shorter time than the average (or indeed, almost any) martian meteorite. Over half of the lunar meteorites have transfer durations of less than 100 kyr, a fact that will serve as an important constraint later. Also observe that the martian meteorites appear to fall into three CRE age groups: 0.7 Myr (1 object), 3 Myr (5 objects), and about 10 ± 1 Myr (4 objects), with ALH84001 is almost certainly independent of this last group based on CRE and compositional data (Bogard 1995). We will explore what these transfer data imply for our dynamical model in the following chapters.

2.3.3 Earth residence and blast-off times

Except for the lunar meteorite Calcalong Creek and the martian falls and finds, all of the meteorites with measured values of $t_{\oplus}$ were found in Antarctica and have residence times consistent with what we know are typical ages for the collection areas (Nishiizumi *et al.* 1989, Vogt 1990); the oldest Antarctic meteorites are about 1 Myr old, but in some collection areas the average is considerably younger (for example, < 0.1 Myr for the Yamato Mountains). When performing this analysis one wants to use a radioisotope with a half-life on the same order as the Earth residence time, and so ^{36}Cl ($\tau_{1/2} = 0.3$ Myr) and ^{14}C (5740 yr) are good choices (Nishiizumi 1986).

Even though $t_{\oplus}$ is rather short for most meteorites, since many lunar meteorites have such small 4π ages it is important to know $t_{\oplus}$ since the launch time (or *blast-off time*) was $t_{bo} = t_{4\pi} + t_{\oplus}$ years ago. Two meteorites that do not share similar blast-off times cannot be source-crater paired.

Table 2.1 Properties of the lunar and martian meteorites, summarized from Warren (1994); a typo in the mass of EET79001 is corrected here. The abbreviation Y = Yamato is used. The martian meteorites that are labeled falls have Earth residence times of effectively zero, and those labelled finds likely have very young $t_\oplus$ (negligible compared to $t_{4\pi}$). The martian meteorites all have $t_{2\pi} = 0$ due to their deep burial (> several meters). The parenthesized 4π ages for some of the lunar meteorites are thermoluminescence transit ages (see ref. 3). REFERENCES: 1. Warren 1994, 2. Nishiizumi *et al.* 1991, 3. Benoit *et al.* 1996, 4. Nishiizumi 1996a, 5. Swindle *et al.* 1995, 6. Eugster *et al.* 1996, 7. Nishiizumi 1996b, 8. Thalmann *et al.* 1996.

Lunar Meteorite	mass (kg)	$t_{4\pi}$ (Myr)	$t_\oplus$ (Myr)	$t_{2\pi}$ (Myr)	depth (g/cm^2)	ref.
Y-793274	0.009	< 0.02	$<.02$–.06	>300	140–180	1
MAC88104/5	0.724	~ 0.04	$0.23\pm.02$	630	360–400	1
ALH81005	0.031	<0.05(0.01)	0.01–.02	580	150–180	2,3
QUE94281	0.023	$\ll$0.05(.001)	0.1–0.2	>100	270–320	4
EET87521	0.031	<0.07(<.001)	<0.06	<0.2	560–590	1,3
Y-791197	0.052	$\ll$0.1(<.019)	$0.06\pm.03$	910	4–8	1
QUE93069/94069	0.024	$0.15\pm.02$	<0.015	1000	10–50	4,8
Calcalong Creek	0.019	0.2	<0.07	>200	~ 40	5
Asuka-881757	0.442	0.9 ± 0.1	<0.05	0.8	>1000	4,8
Y-793169	0.006	1.1 ± 0.2	<0.05	50 ± 10	>500	4,8
Y-82192,3/86032	0.712	9 ± 2	$\sim$0.09	none	>1000	1

Martian Meteorite	mass (kg)	4π CRE (Myr)	$t_\oplus$ (Myr)	$t_{2\pi}$ (Myr)	depth (m)	ref.
EET79001	7.94	0.6	0.012	–	> 2	6,7
QUE94201	0.012	2.6	0.3	–	> 2	7
Zagami	18	2.6	fall	–	> 2	6
Shergotty	4	2.8	fall	–	> 2	6
ALH77005	0.48	3.4	0.2	–	> 2	6
LEW88516	0.013	3.6	0.025	–	> 2	6
Chassigny	4	9.9	fall	–	> 2	6
Governador Valadares	0.16	10.5	find	–	> 2	6
Nakhla	40	10.5	fall	–	> 2	6
Lafayette	0.80	10.5	find	–	> 2	6
ALH84001	1.93	$\approx$15	0.011	–	> 2	6
Y-793605	0.018	?	?	?	?	–

The fact that roughly half of the martian meteorites were found outside of Antarctica (many as large falls) probably requires explanation. Is the lack of large lunar meteoroids in historical times just a statistical fluke, or does it indicate something about the launch process?

2.3.4 2π exposure and surface depths

The 2π exposure ages are also obtained from an analysis of the activities of multiple nuclides. Looking for this kind of 'first stage' activity is often not done for meteorites, which are often assumed to have simple '1–stage' exposure histories (that is, the meteorite is liberated from a completely shielded location and then transferred to the Earth with $t_{4\pi} \gg t_{\oplus}$). This is because the liberation event is often assumed to be the catastrophic disruption of a large parent asteroid, which suddenly exposes massive numbers of meteoroids to cosmic rays. This assumption has been questioned by Wetherill (1980) who believes that complex histories should be more the norm. But in the case of the lunar and martian meteorites, near-surface launch from an impact event immediately suggests that the objects may have resided on or near the surface of the parent body.

The results for the lunar meteorites show in almost all cases that the objects spent several hundred Myr to 1 Gyr within the active layer of the upper few meters of the surface (Nishiizumi *et al.* 1991, Warren 1994). This lunar depth information is obtained by using profiles for the saturation activity taken from Apollo drill core samples within which the activities are known as a function of depth (Carrier *et al.* 1991). Once it is known that the 2π age is long, the drill core activities can be used to determine the depth at which the meteoroid resided before launch. The depth is quoted as an integrated mass depth d_m (in g/cm^2) defined by

$$d_m = \int_0^X \rho(z)\ dz \quad , \tag{2.9}$$

where X is the depth of burial (cm) of the meteorite. Thus, in a uniform surface layer the real depth of burial is therefore just the mass depth divided by the mean density.

A complication is presented in that there exists the possibility that the meteoroid could have been exposed for some time and then buried (by a nearby impact turning over the regolith for example). In such a case the activity produced by the previous exposure would begin to decay away. This confusion can be eliminated by examining stable isotopes (mostly noble gases) that do not disappear with time and which thus measure the integrated surface residence age. In any case, since the interval between a burial and re-exposure is likely to be long compared to the half-life, the 2π age and depth measures the time and depth since the last emplacement in the near-surface layer.

On the basis of this and noble gas concentrations, the conclusion is that the martian meteoroids were all launched from completly shielded locations, *i.e.,* at least several meters below the surface, implying $t_{2\pi} = 0$ (McSween 1995). The deep pre-launch residence of the martian meteorites likely provides clues as to the ejection mechanism, and this difference has prompted speculation that the launch process may differ in some manner from that for the lunar meteorites (Ott 1988, Warren 1994).

Chapter 3

Dynamics of lunar meteoroids

3.1 Introduction

Three decades ago Arnold (1965) and Wetherill (1968) used Monte Carlo simulations to investigate the expected 4π cosmic ray exposure ages (CREs) of lunar meteorites. These authors each found that a steep spectrum of exposure ages should be expected, with the bulk of the objects having 4π CREs < 1 Myr. While lunar meteorites were not actually present in the collection at that time, the age spectrum of the available meteorites combined with the asymmetry in the time of fall (Wood 1961, Wetherill 1968) was largely able to rule out the Moon as a source of much meteoritic material. More recently, Gault (1983) performed some short-term simulations of the geocentric evolution of ejected lunar material showing that most material escaping the Moon is ejected to heliocentric orbit.

Information is also available on micrometeoroid streams (*e.g.,* Svedhem *et al.* 1994) observed in the near-Earth environs. These micrometeoroids have sometimes been hypothesized to be particles of lunar ejecta (see, for example, Dohnanyi 1977). Since the interpretation of these data is quite complex and few firm conclusions can be drawn, I will not consider this topic further.

3.2 Numerical Simulations of lunar ejecta

The Moon is bombarded by a variety of projectiles. The nature of the impactors is not important for our purposes, whether they be 'normal' Earth-crossing asteroids or comets (see discussion in Chpt. 6). I take as incontrovertible that, following impact, some impactors produce a (likely very small) fraction of ejecta fragments that reach speeds above the lunar escape velocity. The relevant acceleration

* This chapter is based on the paper: Gladman, B., J.A. Burns, M. Duncan, and H. Levison (1995), The Dynamical Evolution of Lunar Impact Ejecta, *Icarus* **118**, 302–321 [copyright 1995 by Academic Press, Inc.]

Table 3.1 Initial conditions for the Sun, Earth, and Moon used in the geocentric stage simulations. Masses are in solar masses, lengths in AU, and the unit of time is the mean solar year divided by 2π. The origin is at the 3-body barycenter.

Geocentric Initial Conditions			
	Sun	Earth	Moon
M	1.00000000	3.040438×10^{-6}	3.7536×10^{-8}
x	-0.00000051445068	0.16716510695187	0.16505548128342
y	0.00000298358568	-0.96935160427807	-0.96792780748663
z	-0.00000000034939	0.00011399064171	0.00007492647059
v_x	-0.00000308328240	1.00194735428418	0.98368251410153
v_y	-0.00000053203717	0.17321044856299	0.14390276658609
v_z	0.00000000005244	0.00002041304056	-0.00305048683857

mechanism is uncertain, and not important to this work; both a shock-wave interference model (Melosh 1984) and a vapor-plume acceleration model (O'Keefe and Ahrens 1986) have been proposed. In either case one expects a spectrum of sizes and velocities produced for the ejecta, with the number of launched objects decreasing rapidly with increasing velocity (Gault 1963, Vickery 1987, Frisch 1992). Thus it is likely that most escaping ejecta will leave the Moon's surface barely above the lunar escape velocity of 2.38 km/s (= $\sqrt{2GM_m/R_m}$, with G being the gravitational constant, M_m and R_m the lunar mass and radius, respectively), neglecting three-body effects. The question that will be addressed here is: what is the fate of these objects once they are ejected from the lunar surface and have escaped into geocentric orbit?

A first approach might be to model the particle, Earth, and Moon within the context of a circular restricted three-body problem. This level of approximation is surely too extreme since the Moon's orbital radius of 60 $R_\oplus$ is an appreciable fraction of the radius of the Earth's Hill sphere with respect to the Sun (which is about 230 $R_\oplus$). Thus, even mild increases in the ejecta's apogee, caused by the particles scattering off the Moon's gravitational field, allow their orbits to be strongly perturbed by the Sun even before the particles become unbound from geocentric orbit.

To improve on the three-body model, I undertook a full four-body treatment, with a massless test particle moving under the effect of the Sun, Earth, and Moon; the JPL ephemerides were used to construct initial conditions for the three massive objects, all having their correct relative orbits (Table 3.1). Some details on the method used in the geocentric integrations are presented in the next section. This model should be sufficiently valid during the brief interval that the meteoroid remains in geocentric orbit (called the 'geocentric stage'). Since the particles escape to heliocentric orbit rather quickly (taking typically much less than a few decades), the effects of the other planets on the fragment's evolution in this stage are negligible. However, in this geocentric phase the Moon's presence is critical to the orbital evolution. Once the particle reaches heliocentric space (*i.e.,* the heliocentric stage) a different model is necessary (see section 3.2.2).

3.2.1 Geocentric Phase

I have conducted a large number of simulations of impact ejections off the lunar surface. For each simulation 20 (sometimes 40 or 60) random impact sites were distributed over the lunar surface, weighted so that each unit area was equally likely. For our purposes, a uniform impact distribution is a good approximation; the Earth has little influence as a shield or a focus (see Bandermann and Singer 1973). From each site 18 particles were launched at 45° relative to the surface (Melosh 1989) and spaced evenly in local azimuth (Fig. 3.1).

In each simulation all particles have a common launch speed, with values ranging from 2.3 to 3.5 km/s. While the large number of events should provide a statistical view of the probable fates of most lunar fragments, launch speed is the single most uncertain parameter for this study. This is especially important because, as shown below, the fraction of particles that impact the Earth during the geocentric phase depends strongly on the launch velocity. I believe that the 2.4 km/s case is the most relevant to study since it is quite likely that the number of objects decreases quite rapidly as a function of launch speed; thus the largest number of escaping particles will do so at just above the escape speed (see Burns *et al.* 1984 and Wetherill 1984 for discussions and relevant references).

While a 45° ejection angle may characterize crater excavation flows (Melosh 1989), a spallation process may produce typical ejection angles that are somewhat different (Frisch 1992); similarly the distribution of ejecta masses and velocities may differ. A change in ejection angle will simply alter the direction of the residual velocity vector (defined below), and should have no effect on the results since a large number of impacts have been studied.

After ejection, the particles' orbits are evolved using a sixth-order explicit symplectic integration algorithm (see Gladman *et al.* 1991) using the full 4-body equations of motion. The particles are followed until they impact the Earth or Moon, or they escape to heliocentric orbit. After reaching 10 Hill sphere radii from the Earth (whose Hill radius is $\simeq 0.01$ AU) the particles have their heliocentric orbital elements computed in order to transfer them to the heliocentric stage simulation (Sec. 3.2.2).

The integrator is a brute-force method which simply evaluates the interparticle forces and integrates Newton's equations. Therefore, each of the four particles are given a mass and radius (the test particle has negligible mass and size) as well as initial position and velocity vectors. The algorithm advances the particles forward one time step, detecting collisions by monitoring the relative distance of

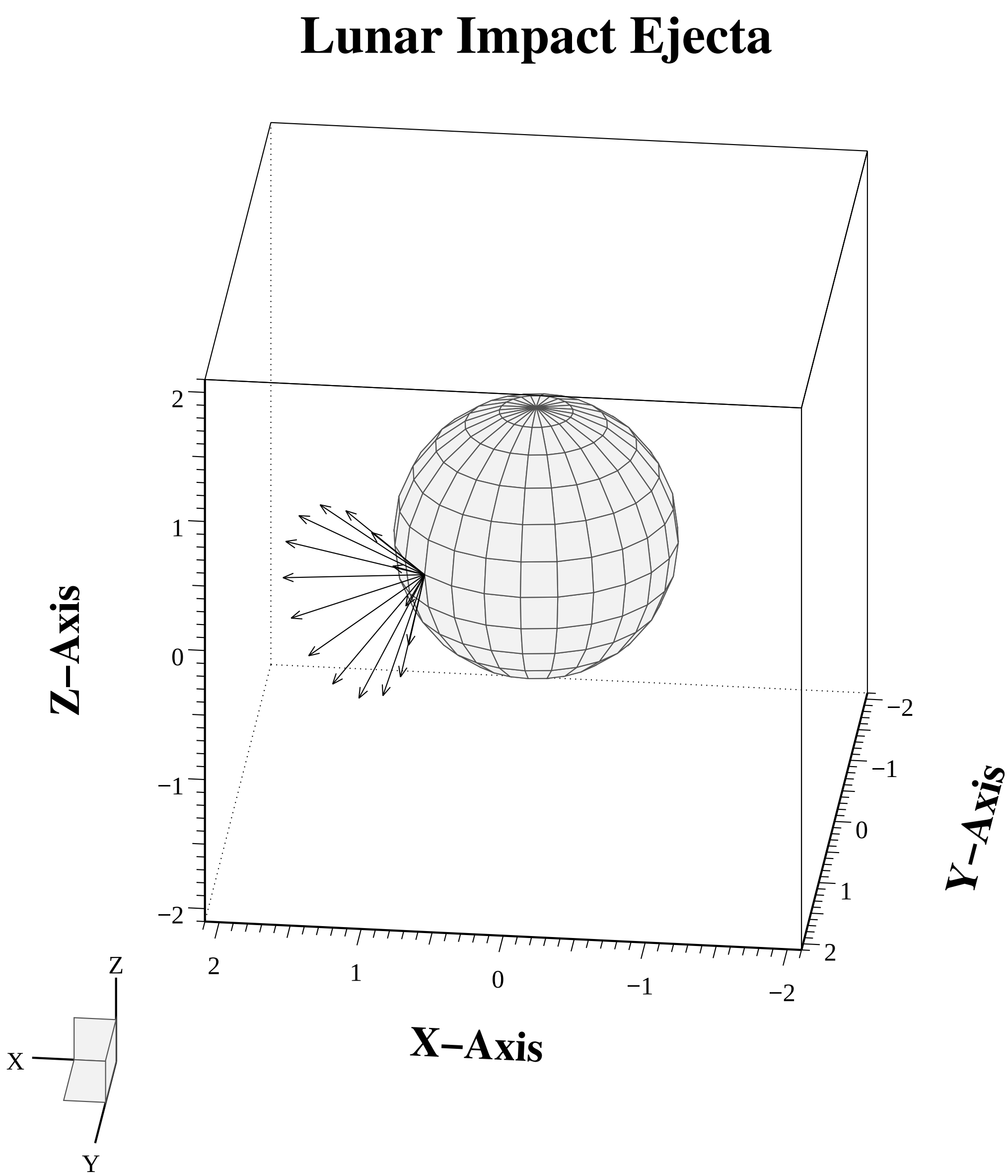

Figure 3.1 The initial velocity vectors of particles launched from a single lunar impact. Impact sites are chosen randomly on the surface of the Moon (equally probable per unit area). From each site 18 particles are ejected, spaced equally in azimuth on a cone of 45^o opening angle (only 15 vectors are shown, for clarity). In this figure the positive X axis points in the direction of the Moon's motion, the positive Y axis points towards the Earth, and the scales are in lunar radii. All particles are launched with a common speed.

the small particle from the Earth and Moon. Since the CPU time required for the geocentric integrations is relatively small, I have used a time step (of 0.04 hours) small enough that the truncation error is below the machine precision (of $\sim 10^{-16}$) for the integration of the Moon's orbit. I have handled close approaches to the Earth and Moon by simply lowering the time step, and insured that the (statistical) results have no dependence on the time step.

Due to the large number of papers in the literature that attempt to establish links between certain meteorites and their launch locations I will spend considerable time discussing the details of the geocentric dynamics. The casual reader may wish to skip to the final paragraph of section 3.2.1 (p. 30) at this point.

Table 3.2 shows the outcomes of the geocentric simulations as a function of the launch speed from the lunar surface. For several launch speeds, more than one simulation was performed; this gives us some estimate of the sampling error due to a finite number of impact sites and launch azimuths. The gross histories of these particles are relatively easy to understand. At $v_l = 2.4$ km/s, particles are barely above the lunar escape speed and by the time they have reached several tens of lunar radii, almost all of their launch velocity (relative to the Moon) is gone; thus they share the nearly circular lunar orbit with its 1 km/s geocentric velocity. Such particles will suffer many strong repeated scatterings by the Moon. (Note that my qualitative discussions, but not the simulations, of the dynamics ignore the complexities of the Moon's eccentric and inclined orbit; these 5% effects are unimportant to a general understanding of the dynamics.)

Interestingly, the Moon is unsurpassed by other planetary satellites (except for Charon) in its ability to scatter particles that share similar orbits. The power of the Moon in this regard can be easily understood. The mean lunar orbital velocity is $\simeq 1$ km/s, while the Moon is capable of providing a maximum gravity assist (in a surface-skimming close encounter) of $v_{esc}/\sqrt{2} \simeq 1.7$ km/s. Thus the Moon can cause major changes in the geocentric orbital elements of particles in orbits similar to its own; indeed a single close encounter can be sufficient to eject particles from geocentric orbit. In fact, approximately 15% of the initially launched particles receive their 'gravity assist' out of geocentric orbit *during* their initial escape from the Moon; these particles make up the apparent clump near $a \simeq 1.05$ AU, $e \simeq 0.045$ to be seen later in Fig. 3.6; this interesting phenomenon is further explored in Appendix A. Compared to the number of particles that escape to heliocentric space, relatively few will suffer the fortuitous chain of events that walk their perigees down to the Earth's radius. The roughly 3% that do impact the Earth via this mechanism all require many months (to a few years) and several strong lunar perturbations to do so. It is much more likely that they will receive a perturbation that ejects them, although $5 - 10\%$ recollide with the Moon during this process. (Since the initial orbits are similar to the Moon's, the encounters occur at low relative velocity, which enhances the Moon's gravitational cross section.) For higher launch velocities, lunar re-impacts become very rare.

Table 3.2 For each geocentric-stage simulation (in which all particles are launched from the Moon at a single launch speed v_l), the table lists the total number N of particles launched (18 particles per impact site), the percentage Esc of particles that escape to heliocentric space, and the percentages that impact the Earth ($\oplus$) and Moon (M). The five simulations marked * were used as initial conditions for the heliocentric simulations.

Geocentric Stage Results				
v_l (km/s)	N	Esc(%)	% $\oplus$	% M
2.3	360	0.0	0.0	100.0
2.4	360	88.1	3.3	8.6
2.4	360	91.7	3.9	4.4
2.4	360	90.0	3.3	6.7
2.4	720	91.1	2.2	6.7
2.4*	360	90.5	3.1	6.4
2.5	360	92.8	5.5	1.7
2.6	360	80.0	18.9	1.1
2.6	720	83.7	16.0	0.3
2.6*	360	81.7	18.0	0.3
2.8	360	81.4	18.1	0.5
2.8	360	77.2	22.5	0.3
2.8*	360	80.2	19.2	0.6
3.0	360	95.3	3.9	0.8
3.0*	360	94.7	5.0	0.3
3.2	360	100.0	0.0	0.0
3.2	1080	99.3	0.7	0.0
3.2*	360	99.1	0.6	0.3
3.5	360	100.0	0.0	0.0

Fig. 3.2 shows the evolution for a typical particle escaping at 2.4 km/s; note the almost-circular initial orbit and the many lunar close encounters.

In each simulation all particles have a common launch speed, with values ranging from 2.3 to 3.5 km/s. To help interpret the results in Table 3.2, let us for the moment ignore the presence of the Earth and Sun, and study particles as they escape the lunar gravitational field (Fig. 3.3). Far from the Moon the particles will retain some 'residual velocity' $\vec{\boldsymbol{v}}_{\boldsymbol{r}}$ which is measured with respect to the (moving) Moon. The magnitude and direction of $\vec{\boldsymbol{v}}_{\boldsymbol{r}}$ will differ depending on launch speed, site, and direction; furthermore, the final orientation of $\vec{\boldsymbol{v}}_{\boldsymbol{r}}$ will be influenced by the bending of the trajectory that occurs as the particle escapes from the lunar field. By considering the geometry of the outgoing hyperbolic orbits one can show, for a 45^o ejection, the angle (in radians) that the path is deflected from its initial launch direction (see Fig. 3.3a) to be:

$$\delta(v_l) = \arccos\left(\frac{-1}{\sqrt{x^2 + (x-1)^2}}\right) + \arctan\left(\frac{x-1}{x}\right) - \frac{3\pi}{4}, \tag{3.1}$$

where the square root of x is the dimensionless ratio of the launch speed to the lunar escape speed ($x \equiv v_l^2 R_m / 2GM_m$); relation (3.1) is plotted in Fig. 3.3b. In agreement with one's intuition, particles launched at high speeds are scarcely turned by the Moon's gravity while the trajectories of those thrown at near the escape speed are pulled significantly away from the local vertical.

Once free of the lunar gravitational field, the residual velocity vector will have a magnitude of roughly

$$v_r \simeq \sqrt{v_l^2 - (2.38\ \text{km/s})^2} \tag{3.2}$$

from conservation of energy, again ignoring the complexities of three-body effects. As will now be discussed, the particle's fate is largely determined by the 'escape angle' θ between $\vec{\boldsymbol{v}}_{\boldsymbol{r}}$ and the Moon's velocity vector $\vec{\boldsymbol{v}}_{\boldsymbol{m}}$ at the time of escape from the lunar gravity field.

To estimate the initial *geocentric* velocity $\vec{\boldsymbol{v}}_{\boldsymbol{i}}$ that appears in the four-body integration, consider the following idealization: the residual component is added vectorially to the lunar orbital velocity $\vec{\boldsymbol{v}}_{\boldsymbol{m}}$ of magnitude $\simeq 1.0$ km/sec to obtain $\vec{\boldsymbol{v}}_{\boldsymbol{i}}$, as shown in Fig. 3.3a. The angle θ between $\vec{\boldsymbol{v}}_{\boldsymbol{r}}$ and $\vec{\boldsymbol{v}}_{\boldsymbol{m}}$ will be called the 'escape angle' and is very important in determining the potential fate of the escaping particles. For a given v_r the fastest (i.e., largest v_i) escaping ejecta will clearly have $\theta = 0$; such particles do not originate from the leading point of the Moon (because the ejecta there are launched at 45^o from the lunar motion), nor from an annulus 45^o away from the leading point (because such particles still suffer deflection unless $x \gg 1$). Instead, the fastest ejecta originate on an annulus $(45 + \delta)^o$ away from the leading point and, even then, only on the small portion of the ejection cone that points parallel to the lunar motion. Similarly, the *slowest* initial

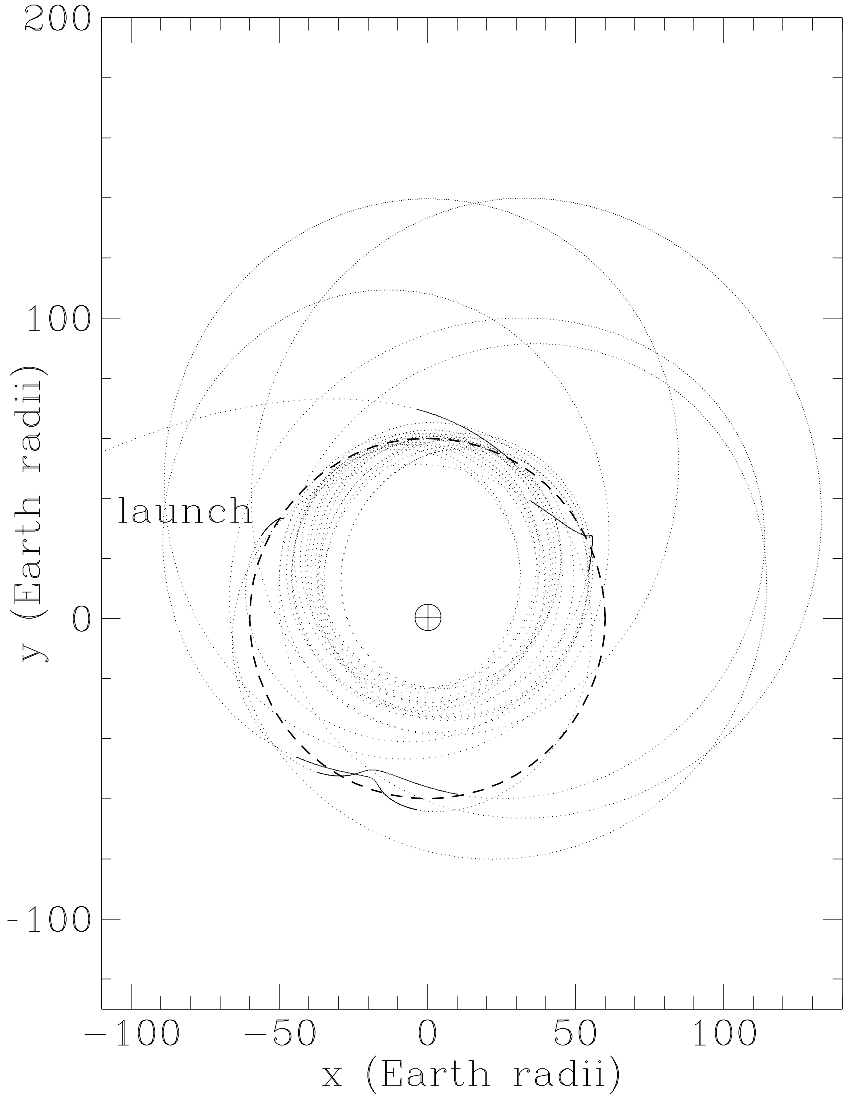

Figure 3.2 The path of a particle escaping from geocentric orbit is shown in a non-rotating geocentric frame, projected onto the ecliptic plane. The particle was launched from the lunar surface at 2.4 km/s. Points are plotted every 3.3 hours unless the particle was within 1 Hill sphere of the Moon (about 9 $R_\oplus$), in which case points are plotted every 0.3 hours (and appear as a solid curve). The dashed circle is at the mean lunar orbital radius (60 $R_\oplus$). The particle is launched from the region just to the right of the word 'launch', outbound on the thick line (due to the Moon's proximity). The multiple close encounters with the Moon before a gravity assist produces escape are typical for particles launched at 2.4 km/s. The particle escapes to heliocentric orbit to the left of the figure after a close encounter with the Moon that provides it with geocentric escape speed. (The Earth's size is not to scale.)

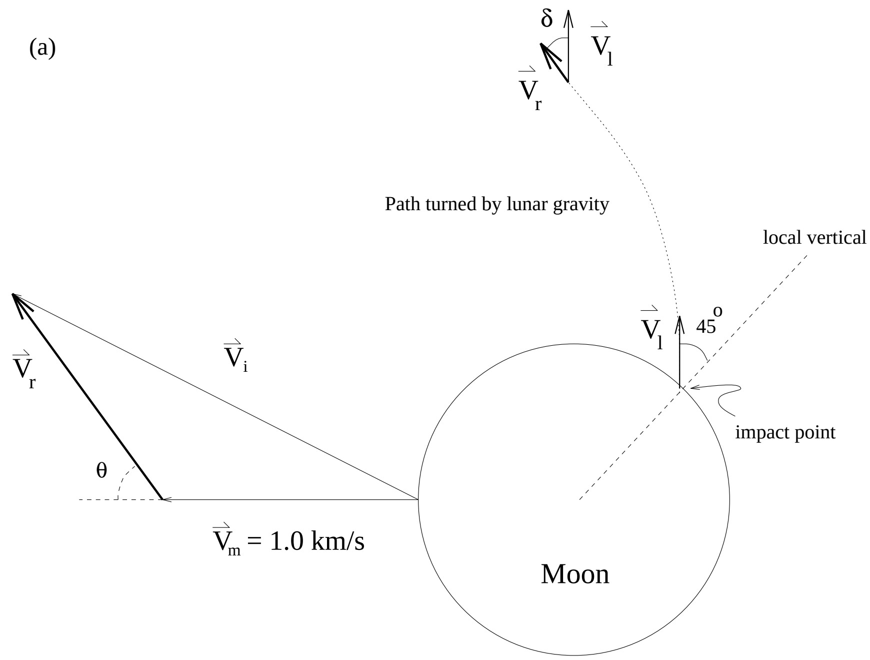

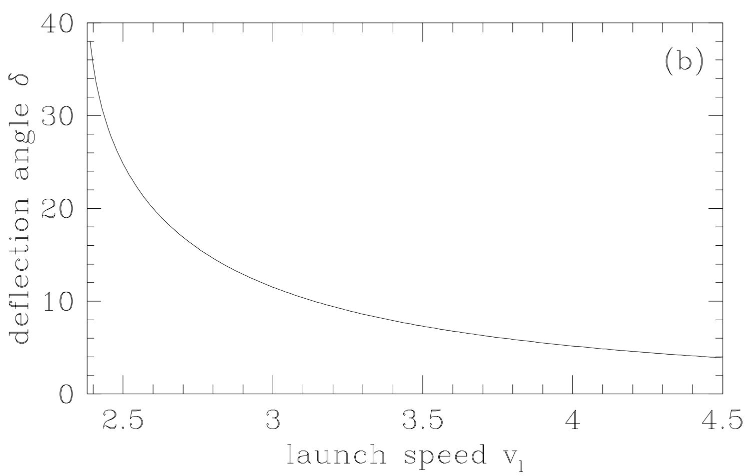

Figure 3.3 (a) A schematic diagram defining various angles for a particle launched from the Moon's surface. Ejecta are thrown at speed v_l and an angle of 45^o to the local vertical off the lunar surface. Due to lunar gravity, the particles are slowed, and their final residual velocity $\vec{v}_r$ (measured relative to the Moon) is turned through an angle δ. The initial *geocentric* velocity $\vec{v}_i$ is the vector sum of $\vec{v}_r$ and $\vec{v}_m$, the Moon's orbital velocity. The angle θ between $\vec{v}_m$ and $\vec{v}_r$ is called the escape angle. Note that *i*) the velocity vectors are not drawn to scale, *ii*) $\vec{v}_r$ and $\vec{v}_l$ are shown twice on the diagram, *iii*) the figure is for a degenerate planar case, and *iv*) the figure geometry is similar to the launch of the particle of Fig. 3.2. (b) The angle δ, given by (3.1), through which particles departing the Moon are deflected from their launch direction, as a function of launch speed v_l.

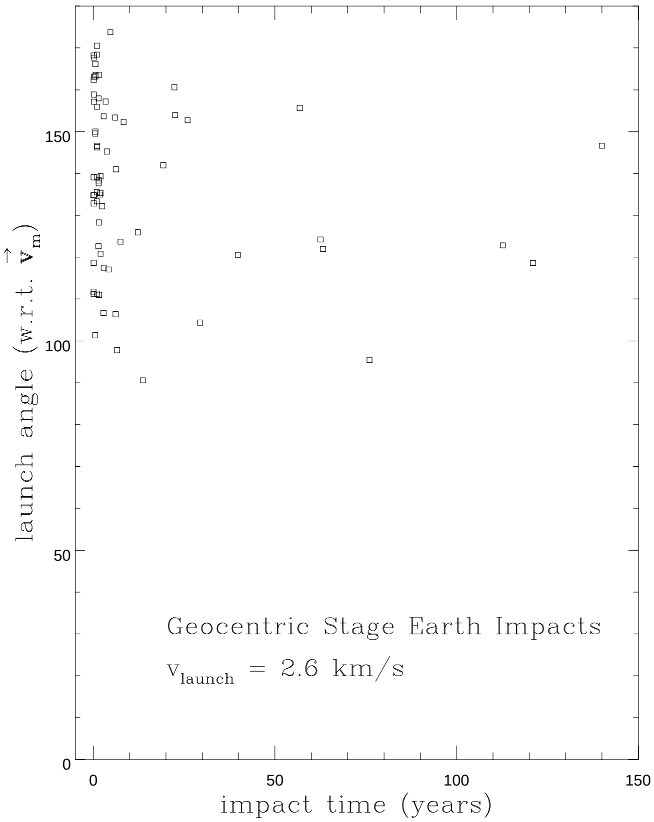

Figure 3.4 The angle between the ejection vector and $\vec{v}_m$ for particles that eventually impact the Earth in a $v_l = 2.6$ km/s geocentric stage simulation. The time until Earth impact is plotted on the abscissa. Particles with angles $< 90^o$ do not impact the Earth since they exceed geocentric escape velocity once free of the lunar gravitational field, and thus escape immediately to heliocentric orbit.

geocentric speeds (which lead to the highest geocentric eccentricities) originate from points $(45 + \delta)^o$ away from the lunar trailing point.

With this as background, let us return to Table 3.2. According to Eq. (3.2), particles with $v_l = 2.6$ km/s escape the lunar field with $v_r = 1.0$ km/s and thus their residual speed equals the lunar orbital speed. If this residual component is vectorially opposite to the lunar orbital velocity ($\theta = 180^o$), the particle will find itself at rest with respect to the Earth after clearing the Moon's gravitational field; thus it will fall directly into the Earth. Particles of this launch speed whose residual components are only roughly anti-parallel to the Moon's velocity will acquire small geocentric velocities; thus they will have prograde geocentric orbits of high eccentricity and, since $v_i < 1$ km/s, will have semimajor axes less than the lunar orbital radius. Subsequent lunar perturbations will push many such particles towards $e \simeq 1$ causing them to impact the Earth. Since their semimajor axes are smaller than the lunar orbit, the Moon's perturbations will have to add

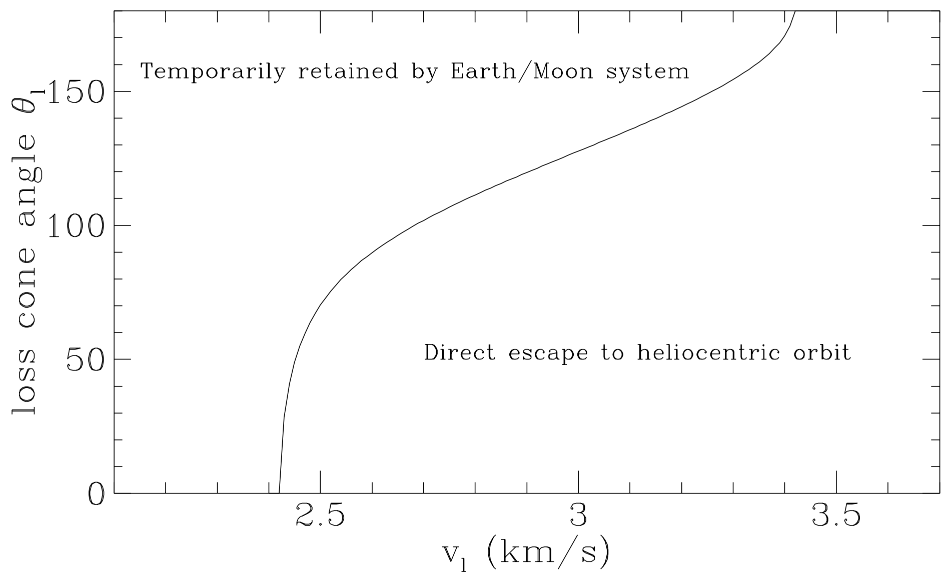

Figure 3.5 The opening angle θ_l of the geocentric loss cone to immediate heliocentric orbit is shown as a function of the launch speed. Particles that have escape angles (after deflection) $\theta < \theta_l$ immediately escape geocentric orbit unless they impact the Earth before reaching their first perigee. The loss cone axis is along the direction of $\vec{\boldsymbol{v}}_{\boldsymbol{m}}$, pointing forward from the Moon's leading point.

constructively to boost these particles finally free from Earth orbit. These two facts explain the increase in Earth impacts at this speed seen in Table 3.2. At the other extreme, $v_l = 2.6$ km/s particles with escape angles less than 90^o have $|\vec{\boldsymbol{v}}_{\boldsymbol{i}}|$ greater than the local geocentric escape speed (of $\sqrt{2}v_{\rm orb} \simeq 1.4$ km/s at the distance of the lunar orbit), and thus exit immediately from geocentric orbit. Figure 3.4 shows clear evidence for this: the Earth is impacted by no particles with an ejection vector within about 90^o of the lunar velocity vector (at launch).

We generalize the above discussion to introduce the concept of a 'loss cone', which is the totality of all escape directions (indicated by $\vec{\boldsymbol{v}}_{\boldsymbol{r}}$) that provide immediate access to heliocentric space. As seen in Fig. 3.3a, these escape directions all lie within some angle θ_l of the lunar motion (i.e., $\theta < \theta_l$ within the loss cone). Fig. 3.5 shows how the opening angle of the loss cone (symmetric about $\vec{\boldsymbol{v}}_{\boldsymbol{m}}$) depends on the ejection velocity; we note that at $v_l \simeq 2.6$ km/s, θ_l is 90^o, so that for this case all (post-deflection) particles moving 'forward' after escaping the lunar field are lost.

At ejection velocities above about 2.6 km/s (where direct transfers to the Earth in a single orbit become permitted since $v_r \geq v_m$), three classes of behavior are possible.

1. Immediate escape (if $\theta < \theta_l$);
2. Immediate collision with Earth (geocentric eccentricity ~ 1); and
3. Geocentric orbit with subsequent lunar perturbations.

Particles in class 1 can still collide with the Earth if, on their outbound path, their trajectories intercept our planet's surface. That this fate occurs often at these velocities can be stressed by considering that at $v_l = 2.8$ km/s a particle launched with $\vec{v}_r$ pointed directly at the Earth has $v_i \simeq 1.7$ km/s and sees a gravitationally enhanced cross-sectional area (corrected to v_∞) of roughly 150 times the Earth's geometric area! Above 2.8 km/s significant numbers of particles in class 3 turn out to have very large eccentricities due to the fact that the most likely escape angle is just outside of the loss cone when the loss cone angle is greater than 90^o (due to the $\sin\theta$ dependence of available area on a unit sphere). This explains why the collision percentage at this velocity remains high. Another point of interest is that above 2.6 km/s all of the particles that do not fall inside the loss cone will be on *retrograde* geocentric orbits.

At even higher launch speeds the 'loss cone' for immediate escape widens until at just above 3.4 km/s a particle launched from anywhere on the lunar surface, regardless of the direction of its residual velocity, will leave the lunar field retaining at least the geocentric escape speed. An Earth impact can now only occur if the outgoing path of the particle intercepts the Earth; there will be no subsequent chances. In fact, the simulation for $v_{ej} = 3.5$ km/s recorded no impacts with the Earth or Moon; all particles escaped to heliocentric orbit. For a particle ejected at 3.2 km/s on a trajectory pointing roughly at the Earth, the gravitationally enhanced capture-area is about 20 times the Earth's geometric cross-sectional area. This covers 0.13% of a unit sphere centered on the Moon, so from the 1800 particles launched at this velocity one statistically expects about 2 direct (before first perigee) impacts. In fact 4 were observed.

The claim was made above that there should be no statistical dependence on the 45° angle assumed for the initial launch cone. This was confirmed in a set of experiments presented in Table 3.3, in which the launch velocity was held fixed at 2.4 km/s but the cone angle of the ejected particles was varied. There is no apparent dependence on the angle of the launch cone for the fractions of particles that suffer each fate.

These results on the short-term fate of lunar ejecta, as given in Table 3.2, compare well with those of Gault (1983). My initial conditions differ from Gault's in that I have used a fully three-dimensional model with the Moon in its proper orbit, and I have broken down the statistics by launch speed. Gault's percentages effectively assume a flat spectrum for the numbers of ejected objects as a function of launch speed; when weighted in a similar way, the results agree. In addition, all my geocentric simulations had maximum time limits of 300 years (rather than Gault's 30 years). Gault found that 2 of his 768 particles remained in geocentric orbit after 30 years, while I have no objects (out of more than 8000) that survived as long as 300 years. Escape from the Earth's Hill sphere typically occurs within two months for high-velocity particles inside the loss cone, and within a few years for low-velocity ejecta that require many lunar scatterings to escape. Particles

Table 3.3 For each geocentric-stage simulation (in which all particles are launched from the Moon at 2.4 km/s), the table lists the percentage Esc of particles that escape to heliocentric space and the percentages that impact the Earth ($\oplus$) and Moon (M). The cone angle is the angle with respect to the local vertical of the initial velocity vectors. The 45° simulations are reproduced from Table 3.2

Dependence on cone angle			
Angle	Esc(%)	% $\oplus$	% M
10°	90.5	3.1	6.4
25°	93.0	2.8	4.2
45°	88.1	3.3	8.6
45°	91.7	3.9	4.4
45°	90.0	3.3	6.7
45°	91.1	2.2	6.7
45°	90.5	3.1	6.4
60°	91.7	2.2	6.1
75°	91.6	1.7	6.7
89°	90.7	3.3	5.8

impacting the Earth or Moon usually take several years before doing so, with re-impacts into the lunar surface occurring somewhat sooner. The time distribution of geocentric impacts onto the Earth is shown for one simulation in Fig. 3.4. Note that the lunar meteorites with only upper bounds on their 4π CREs (Table 2.1) could be objects that were delivered to the Earth during their geocentric phase.

3.2.2 Heliocentric Phase

Once the particles move onto a heliocentric orbit, the previous numerical model will be insufficient to describe accurately the continuing orbital evolution of the particles. Experiments show that modelling the system as an Earth–Sun–fragment restricted three-body problem totally fails to capture important facets of the problem. As the Earth's orbit itself illustrates, on a time scale of 10^5 years the influence of the other planets cannot be neglected. To the lowest approximation, the Sun, Earth, and Venus form a three-body subsystem; the planets exchange angular momentum on a time scale of 10^5 years. Jupiter then modulates this interchange on the slightly longer time scale of a few hundred thousand years. I have thus used a regularized, mixed-variable symplectic (RMVS) code in order to perform a full N-body integration of the motion of the test particles. The algorithm is discussed in Appendix B.

The long-term model for the heliocentric simulations includes all planets from Mercury out to Saturn, with the Earth-Moon system in this stage considered as

Table 3.4 Planetary heliocentric ecliptic initial conditions used in the heliocentric stage simulations (note that the Earth-Moon barycenter is integrated). Masses are in $4\pi^2$solar masses and lengths in AU, so that the unit of time is the mean solar year and $G = 1$. The solar radius given is the inner boundary used by the simulations.

Heliocentric Initial Conditions		
Object	Mass	Radius
x	y	z
v_x	v_y	v_z
Sun	39.478417604357354	(0.01)
0	0	0
0	0	0
Mercury	$6.5539573684104773\times10^{-6}$	$1.5635249278985897\times10^{-5}$
0.27017937502239237	-0.32228686492574826	-0.051128121581458611
5.8318090354768924	7.0975268449586078	0.044360942040638282
Venus	$9.6636715601426955\times10^{-5}$	$4.0455121263968631\times10^{-5}$
-0.49162157533769937	-0.53077934414038334	0.021133635065132573
5.3678514269101589	-5.0550501344200581	-0.37886320104278040
Earth-Moon	$1.2003167407831363\times10^{-4}$	$4.2634296665828146\times10^{-5}$
-0.82923885617600000	-0.54695064895900000	0.0000610063730000
3.5614549941450000	-5.2271971541900000	0.0006199730700000
Mars	$1.2740275019074827\times10^{-5}$	$2.2707542454345911\times10^{-5}$
-1.5085575023881349	0.70508397896622987	0.051870243545010893
-1.9717133809842210	-4.1945337139270886	-0.039379874024183254
Jupiter	$3.7693444538248594\times10^{-2}$	$4.7721267465874447\times10^{-4}$
-5.3402409482531853	-1.0991402891868280	0.12414342224252320
0.52021430151605930	-2.5741732287263259	-0.00099790164736608
Saturn	$1.1284384051552765\times10^{-2}$	$4.0107522733610672\times10^{-4}$
7.8893232093398913	-5.8757155350551813	-0.21133975684872742
1.1066909037177797	1.6285514822320565	-0.072412495822685855

a single particle at the Earth-Moon barycenter (Table 3.4). The orbital motion of the Moon may be ignored in the heliocentric phase since the (gravitationally focussed) collision cross-section of the Earth is roughly two orders of magnitude larger; this approximation is supported by Whipple and Shelus (1994), who found that the Moon was unimportant in the dynamical evolution of the near-Earth asteroid Toutatis. Particles are removed from the integration once they (i) collide with a planet, (ii) cross the orbit of Jupiter, or (iii) have their perihelia reduced below a lower limit $q_{min} = 0.01$ AU (about 2 solar radii; these particles have become Sun-grazers, a common fate which will be discussed below). The time step used for the lunar simulations (0.015 years) was sufficient to allow for accurate integrations on 10-Myr time scales provided that the particle semimajor axes remained above 0.3 AU; no particles were observed to violate this condition. Within this model, the dynamical evolution of the particles was followed for ten million years (the largest CRE age of a known lunar meteorite).

I have adopted a purely gravitational model for our simulations of 10^7 years duration. If the lunar meteorites existed as decimeter-sized or larger rocks while in space (Warren 1994), radiation pressure forces are negligible over lifetimes of < 10 Myr (see Burns *et al.*, 1979, Eq. 50); these effects are even less relevant for the short CRE age (< 50 kyr) objects. The lifetimes of $\sim 10^2$ g meteoroids at 1 AU against disruptive collisions are estimated by Grün *et al.* (1985) to be only 10^5 years. However, this would seem to contradict the existence of Asuka-881757/Y793169 with its $\simeq 1$ Myr CRE age, and Yamato 81912/86032 with its $\simeq 10$ Myr CRE age (since both of these meteoroids were likely only a few thousand grams while in space) unless the collisional lifetime rises precipitously for masses greater than 10^2 grams. Since the collisional lifetimes derived by Grün *et al.* are intended to model the destruction of dust and are highly model dependent, I will assume below that collisional effects are negligible for lunar meteoroids over $10^6 - 10^7$ year time scales. It turns out that more than 90% of the meteoroids that will eventually return to the Earth do so well within 1 Myr, so if the collisional lifetimes are in fact $\sim 10^6$ years it will have a negligible effect on the age spectrum of the returning objects (see Secs. 3.4 and 4.3).

The usual proviso of numerical celestial mechanics applies to the long-term heliocentric integrations. The Lyapunov times of these particles are so short (several hundred years, Whipple and Shelus 1994) that one cannot claim that the computed trajectories are accurate for specific particles. The calculations must be viewed as statistical studies of the fates of large numbers of particles. Milani *et al.* (1989) and Levison and Duncan (1994) discuss this point further.

After escape from the Earth's influence in the geocentric simulation, particles were inserted into the RMVS simulation with the same position and velocity relative to the Earth-Moon barycenter as they had at the end of the geocentric simulation. The orbital elements for the $v_l = 2.4$ km/s simulation at the time of escape from the Earth-Moon system are shown in Fig. 3.6. The semimajor axes

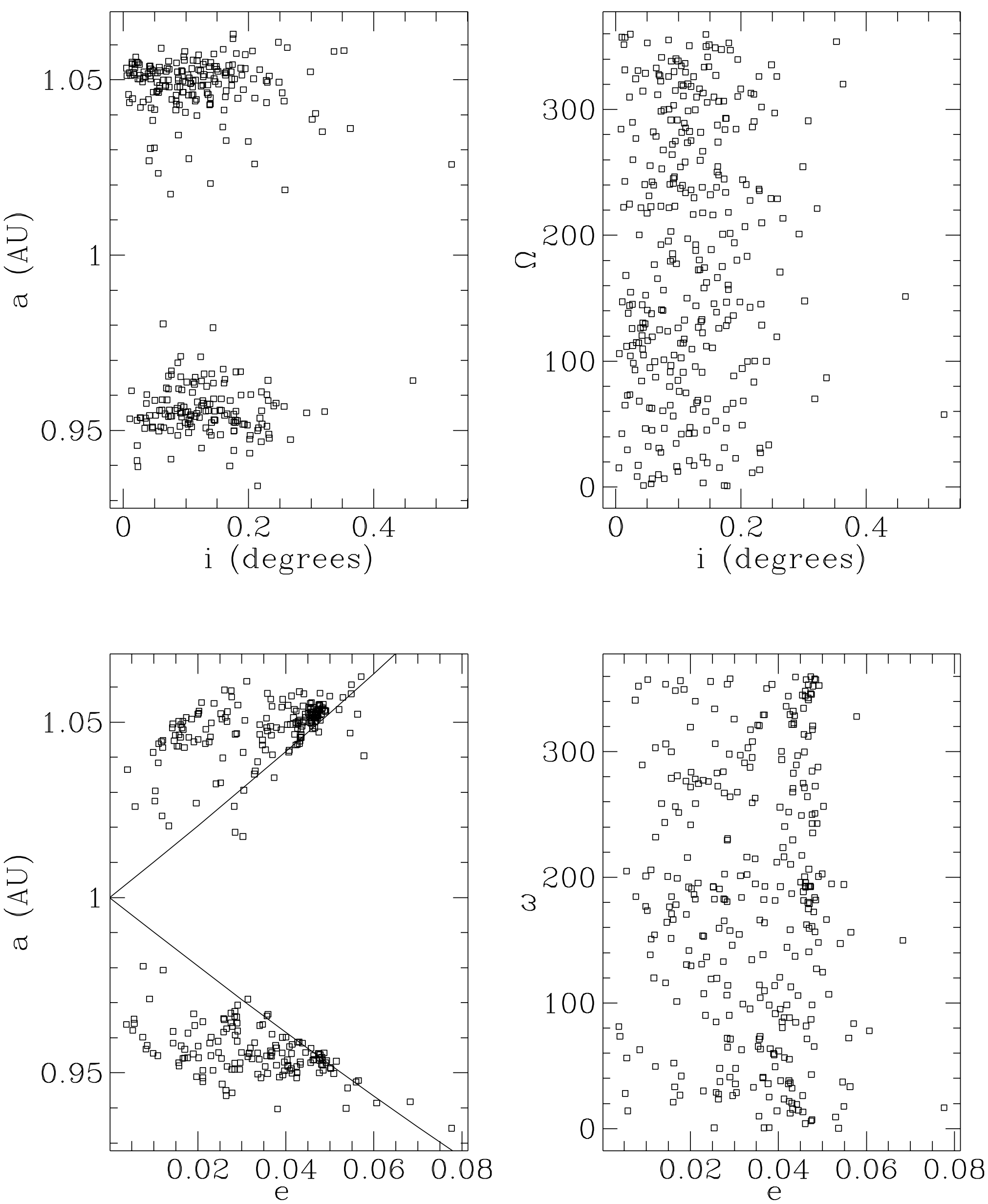

Figure 3.6 The initial orbital elements after escape from the Earth/Moon system for 326 particles originally ejected at 2.4 km/s from the lunar surface. The inclinations (in degrees) are with respect to the ecliptic plane. The two lines in the (a, e) plot show the loci of $q = a(1 - e) = 1$ AU (upper line) and $Q = a(1 + e) = 1$ AU (lower line) for reference; particles to the right of these lines cross the Earth's mean orbit. Note that many of the particles are on geometrically non-Earth-crossing orbits (see text).

and eccentricities are those that one would expect for particles that have barely escaped from the Earth-Moon system through the collinear Lagrange points of the Earth-Sun restricted three-body problem. Note the very low inclinations and eccentricities which indicate that many particles escape the Earth/Moon system with only several hundred m/s excess velocity. At these very low relative velocities particles are deflected enough on their outbound paths that they appear to be on geometrically non-crossing orbits in Fig. 3.6, having receded to several Hill sphere radii. However, if time were run backwards, the focussed gravitational cross-section of the Earth is sufficient to bring them to crossing (see, for example, the discussion of Greenberg *et al.* 1991).

The distribution of the particles in Fig. 3.6 is effectively controlled by the requirement that they have almost no velocity relative to the Earth and that they conserve their Jacobi constants on this short time interval. Note the absence of $a = 1$ particles. These are forbidden since an $a \simeq 1$ particle with low eccentricity would be on a horseshoe orbit (Dermott and Murray 1981) and never approach the Earth; clearly a particle launched from the Earth cannot be on such an orbit (by invariance under time reversal). I have studied the $v_l = 2.4$ km/s case in the greatest detail, believing it to be the speed near which most escaping lunar ejecta is launched (as discussed earlier). Given the re-collision rates discussed below, this case is even more important to study since it contributes the largest fraction of the returned meteorites that escape to heliocentric space. The initial conditions for the higher launch speed simulations look similar to Fig. 3.6, but the particles extend to higher eccentricities and inclinations, as well as having a few $a = 1$ particles (which all have high eccentricity).

The particles now proceed to be scattered by the Earth's gravitational field at each conjunction. Some collisions occur, but most objects receive a relative velocity change due to a gravity assist. The a, e evolution of the particle swarm for the 2.4 km/s simulation is shown in snapshots at $10^3, 10^4, 10^5$, and 10^6 years in Fig. 3.7. The general trend is for objects to increase their eccentricities and to walk along the web of lines which maintain either the particle's aphelion or perihelion at one of the terrestrial planets, because on short time scales the local Tisserand invariant T:

$$T = \frac{1}{a'} + 2\sqrt{a'(1-e^2)}\cos i, \tag{3.3}$$

is conserved (Danby 1988); here a' is the ratio of the particle's semimajor axis to that of the scattering planet, and i is their mutual inclination. Note that the lines of $T = 3$ corresponding to small Earth-encounter velocity are not quite the same as $q = 1$ or $Q = 1$ (cf. Greenberg and Nolan 1993). The mean inclination also rises until the particles are roughly uniformly distributed up to 30 degrees (the inclinations at 10^4 years are shown later in Fig. 3.12). After 10^4 years three particles have had close encounters with Venus (they can be easily identified in Fig. 3.7), and after 10^5 years a few have had close approaches with Mars. The

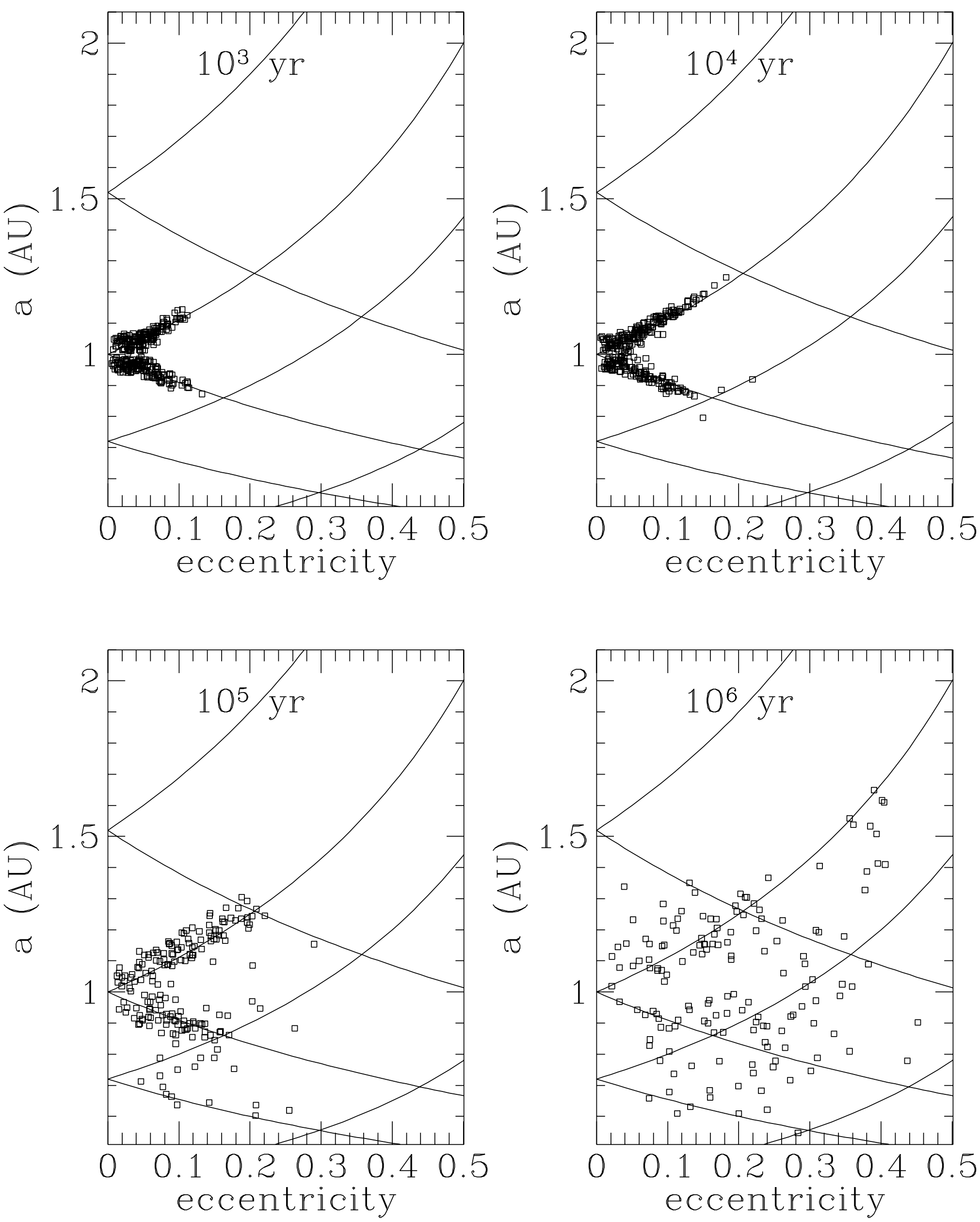

Figure 3.7 Semimajor axes and eccentricities for the surviving particles (from the $v_l = 2.4$ km/s simulation) after 10^3, 10^4, 10^5, and 10^6 years. The lines show perihelia/aphelia at Mercury, Venus, Earth, and Mars; for example, the upper branch of particles in the upper left plot all have perihelia at 1 AU. Particles tend to diffuse along this web of lines due to conservation of the Tisserand parameter with the dominant perturber. This is disrupted by secular perturbations and close encounters with multiple planets.

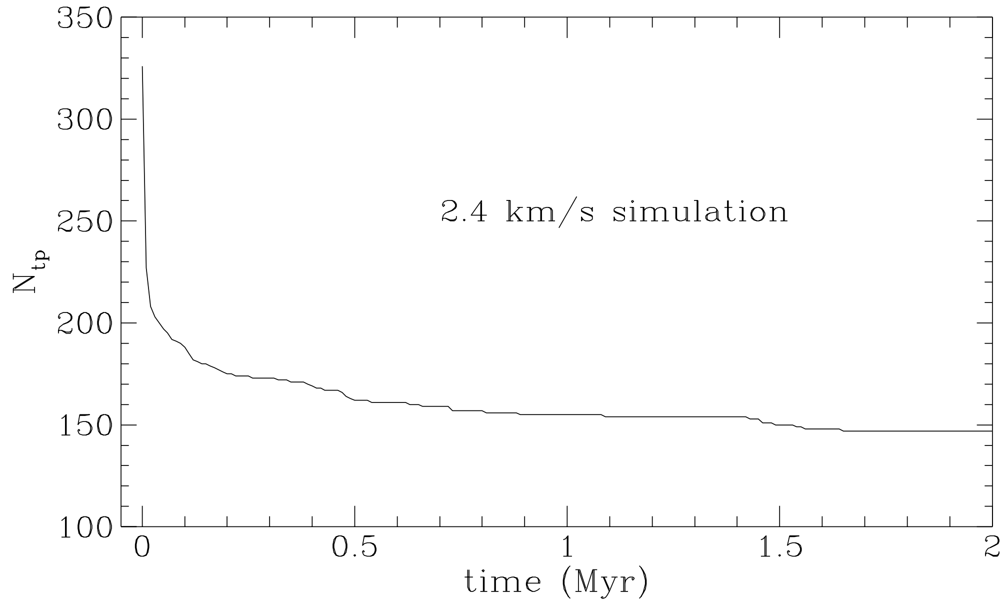

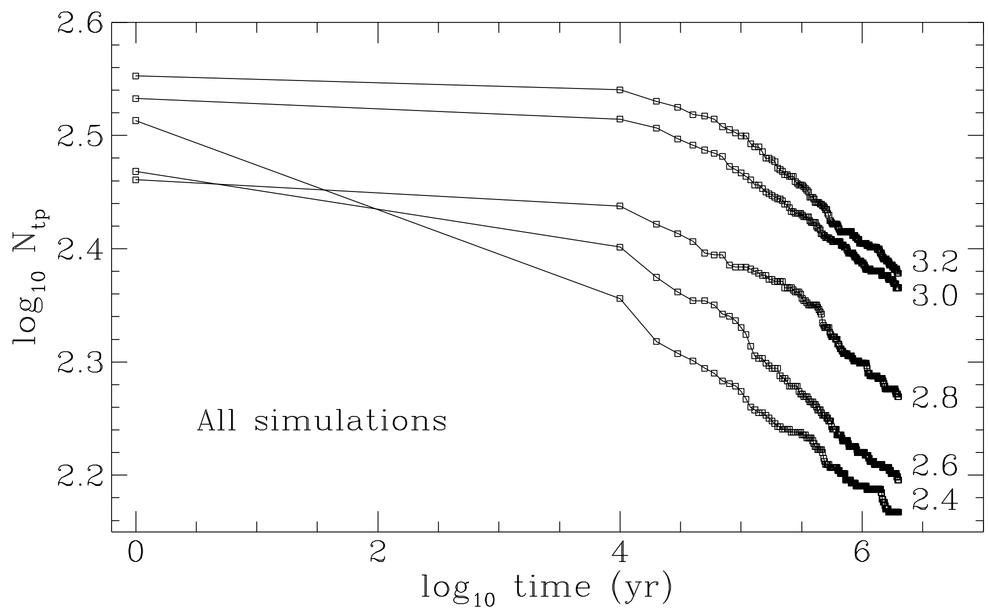

Figure 3.8 The number of particles remaining in a simulation is plotted as a function of time, on a linear plot for the 2.4 km/s simulation (upper panel) and on a log-log plot for all the simulations (lower panel). Loss mechanisms are summarized in Table 3.5. and are not confined to re-collision with the Earth. Note the extremely large loss rate (all from Earth collisions) in the initial stages. The labels in the bottom panel indicate the initial launch speed of the particles. Note that the log-log plot shows that all the simulations eventually follow a common logarithmic fall-off, indicating a similar loss mechanism.

first collision with a planet besides the Earth is, as one would expect, with Venus at 73,700 years after launch. The number of particles remaining as a function of time for the simulations is shown in Fig. 3.8. Note the *extremely* high collision rate initially; more than a third of all the particles that started the 2.4 km/s simulation re-impact the Earth within 50 kyr. The relative loss rate for all the other ejection velocities is also highest in the first 50 kyr. I show below that this is in agreement with the available ages of the lunar meteorites. After the initial burst of collisions, Fig. 3.8 shows that all of the simulations level off to a similar loss rate, which decreases roughly as $1/t$, and seems to be a common result in simulations of swarms of test particles affected by nearby planets (Holman and Wisdom 1993).

The extremely steep initial accretion rate is due to the fact that the relative encounter velocities v_∞ (that is, uncorrected for the acceleration caused by the Earth as the particles fall into its gravity well) are small since they just barely leaked out of geocentric orbit due to a close lunar encounter. The Earth's gravitational cross-section for accretion, the area at ∞ through which passing particles will impact the body, is:

$$\pi b^2 = \pi R^2[1 + (v_{\rm esc}/v_\infty)^2] \tag{3.4}$$

where the planet has radius R and escape speed $v_{\rm esc}$, and b can be interpreted as the impact parameter below which accretion will occur. The Earth's escape velocity of 11.2 km/s dwarfs the typical initial relative velocity of 0.1–1 km/s, resulting in an accretional cross-section several orders of magnitude larger than the Earth's geometric cross-section. If v_∞ were to stay constant, then the number N of surviving particles should follow $dN/dt \propto -N$ and we would expect an exponential drop in numbers. The leveling off of the loss rate apparent in Fig. 3.8 is due to the fact that the relative velocities of the surviving particles are increasing, as evidenced by the spreading of the orbits in 3.7.

Figure 3.9 shows a set of orbital elements for those particles that survived for 10 Myr. The test particles are distributed somewhat uniformly in semimajor axis between Mercury and Mars, and also fairly uniformly in eccentricity from 0 to 0.5. Many particles now have their aphelia inside the asteroid belt and will be prone to collisional erosion (Bottke *et al.* 1994). In any case the fraction of lunar particles that come back to the Earth after having spent more than 1 Myr in the main belt is small, so this effect is not of great importance. It seems that the inner planets are unable to drive particles to $e > 0.5$ or i=25°, and that secular resonances are required (see below). This is not surprising. Even an atmosphere-skimming close encounter directly over a pole of the Earth cannot provide a vertical component of relative velocity larger than $v_{\rm esc}/\sqrt{2} \simeq 8$ km/s, which produces an inclination of no more than 15°.

Table 3.5 lists the reasons for terminating the 224 particles (out of an original 326) that were removed from the 2.4 km/s simulation, as well as similar statistics

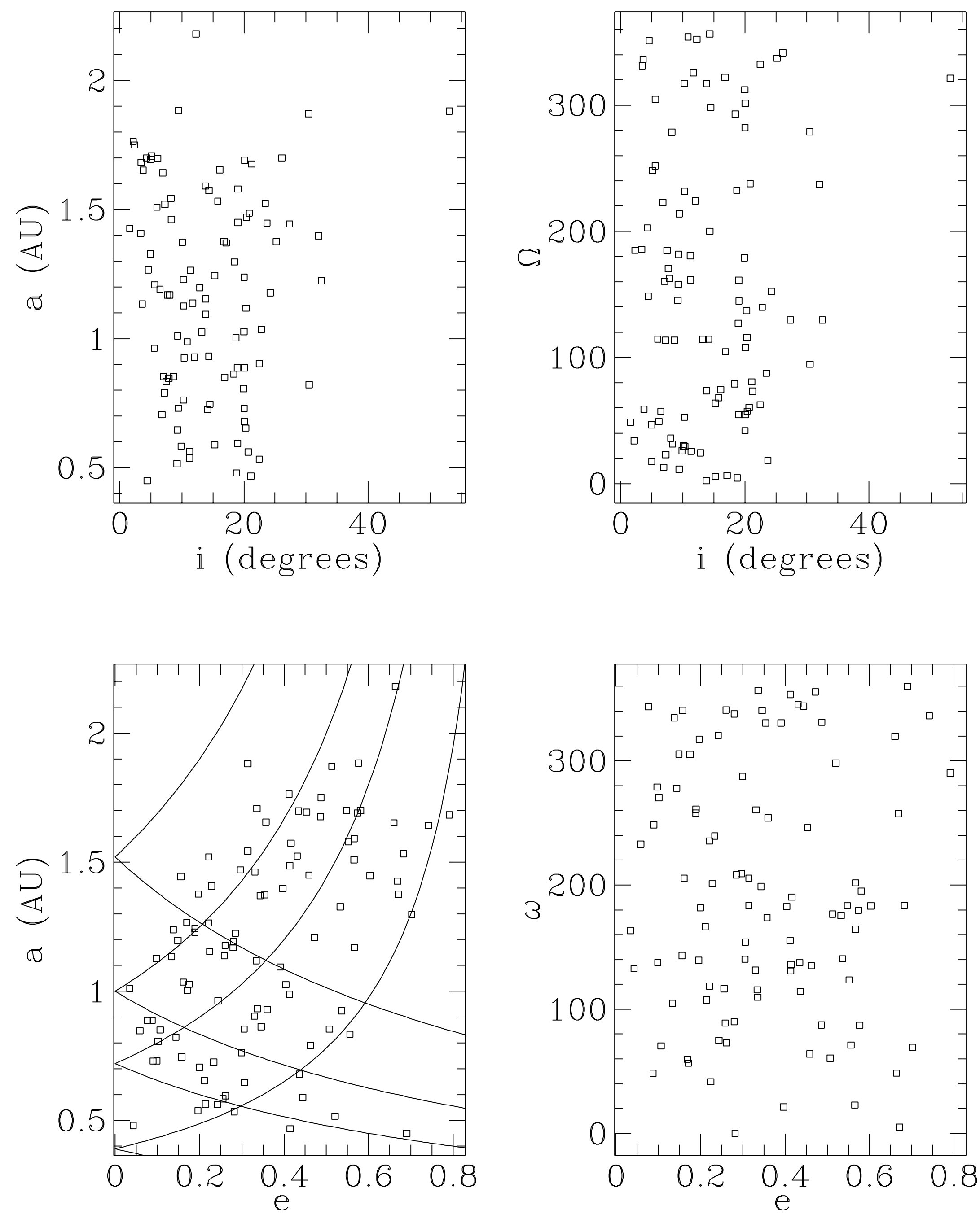

Figure 3.9 Orbital elements for the surviving particles at 10 Myr in the $v_l = 2.4$ km/s simulation. See the text and the captions to Figs. 3.6 and 3.7

Table 3.5 The number of particles removed in each 10-Myr simulation is given for each listed mechanism: collision with a terrestrial planet, or passage into regions of heliocentric space where the simulation would not be accurate. Note the different numbers of starting particles; the remaining particles (out of the 360 launched from the Moon) impacted the Earth or Moon in the geocentric phase.

Heliocentric Stage Removal Statistics					
v_l (km/s):	2.4	2.6	2.8	3.0	3.2
Initial number N_0:	326	294	289	341	357
TERMINATION REASON					
Mercury collision	2	0	0	0	1
Venus collision	23	30	35	41	67
Earth collision	182	142	98	109	96
Mars collision	0	0	1	0	1
$q < 0.01$ AU	14	10	18	18	16
$Q > 6.0$ AU	3	3	3	4	4

for all the other simulations. At the instant of removal we record a particle's position and velocity, as well as those of all the planets, for later processing (to calculate impact velocities and geometries for example). Generically one finds that a large number of collisions occur with the Earth initially and that, after about 500 kyr, impacts with the Earth and Venus occur at roughly equal rates. Two collisions with Mercury were observed in the 2.4 km/s simulation, at t=3.5 Myr and 7.8 Myr after lunar ejection, with impact speeds of 22 and 24 km/s respectively. Only a few collisions with Mars were recorded in all our simulations. The paucity of martian impacts is not surprising since we expect the collision time scale with Mars to be at least several tens of millions of years (from a simple Öpik calculation, see Sec. 3.3). After several Myr the algorithm begins recording the loss of particles inside the q_{min} boundary (they become Sun-grazers). The mechanisms behind this behavior are discussed below.

A typical orbital history is shown in Fig. 3.10. Note the occasional periods of resonance lock, where the semimajor axis is roughly constant and the rate of evolution of the other elements slows down. The lock at $t \simeq 4$ Myr is especially interesting since here the particle has its perihelion well inside the orbit of Venus, yet it is protected by jumping between a series of first-order mean motion resonances with Venus (the 11:12, 12:13, 14:15, and 18:19). The particle's approximately 15° inclination and the Kozai resonance (Michel *et al.* 1995) keep its perihelion at its descending node for several hundred thousand years and thus protects it from close approaches during some of this period. The object shown in the figure entered the Hill spheres of Venus, Earth, and Mars 917, 2454, and 362 times, respectively, during its 10-Myr existence. Most particles that survive

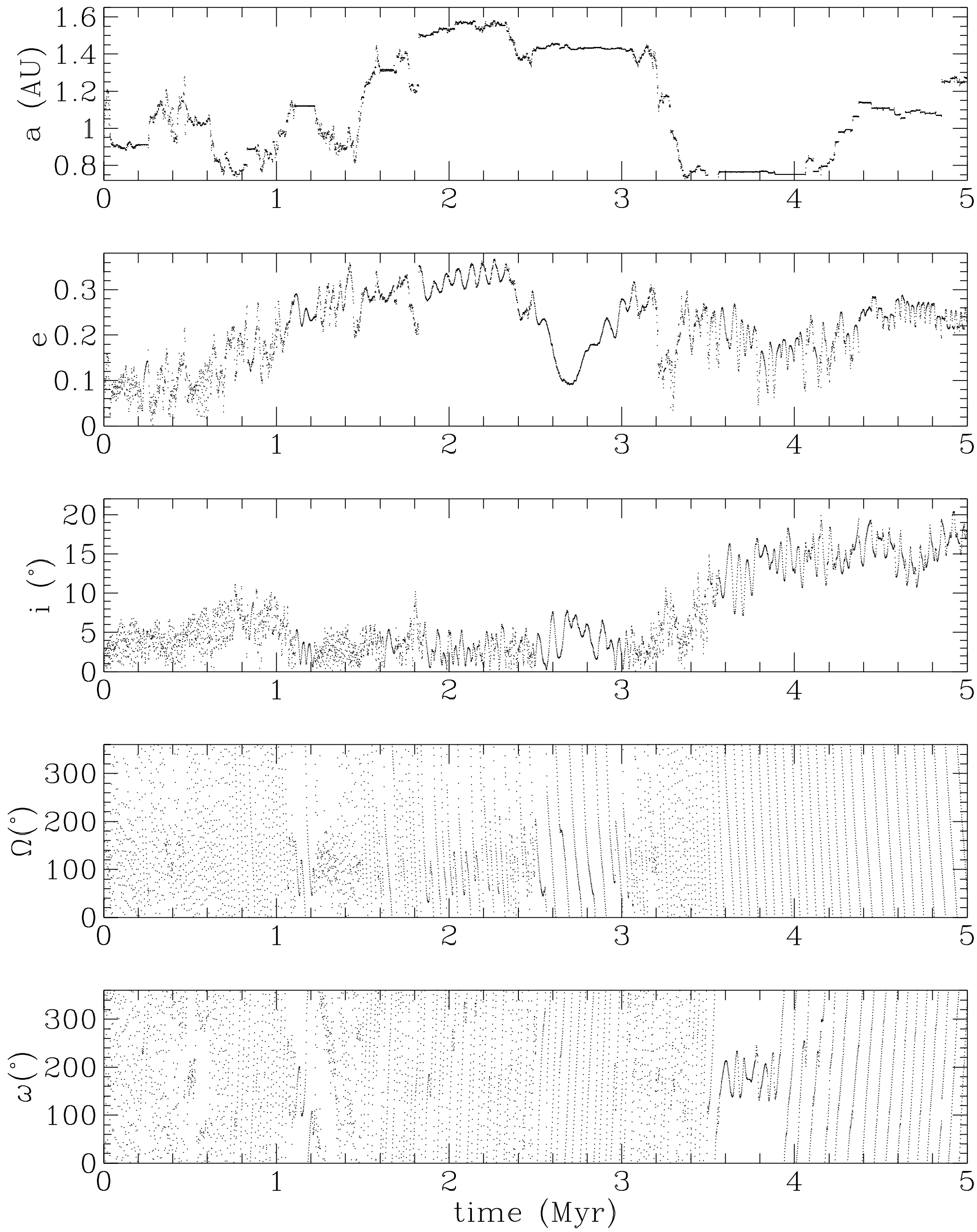

Figure 3.10 Orbital element evolution for the first 5 Myr of a particle launched with $v_l = 2.4$ km/s. See the text for details.

the initial Earth-crossing phase explore much of the inner solar system, being dominated at various times by different terrestrial planets.

An incredibly fascinating array of dynamical behaviors are exhibited by the thousands of particles studied. Most of the particles would belong to the Geographos class for much of their lifetimes, according to the Milani *et al.* (1989) SPACEGUARD classification of Earth-crossing objects. But, for example, the particle shown in Fig. 3.10 is an Eros object from $t \simeq 2-3$ Myr. The variety of evolutions is bewildering. Although these dynamical behaviors are not the main point of this study, we shall pause to discuss a few of them.

It was observed that 3-6% of the particles in the lunar simulations became Sun-grazers in the last 8 Myr of the simulations. This fate has been observed in numerical integrations of the orbits of short-period comets (Bailey *et al.* 1992) and near-Earth asteroids (Farinella *et al.* 1994). Almost all of the objects observed to undergo this behavior did so upon having their semimajor axes first modified to $a > 2$ AU, where secular resonances due to the outer planets are located, and subsequently having their eccentricities raised to almost unity. I note, as Farinella *et al.* (1994) do, that this end state is more common than having a particle's aphelion raised to Jupiter-crossing (see Table 3.5). During the final stages of the simulations, Sun-grazing in fact becomes the most common end-state for those particles that are removed. I also note that the particles that end their lives in this way often seem to become influenced by the secular resonances while still deep inside the terrestrial region. Fig. 3.11 displays the orbital history of one of the Sun-grazers. The bottom two panels of this figure show that in the period between 3 and 4 Myr after launch the particle becomes locked in the ν_5 resonance (see Sec. 4.2.1 or Froeschlé and Morbidelli 1994), although this seems to have little effect on its evolution. But near 6 Myr after launch the particle becomes strongly affected by the ν_6 resonance, which proceeds to drive its eccentricity up to nearly unity. However, only a small fraction of the Sun-grazers end their lives while clearly locked in one of these classical resonances. This topic could easily be the subject of considerable further research.

Interesting behavior can also be discovered by mistake. In some of the preliminary simulations (not included here) an error in the transformation to the heliocentric initial conditions caused the escaping particles to be uniformly spread in orbital longitude relative to the Earth at the start of the heliocentric phase. Although easily rectified, this error revealed the existence of Trojan-type horseshoe orbits (although these would NOT come from particles that were launched from the Moon). These orbits exhibited stability for the entire 5-Myr integration, providing independent confirmation of previous hypotheses (Mikkola and Innanen 1992). Whether or not one would expect these stable orbits to be populated in the current solar system is an open question.

Another curiosity is shown in Fig. 3.12 where we exhibit the values of the inclination and longitude of the ascending node for the particles after 10^4 years.

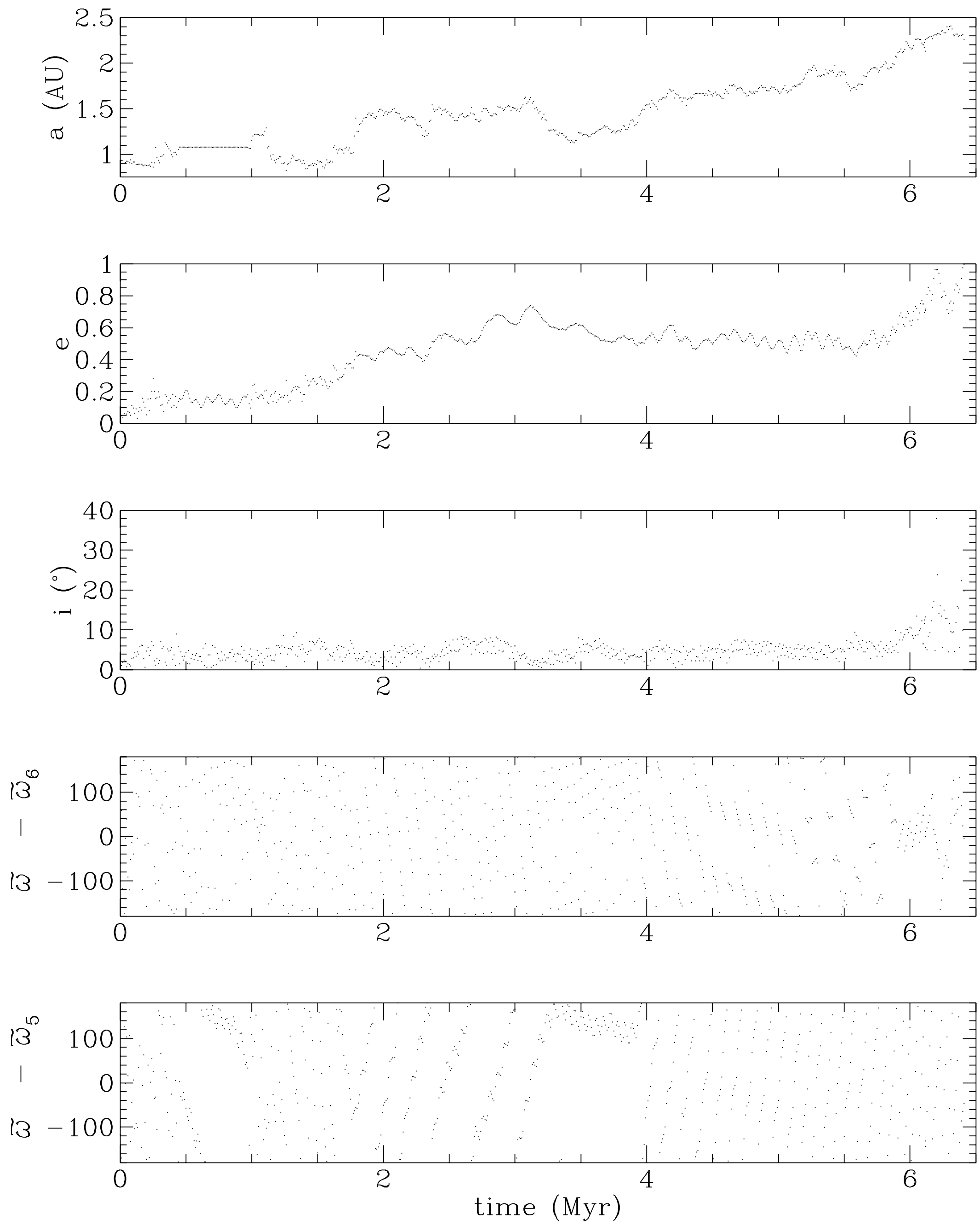

Figure 3.11 The orbital element history of a Sun-grazer. Shown is the a, e, i history for the 6.4 Myr lifetime of a particle from the 2.4 km/s simulation. Also shown are the differences in the longitudes of pericenter of the particle with Jupiter and Saturn. Libration of one of these critical arguments indicates that the particle is locked in the resonance. Observe that the eccentricity is driven to 1 when the ν_6 resonance is entered near $t = 6$ Myr.

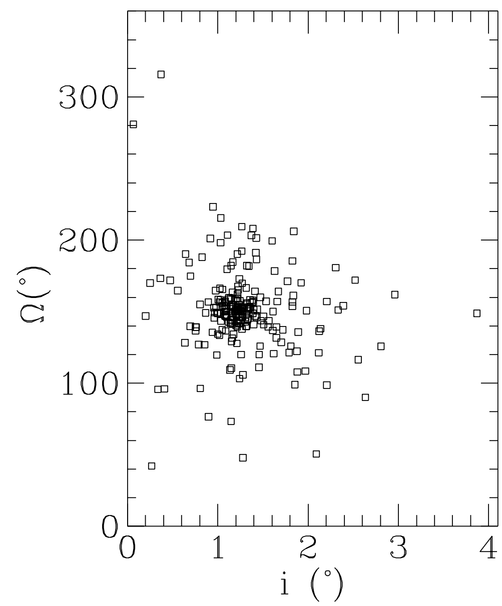

Figure 3.12 The inclination of the test particles in the 2.4 km/s simulation after 10^4 years of evolution. The particles are preferentially confined to have their orbital planes coincident with the Earth.

The initially uniform distribution has now been strongly concentrated towards $\Omega \simeq 150^o, i \simeq 1.2^o$, which are the Earth's values at this epoch. Compare this with Fig. 3.6, in which the initial nodes are randomly distributed. This apparent concentration is a coordinate-system artifact caused by referencing all the inclinations and nodes to the initial ecliptic plane. The test particles have all been precessing around their Laplace planes (see Ward 1981); the latter planes have been following the Earth's slowly moving orbital plane, which is rotating mostly due to the Earth's interaction with Venus. Since the particles all have almost zero free inclination initially, the dominant secular effect will be to maintain this state. This will be disrupted by close encounters which gradually raise the mutual inclinations of the particles with the Earth. Once the mean mutual inclination reaches the Earth's instantaneous inclination (with respect to the reference plane), this correlation disappears. This requires several hundred thousand years, and it can be seen that such a concentration is absent in Fig. 3.9. When the nodes are measured with respect to the Earth's *instantaneous* orbital plane, the distribution is indeed random. This common precession of the nodes with respect to another fixed plane (whether it be the ecliptic plane at t=0 or the invariable plane) is a very important effect since it keeps the mutual inclinations with the Earth low and thus the collision probabilities (as discussed in the next section) high. It would be erroneous to compute collision rates (using an Öpik

Table 3.6 For each launch speed v_l (km/s) N_o particles escaping to heliocentric orbit were followed for 10 Myr (all times are in Myr). The number of particles N_{tp} still in the simulation (allowing for *all* removal mechanisms) at $t = 0.05$, 1, and 10 Myr is then given. The number removed by *Earth collisions* during the geocentric simulation, and the heliocentric simulation in the time intervals 0-50 kyr, 50 kyr–1 Myr, and 1–10 Myr, is shown. The percentages for these cases are given in the last 3 columns, with the geocentric collisions absorbed into the <50 kyr column.

Heliocentric Stage Results											
	N_{tp}				Number of $\oplus$ collisions				% $\oplus$ collisions		
v_l	$N_\circ$	0.05	1.0	10.0	Geo	$\leq$0.05	0.05-1	1-10	$\leq$0.05	.05-1	1-10
2.4	326	197	155	100	13	129	33	20	73	17	10
2.6	294	226	166	109	65	68	51	23	64	25	12
2.8	289	249	199	155	69	49	26	23	71	16	14
3.0	341	307	244	174	18	33	49	13	45	43	12
3.2	357	329	254	171	2	27	53	16	30	54	16

theory for example) assuming that the relative node on the reference plane of the test particles and the Earth was distributed uniformly.

Table 3.6 summarizes all the heliocentric stage simulations, as well as information on the impact distribution (in time) of the objects that strike the Earth. Each simulation started with $N_\circ \sim 300$ test particles (all of which had originally been ejected from the Moon at a common speed) and lasted for 10 Myr. The number of test particles surviving at 50 kyr, 1 Myr, and 10 Myr is shown to give some idea of the loss rate, and includes all the loss mechanisms summarized in Table 3.5. I then present the information on only the Earth collisions, which are relevant for comparisons with the lunar meteorite data. These same data are presented in a more detailed graphical format in Fig. 3.13, and will be discussed further below.

3.3 Comparison with Monte Carlo Methods

An alternate approach to the heliocentric stage of this problem would be to conduct a Monte Carlo simulation of the orbits of the particles. In this method, collision probabilities (Öpik 1976) are used to calculate the frequency of close approaches, at which time collisions or orbital modifications occur after randomly determining the close encounter distance; when implemented numerically this is called an Öpik-Arnold approach. In this way Arnold (1965) and Wetherill (1968) found a steep spectrum of expected collision ages with the Earth, with the vast majority of the collisions occurring in the first Myr (see Arnold's Fig. 2 or Wether-

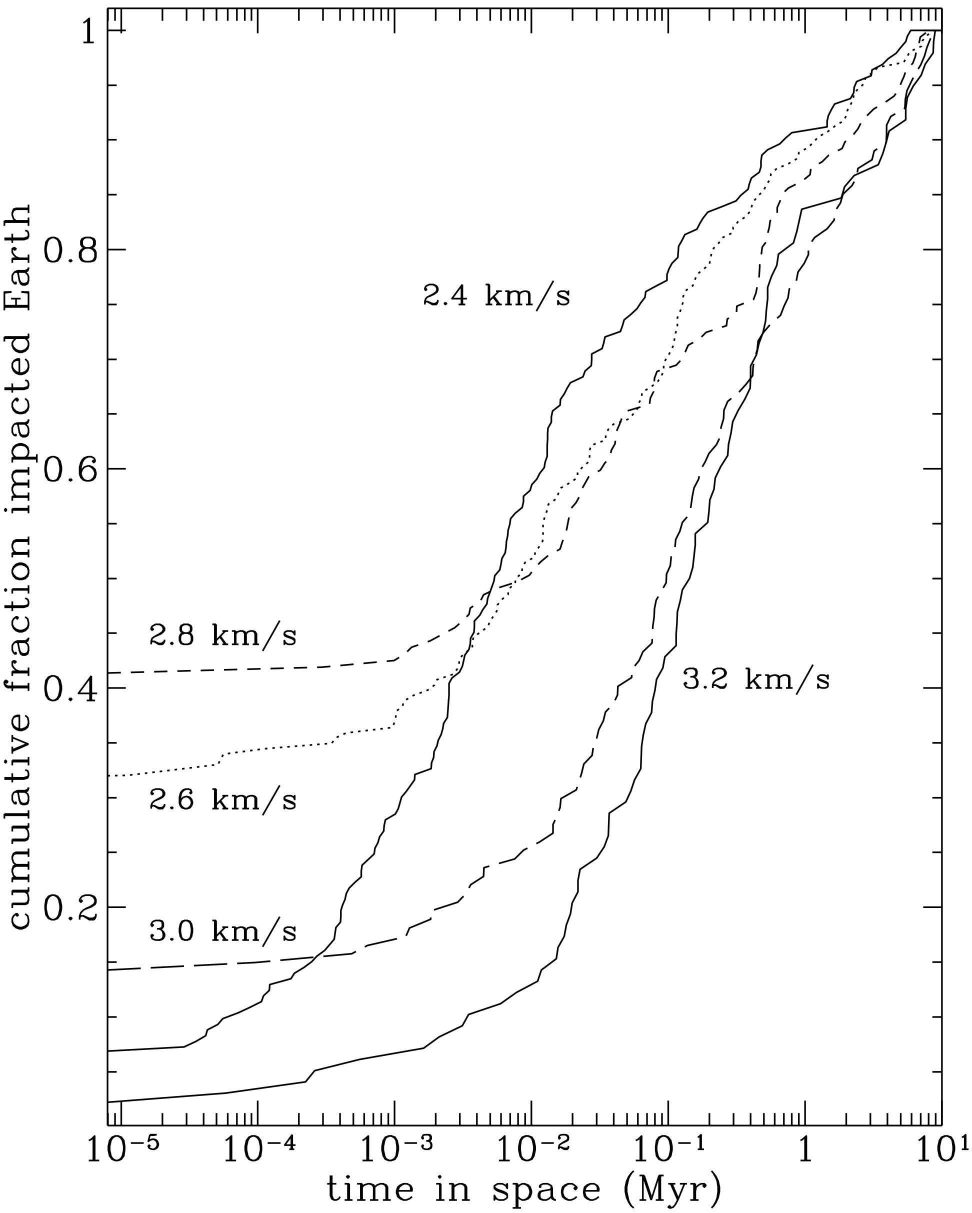

Figure 3.13 This plot presents, as a function of time, the cumulative fraction of simulated meteorites that have arrived on the Earth, to all those that will within 10 Myr. One curve is shown for each lunar launch speed. For example, by 0.1 Myr 40% of the meteorites that will arrive have returned to the Earth for the v_l = 3.2 km/s simulation, whereas about 80% of the meteorites delivered in the 2.4 km/s simulation have already arrived by that same time. For the purposes of this figure all geocentric deliveries were deemed have arrived in <10 years; these deliveries are responsible for the non-zero values at t=10^{-5} Myr.

ill's Fig. 7). Until recently, it has not been feasible to carry out direct integrations of particles that are in close-crossing orbits in order to confirm the Monte Carlo results (although Milani *et al.* 1990 conducted a $\sim 10^5$ year comparison for the deep Earth-crossing asteroids). The RMVS code now allows us to do this.

The subject of study here is especially difficult for an Öpik approach since the initial orbits are very Earthlike and thus have tiny relative velocities. This causes degeneracies in the Öpik equations, owing to the many cases of small mutual inclinations, tangent orbits, and partial crossings. A comparison of my results with Monte Carlo simulations (G. Wetherill, private communication, 1994) shows that over a variety of time scales the Öpik approach underestimates the re-collision fraction with the Earth by factors of 3 to 12. The error lessens as the length of the simulation is extended: the more than order of magnitude error in the fraction of returned objects during the first 10^5 years is reduced to a factor of three if one considers 10-Myr time scales. Despite this problem, the overall *relative* distribution of re-collision ages (e.g., the fraction of objects returning within 10^5 years compared to those that return within 10^7 Myr) given by the Monte Carlo approach is roughly correct (to within a factor of a few). This conclusion is also reached by Dones *et al.* (1996a).

The comparatively short recollision times found early in both the Monte Carlo simulations and the direct integration principally result from the low relative velocities of particles with respect to the Earth. As the particles scatter repeatedly off of the Earth's gravitational field, the relative velocities increase and collisions become less likely. Thus, all methods should find a steep drop-off in the collision rate as the Earth's gravitationally enhanced cross section shrinks *and* the number of impactors falls because collisions are occurring. The resulting 'faster than exponential' drop in the impact rate is apparent in Fig. 3.8.

The initially Earth-like orbits of the particles introduce complications for the Öpik-Arnold approach. Furthermore, as noted above, much of the evolution in the simulations is influenced by the presence of resonances. Resonance effects are clearly important, but the manner in which they affect the results is complicated. In fact, the common occurrence of short-term resonance locks is likely one reason why the Öpik collision rates are in error. The Monte-Carlo methods also suffer from an inability to discover interesting dynamical processes like those discussed in the previous section. These issues are further explored by Dones *et al.* (1996b). The Öpik approach provides a good qualitative understanding of the problem nevertheless. In fact, the Monte Carlo calculations were well suited to address the questions posed originally by Arnold and Wetherill (namely, a possible lunar origin for chondrites and the time of fall asymmetry). In summary, I find that the steep collision spectrum found by the method used by Arnold and Wetherill is correct, but a large fraction of the material returns in only 50 kyr, and that the absolute yields are too low by a factor of a few.

3.4 Comparison with Lunar Meteorite Data

I now return to the CRE data on the lunar meteorites (Table 2.1). How do the CREs of the meteorites compare with the simulated collision results, and what can be said about the transfer process from the available samples? Of the eleven objects with reliable ages, seven have CREs of less than 50 kyr, although all but one of these are upper limits. Fig. 3.14 compares the cumulative distributions of the expected CREs from the $v_l = 2.4$ and 3.2 km/s simulations with the available data. The plot includes those particles that impacted the Earth while still in the geocentric stage. Since the collisions occur so quickly in the initial part of the simulation, it is best to examine the distribution binned logarithmically in time. The steep time spectrum is in qualitative agreement with the CRE age data, with a large amount of material returned in less than 0.1 Myr; in fact, for the 2.4 km/s simulation more than half of the returning material arrives in less than 10 kyr.

The prevalence of upper limits on the 4π CRE ages is due to the difficulty of measuring the presence of isotopes having such short half-lives and small abundances in the meteorite. Thus, Fig. 3.14 does not very well discriminate amongst launch velocities, nor is it probably a very good representation of the actual spectrum, since the meteorites could very well have 4π ages orders of magnitude smaller than their upper limits. To obtain a fairer comparison I have re-plotted the data using the thermoluminescence ages from Table 2.1 for the lunar meteorites that have only upper bounds on their CRE ages (Fig. 3.15; *cf.* Sec. 6.2.5). For objects that have only upper bounds on their CRE and thermoluminescence ages, I have assumed a 100-year transit time (which could be in either the geocentric or heliocentric stages). Fig. 3.15 shows that, given the small sample of actual lunar meteorites, the 2.4 km/s model provides a reasonable match to the data. The 3.2 km/s simulation delivers almost all its meteorites in the period after 50 kyr from launch, in disagreement with the data. Unfortunately, the 11-object sample size means that the cumulative distribution may be significantly altered by the addition of another data point. Although the spectrum derived from the data in Fig. 3.15 is somewhat ad hoc, it is almost certainly a more accurate representation of what the real delivery spectrum looks like than Fig. 3.14.

3.4.1 The lunar velocity spectrum

Because the delivery spectrum (in time) changes as the launch speed varies, we are able to rule out a large preponderance of higher launch speeds since they have a much smaller fraction of quick deliveries (due to having much higher relative velocities to the Earth after the initial escape to heliocentric orbit). Referring back to Fig. 3.13, we see that if $v_l \leq 2.8$ km/s then approximately half of the meteorites should have transit times of less than a few thousand years (with the interesting difference that for $v_l \approx 2.6 - 2.8$ km/s most of these rapid returns

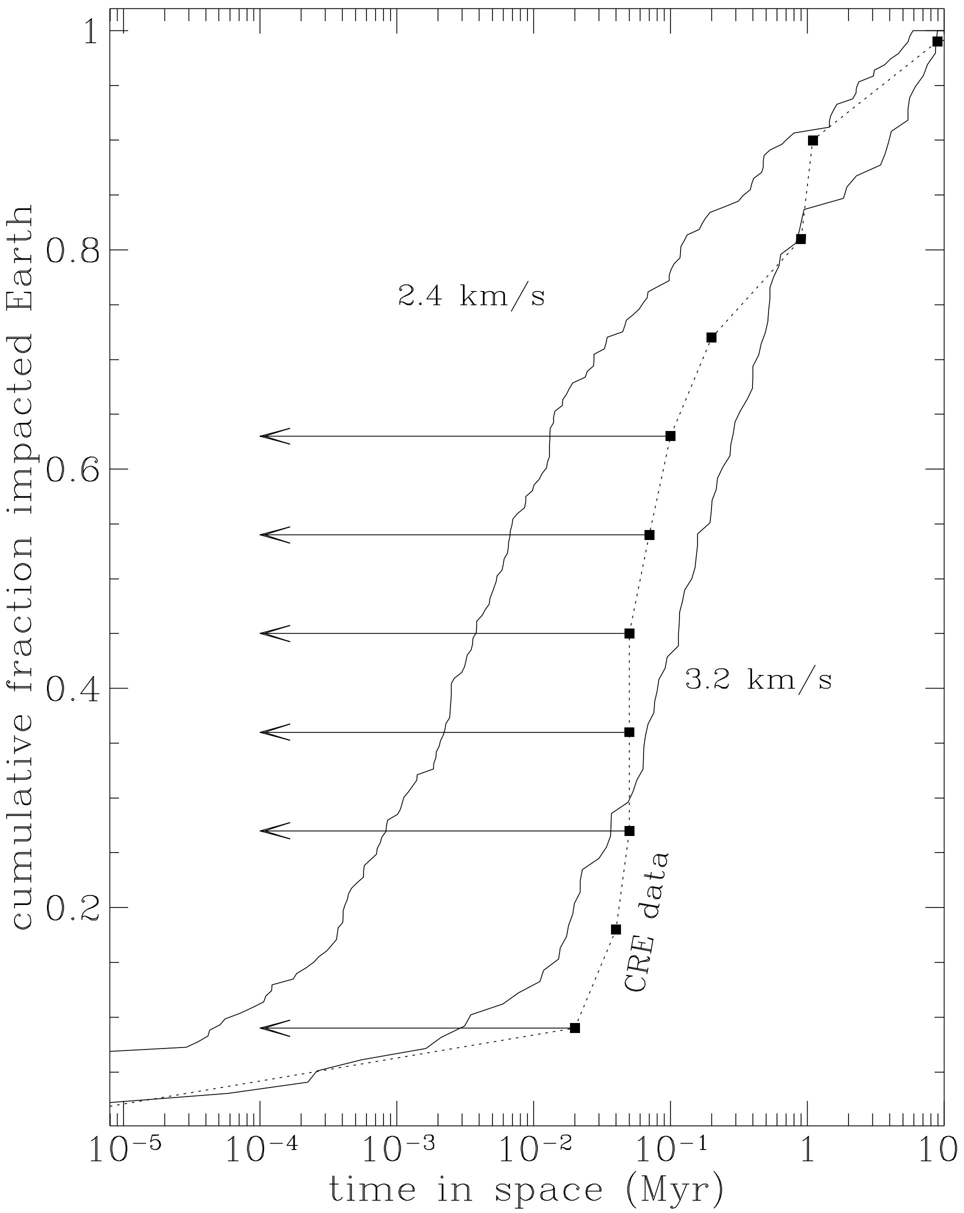

Figure 3.14 The time spectrum of the CRE age data for the lunar meteorites is compared with two of the simulations. See the caption to Fig. 3.13 and the text. The arrows indicate that the data point is only an upper limit of the 4π age of the meteorite.

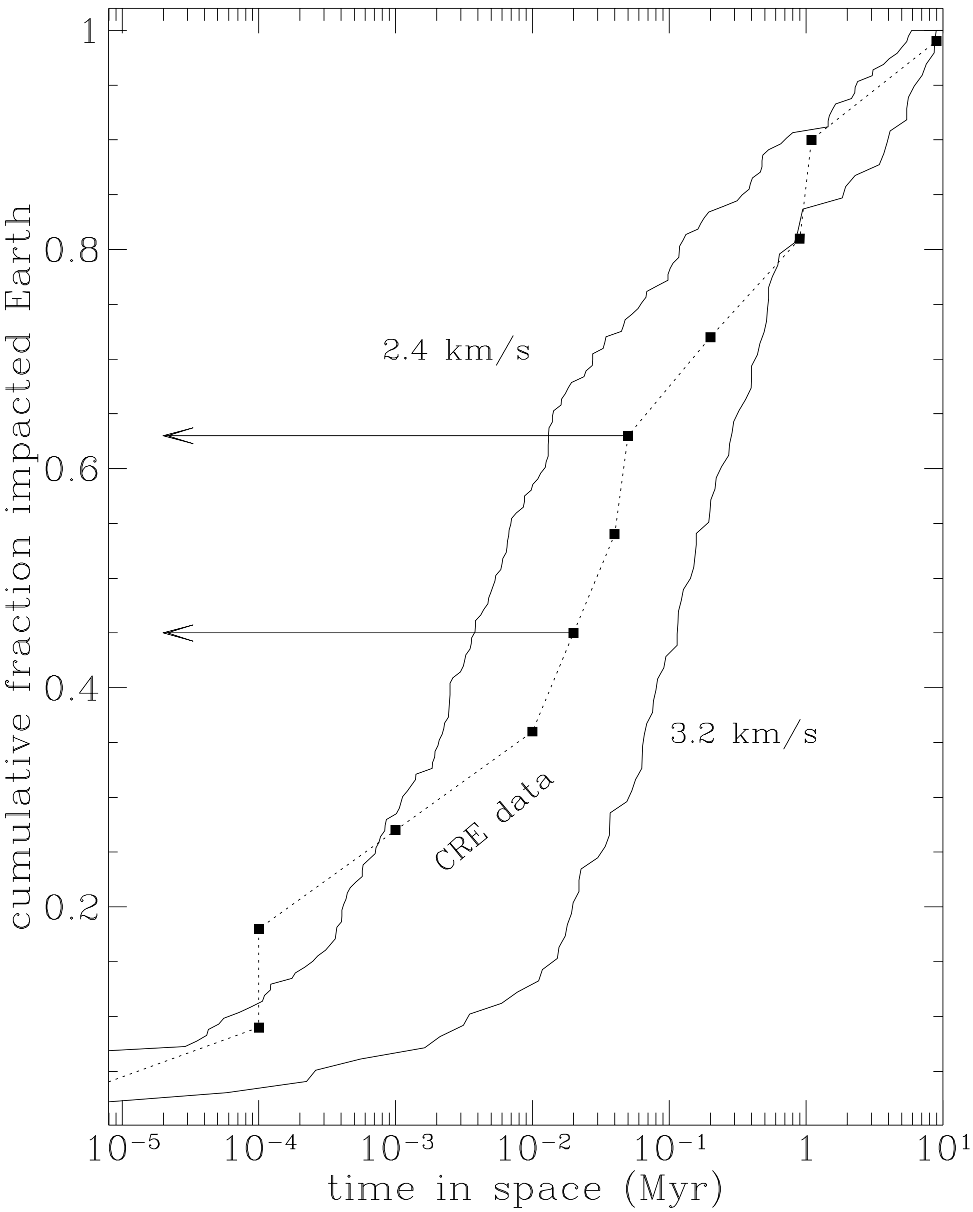

Figure 3.15 Cumulative spectrum, modified TL data and assumed geocentric impacts, as explained in the text.

actually take place in the geocentric stage). Because of the prevalence of upper limits in the transit time data, we cannot say for certain if this is true of the meteorites. However, above $v_l = 3$ km/s, one must wait 0.1 Myr for half of the meteorites to arrive. Therefore we can conclude that most of lunar meteorites must be launched with $v_l < 3$ km/s, for if this were not the case very few would have CRE ages < 0.1 Myr. Since the ejecta velocity distribution is likely some form of a power law, the strongest statement that can be made is that not all of the lunar meteorites were launched with speeds > 2.6 km/s. This can be quantified in the following way. If the number of meteoroids ejected at velocity v ($v > v_{\rm esc}$) obeys

$$N(v)dv \propto v^{-p}dv \ , \tag{3.5}$$

then the fraction of particles (of those that escape) that leave with velocity $v > v_*$ is

$$f = \frac{N(v > v_*)}{N(v > v_{\rm esc})} = \left(\frac{v_{\rm esc}}{v_*}\right)^{p-1} . \tag{3.6}$$

The experimental results of Gault *et al.* (1963) imply $p \approx 4.5$ (Wetherill 1984), in which case Eq. 3.6 implies that $\approx$ half of the ejecta should leave at faster than 3 km/s. This is consistent with the data since then, weighting the contributions of the various launch speeds given in Fig. 3.13, about 30% of the meteorites should arrive in 6,000 years and 65% in 0.1 Myr, in good agreement with Fig. 3.15. Further discussion of this topic will be postponed until Chpt. 6.

It is again worth nothing that, at launch speeds of $v_l = 2.6$ and 2.8 km/s, a large fraction of transfers with CREs < 50 kyr happen in the geocentric phase (see Table 3.2). Thus, in these cases (see Table 3.6), the deficit of fast heliocentric returns is more than compensated for by the large number of geocentric stage impacts. This makes the velocity spectrum (given roughly by the last three columns of Table 3.6) difficult to distinguish from the 2.4 km/s case if one cannot separate out those lunar meteorites that never left geocentric orbit. If the geocentric stage meteorites could be distinguished from those that escaped to heliocentric space on the basis of their CRE ages, one might be able to rule out $v_l = 2.6 - 2.8$ km/s as a common launch speed, since for these velocities lunar meteorites with CRE ages <300 years should comprise a fair fraction of the objects (about a third). Measuring such short cosmic ray exposure ages is unfortunately very difficult, if not impossible; thus the current upper bounds on many of the 4π CRE ages in Table 2.1 are insufficient to determine whether or not these particular objects escaped to heliocentric space. Measurement of short CRE ages would require a lunar fall to be observed (so that the residence time on the Earth is known to be negligible); it is likely that we must wait awhile for a statistical sample.

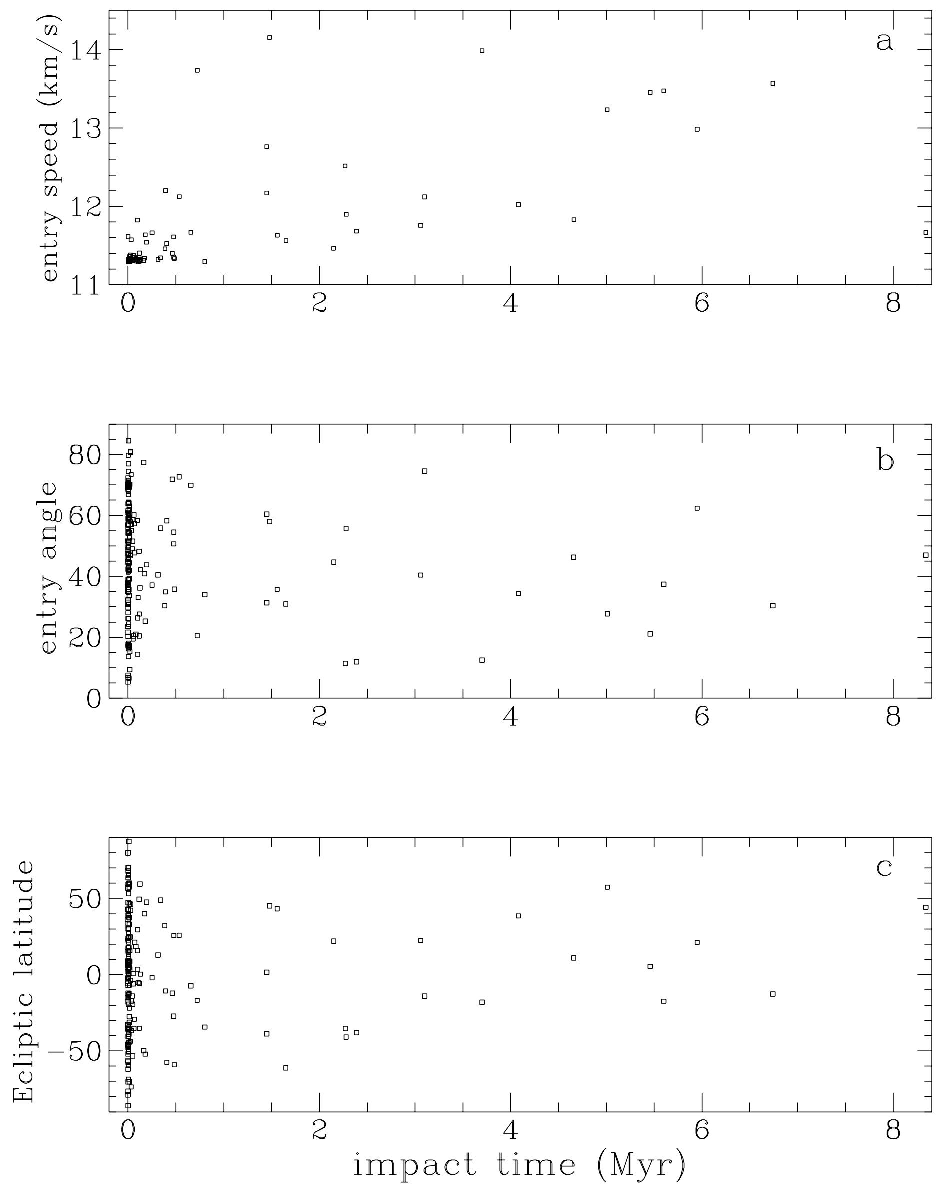

Figure 3.16 Collisional data as a function of time for the heliocentric stage impactors in the 2.4 km/s simulation. (a) Entry speed at the top of the atmosphere. (b) Entry angle (with respect to local vertical). (c) Ecliptic latitude of the impacts on the Earth.

3.4.2 Entry statistics

Fig. 3.16 displays additional information on the collision circumstances of the Earth-impacting particles from the heliocentric stage of the simulation. Figs. 3.16a and b, respectively, give the entry speed and angle (with respect to the local vertical) at the top of the atmosphere at the time of collision. As one would expect, because the orbits of the particles are very Earthlike early in the simulation, the entry velocities then are just barely above the Earth's escape velocity of 11.2 km/s. (Of course, the entry velocities of *all* the impacting particles during the geocentric phase are also just above the escape speed since such particles start at the lunar orbit with geocentric velocities small compared to 11.2 km/s). The mean entry velocity for heliocentric stage impacts rises with time as the average eccentricity and inclination (and hence encounter speed) of the particle swarm rise. This will presumably produce a slight bias *against* lunar meteorites with CREs > 1 Myr since they will suffer heavier ablation; perhaps a factor of 2 more mass loss if the entry velocity rises from 12 to 18 km/s (ReVelle 1979). Furthermore these same objects will have been more prone to collisional disruption near their aphelia (Bottke *et al.* 1994). This bias will presumably concentrate the distribution of *recovered* meteorites somewhat more strongly towards younger ages. The entry angles α (Fig. 3.16b) for the returning heliocentric particles follow a $\sin 2\alpha$ distribution as expected (see Shoemaker 1962). In contrast (see Fig. 3.17), the entry angles for the geocentric stage impactors have a small bias to be concentrated towards larger entry angles (i.e., shallower entries). The mechanism that causes this effect is simply that the particles are in geocentric orbits that are perturbed into collision by having their perigees lowered to (most likely) just below the Earth's radius, resulting in an entry closer to tangency. This does not violate the standard $\sin 2\alpha$ result since the geocentric stage impactor-flux does not satisfy the assumption of being isotropic nor is it comprised of hyperbolic orbits coming from infinity. This could result in a slightly higher survival rate, due to less severe ablation, for particles that impact the Earth without having ever reached heliocentric orbit.

To examine the expected distribution of lunar meteorites on the Earth, I plot the *ecliptic* latitudes of the entry points in Fig. 3.16c. I have used the latitude on the Earth with respect to the ecliptic plane since I have not kept track of the Earth's polar precession in the simulation. Thus the latitudes with respect to the Earth's equator may differ by as much as $\pm 23^\circ$. Nevertheless, a χ^2 test shows that the distribution on the Earth is statistically consistent (at the usual 5% level) with uniformity (i.e., there are no favored latitudes). The Earth should be uniformly covered with lunar meteorites, and there is no bias for or against Antarctica on dynamical grounds (cf. Halliday and Griffen 1982, who claim a slight 15% observational bias against polar returns for fireballs). The unbiased distributions of impact latitudes is also true for those particles colliding during the geocentric stage of the simulations.

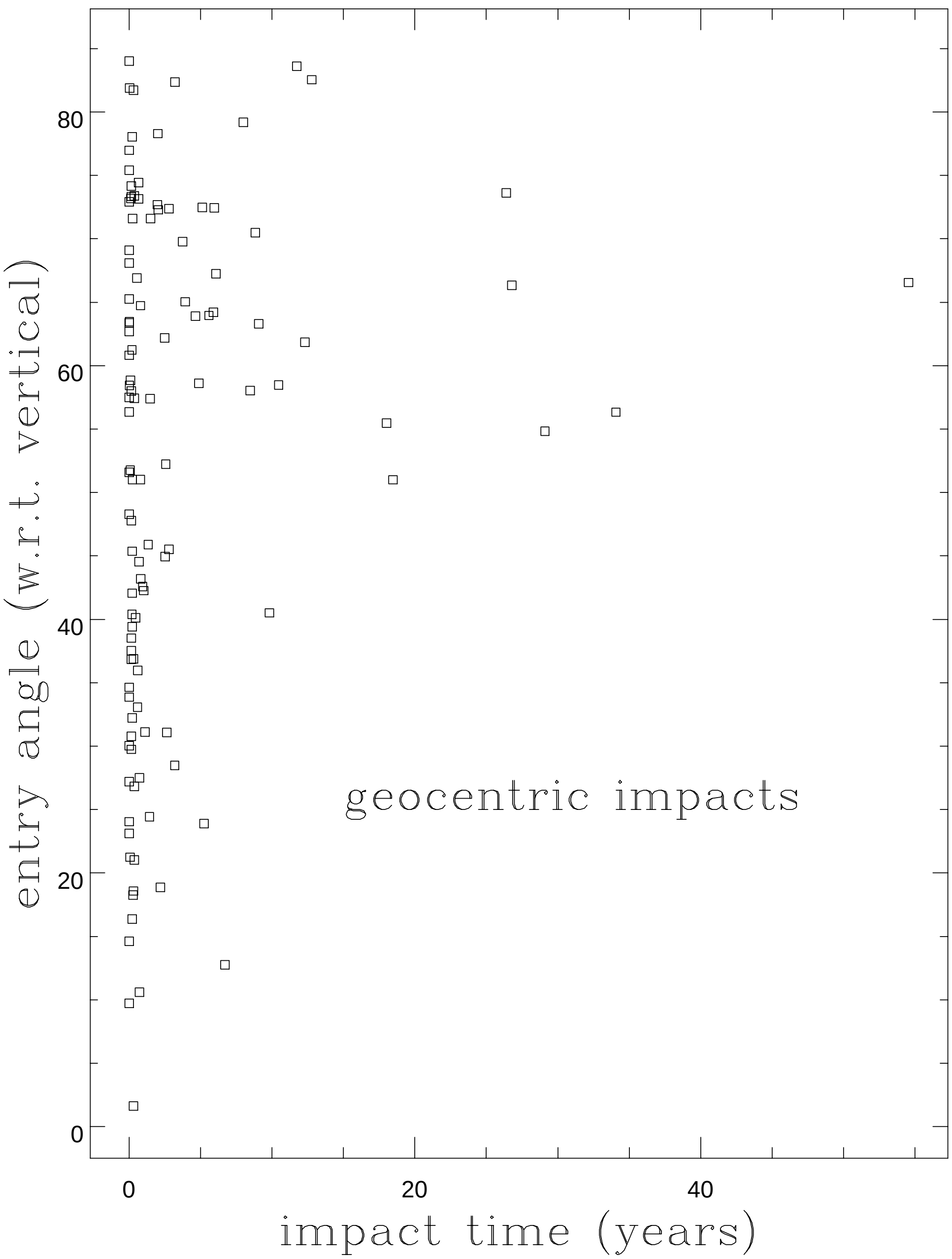

Figure 3.17 Entry angles for the geocentric stage impactors from one of the 2.6 km/s simulations. There is a bias towards entry angles larger than 45^o due to the fact that particles in geocentric orbit are likely to collide with Earth after having their perigees lowered to just below the Earth's surface. This produces a greater likelihood of shallow entries.

One thus concludes that the discovery location on the Earth imparts no information as to where on the Moon a lunar meteorite was launched. Nevertheless Fig. 3.4 demonstrates that objects launched with high velocity (more than 2.6 km/s) have an extreme bias towards coming from the trailing half of the lunar surface *if* those particles are delivered to the Earth without ever escaping geocentric orbit. If the launch-velocity spectrum is flat enough that high-speed particles make up a majority of the escaping ejecta, then geocentric stage deliveries from the leading half of the Moon would be rare. Accordingly, in the absence of other information, the three lunar meteorites with only upper bounds on their CREs (that is, those which might never have been in heliocentric orbit) are somewhat more likely to come from the trailing hemisphere of the Moon. Beyond accepting this very tentative chain of reasoning, one can conclude little. If the 4π CRE of an object could be shown to be only a few days (so that the meteorite arrived via a 'direct' transfer), then one might be able to deduce more, but only if the ejection velocity and angle were known (see Gault 1983). Since such information will not be available, we must conclude that the dynamics can do little to narrow down the source regions of lunar meteorites. In particular, until CREs can be determined to 100-year accuracy, there is little reason to try to distinguish particles that arrived on 'direct' trajectories (transfer times of a few days) from those that conduct many geocentric orbits before impacting the Earth (surviving up to several decades), or even escape to heliocentric orbit and re-impact with the Earth in $< 10^3$ years. Note that if the $v_l \simeq 2.4$ km/s case is the most common (as we might expect), then there are no preferred source regions for either the geocentric or heliocentric stage deliveries.

Any rigorous comparison of the data with simulations like those presented here should attempt to correct for: bias against high entry velocity objects, selection biases in discovery of the lunar meteorites, and biases (due to collisional disruption) against long-lived objects that reach orbits with large aphelia. Construction of a self-consistent model of lunar meteorite delivery, given what is known about the impactor flux, will be the subject of Chpt.6.

3.5 Relevance for the Small Earth Approachers (SEAs)

The Small Earth-Approachers (SEAs) are objects with diameters of 5-50m that have orbits passing close to the Earth. A lunar origin (Rabinowitz 1993) has been proposed for this recently discovered class of objects as a possible explanation for their Earthlike orbits. The simulations performed here are well suited to address the *dynamical* consistency of this hypothesis. I find that the steady-state population after 10 Myr produces a reasonable match to the low-eccentricity component of the SEA population (Rabinowitz 1996) after biasing for telescope detection efficiency and correcting for dynamical protection mechanisms that prevent some surviving objects from entering the observable region (D. Rabinowitz, 1994, private communication). The inclination distribution shown in Fig. 3.9, with very few particles having $i > 30^o$, agrees with the observations. However, too many Aten-type orbits ($a < 1$) are naturally produced, and these are absent in the observed population; this is addressed by Bottke *et al.* (1996), who for this reason claim that martian ejecta supply a better match to the SEA observations.

Perhaps an even more compelling argument against a lunar origin for the SEAs is as follows: The number of SEAs observed so far imply a very large population of SEAs ($\sim 10^{8-9}$ objects of 10m diameter exist according to Rabinowitz 1994). Even if the number of low-eccentricity objects (from a lunar origin) is only 5-10% of this population (Rabinowitz 1994), as might be true if the SEAs are the large-size end of a continuously injected population of lunar impact debris, then one would probably expect much greater numbers of recovered lunar meteorites in the available smaller size range. This problem remains even if the SEAs are the remnants of a single large impact event occurring more than a Myr ago (which would now have a low delivery rate of fragments of all sizes to the Antarctic ice sheet). This issue will be quantified in Chpt. 6. Finally, the lunar SEA hypothesis cannot be ruled out on orbital-dynamics grounds, but it may be difficult to produce the required number of large objects self-consistently. In fact, Bottke *et al.* (1996) calculates that only a few hundred 10-m objects would be launched by the 39-km impact crater Harpalus, and craters larger than this are unlikely to have been produced in the last 10-20 Myr.

3.6 Summary

Available lunar meteorite data are consistent with the simple dynamical model of lunar ejection, geocentric escape, and subsequent heliocentric evolution. The qualitative nature of the delivery of lunar material to the Earth is relatively insensitive to the ejection velocity and typical ejection angle, and thus the details of the launch process should not affect the results.

The numerical studies are fully consistent with the predominance of short CREs that are found in the lunar meteorite sample. One finds that roughly one-quarter to one-half of the ejected lunar material is re-accreted by the Earth in 10 Myr, with a large fraction arriving within the first 50 kyr. An Öpik approach to the problem will underestimate the absolute yield of lunar meteorites by a factor of three to twelve. The spectrum of launch speeds seems to be steep enough that ejecta leaving with speeds greater than 3 km/s are rare. I also conclude that the Earth should be uniformly covered with lunar meteorites, and that the discovery location provides no clues as to the source region on the Moon. There are no preferred launch locations on the Moon for Earth delivery either, given current knowledge about the lunar meteorites.

Chapter 4

Dynamics of martian meteoroids

In order to calculate the expected flux of martian meteorites, either in a relative or absolute sense, we must first calculate the delivery efficiency for martian material (the fraction of escaping material that arrives at the Earth).

4.1 Introduction

Martian meteorites have taken much longer to reach the Earth than the lunar ones (Table 2.1, page 16), simply because the orbits of most ejected martian meteoroids do not initially cross that of the Earth. However, because of the eccentric orbit of Mars, the v_∞ of escaping particles need only be about 2.3 km/s (corresponding to ejection speeds of 5.5 km/s, merely 10% greater than the 5 km/s escape speed) in order for some ejecta to be on orbits that immediately cross Earth's. Thus, fast transfers are occasionally possible and the short 0.6 Myr 4π CRE age of EET79001 is not especially surprising. In fact, transfers as rapid as 16,000 yr were observed in the simulations.

The ground-breaking work of Wetherill (1984), who a decade ago addressed the delivery efficiency of martian meteorites using Monte Carlo simulations, presents, in hindsight, a puzzle given what we now know of the 4π CRE ages of these meteorites. Even though collisional destruction was included in those simulations, the majority of martian objects arrived at the Earth having taken longer in their journeys than the recovered meteorite with the greatest CRE age ($\approx$15 Myr), unless the mean ejection velocities are very large indeed ($>$ 6.4 km/s). Since the lunar results seem to indicate that proportionally little material is launched at speeds greater than 125% of the escape speed, one might expect that most martian meteoroids should be launched at $<$ 6 km/s. Of course, it may

* This chapter is a considerably expanded version of discussion given in the paper: Gladman, B., J.A. Burns, M. Duncan, P. Lee, and H. Levison (1996), The Exchange of Impact Ejecta Between Terrestrial Planets, *Science* **271**, 1387–92 [copyright 1996 by the American Association for the Advancement of Science].

be that the regolithic structure of the lunar surface is responsible for the sharp drop-off with velocity, and that this result does not apply to Mars. However, Vickery (1987) studied secondary crater fields around martian, lunar, and mercurian impact craters and found power-law decreases in the fragment size with increasing ejection speed that had little variation between the planetary bodies.

4.2 Simulations

I have simulated the gravitational evolution of 2100 particles escaping from Mars at various speeds, for up to 100 Myr. The planets from Venus to Neptune were included in the simulations. The initial conditions for the test particles consist of placing the test particles uniformly on the surface of a sphere 100 martian radii away from the planet, moving radially outward at a chosen velocity v_∞ (this corresponds to uniform cratering of the planet). Previous work (Wetherill 1984) has shown that the delivery efficiency is relatively insensitive to the orbital phase and current orbital elements of Mars. Ejection from the planet results in the escaping particles being in heliocentric orbit immediately; no intermediate phase of orbit around the planet need be considered. Particles were removed for the same reasons as in the lunar case: planetary collision, $Q > 6$ AU, or Sun-grazing. The Sun-grazing criterion was changed to the actual solar radius (*i.e.*, $q = 0.005$ AU); the frequency of Sun-grazing was found to be insensitive to whether one or two solar radii were used as the termination distance.

The depletion rate of the ejected particles (Fig. 4.1) is clearly different from the other cases (launch from Mercury and Venus is discussed in Chpt. 5) because, even at this low ejection speed, re-collision with Mars is not a significant removal mechanism. Of the few Mars re-impacts that do occur, more than 90% take place in the first few Myr; once the relative velocities increase above the escape velocity, collisions with Mars remove an insignificant fraction. For higher ejection speeds, typically less than 2% of the particles re-collide.

The delivery efficiency of martian meteoroids to the Earth for $v_\infty = 1$ km/s is $\simeq 7.5\%$, with about one-third of these occurring in the first 10 Myr (Table 4.1). Interestingly, Mars, Venus, and Earth all receive comparable fractions of the material ejected from Mars. Raising the ejection velocity causes a small increase in the delivery efficiency to Earth (Table 4.2). The yields shown here are about an order of magnitude larger than those seen in Monte Carlo simulations (Wetherill 1984), although I have not yet included the possibly important effects of collisional destruction. These collisional effects lower the transfer efficiency by a factor of 2 at most, but this still results in a significant difference with the Monte Carlo results. The discrepancy can be understood by examining Fig. 4.2, which shows how the orbits of the escaped ejecta evolve after launch. It can be seen that the particles remain in the vicinity of Mars ($a = 1.52$ AU) only for the first 100,000 years. By 1 Myr several interesting phenomena have occurred: a few particles

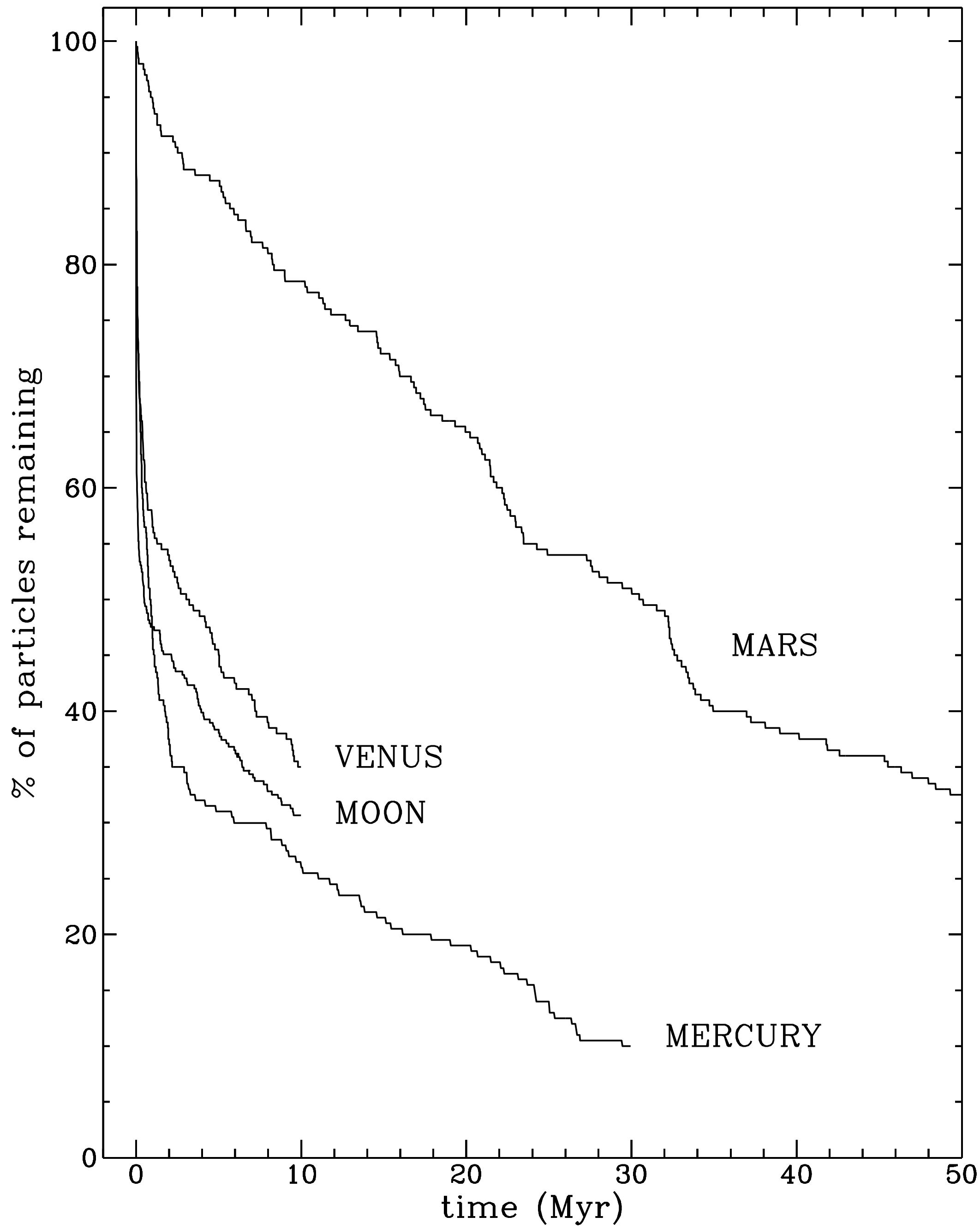

Figure 4.1 The fraction of escaping particles remaining in the simulations as a function of time. The simulations for Mercury, Venus, and Mars are the $v_\infty = 1$ km/s cases, while the lunar simulation shown is for an ejection speed v_l off the lunar surface of 2.4 km/s.

Table 4.1 Fates of the particles from a compilation of five v_∞=1 km/s martian ejecta simulations containing a total of 900 particles and lasting up to 100 Myr. No collisional effects are included in these simulations.

Meteoroid fate	Fraction
Impact Venus	7.5%
Impact Earth	7.5%
Impact Mars	9.0%
Sun-grazing	38%
Reach Jupiter	15%
Survivors	23%

Table 4.2 Transfer efficiencies for Mars ejecta in the first 15 Myr after launch, as a function of the ejection speed, with no correction for collisional destruction. All simulations used 300 particles. (*) Note that Sun-grazing and Jupiter-crossing only begin to operate efficiently after 10 Myr, and thus are under-represented here (compare with Table 4.1).

Ejection speed (km/sec)		Efficiency, in 15 Myr (%)				
v_∞	Surface	Earth	Venus	Mars	Sun*	Jupiter*
1.0	5.13	3.1	1.5	9.5	9.0	3.0
1.8	5.34	4.0	2.7	2.7	8.0	6.0
2.3	5.53	7.7	4.7	0.7	9.0	5.0
2.7	5.71	5.3	4.0	1.7	9.3	5.0
3.3	6.02	6.3	3.7	2.0	13.3	6.7

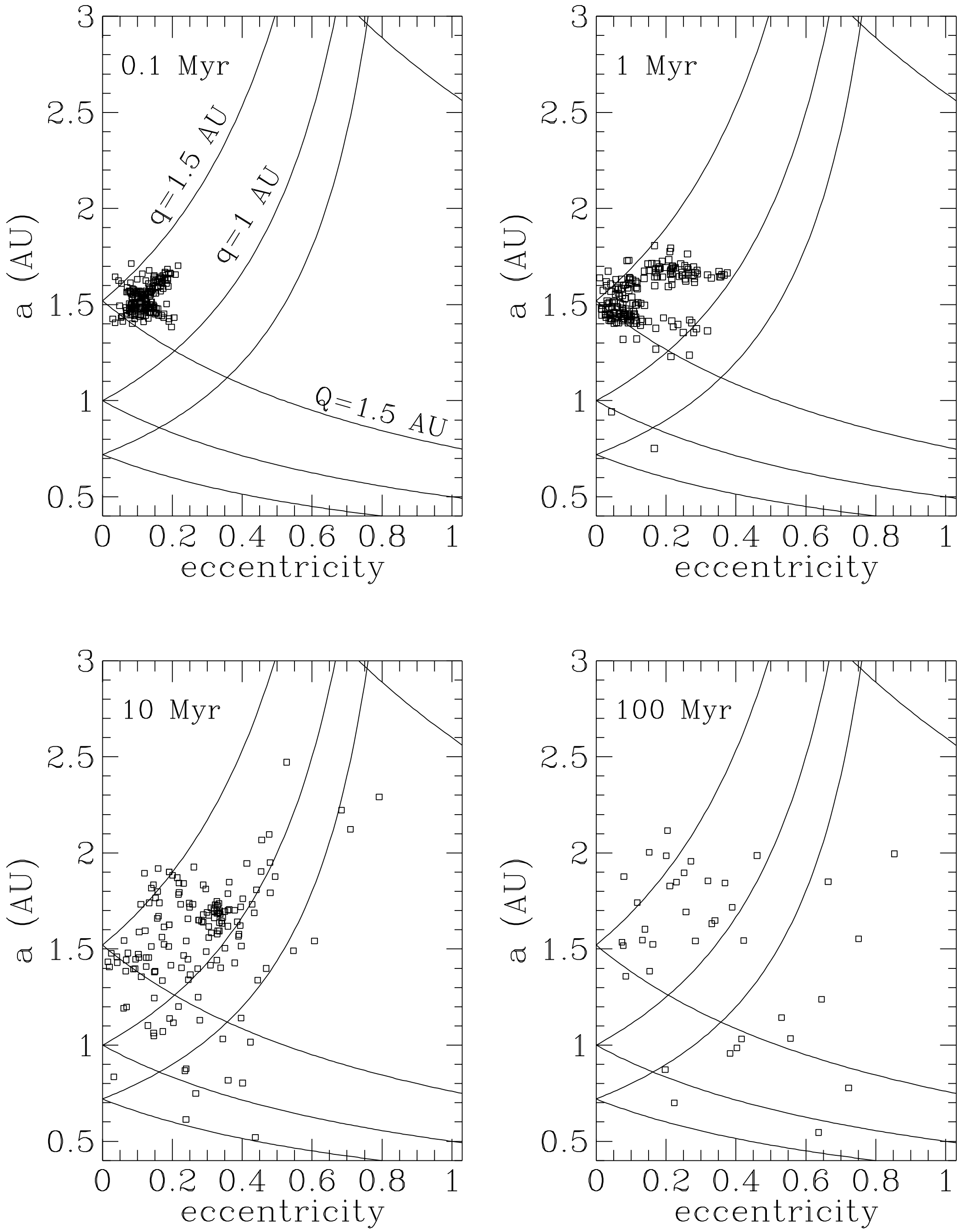

Figure 4.2 Orbital evolution of 200 particles launched from Mars with v_∞=1 km/s. The web of lines shows the locations where the perihelion or aphelion of a particle would lie at a planet's semimajor axis (the curve in the upper right corresponding to Jupiter).

have diffused down the $Q = 1.5$ AU line due to multiple close encounters (in a manner similar to that observed in the lunar simulations), and some of these particles have had their orbits drastically modified by the Earth (having crossed the $q = 1$ AU line). The obvious feature at $a \simeq 1.65$ AU is caused by secular resonances discussed in the next section. By 10 Myr most of the particles have been removed from Mars-like orbits, and by 100 Myr it is apparent that the population has been heavily depleted.

4.2.1 Secular resonances near Mars

Unlike the lunar simulation, diffusion up the $q = 1.5$ AU line is halted by the presence of two nonlinear, second-order secular resonances, which are thought to be located near $a \simeq 1.6 - 1.7$ AU using a perturbation theory calculation (Froeschlé and Morbidelli 1994). The resonances are $2g = g_5 + g_6$ and $g - s = g_5 - s_6$, with the former the more dynamically effective of the two. The libration of the two resonant arguments is shown for one of the test particles in Fig. 4.3. Note that in these figures the plotted resonant angle is indicated by the resonant frequency (*e.g.,* the angle $2\tilde{\omega} - \tilde{\omega}_5 - \tilde{\omega}_6$ is plotted in the $2g = g_5 + g_6$ panels. Here g and s denote the precession rates of the perihelion and ascending node of the particle, and g_i and s_i are the i^{th} fundamental secular eigenfrequencies of the solar system (Brouwer and Clemence 1961). First-order secular resonances occur when a single secular frequency is matched; for example, if $g = g_5$ then the particle's pericenter precesses at the same rate that Jupiter's does and the particle would be in the classical ν_5 resonance (the two notations are equivalent). In the current case the resonances are non-linear because they involve more than one fundamental frequency, and second-order because they do not appear in the expansion of the secular disturbing function until quadratic terms in the planetary masses are considered.

These resonances cause oscillations, with periods of $\sim 10^5$ yr, in the eccentricities of particles in this region up to Earth-crossing values ($e \simeq 0.4$) thereby raising the efficiency of delivery for martian meteoroids (Fig. 4.4). Since these resonances were not incorporated into earlier Monte Carlo simulations and appear to have such dramatic effects, it is not surprising that the results differ. These two secular resonances appear to be present in much of the phase space near the martian region; a large fraction of the particles (at many different values of a, e, and i) have precession rates (presumably induced by Mars) matching one of these secular frequencies, even though they may not be at the locations determined by Froechlé and Morbidelli (1994). Fig. 4.4 illustrates that particles can be at a variety of semimajor axes and eccentricities and still be locked in these resonances.

Besides the potential for Earth impact, another consequence of the delivery of particles to the $q = 1$ AU curve is that their semimajor axes can be raised by

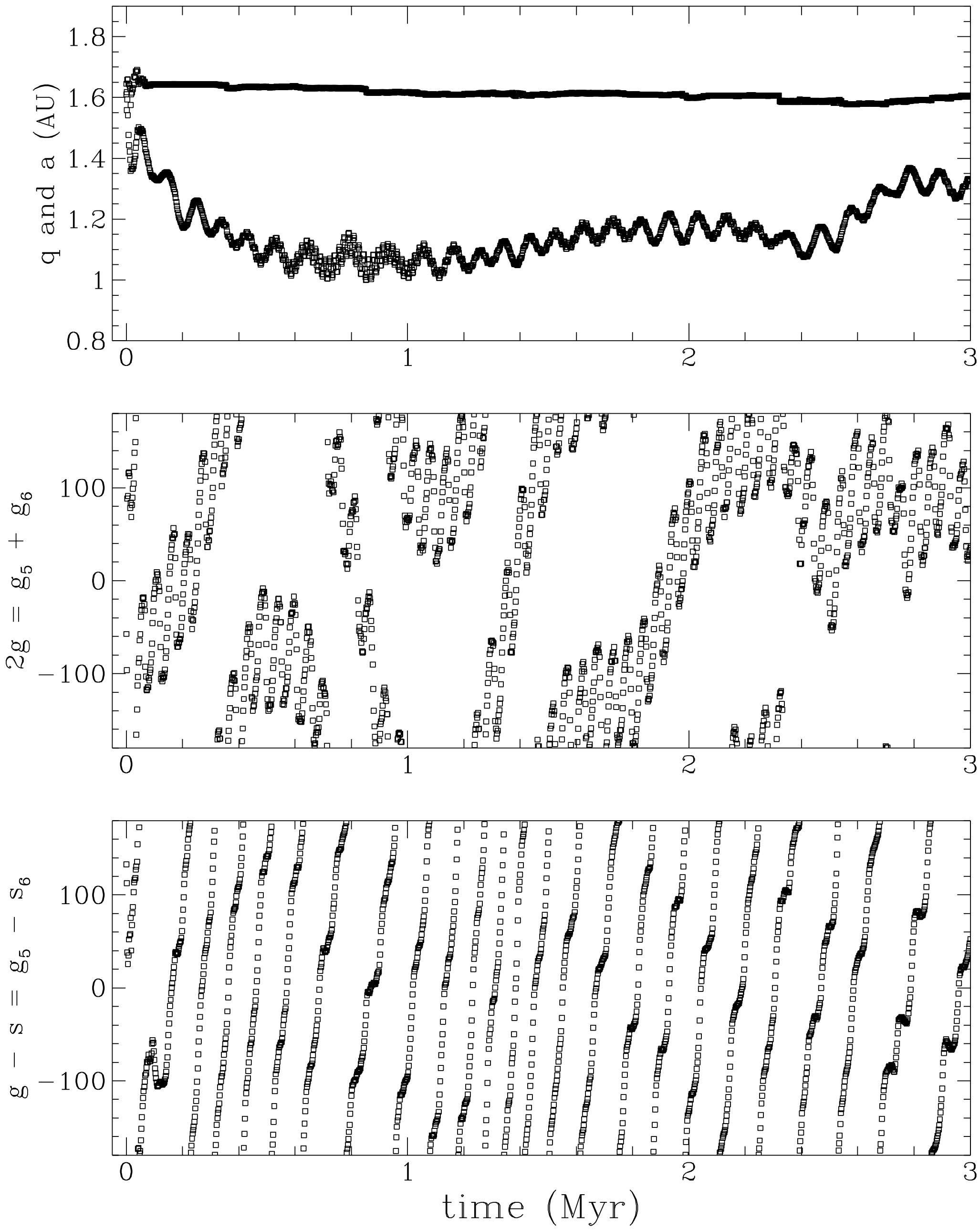

Figure 4.3 An orbital history of a martian meteoroid. The semimajor axis and perihelion distance are shown. This particle spends the duration of this simulation with an inclination $i < 20°$, and with ω and Ω circulating. The resonant angles indicate that the particle is near, but not exactly at the two second-order secular resonances, which nevertheless quickly increase its eccentricity to 0.3, and the particle becomes mildly Earth-crossing. The perihelion then decouples from the Earth, although the particle then firmly locks in the $2g = g_5 + g_6$ resonance.

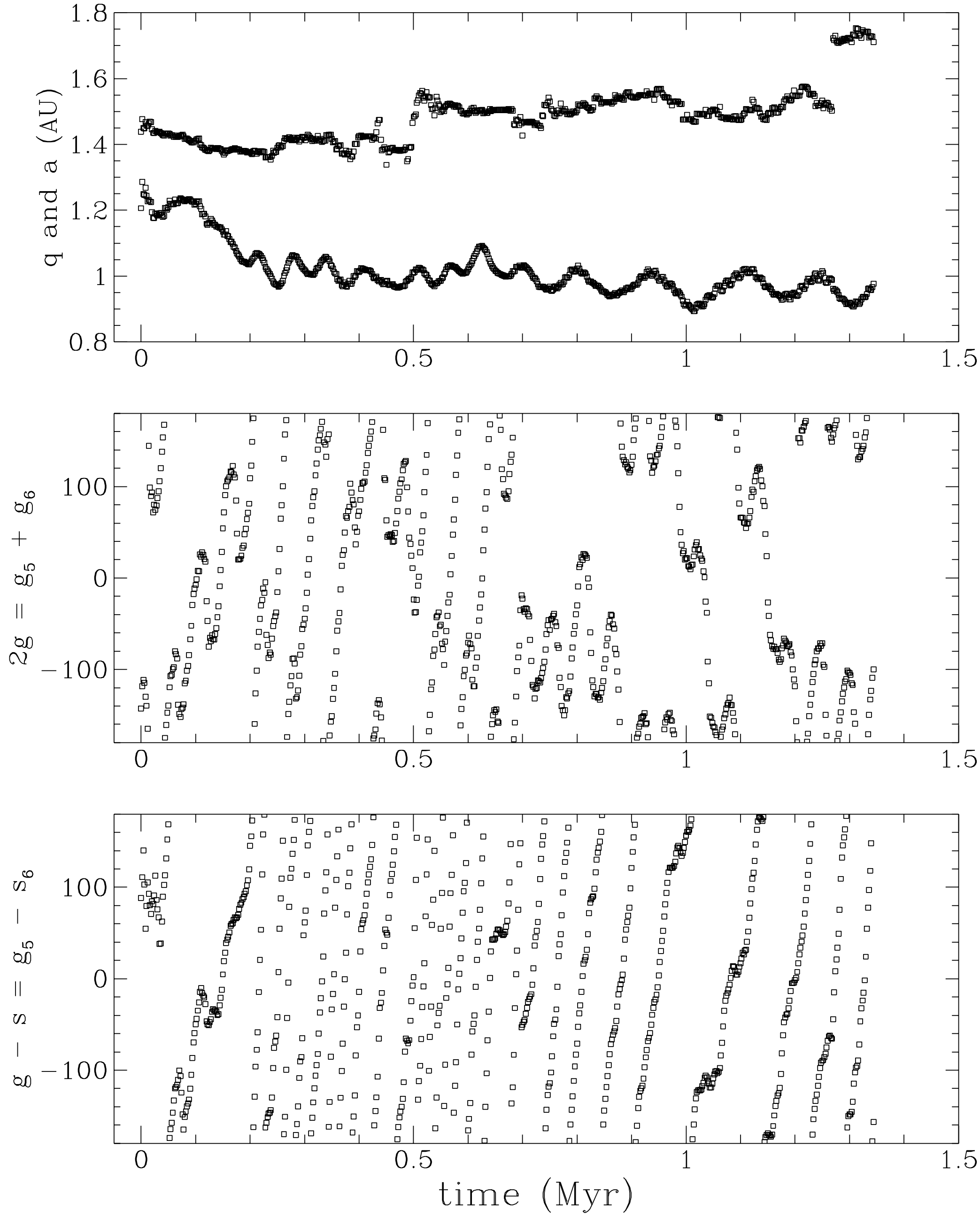

Figure 4.4 Libration of the two second-order secular arguments for a martian meteoroid that impacts the Earth. This particle appears to begin the simulation in the resonances (as indicated by the libration of the resonant angles), and they cause the eccentricity e to rise and thus perihelion q to be lowered to Earth-crossing values (the top panel also shows the semimajor axis a). The particle spends most of its lifetime locked in the $2g = g_5 + g_6$ resonance. Even the close encounter at $t \simeq 1.27$ Myr does not disrupt the resonant behavior. At $t = 1.38$ Myr the particle collides with the Earth.

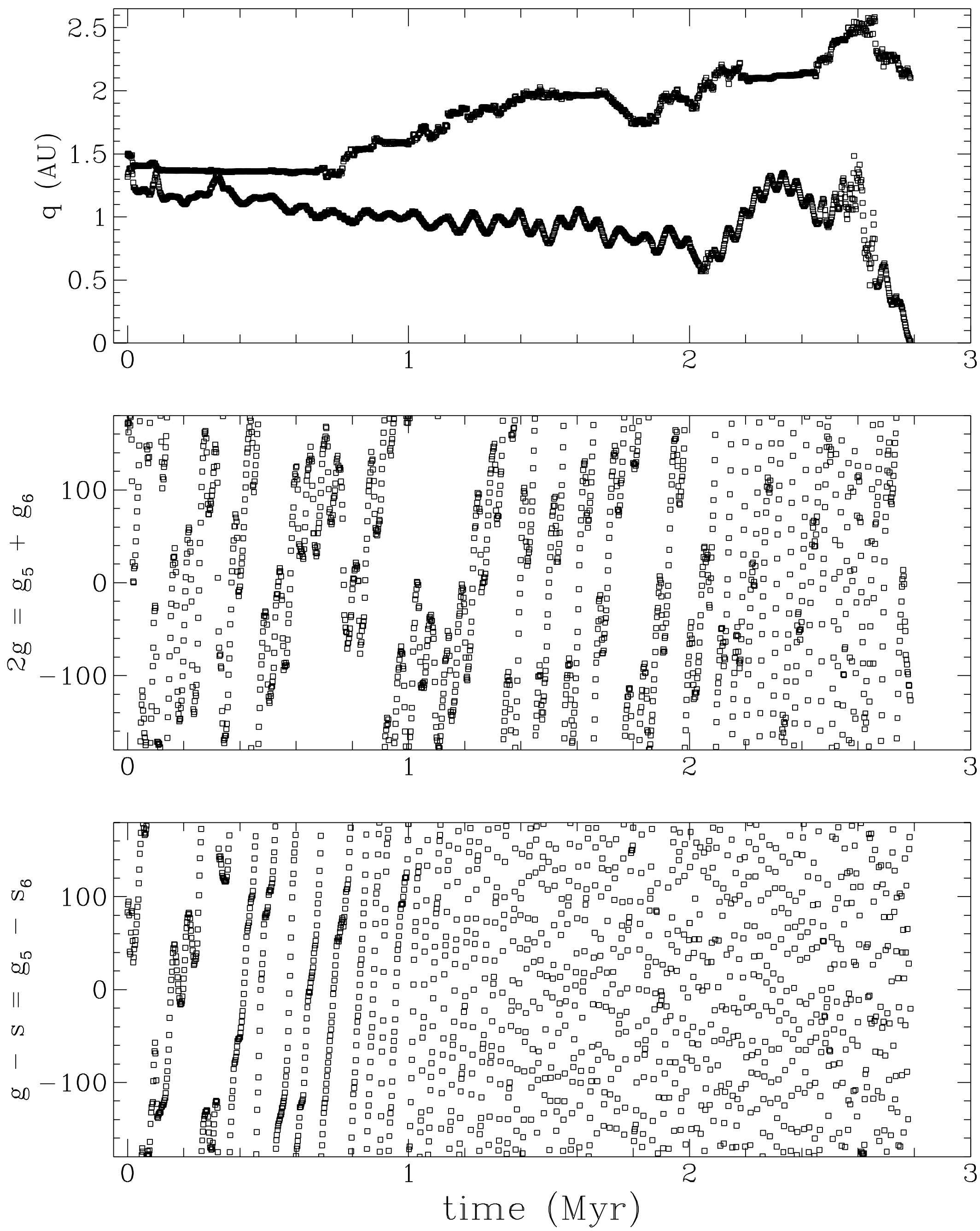

Figure 4.5 Libration of the two second-order secular arguments for a martian meteoroid that becomes a Sun-grazer. Starting at $t = 2.6$ Myr the eccentricity is driven to unity and the particle impacts the Sun. The other orbital elements and resonant arguments are shown in Fig. 4.6; note especially the resonant angle for the ν_6 resonance.

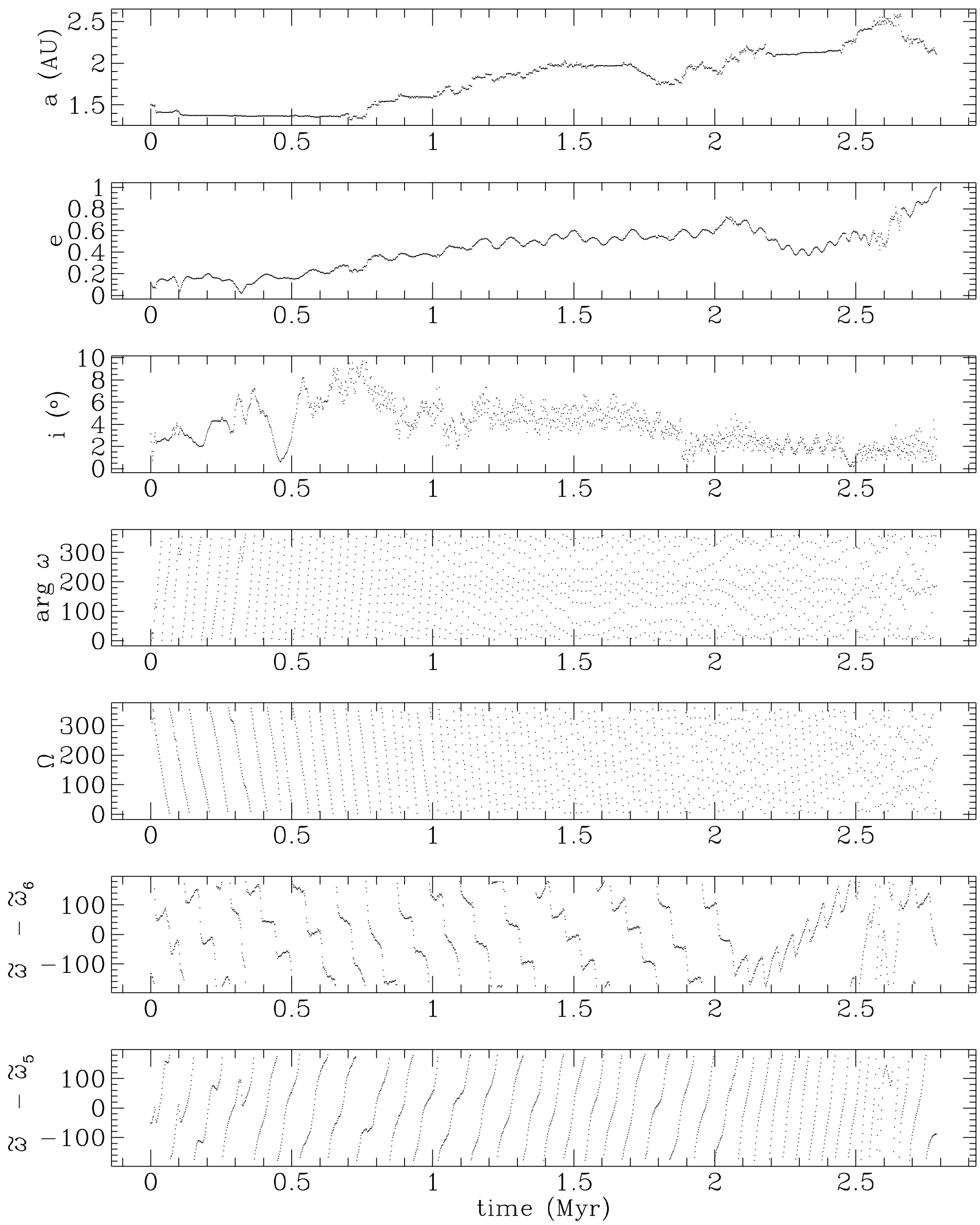

Figure 4.6 The other orbital elements for a martian meteoroid that becomes a Sun-grazer. This is the same particle as in Fig. 4.5. Note that ν_5 and ν_6 resonances are important near the end of the evolution; the eccentricity rises rapidly when the semimajor axis reaches $a > 2$ AU and both ν_5 and ν_6 are important. Note also that the particle seems to leave $2g = g_5 + g_6$ at 2.1 Myr when it becomes locked in ν_6.

close encounters (with the Earth and Venus) to the inner edge of the asteroid belt ($a \simeq 2.1$ AU), where the powerful secular resonances ν_6, ν_5, and ν_{16} operate; these resonances are capable of driving the eccentricities of test particles to unity at which point the particles strike the Sun, as discussed previously. Sun-grazing is discussed for near-Earth asteroids by Farinella *et al.* (1994), for the short-period comets by Bailey *et al.* (1992), and for the Jupiter family comets by Levison and Duncan (1994).

Sun-grazing (illustrated in Figs. 4.5 and 4.6) is in fact by far the dominant loss mechanism after 10 Myr. By 100 Myr almost 40% of the particles have been driven into the Sun, more than twice the number removed from the system by crossing Jupiter's orbit. These two effects ultimately deplete the swarm and yield an almost linear decline in the number of surviving meteoroids (Fig. 4.1); this partly explains why no martian meteorites have 4π ages older than ~ 15 Myr; collisional effects, which also contribute, will be discussed in the next section.

To conclude our discussion of the simulations, Fig. 4.7 presents cumulative spectra (over 15 Myr of evolution only) for the simulations presented in Table 4.2. In contrast to the lunar case, the delivery rate of martian meteorites to the Earth appears to be almost constant (note the linear time axis, as opposed to the logarithmic one for the lunar case of Fig. 3.13). Given the relatively small number statistics of the simulations there is little difference between the launch velocities. The only slight difference is that the $v_\infty = 2.3$ km/s case has an increase in early deliveries due to the fact that at this value of v_∞ a fair number of particles have $q \simeq 1$ AU at the very beginning of the heliocentric simulation, allowing almost immediate deliveries.

4.3 Comparison with meteorite data

Fig. 4.8 shows, in a cumulative plot, the expected CRE age spectrum for the purely gravitational N-body simulation with $v_\infty = 1$ km/s, which was run for 100 Myr of simulated time in order to extend well past the 4π age of the oldest martian meteorite. The agreement with the martian meteorite data does not appear to be as good as in the lunar case; only a little more than half of the meteorites delivered in the simulation arrive within the 15-Myr upper bound of the recovered meteorites (a problem mentioned in Sec. 1.5). However, this disagreement is not surprising at this stage. The delivery time scale is many millions of years (as opposed to tens to hundreds of thousands of years for the lunar meteorites). Many of the martian meteoroid orbits reach out to the asteroid belt ($Q > 2.1$ AU) for at least some of the time during their journey to the Earth and thus the meteoroids will be prone to collisional disruption, with a half-life of ~ 1–10 Myr (Bottke *et al.* 1994). This is in rough agreement with the observed CRE ages of the ordinary chondrites (Wasson 1985). Wetherill (1988) postulates

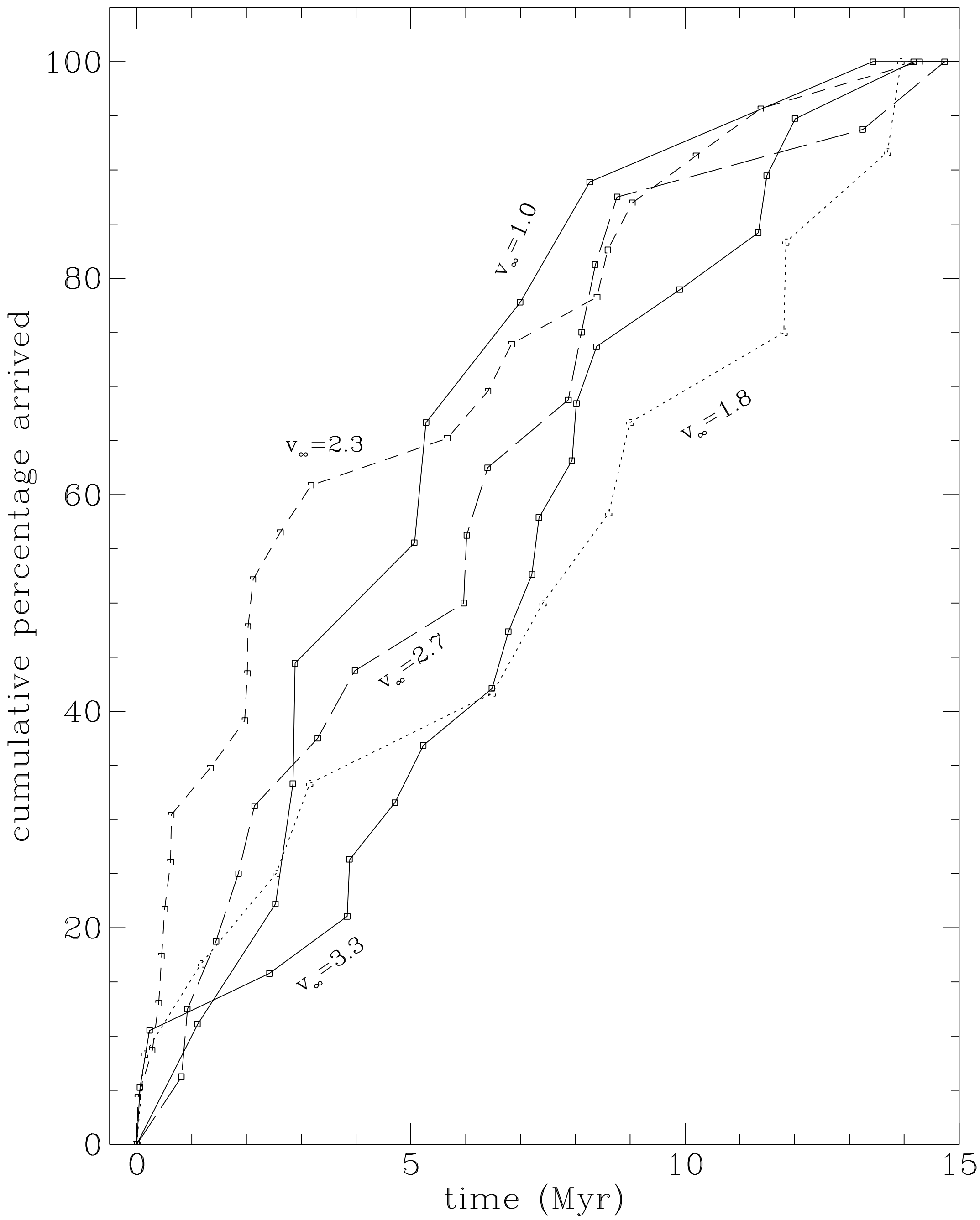

Figure 4.7 Cumulative delivery spectra for all 15 Myr martian simulations. The vertical axis is the cumulative fraction of objects that have struck the Earth, *of all those that will within 15 Myr*. The points shown represent each individual impact seen in the simulation (of 300 particles). Given the relatively small number of deliveries, these spectra are all well represented by a constant delivery rate, although note that the total efficiency varies by a factor of about 2 (Table 4.2).

a collisional half-life for a meteoroid of radius r (in cm) of

$$\tau_{\rm coll} = 1.2 \times 10^6 \; r^{1/2} \;\; {\rm yr}, \tag{4.1}$$

when $Q > 2.1$ AU. Thus a $r \simeq 3$ cm meteoroid (pre-atmospheric mass ~ 300 g) with aphelion in the main belt would have a collisional lifetime of only 2 Myr. Since the half-life scales only as $\sqrt{r}$, the range of a factor of 10^3 in martian meteorite masses corresponds to a variation of only a factor of 3 in $\tau_{\rm coll}$. Even the 40-kg Nakhla meteoroid would have had a collisional half-life of no more than ~ 5 Myr if it entered the main belt. Thus I have used the value of 2 Myr (roughly the lifetime for the median martian meteorite mass) for all meteoroids; further refinements are unwarrented in any case given the small numbers of meteorites.

The time spent in the main asteroid belt as a function of transit time to the Earth was tabulated from the simulations (Fig. 4.9). It is apparent that most meteoroids that arrive at the Earth in less than 10 Myr spend little, if any, time transiting through the main belt. On the other hand, most objects taking more than 10 Myr to arrive at the Earth spend many millions of years in the main belt, and are unlikely to survive this given their small sizes. (Chondrites with CRE ages of tens of Myr are known, but this cosmic ray exposure was almost certainly acquired while the material was in roughly meter-sized bodies, in concordance with Eq. 4.1).

I am assuming a model in which hypervelocity collisions into martian meteoroids smaller than several tens of kilograms are so catastrophic that no collisional products are capable of surviving until Earth delivery (if this were not true, then we should presumably have martian meteorites with transit ages as old as the oldest chondrites). The mean residence time in the belt was calculated from Fig. 4.9 as a function of transit time (using 3-Myr bins) and convolved into the delivery spectrum (Fig. 4.8). With such a collisional model, the N-body simulation matches the CRE data reasonably well; however, the collisions lower the delivery efficiency for the $v_\infty = 1$ km/s case from 7.5% to $\simeq 3$%.

4.4 Implications for the launch process

The age distribution of the martian meteorites is consistent with a model in which all fragments are launched, at speeds modestly above the escape velocity, as small bodies and delivered independently to Earth. The orbital elements just before impact of the particles in one of the v_∞=1 km/s simulations are shown in Fig. 4.10. The simulated meteorites delivered in the first 15 Myr almost all have entry velocities into Earth's atmosphere in the range 11–17 km/s (Fig. 4.11), in agreement with the ablation data for the SNCs (Bhandari *et al.* 1988). In fact, there is some cosmogenic nuclide evidence that the quickly arriving shergottites have systematically lower ablation than the other martian meteorites (Garrison

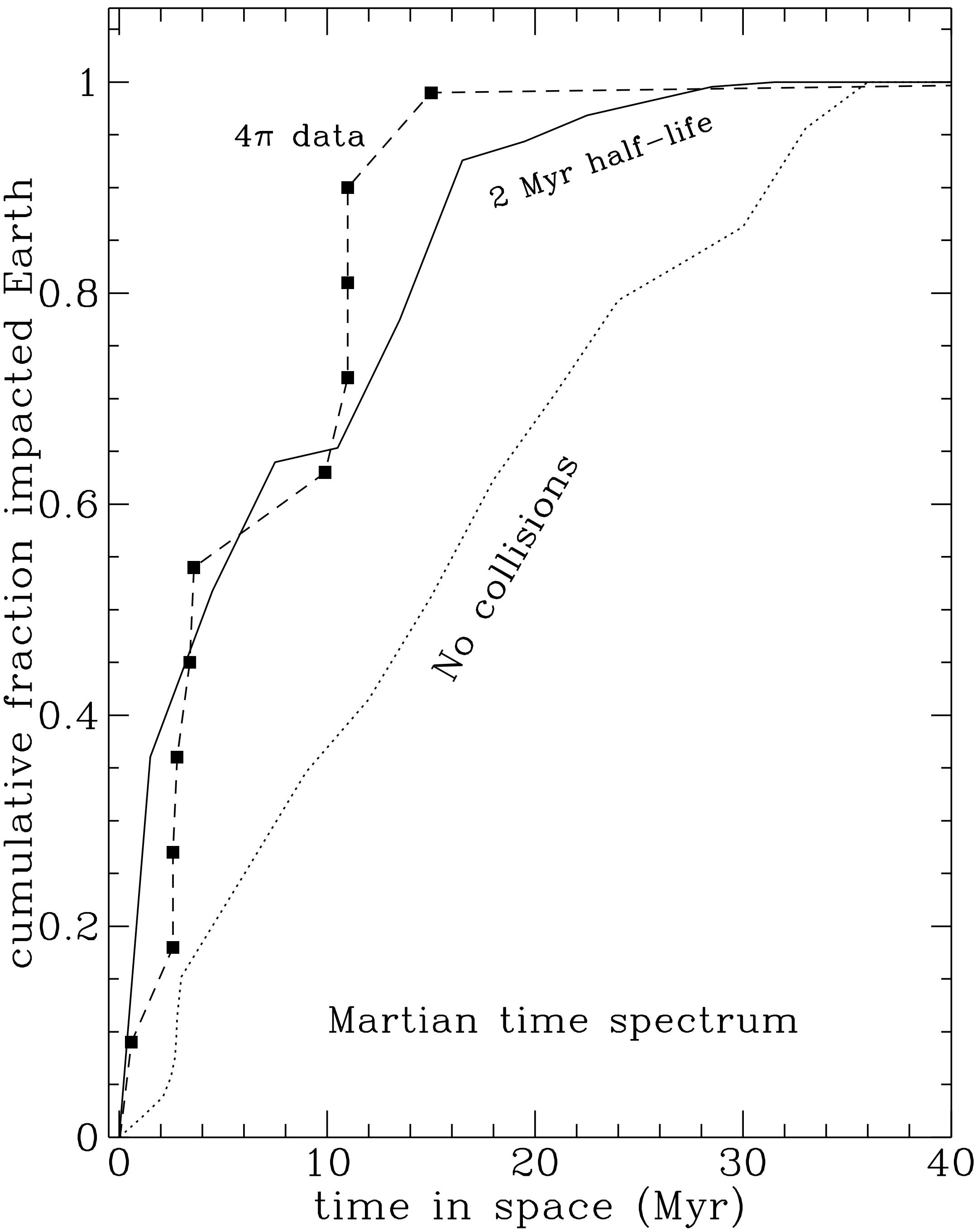

Figure 4.8 Cumulative plot of the expected CRE age spectrum of the martian meteorites. The curves show (as a function of time) the cumulative number of meteorites that have struck the Earth (as a fraction of those that do within 40 Myr. The solid and dotted curves show predicted spectra, one incorporating catastrophic collisions (solid) and the other without (dotted). The dashed line connects the data points for the martian meteorites.

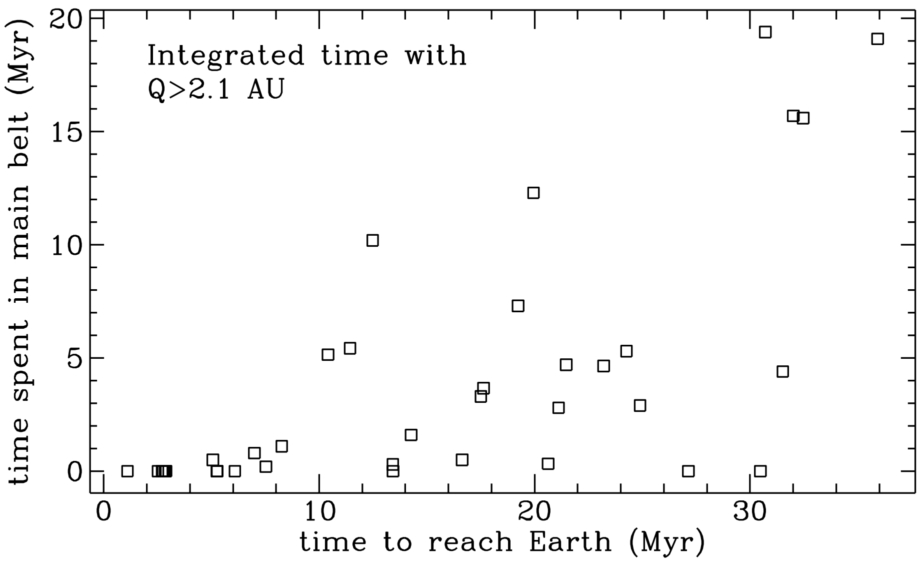

Figure 4.9 For the particles that struck the Earth in the first 40 Myr of the 100-Myr, v_∞=1 km/s simulation, the integrated amount of time spent in the main asteroid belt is plotted as a function of the time it took for the meteoroid to reach the Earth. (Only 1 particle struck the Earth after this, at $t = 73$ Myr).

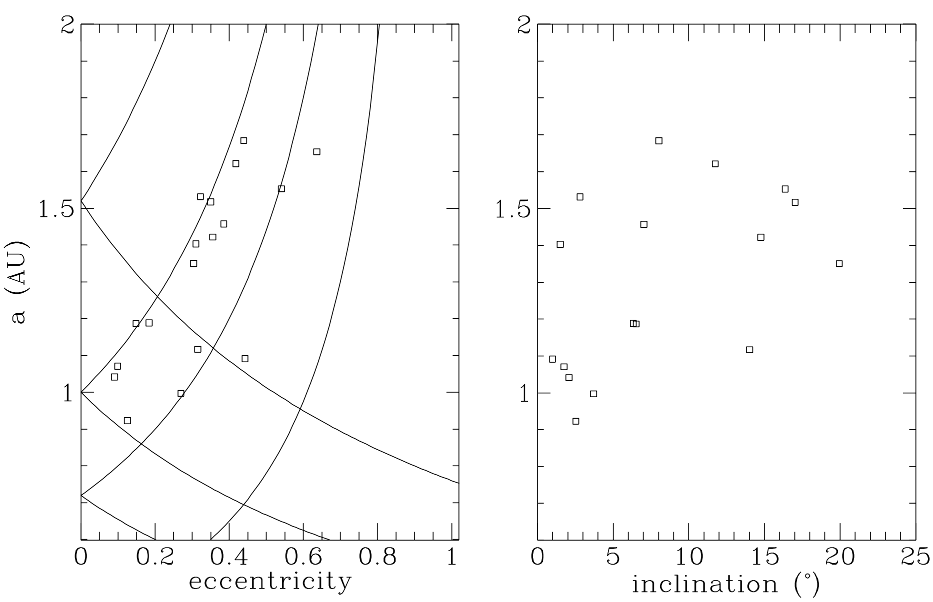

Figure 4.10 The orbital elements just before impact of the simulated meteorites from one of the 100-Myr simulations.

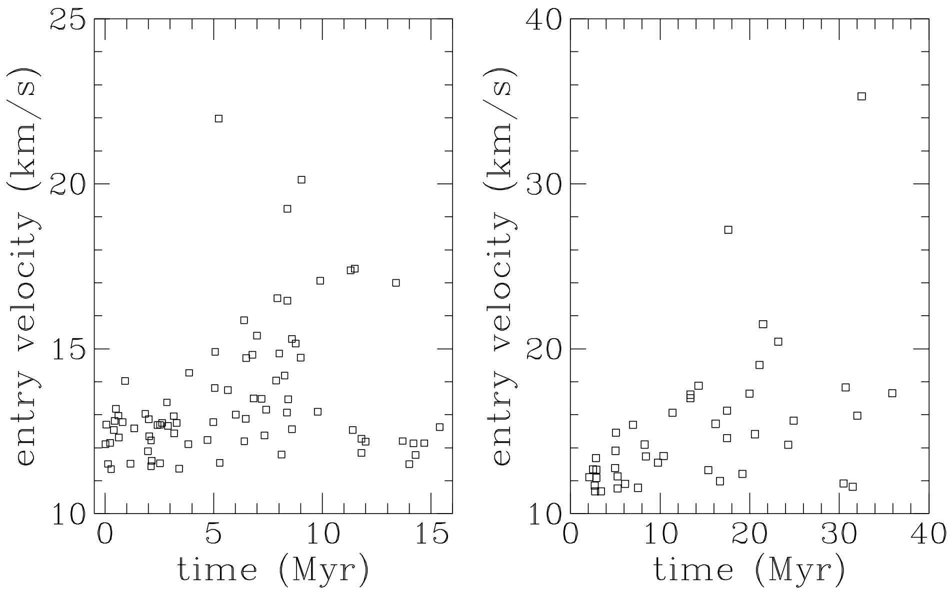

Figure 4.11 The entry velocities for the simulated martian meteorites that reach the Earth. Left panel: All particles from the 15-Myr simulations. Right panel: particles from the 100-Myr simulation. Note the differing axes.

et al. 1995, Swindle *et al.* 1996). This tendency is definitely supported by the simulations; Fig.4.11 shows atmospheric entry velocities at the Earth for the meteorites from all of the 15-Myr simulations as well as the 100-Myr simulation. Meteorites arriving as rapidly as the shergottites (<4 Myr) seldom seem to have atmospheric entry velocities greater than the relatively low value of 13 km/s, which would result in ablative mass losses of 40–60% (ReVelle 1979), corresponding to about 20% of the meteoroids radius. This could explain the systematically lower ablation seen in the shergottites (Garrison *et al.* 1995).

However, the simulations do not explain the apparent clustering of the 4π CREs into at least 3 groups: 0.6 Myr (1 object), 3 ± 1 Myr (5 objects), and 13 ± 3 Myr (5 objects). Are these groups due to source-crater pairing (p. 2) or, alternatively, to separate collisional fragmentations of large meteoroids in space (Bogard 1995)? Note that the cumulative spectrum (Fig. 4.8) would be unchanged by source-crater pairings. Tremain and co-workers (Tremain *et al.* 1994, Tremain 1995a) argue for one-stage exposures as small bodies, but allow for source-crater pairing of the shergottites or nakhlites/Chassigny. The martian meteorites share much closer petrologic affinities than the lunar meteorites (McSween 1995): the 3-Myr group contains only shergottites, and 3 of the 13-Myr group are the nakhlites. Recently, Eugster (1996) claims the following source-crater pairings on the basis of CRE evidence: three of the basaltic shergottites (Shergotty, Zagami, and QUE94201) at $\simeq 2.7$ Myr ago, the two lherzolitic shergottites at $\simeq 3.5$ Myr ago, and all three nakhlites at $\simeq 10.5$ Myr ago (*cf.* Tables 1.2 and 2.1). I agree that these age clusters likely represent individual impact events into distinct source terrains (see Chpt. 6).

A previously considered hypothesis (Vickery and Melosh 1987) – that all the martian meteorites are derived from recent catastrophic fragmentations of large bodies that were launched 200 Myr ago and then stored in space – is rendered very unlikely since the simulations demonstrate that few parent bodies can dynamically survive for this time owing to the efficiency of meteoroid destruction, especially by Sun-grazing. This model would also have to explain why (i) there are no meteorites from the upper few meters of the parent meteoroids (half of even a 10-m meteoroid is within 2 m of its surface and thus exposed to cosmic rays!), (ii) no impacts more recent than 200 Myr have been sampled, and (iii) only shergottite parent meteoroids have been disrupted in the last 3 Myr, and none before. The results presented here show that the simpler model, which produces exclusively small meteoroids, explains all the CRE evidence, although source-crater pairings and relative surface properties of the Moon compared to Mars may be important. The issues of why such groupings occur for Mars but not for the Moon and why there are equal numbers of lunar and martian meteorites (Wetherill 1984) remain, and will be considered in Chap. 6.

Chapter 5

Delivery from Other Terrestrial Bodies

The numerical simulations indicate that particles diffuse readily throughout the inner solar system, and so, for completeness, this chapter presents discussions about delivery efficiencies from the solar system's remaining parent bodies. The fact that we have no meteorites from these objects argues that either (1) the transfer process is less efficient, (2) the launch process is less efficient, or (3) we have such meteorites and simply do not recognize them. The last possibility is probably the least likely (but see the discussions in Lindstrom *et al.* 1994; Love and Keil 1995). The second possibility is not inconceivable, but it is perhaps difficult to devise a reason that at least the mercurian surface should be dramatically different from that of the Moon.

5.1 Mercury

It should be possible to liberate meteoroids off the surface of Mercury, as its escape velocity (4.2 km/s) is lower than that of Mars (5.0 km/s), and the impact velocities on Mercury should be higher, thus making more energy available for the launch. However, the dynamical transfer of this ejecta to Earth is substantially more difficult because Mercury lies deep in the Sun's gravitational well. Ignoring resonance effects, a series of properly-timed Mercury scatterings will be needed for the meteoroids to be pushed across Venus's orbit and thence to Earth. Monte Carlo calculations (Wetherill 1984, Melosh and Tonks 1993) had found the total delivery efficiency to the Earth to be on the order of 10^{-4} in 10^7 yr.

* This chapter is an expanded version of discussion given in the paper: Gladman, B., J.A. Burns, M. Duncan, P. Lee, and H. Levison (1996), The Exchange of Impact Ejecta Between Terrestrial Planets, *Science* **271**, 1387–92 [copyright 1996 by the American Association for the Advancement of Science].

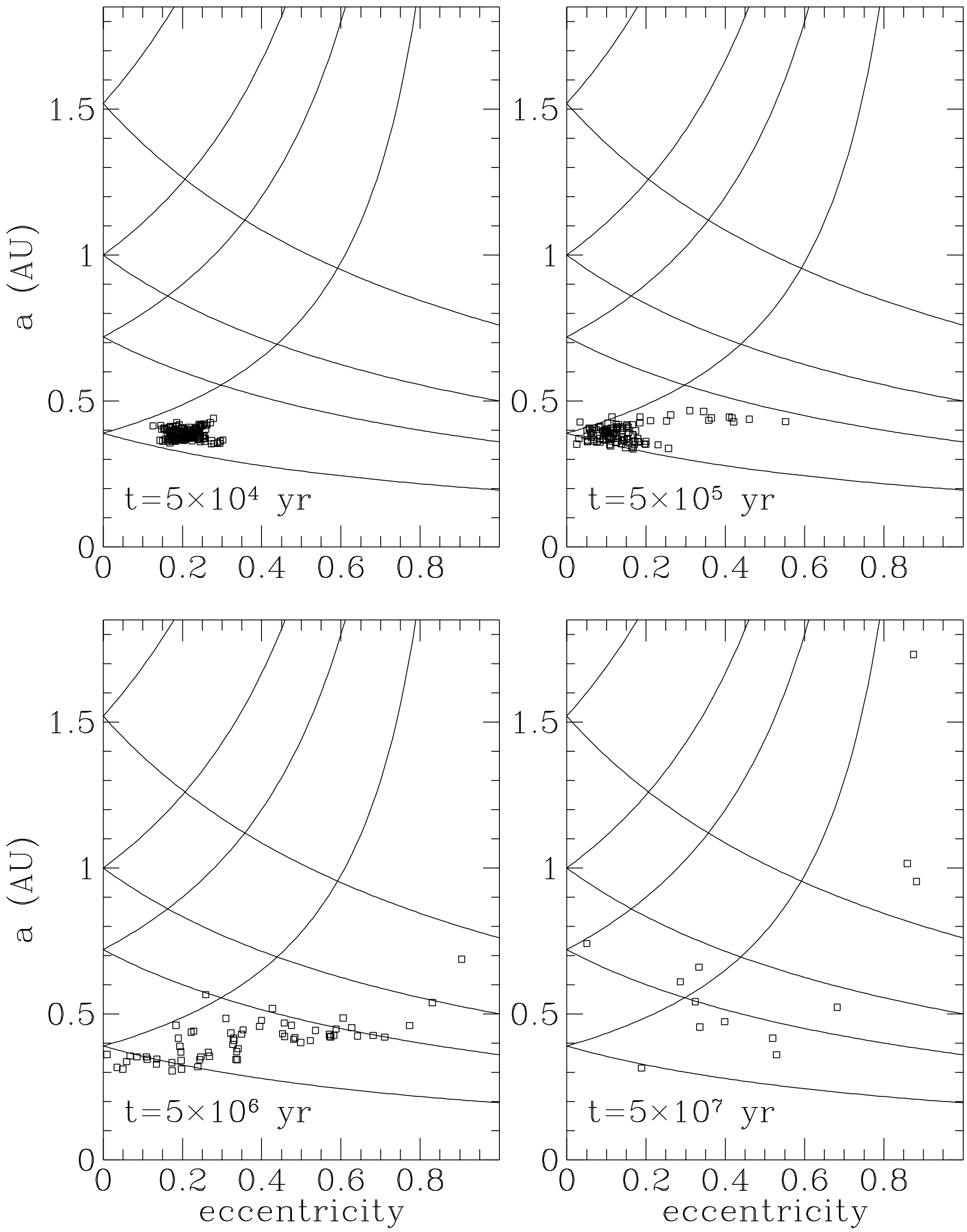

Figure 5.1 Orbital evolution of 200 particles launched from Mercury with v_∞=1 km/s. The web of lines show the locations where the perihelion or aphelion of a particle would lie at a planet's semimajor axis. The orbital inclinations never rise above $\simeq 35°$.

Table 5.1 Fates of the particles from simulations of mercurian and venusian impact ejecta. Both simulations used 200 particles. No collisional or radiation effects are included in these simulations.

Parent Body:	Mercury	Venus
Duration (Myr)	50	10
Meteoroid fate (%)		
Impact Mercury	78.5	0.5
Impact Venus	7.0	47.0
Impact Earth	0.5	8.5
Impact Mars	0	0
Sun-grazing	3.5	4.5
Reach Jupiter	1.5	4.0
Survivors	9.0	65.0

To address this problem I have tracked 200 particles launched from Mercury in random directions having $v_\infty = 1$ km/s after escaping from the planet. The re-accretion rate is initially very high (Fig. 4.1) due to the low relative velocity of the particles with respect to Mercury, whose heliocentric orbital speed of $\simeq 48$ km/s is very large. The lunar and mercurian cases are similar because, compared to the planetary orbital speed, the initial random velocity is very small. For Mercury, about three-quarters of all launched particles are re-accreted during the 50-Myr simulation (Table 5.1). Snapshots of the orbital elements spaced logarithmically in time are shown in Fig. 5.1.

Just 1 of the 200 particles was found to hit the Earth, after 23 Myr. Its orbital history is shown in Fig. 5.2. Note that this particle occasionally librates in the ν_5 or ν_6 resonance, and that these periods seem to be characterized by stability rather than instability. It is unclear whether the particle is simply near the resonant frequency by chance and in an epoch of few close encounters, or whether the resonance is actively maintaining the resonant state. The particle appears to be delivered to Earth-crossing by a large number of close encounters with Venus, that begin after 14.5 Myr.

The 0.5% Earth delivery efficiency is 50 times higher than previously suggested, but is obviously based upon rather poor statistics; it is about an order of magnitude smaller than the efficiency for Mars. The current formation rate of >10 km diameter craters is thought to be a factor of two larger on Mercury than on Mars, although most of the crater-producing projectiles on Mercury are cometary (Wetherill 1989). Mercury's smaller escape velocity should therefore result in a larger meteoroid liberation rate. Thus, if we accept the 0.5% efficiency, the existence of 12 martian meteorites would lead us to expect a few mercurian meteorites. Alternately, a comparison based on the Moon's meteorite

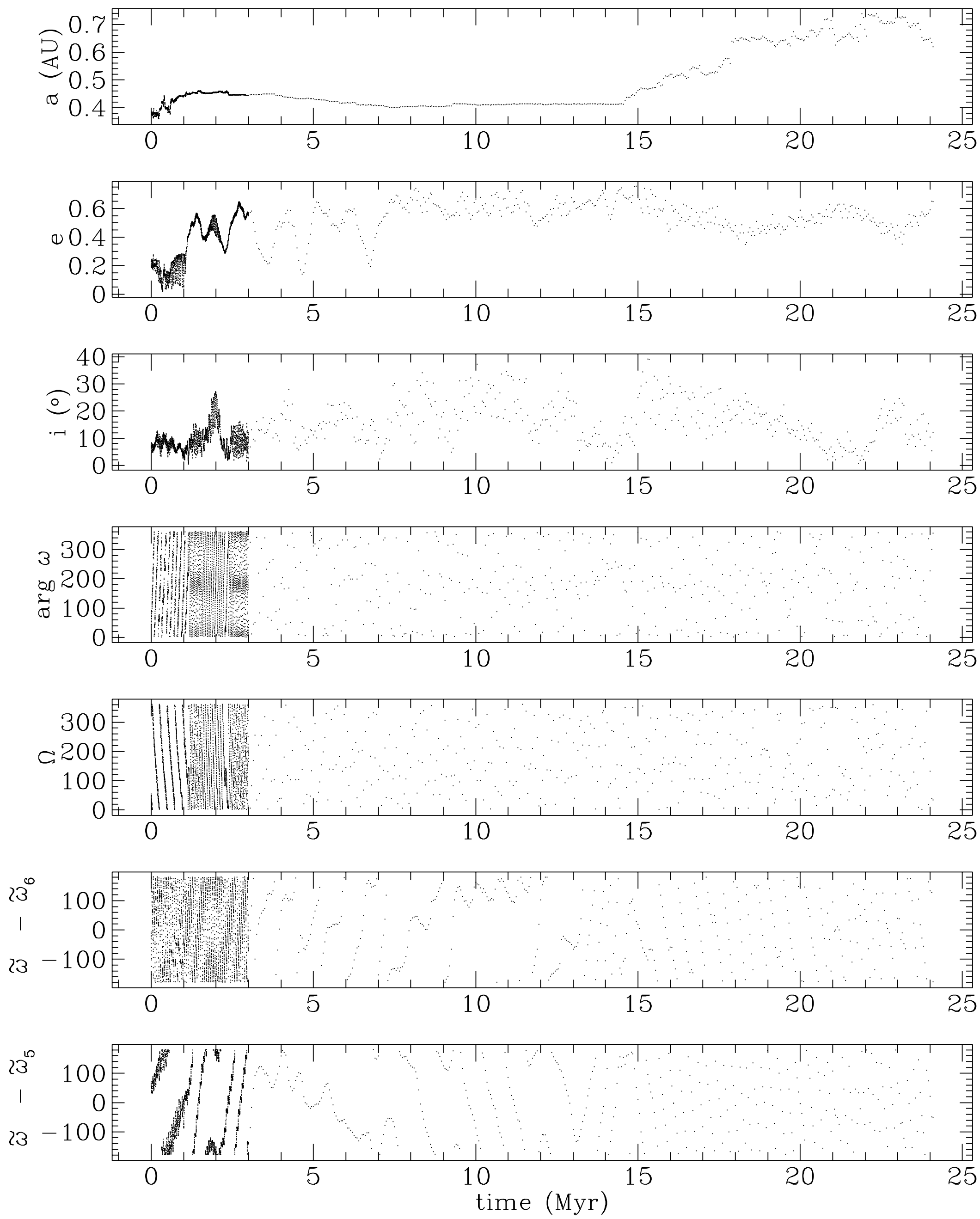

Figure 5.2 Orbital evolution of the single mercurian particle that impacts the Earth (at 24.1 Myr after ejection). The output sampling interval of the simulation was lowered after 3 Myr.

contribution (where the present cratering rate for Mercury is at least an order of magnitude larger, but the delivery efficiency 100 times smaller) also yields a few expected mercurian meteorites.

However, a purely gravitational model may not be sufficient to accurately simulate the transfer of material from Mercury to the Earth. Radiation forces in the inner solar system cause significant orbital evolution over tens of Myr, times like that required for the single simulated meteoroid to reach the Earth. Orbital collapse due to Poynting-Robertson (P-R) drag at Mercury's heliocentric distance occurs on a time scale:

$$\tau_{\mathrm{PR}} = \frac{7 \times 10^6}{Q_{\mathrm{pr}}} s \rho R^2 \tag{5.1}$$

where s and ρ are the radius and density of the particle (in cgs units), R is its heliocentric orbital radius (in AU), and Q_{pr} is a coefficient of order unity that depends on the scattering properties of the particle (Burns *et al.* 1979). Orbital collapse thus takes only ~ 5 Myr for a 5 g/cm^3, 1 cm radius meteoroid at 0.39 AU. On the other hand, the Yarkovsky effect, which dominates over P-R effects for particles of this size with spin periods longer than 1 s (Burns *et al.* 1979), may induce some mercurian meteoroids to spiral outward to Earth. Love and Keil (1995) discuss the Yarkovsky effect and the problems of identifying mercurian meteorites. However, mercurian meteoroids may be catastrophically fragmented by dust-sized impactors which, due to gravitational focussing, increase significantly as the Sun is approached. Collisional lifetimes of 100 g bodies at Mercury's distance are estimated to be $< 10^5$ yr (Grün *et al.* 1985). Because of these complications, the likelihood of finding mercurian meteorites is difficult to quantify, and must be left as an open question. It appears dynamically possible, but the abundance will certainly be smaller than those from the Moon or Mars.

5.2 Venus

The identification of meteorites from the Moon and Mars has allowed scientists to consider more seriously the possibility of finding meteorites from Venus or the Earth (hereafter, 'venusian' and 'terrene' meteorites). The higher escape velocities of these planets will only be overcome by a tiny fraction of the ejecta, and then only in the larger and much rarer impact events. The difficulty of successful ejections is heightened by the presence of massive atmospheres on the Earth and Venus since such atmospheres effectively screen out all crater-producing impactors below a certain threshold size, and launched fragments have to plow back through the atmosphere (Melosh 1988). Chyba (1993) points out that the Earth's atmosphere prevents stony objects with diameters < 50 m from reaching the ground and creating hypervelocity impact craters; For Venus, data from the Magellan spacecraft has shown that impactors below $\sim$i 1 km are hindered from reaching the surface (Schaber *et al.* 1992). The ejecta liberated by impactors that successfully reach the surface of Earth or Venus must find their way back out through an atmosphere just as dense as the one faced by the impactor; the ejecta is likely moving much slower than the impactor and will have a smaller ratio of mass to surface area, making the atmosphere even more of an obstacle. One way around this final difficulty is the possibility that some of the ejecta could exit out the 'tunnel' left in the atmosphere by the impactor's entry, which would not have had time to close before the ejecta exits (Melosh 1988).

For completeness, I have performed a single 10-Myr simulation of the evolution of venusian impact ejecta with $v_\infty = 1$ km/s (Table 5.1). The loss rate was shown in Fig. 4.1 (page 59). Unsurprisingly, Venus re-accretes almost half of its ejecta in 10 Myr, comparable to the Earth's re-accretion rate (*cf.* Table 3.5). Based on these simulations, we expect that the re-accretion efficiency by the Earth of its own ejecta will be several times higher than Earth's accretion of Venusian ejecta. Given the much more massive atmosphere of Venus, if venusian meteorites are possible then certainly terrene meteorites should be much more abundant. Thus let us now restrict our attention to the latter.

5.3 Earth

The lunar simulations should suffice to estimate the Earth's re-accretion efficiency for its own ejecta. Assuming a small v_∞ for the departing material, if the Earth has been struck by an impactor large enough to eject material, then it would have re-accreted roughly 20–50% of the ejecta, on a short (< 1 Myr) time scale. How could a terrene meteorite be recognized and distinguished from untravelled material? Presumably only falls, or finds with preserved fusion crusts, would be readily accepted as bona fide terrene meteorites: anomalous Earth rocks found on the Antarctic ice sheet are probably our best hope. Since only massive rare impacts are capable of launching such objects, it is unfortunately (or fortunately!) the case that the Earth likely has not recently experienced an event capable of ejecting Earth rocks at greater than the escape velocity. Thus we should not expect terrene meteorites in the relatively young (< 1 Myr old) Antarctic ice sheet. The problem of distinguishing such meteorites, even in Antarctica, is paramount.

The only Earth-objects that we now know to have been ejected into space space are tektites (impact glasses), some of which may have been launched along sub-orbital trajectories arching above the Earth's atmosphere before re-entry (see Koeberl 1986 and references therein). With slightly higher speeds, other tektites might have escaped the Earth's gravitational field. Such objects would have a high probability (≈ 30–50%) of rapidly re-impacting the Earth. Isolated tektite finds (that is, not part of a strewn field) would be worth examining for evidence of a brief ($\ll 1$ Myr) CRE. Searches for CR-induced radionuclides in tektites have produced only upper limits on their time in space varying from < 900 to $< 90,000$ years. Relevant papers are reviewed by O'Keefe (1976). Since the tektites examined were from strewn fields, which implies that they never escaped to heliocentric orbit, these results do not necessarily constrain theories of objects that escape from the Earth.

A proviso in this picture is that tektites are not strictly analogous to the relatively lightly shocked lunar and martian meteorites. It may be perhaps more relevant to ask: where are the tektites from the Moon and Mars? Presumably the answer is simply that this highly shocked, jetted material makes up a negligible fraction of the mass ejected in any given impact.

The orbital histories of terrene meteoroids, if any exist, are also of interest in view of the enormous efforts expended to sterilize spacecraft to prevent the contamination of Mars by terrestrial organisms. This sterilization would make little sense if terrestrial microorganisms have already been carried to Mars aboard terrene meteorites (Melosh 1988).

5.4 Phobos and Deimos

The only remaining permanent denizens of the inner solar system are the two martian moons. Their relatively small geometrical cross-sections compared to Mars (10^{-5} and 3×10^{-6} that of Mars for Phobos and Deimos, respectively) may be more than compensated for by the much greater ease that ejecta will have in escaping the martian gravity well. With orbital velocities of 2.1 and 1.4 km/s, ejecta need only leave the surface of the moons at less than 1 km/s in order to escape out to heliocentric orbit, since the escape velocities of the moons are negligible (Dobrovolskis and Burns 1980). The number of meteoroids relative to Mars that do escape will depend very critically on the velocity spectrum of escaping ejecta. If $\sim 10^5$ times more ejecta above the 'escape velocity' are generated per unit time (smaller, more frequent impactors should be able to produce ejecta), then the production could be comparable to that of Mars.

Once liberated to heliocentric orbit, the delivery efficiency to Earth should be basically the same as that from Mars ($\simeq 4\%$ after correcting for collisional effects). The problem here is one of recognition. Phobos and Deimos are believed to be compositionally very similar to C-type asteroids (Thomas *et al.* 1992), and there is no obvious way to tell any meteorites from these moons apart from the C chondrites. Some more recent work may point to the martian moons being a better spectral match to D-type rather than C-type asteroids (Zellner and Wells 1994, Murchie and Erard 1996). Until more is known about the detailed surface composition of Phobos and Deimos, this topic can only be one for interesting speculation.

5.5 Meteorites from the outer solar system?

A short discussion of the possibility of meteorites whose origin is the surface of a body in the outer solar system is in order. I rule out the outer planets themselves immediately; even if they had solid surfaces, no impactor is likely to be able to penetrate their immense atmospheres to launch material off of these planets at the very high velocities necessary to escape. By far more likely is the chance that we could have fragments of the satellites of these planets. Objects striking the satellites may have very high relative velocity due to gravitational acceleration of the impactors as they fall into the gravity wells of these gas giants.

However, it is no small feat for the ejecta to escape to heliocentric orbit. Even though the escape velocities of these bodies are no larger than Mars, escape from the satellites is only the first step. As in the case of the Moon, the escaping particles will find themselves in orbit about their primary, and must rely on gravitational scatterings from their parent (and perhaps other) Moons to escape. However, unlike the lunar case, the escape velocities of these objects are smaller than their orbital speeds (*e.g.*, $v_{orb} = 5.6$ km/s for Titan, while $v_{esc} = 2.6$ km/s). Therefore, only by a fortuitous sequence of encounters, all of which increase the orbital velocity, can fragments escape to heliocentric orbit.

The transfer efficiency to the Earth of the few such escaping particles is bound to be very small. Any such particles would have to pass through a stage in which their orbits are Jupiter-crossing. Jupiter is extremely efficient at ejecting particles from the solar system, although some small fraction of particles can be pushed down into the inner solar system as evidenced by the existence of the short-period comets (Levison and Duncan 1994). Clearly the outer planets are also quite capable of accreting such particles as well, as evidenced by the comet Shomaker-Levy 9 impact.

In summary, the flux of 'outer solar system meteorites' to the Earth will be very much smaller than the flux of lunar or martian material (possibly by several orders of magnitude). The likely icy composition of many of the surfaces (and thus of their meteorites) can only hinder their recovery. It is not surprising that we have no such objects.

Chapter 6

Modelling the Complete Problem

This chapter attempts to construct a self-consistent model for launch and delivery of the lunar and martian meteorites. The major problem for this enterprise is we have a poor understanding of the launch physics. For this reason, this thesis has tried very hard to not invoke any particular model of cratering physics. Up to this point, none of the results have depended on any model of the ejection physics; all that has been important so far is the celestial mechanics of the particles *after* launch (and some collisional disruption in the case of martian meteoroids). Of the five puzzles regarding the lunar and martian meteorites (p. 7), only that regarding the fairly short 4π ages of the martian meteorites has been resolved (Chpt. 4). The most puzzling of the remaining facts is the approximately equal numbers of lunar and martian meteorites. My chief goal is to understand how to reduce the expected ratio of lunar to martian meteorites from order 10^3 (Wetherill 1984) to order 1. I begin by reviewing the constraints available from the meteorite data, the simulations, and proposed theories for cratering ejection at high velocity.

6.1 Constraints

6.1.1 Meteorite data

The greater average masses of the martian meteorites has already been noted. Note that the four martian falls (Table 2.1) account for four of the five large (>3 kg) martian meteorites; this could be blamed on a selection effect, but one must still explain why there are no comparably large lunar falls. The depth data show that all the lunar meteorites with short blast-off times ($t_{bo} < 0.3$ Myr; p. 15) originate at shallow depths. Only the three meteorites that left the Moon more than ~1 Myr ago were buried deeply at the time of their ejection. In contrast, all the martian meteorites were buried very deeply at the time of their ejection.

6.1.2 Source-crater pairing (SCP)

Warren (1994) concluded that at least six source craters were required to launch the (then nine) lunar meteorites. More recently, Thalmann *et al.* (1996) claim at least six, and possibly eight, separate craters for the eleven meteorites listed in Table 2.1. Both works feel that a source-crater pairing (SCP) between Y-793169 and Asuka 881757 is very probable; the recently determined difference in the depth provenance of these two meteorites (Thalmann *et al.* 1996) probably rules out their being launched in a single meteoroid and paired in the conventional sense. In addition, Warren suggests as plausible a SCP between EET87521 and Y-793274, but rejects claims for a SCP between ALH81005 and Y-791197, as well as any pairing of these latter two with any others. Source-crater pairings, although interesting, do not affect comparisons of the meteorite data with the simulated CRE age spectra, since the latter are only sensitive to the fraction of transits that occur in a given time, and SCP bodies are delivered independently. I believe that the overlap of (relatively uncertain) cosmic-ray exposure ages is a necessary, but hardly sufficient, condition to establish SCPs; the petrologic data are at least equally important. Thus if isotopic ratios (Warren 1994, Thalmann *et al.* 1996) in two meteorites that are SCP candidates do not match, the pair can be rejected since such ratios are known to vary little over the length scale of Apollo traverses.

Martian meteorites separate rather naturally into age *and* petrographic groups. ALH84001 is distinct in both ways. The three nakhlites were all launched about 10.5 Myr ago (again, errors of 20–30% in these ages are likely). Chassigny, at $t_{bo} \simeq 9.9$ Myr (Eugster *et al.* 1996), cannot be split from the nakhlites on CRE grounds, but its petrology is so distinct that it conceivably represents a separate event; since three of the NCs are isolated falls, none of these four can be paired in the conventional sense. Eugster *et al.* (1996) provide support that the lherzolitic shergottites CRE ages of $\simeq 3.5$ Myr are distinct from the basaltic shergottites at 0.6 and 2.7 Myr. If these three CRE ages are due to three martian impact ejection events, then it is rather curious that no other shergottite ejection events are present in the record after 4 Myr (since presumably this implies that such events are common); it is also puzzling then that no events *other* than shergottite ejections are represented during the last 10 Myr. If all the shergottites were spawned in a single impact (presumably ~ 3.5 Myr ago), then this problem is reduced, but in this case the launch of large bodies is required to shield the younger meteorites, with all the attendant difficulties of this hypothesis (Sec. 4.4).

6.1.3 Source regions on Mars

Warren (1994) points out that the lunar meteorites seem to representatively sample the various geological regions of the lunar surface, and thus we have no reason to speculate that any region of the Moon is particularly favored by the launch physics. The simulations of Chpt. 3 also indicate that no regions of the lunar surface are dynamically favored for delivery. In contrast, as mentioned in Chapters 1 and 2, the martian meteorites are distinguished (except for ALH84001) by the fact that they all have young crystallization ages. This prevalence of young ages (11 of the 12 meteorites) is unexpected since only a small fraction ($\simeq$15%) of the martian surface is thought to be this young (Tremain 1995a). This fact favors a small number of launch events (even one), for then the youth of the samples could be attributed to small-number statistics. If one postulates only 3 launch events (one each for S, NC, and ALH84001), then the probability that 2 of them occur in young terrain is $\approx$5%, which is perhaps acceptable; however, the 10-Myr impact must overlap both N and C terrain as well as launch large bodies in order to produce different shielding times for the shergottites (as just discussed). If more than 3 impacts are responsible for launching the martian meteorites, then sampling only young terrain by chance becomes very unlikely. Treiman (1995a) presents a more detailed discussion of this topic.

Warren (1994) has proposed that the lack of geologically old martian rocks is not due to chance, but instead indicates something important about the surface properties of the older regions of Mars. He proposes that weathering processes have degraded the surface structure such that meteorite launch from older portions of the surface is inhibited. This hypothesis would then offer the following explanations: (1) we collect fewer martian than lunar pebble-sized meteorites because coherent un-weathered pebbles are rare on Mars; (2) few martian meteorites are launched from shallow depths because only a small fraction of the outer several meters of Mars have escaped weathering; and (3) SNC meteorites are young mafic rocks because (a) only young rocks are free of pervasive weathering; (b) even without weathering, sedimentary rocks and most impact breccias are not strong enough to survive the rigors of ejection; and (c) most young, igneous rocks on Mars are probably mafic.

Sec. 6.3.3.2 discusses the influence on the transfer model of restricted portions of the martian surface being available for launch, including the possibility that the martian atmosphere favors launch from terrains at high altitude. It is likely that the meteorite data will never be able to answer this question definitively; only a sample return mission to Mars will.

6.1.4 The simulations

We have already seen that the time scales for lunar and martian meteorite delivery agree well with the 4π ages of the meteorites. In the case of the Moon, the prevalence of quick transfers in the time spectrum of the deliveries leads one to conclude that most of the ejecta barely escapes the Moon, *i.e.,* the ejecta's velocity spectrum must be relatively steep; this will be quantified below. In contrast, the ejection velocity makes little difference to the CRE age spectrum from Mars, so we are unable to constrain this using the 4π ages of the martian meteorites, only the average collisional lifetimes (relatively unimportant for the lunar case) of martian meteoroids were deduced.

In both cases the simulations provide the time spectra for delivery as a function of launch velocity, and the absolute delivery efficiency. The latter yield is approximately Y=40±15% for the Moon, depending on the launch velocity, and Y=4±2% from Mars. The error in the martian delivery efficiency is due to small number statistics in the simulations (only 10-20 particles from each 300-particle simulation impacted Earth) and the unknown collisional effects (both the time scale and whether all collisions should be viewed as catastrophic). The roughly 50 percent uncertainty in these absolute delivery efficiencies will be more than sufficient for our purposes, since we are only trying to match fluxes to order of magnitude.

It is useful at this point to define two quantities. If $n_\oplus(t)dt$ is the number of (lunar or martian) meteorites arriving at Earth between t and $t + dt$, then the Earth transfer efficiency $\mathcal{E}(t)$ is given by

$$n_\oplus(t)\; dt = N_{esc}\, \mathcal{E}(t)\; dt \;, \tag{6.1}$$

where N_{esc} is the number of objects that escaped from the parent body in some impact event. (Note that, for clarity, I always use the term 'impact' to refer to the launch event; the term 'arrival' or 'delivery' is used for the reception of the meteorite at Earth). Then for any given impact, the total number of objects that have ever arrived on Earth by time T after launch is

$$N_\oplus(T) = N_{esc} \int_0^T \mathcal{E}(t)\; dt \equiv N_{esc} \times Y \times \mathcal{F}(T) \;\;, \tag{6.2}$$

where Y is the total yield (the fraction of launched particles that will ever reach Earth) given above, and $\mathcal{F}$ is the cumulative fraction of material arrived. In general, $\mathcal{F}(T)$ satisfies $\mathcal{F}(0) = 0$ and $\mathcal{F}(\infty) = 1$, and is basically given by the cumulative CRE age plots presented earlier (Figs. 3.13 and 4.7). Of course, since the simulations are of finite duration they only provide an approximation to $\mathcal{F}(T)$. Since the delivery rate has dropped so much in the later part of the simulations and Sun-grazing or collisional destruction will be destroying ever-increasing numbers of meteoroids, I believe that relatively few particles will arrive at Earth after the termination of the simulations and thus the simulated spectra are sufficient.

Note that the cumulative plots do not indicate the differences in total yield Y between the simulations, which can be obtained from Tables 3.5 and 4.2. For the Moon $\mathcal{F}(1\text{ Myr}) > 0.8$ for all the simulations, so that almost all of the lunar meteorites that will arrive at Earth will do so in <1 Myr. For the 2.4 km/s simulation, the delivery is so rapid that $\mathcal{F}(0.7\text{ Myr}) = 0.9$, *i.e.,* only 10% of meteorites take longer than 0.7 Myr to arrive at Earth. The lunar and martian

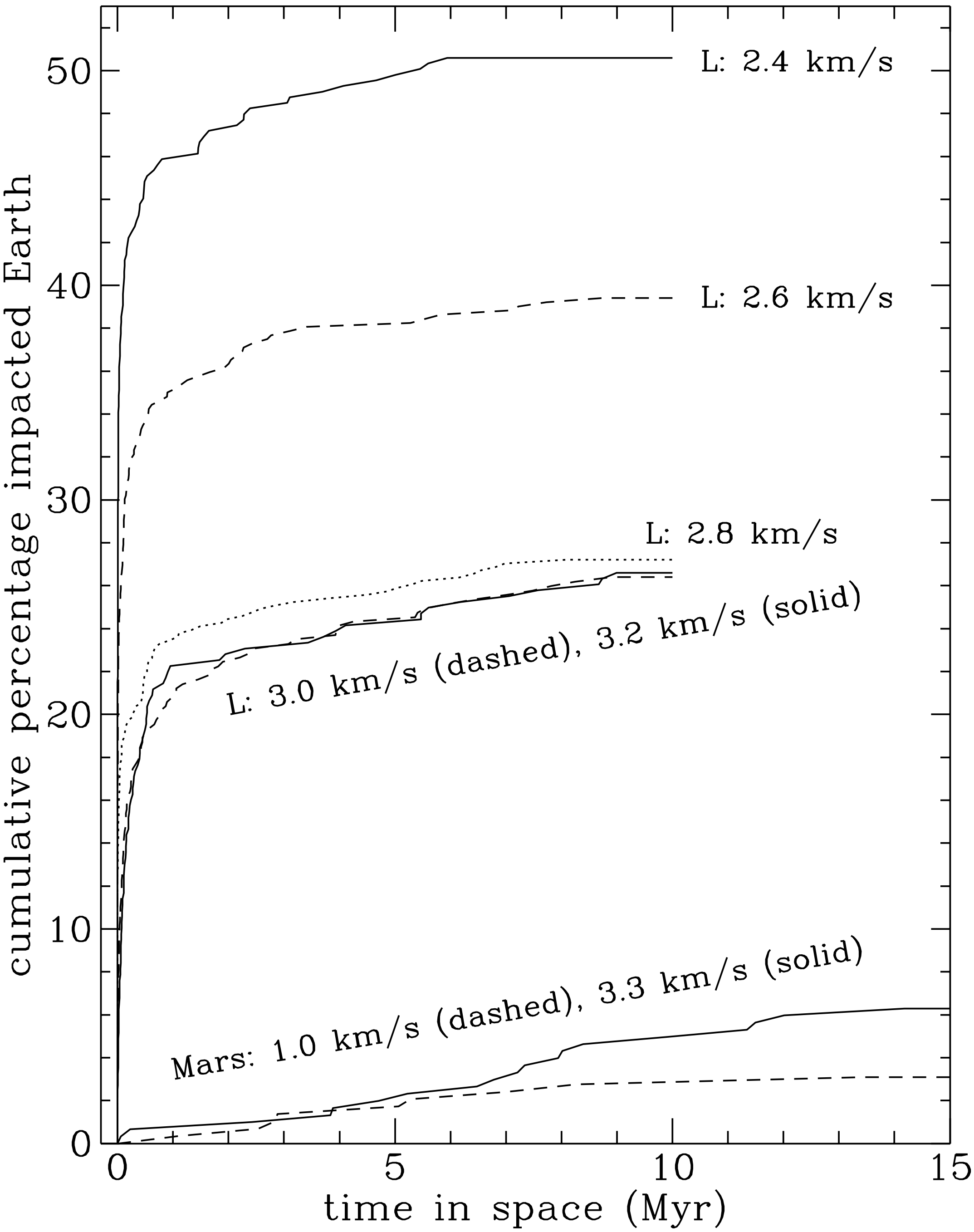

Figure 6.1 The percentage of *launched* particles that impact Earth from lunar (L) and martian simulations. The lunar curves are marked with the ejection velocities, while the martian speeds are v_∞'s. The vertical axis is $Y \times \mathcal{F}(T)$ (*cf.* Eq. 6.2).

$N_\oplus(T)$ curves are plotted using a linear time axis in Fig. 6.1, which brings home how sharply the delivery of lunar material tails off compared to that from Mars.

6.1.4.1 Age of the ice sheet

It is important to realize that the bulk of our meteorite sample was collected in Antarctica (Sec. 1.2). The foregoing discussion does not take into account that the ice sheet is of finite age (denoted $A_{\rm ice}$). This age should not be viewed strictly as how old the ice is, but rather the typical lifetime of a meteorite in the ice before it is destroyed.

Eq. 6.2 gives the number of meteorites that have arrived on Earth since the lunar or martian impact T years ago. However, if the launch occurred longer ago than $A_{\rm ice}$, then many of the meteorites that landed on the ice sheet have since been destroyed. Therefore, the actual number of meteorites currently in the ice sheet is given by

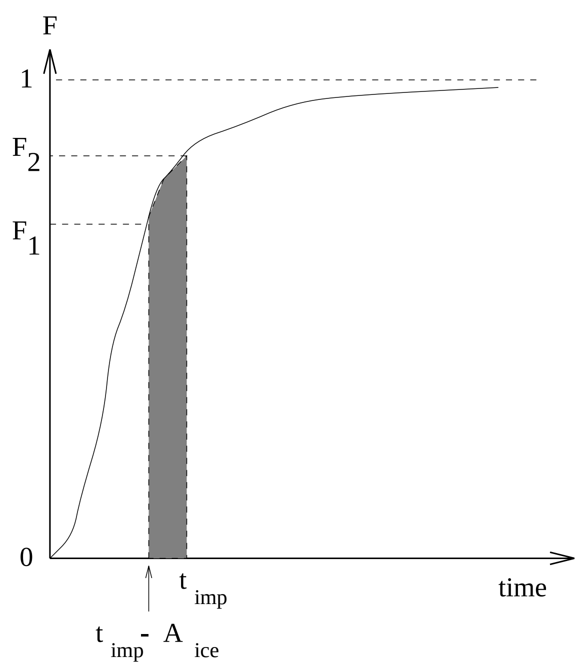

Figure 6.2 The ice sheet will only accumulate meteorites during its age $A_{\rm ice}$, and thus only the fraction $\mathcal{F}_2 - \mathcal{F}_1$ of all the meteorites that arrive are currently in the ice sheet if the impact occurred before $A_{\rm ice}$.

$$N_\oplus = N_{esc} \times Y \times \begin{cases} \mathcal{F}(t_{imp}) & \text{if } \; t_{imp} < A_{\rm ice} \\ \mathcal{F}(t_{imp}) - \mathcal{F}(t_{imp} - A_{\rm ice}) & \text{if } \; t_{imp} > A_{\rm ice} \; , \end{cases} \tag{6.3}$$

where t_{imp} is how long ago the impact occurred. This is illustrated in Fig. 6.2. The effect will be especially important for the lunar meteorites since most of them arrive in a short burst after the impact. If this burst finishes more than A_{ice} ago, then most of the meteorites from that impact are no longer recoverable.

The age of the ice sheet can be estimated from studies of the CRE data for Antarctic meteorites (Cassidy and Rancitelli 1982; Nishiizumi *et al.* 1989). The number of Antarctic meteorites drops almost exponentially with terrestrial age ($t_\oplus$), with a half-life of perhaps just slightly less than 100 kyr (Nishiizumi *et al.* 1989). The *median* terrestrial age of the lunar meteorites is somewhere between 30 kyr to 60 kyr; unfortunately many of the $t_\oplus$'s are just upper limits (Table 2.1). The *mean* age may not be a good representation as the 230 kyr age of MAC88105 unrepresentatively skews the distribution. The ice fields, and even the various stranding areas of each ice field, have different distributions of terrestrial ages, so deciding upon a single number may be difficult (and/or misleading). Certainly the 'mean age' is more than 10 kyr and less than 150 kyr. The martian meteorites have only 4 Antarctic terrestrial ages determined: 10, 11, <100, and 200 kyr, and so are not clearly any different in this regard.

The model used in Eq. 6.3, in which the single cutoff $t_\oplus = A_{\rm ice}$ is imposed, is perhaps overly simplistic. A more realistic model could include an exponential loss process, in which each delivery has some probability of being destroyed before recovery. We should note that since the average mass of lunar meteorites is smaller than the martian meteorites (or the bulk sample of all meteorites) one might suspect the average retention time to be somewhat smaller. I have not included these additional complications in the current model.

6.1.5 Cratering mechanics

In order to make some estimates of the efficiency of meteoroid launch from an impact so that a complete picture can be developed, at this point we must examine a model for the ejection physics. The results available in the literature are based on hydrocodes (*e.g.,* O'Keefe and Ahrens 1977; Holsapple and Choe 1988), analytical models (*e.g.,* Zel'dovich and Raizer 1967, Melosh 1984), and laboratory cratering experiments (*e.g.,* Gault *et al.* 1963, Gratz 1993, Kato *et al.* 1995).

It is crucial to realize that much of the work that has been done on understanding impact cratering is concerned with the excavation of the crater itself. The crater's cavity is formed by a subsonic excavation flow (see Melosh 1989 for a general introduction to cratering phenomena). In contrast, the physics that ejects the very fastest, lightly shocked material represented by the lunar and martian meteorites is probably quite different from that taking place in the excavation. The ejecta blocks that create secondary crater fields are interpreted to have been launched from the original crater at up to 1 km/s (Vickery 1987), in a process which ejects material from a near-surface spall zone (Melosh 1989). It is plausible, but not proven, that this same process is responsible for the ejection of material at faster than the escape velocity; there is some indication in the work of Gault *et al.* (1963) that some transition occurs in the ejection physics at about 1 km/s (at least for basalt targets).

Any model of the launch process must explain the lightly shocked state of the lunar and martian meteorites (Chap. 1). This historically surprising fact is now viewed as a major constraint on the launch process. Two processes have been suggested in the literature. The first is oblique-impact-induced, vapor-jet plume entrainment (Nyquist 1983, O'Keefe and Ahrens 1986), in which the ejecta are entrained in an expanding gas cloud which accelerates them to escape velocity. The second model relies on the interference of shock waves (Melosh 1984, 1985) in a near-surface spallation layer to propel particles to speeds greater than escape while maintaining low peak pressures. I have chosen to base all of my discussion on the Melosh model because (1) production of lightly shocked, high-velocity spalled ejecta has been observed in laboratory experiments (Gratz 1993), and (2) the quantitative predictions of the model are in reasonable concordance with a number of features of the meteorite data. It is important to realize though that the transfer dynamics are probably not sufficient in themselves to distinguish between these launch models.

6.1.5.1 The spallation model

I will briefly summarize the shock-wave interference model, for which the best introduction is Melosh (1985). Consider a projectile of diameter D striking a surface with a component of velocity U normal to the surface. The impact produces a shock wave which appears to travel spherically outward from the *equivalent center*, a point roughly one projectile diameter below the target's surface. As the shock wave sweeps past any given point, the pressure increases with a characteristic 'rise time' τ equal to the time it took the impactor to penetrate into the surface by its own radius,

$$\tau \sim \frac{D}{2U} \,. \tag{6.4}$$

After this, the pulse decays away in a time $\beta\tau \sim D/c_L$, where c_L is the sound speed in the target, and β is a constant. The total time duration of the pressure pulse is thus $(1+\beta)\tau$. The model relies on the fact that, near the surface of the target, two waves arrive at any given point from the equivalent center: a direct wave, and one reflected from the nearby surface. Since the sign of the reflected pressure wave is reversed, these two waves interfere and in fact the peak pressure reached is considerably smaller than the maximum pressure in the wave. However, even though rocks at the interference zone do not feel the full stress pressure, they are still accelerated because the final velocity of material after the wave has passed depends on the pressure gradient rather than the pressure itself. In the interference zone the pressure actually rises twice as rapidly as the case when no interference occurs, due to the presence of the free surface; this can accelerate material to nearly twice the particle velocity of the wave itself. This mechanism can therefore eject lightly-shocked particles at high speeds.

Melosh's estimate of the depth z of the interference layer is important for our purposes. This layer is a lens-shaped region, the depth of which increases with the horizontal distance s from the impact point:

$$z = \frac{c_L \tau}{2} \sqrt{1 + \frac{s^2}{D^2 - \left(\frac{c_L \tau}{2}\right)^2}} \,. \tag{6.5}$$

From Eq. 6.4, $c_L \tau \simeq c_L D/(2U)$, and so

$$z = \frac{c_L D}{4U} \sqrt{1 + \frac{s^2/D^2}{1 - \left(\frac{c_L}{4U}\right)^2}} \tag{6.6}$$

For a hypervelocity impact ($U > c_L$) we can approximate the denominator of the second term as unity. Since the launch velocity drops off roughly as s^{-3} (Warren 1994), the majority of the highest velocity ejecta should be launched within a few impactor diameters of the contact point ($s/D \sim$ 2–3), and thus it is roughly correct to say that the spall zone has an approximately constant thickness of order

$$z \sim D \frac{c_L}{U}. \tag{6.7}$$

For U=10–20 km/s impacts into pristine rock (where $c_L \sim$6 km/s), the spall zone depth is of order an impactor radius. However, impacts into a regolith layer (where $c_L \ll$1 km/s) will have interference zones very much shallower than the impactor. This is of great importance, since the sound speed in the upper few meters of the lunar regolith is measured by the Apollo experiments to be only $c_L \approx$100 m/s (McKay *et al.* 1991). Thus, a 100-m projectile hitting the lunar regolith at 10 km/s engenders an interference zone of depth only one meter! Since the lunar regolith is generally 4–5 m in the mare and perhaps 10–15 m in the highlands (McKay *et al.* 1991), only impactors of order 1 km can mine down below the regolith to launch particles from depth. However, the Melosh spallation model may need to be modified to cope with a layered target (Warren 1994).

Therefore, the low sound speed of the Moon's surface results in a drop in the number of expected meteoroids launched in any single impact, by up to two orders of magnitude. It is not certain that the martian surface should be any more favorable (in a relative sense) for meteorite launch, but the megaregolithic structure (McKay *et al.* 1991) of the lunar surface is probably not present on Mars, especially in the younger terrains, due to ongoing surface processes and recent volcanism on Mars (Christensen and Moore 1992). Therefore one expects a relative dearth of ejections from the Moon, which may be a major reason for the 'over-representation' of martian meteorites in the collection. I will return to this topic below.

6.1.6 Size distributions of surface material

Since a regolith cannot support tensile stress, the surface layer is simply ejected in a spall process (Melosh 1985). In contrast, in a solid target ejecta is spalled off in plates that then break up in flight into fragments whose size can be estimated (Melosh 1989). The 2π CRE evidence tells us that the martian meteorites have come from depths below several meters, and so the size distribution of martian surface material may be irrelevant for understanding the sizes of its meteorites. Nevertheless, for completeness, note that the surface size distribution of martian rocks has been estimated from Viking lander photography by Golombek and Rapp (1996).

In the case of lunar launch, the size distribution of the escaping meteoroids should presumably be that of the regolith since the surface layer has little strength. The size distribution of lunar soils is well catalogued (Graf 1993), but little information is readily available about the relative number of rocks in the range from 1 mm to 10 cm (the size of the meteorites) in the upper few meters of the regolith. Particles in these size ranges are too large to be well represented in drill cores, and it is difficult to reach firm conclusions from radar studies due to model uncertainties (Carrier *et al.* 1991).

The surface photography performed by the Surveyor missions (Shoemaker *et al.* 1969) is the best source of this size information. All of these spacecraft landed in mare areas, except Surveyor VII which landed in highland terrain and next to a large young crater (Tycho). From television pictures of the Surveyor I, III, V, VI, and VII landing sites, the cumulative number of particles N per 100 m^2 was fairly well represented by a relation of the form $N = Kd^\gamma$, with γ ranging from -1.8 to -2.6, for particle diameters d from $\simeq$1–500 mm. The absolute normalization varied from site to site, as some sites were especially rich in larger rocks. The surface density distributions were then used by Shoemaker *et al.* (1969) to estimate the volumetric particle-size-frequency distribution functions. Except for the Surveryor VII site (which was atypical due to being so close to Tycho), these authors find that rocks larger than $d \simeq$1 cm in diameter (mass $\sim$1 g) occupy only $\simeq 2 \pm 1\%$ by volume of the lunar regolith. Thus, even allowing for some uncertainty, to obtain $\sim$1 10-g lunar meteorite requires launching *at least* two orders of magnitude more material (by volume) since so much of the regolith consists of fine soils.

The lunar meteorite size distribution is statistically consistent with a d^{-2} power-law, but only for those meteorites larger than 30 g. This is not surprising; collected Antarctic meteorites are believed to be representative of those actually in the ice only at masses above this limit (Huss 1990). There is therefore no reason to suspect that the lunar launch process favors any particular mass range.

6.2 Modelling lunar launch

I shall now adopt the goal of using the meteoroid dynamics to determine as much information as possible about the lunar launch process.

6.2.1 Launch rate, lower limit

The observed number of lunar meteorites (LMs) can be used in conjunction with transfer efficiency to estimate a lower limit to the meteoroid launch rate. Consider the following four assumptions:

1. All LMs in the collection have been identified,
2. LMs are no more difficult to recognize than other meteorites,
3. LMs are not more prone to destruction by weathering,
4. LMs are just as strong during entry as other meteorites.

If any of these assumptions are incorrect, then the launch rate we are about to estimate will rise. Now, of the $\simeq$ 20,000 Antarctic meteorites, 15 are lunar if we count all the meteorites uncorrected for pairing, or of order one in a thousand if assumptions 1–3 are correct. If assumption 4 is correct, then this ratio of 1 in 10^3 is also representative of the fraction of meteoroids that are presently in Earth-crossing space (at least, over the last $A_{\rm ice}$ years). Therefore we can use reasonably well calibrated estimates of the total flux of meteorites (Halliday and Griffen 1992; Halliday *et al.* 1984, 1989, 1991; Huss 1990) to estimate the lunar fall rate. The smallest flux estimate in the literature is that of Halliday *et al.* (1989) who estimate the number of incident meteoroids larger than some total meteorite mass m_T (in grams) to be

$$N(m > m_T) = 260 m_T^{-0.49} \ \ /10^6 {\rm km}^2/{\rm yr} \tag{6.8}$$

for meteorites with total masses of <1 kg. The smallest lunar meteorite is 6 g, and probably had a pre-atmospheric mass of at least 10 g. Using this 10-g mass as a lower bound in Eq. 6.8, the fall rate of meteorites is $\sim$100 /10^6 km^2 /yr, and therefore the lunar fall rate is at least $\sim$0.1 /10^6 km^2 /yr. Accordingly, the Earth's surface area receives an integrated flux of at least 50 lunar meteorites per year. The lunar transfer efficiency is 40$\pm$15%, and using 50% gives us a lower bound on the (averaged) launch rate of at least 100 meteoroids per year. This launch-rate estimate applies to strong meteoroids bigger than 10 g over the last Myr or so that the CRE ages span. Given that we have had several lunar launch events in the last 10^5 years, the impactors are probably striking the Moon every $\sim 10^4$ years, implying a time-averaged estimate of at least 10^6 meteoroids launched per event.

It is unlikely that any of the 4 assumptions given above are wrong even to a factor of 2. The strength assumption (#4) is the most interesting, as Warren (1994) points out that lunar meteorites tend to have much higher crushing strengths than Apollo samples. It is not clear, however, whether lunar meteorites are systematically stronger or weaker than chondrites, or if crushing strength is the relevant parameter for survivability during atmospheric entry. Nevertheless, let us assume that the lunar meteorites are of comparable strength to other meteorites (or alternately that the launch estimates are only of rocks at least this strong), and calculate a best estimate of the launch rate instead of a lower limit. Huss (1990) believes the most realistic estimate of meteorite infall rate from 1 g to 1000 kg to be

$$N(m > M) = 6800\ M^{-0.833}\ \ /10^6\mathrm{km}^2/\mathrm{yr}\ , \tag{6.9}$$

where M is the terminal mass (in grams) of the meteorite; Halliday *et al.* (1996) give a relationship that is similar within a factor of 2 for masses >2 kg. The factor of a few difference between the terminal and total mass need not concern us much here, but let us use a terminal mass of 6 g for the sake of argument. Assuming that 1 in 10^3 of this flux is lunar yields a best estimate of the lunar launch rate of ~1500 meteoroids/year being injected into near-Earth space (in a time-averaged sense).

6.2.2 Impactor flux

The flux of lunar impactors is estimated by crater counting on the Moon and Earth (Melosh 1989, Neukum and Ivanov 1994, Hartmann 1995) and telescopic observations of near-Earth objects (Shoemaker 1984, Rabinowitz 1994, Shoemaker *et al.* 1994, Bottke *et al.* 1994). Observationally, the impactor population can be described by a *cumulative* distribution N(diameter > D) satisfying:

$$N(D)\, dD = CD^{-\beta}\, dD\ , \tag{6.10}$$

with $\beta = 2$ for $D > 100$m. There is some evidence (Rabinowitz *et al.* 1994, Warren 1994) for a steepening of the size distribution to D^{-3} below 100 m. I will examine below the effect of allowing the exponent to change to $\beta = 3$ at sizes less than 100 m.

I bin the impactors into an incremental size distribution (see Melosh 1989, p. 186) with bins of size $(D, \sqrt{2}D)$, *i.e.,* the upper boundary of each bin is $\sqrt{2}$ of its lower boundary. This binning has the property that the number of impactors per bin also scales as D^{-2} (or -3). That is,

$$N(D, \sqrt{2}D) \propto D^{-\beta} \tag{6.11}$$

I have pegged the impact *rate* to the frequency of a 1-km impactor, and scaled all others via the number distribution above. According to many sources (*e.g.,* Bottke *et al.* 1994), an impactor larger than 1 km currently hits the Moon every $t_{peg} \simeq 2$ Myr, with probably at most a factor of 3 error. This implies that an impactor between 1 and $\sqrt{2}$ km hits the Moon every 4 Myr. Some have suggested, however, that at present the lunar impactor flux is twice that of several Gyr ago (Shoemaker 1983, Moore and McEwen 1996). The lunar CRE age spectrum turns out to be relatively insensitive to these uncertainties, although the absolute flux of meteorites will of course depend linearly on the impactor flux.

I have arbitrarily chosen the upper end of the largest impactor diameter bin to be at $D = 32$ km, thus the last bin is (22.62,32) km. For $\beta = 2$, an impactor with $D > 32$ km currently hits the Moon only every $\sim$1 Gyr, so ignoring events less frequent than this will be irrelevant to the study of meteorites that are now in the Antarctic ice sheet. This upper bin choice also has the convenience of having one bin boundary at $D = 1$ km. The sensitivity of the results to the *lower* end of the impactor size distribution will be discussed. For impacts to occur at least every 10,000 years the smallest impactors must be < 100 m.

6.2.3 Launch scaling

It is now unavoidable that some form of scaling be introduced for the cratering events. I will attempt to make minimal, and reasonable, assumptions. Clearly we expect larger, more energetic impacts to liberate more particles than smaller ones, and thus the launch scaling I will use is that the number $\mathcal{N}$ of particles launched between v and $v + dv$ drops off as a power law, with exponent p:

$$\mathcal{N}(v)dv \propto \Phi(E)v^{-p}dv \ , \tag{6.12}$$

where Φ is some monotonically increasing function of the impactor's kinetic energy E. Power-law relationships like Eq. 6.12 are often observed as the results of cratering experiments (Gault *et al.* 1963, Frisch 1992, Kato *et al.* 1995). This relation implies that the number of *escaping* particles is

$$N_l(p, E, v_e) = \int_{v_{esc}}^{\infty} \mathcal{N}(v)dv = k\frac{\Phi(E)}{p-1}\left(\frac{1}{v_{esc}}\right)^{p-1} \ . \tag{6.13}$$

I am assuming that the impactors all arrive with a median velocity, and a velocity spectrum that is independent of size. The former assumption is known to be wrong. Chyba *et al.* (1994) shows the distribution of lunar impact velocities for Earth-crossing asteroids; the median value of v_∞ is only 12 km/s, the majority occur at under 15 km/s, and 25% of the impacts occur at <10 km/s. Less than 10% of lunar impacts occur at >25 km/s, which would boost the energy by more than a factor of 4 compared with the median value (for an impactor of a given diameter). I will assume that all impactors arrive at the median velocity, or at least that the increased effect of fast impactors of a given size is cancelled out by the underestimated effect of slower speed impactors of a larger size. This single-speed hypothesis will be less valid if comets (which impact at higher velocities and for which the ejection physics may differ) make up a reasonable fraction of the relevant impactors, or if it is only the highest velocity impactors that produce most of the ejecta. In any case, removing the impactor velocity as a parameter means that the impactor's kinetic energy is a function only of the impactor's diameter D, and

$$\Rightarrow \Phi(E) = \Phi(D) \ . \tag{6.14}$$

Following Warren (1994), I adopt a power-law expression for the number of meteoroids launched as a function of the impactor diameter of the form

$$\Phi(D) \propto D^{\alpha} \ . \tag{6.15}$$

If ejected meteoroids were all of comparable diameter, then Vickery and Melosh (1987) calculate $\alpha = 3.84$, but Melosh (private communication, 1996) is cautious about this result since it is based on a 2-D hydrocode. Warren (1994) believes α must be near 2 for the Moon, but that $\alpha \approx 3$ for Mars in order to make sense of the meteorite CRE data; I will show that Warren's conclusions are justified by my simulations.

Substituting this form of Φ into Eq. 6.12 yields

$$N_l(p, E, v > v_e) = \int_{v_e}^{\infty} \mathcal{N}(v) dv = k \frac{D^{\alpha}}{p-1} \left(\frac{1}{v_e}\right)^{p-1} \ . \tag{6.16}$$

However, since at the moment we are interested only in a single body (the Moon), this simply says

$$N_l \propto D^{\alpha} \tag{6.17}$$

since all other quantities are fixed.

In light of the discussion of Sec. 3.4.1, let us quantify what we can say about the value of p (assuming a power law is valid) from the lunar meteorites. As discussed earlier, the majority of meteoroids must not leave the Moon at more than 3 km/s. It is easy to show from Eq. 6.16 that the fraction f_* of *escaping* meteoroids that leave at velocity *greater* than v_* is

$$f_* = \left(\frac{v_e}{v_*}\right)^{p-1} \ . \tag{6.18}$$

If at least 50% of the escaping lunar ejecta is to leave at less than v_*=3.0 km/s, then $p \geq 4$; if 90% then $p > 11$.

6.2.4 The cratering algorithm

I now proceed to simulate the cratering and delivery history from the Moon. The goal is to compile both the meteorite-time and impactor-size spectra over the entire impact history. That is, I will compute the expected CRE age spectrum (hereafter called the 'age spectrum') and the fraction of meteorites contributed by each size bin of the impactors (hereafter called the 'launcher spectrum', not to be confused with either the size distribution of the impactors or the size distribution of the ejecta). It should be noted that because there is a delivery 'window' of duration $A_{\rm ice}$, the algorithm below actually calculates the spectrum of *blast-off times* (Sec. 2.3.3), since all that is done is to compile the number of meteorites that have arrived in the last $A_{\rm ice}$ years.

The algorithm is as follows: for each size bin $(D, \sqrt{2}D)$, beginning with the largest and decreasing through the smallest $D_{\rm small}$, I perform the steps described below. The parameters are summarized in Table 6.1.

1. Compute the number of meteoroids launched by the impactor of this size, scaled from Eq. 6.17. I arbitrarily take 10^6 meteoroids to be launched by a 100-m impactor. This normalization is for convenience, its value makes no difference to the results.

2. For this bin, compute the number of impactors X_{imp} relative to the 1-km impactor bin, using Eq. 6.11. If desired, one can use a size distribution for $D < 100$ m with exponent $\beta \neq 2$, in which case one first computes the number of 100-m impactors and then scales from there using $D^{-\beta}$.

3. The *mean rate*, or average spacing in time, of impacts in this size bin D is thus $t_{space} = t_{peg}/X_{imp}$.

4. Now work backwards in time through the impact history. Each impact occurs randomly in time, and so the probability of *not* having had an event by time t is $\exp(-t/t_{space})$. Thus, generate a random number R from 0 to 1, and the next impact time is $t_{imp} = t_{space} * \ln(1 - R)$ farther back in time. When constraining the parameters I have sometimes turned off this random timing so that $t_{imp} = t_{space}$ always.

5. Use Eq. 6.3 to determine the number of meteoroids that this impact has delivered to the ice sheet during the recent past. Keep track of which size bin and time bin the particles are from, as well as the total number of lunar meteorites that have arrived. I have used the 2.4 km/s delivery spectrum to compute $\mathcal{F}(T)$.

6. Return to step 4, and continue generating events until $t > 100$ Myr. That is, assume that impacts occurring longer ago than 100 Myr are not delivering any appreciable number of meteorites today. (The lunar simulations in fact ended at 10 Myr, but I use the 100 Myr number to be consistent with the martian study to be done below.) I assume that only a negligible fraction of lunar meteorites return after 10 Myr; this is supported by both their absence in the collection and the relatively small delivery rate in the later stages of the simulations.

7. Once this impactor diameter class is finished, return to step 1 and repeat for impactors that are $\sqrt{2}$ smaller, until we reach the smallest impactor class D_{small} considered.

To summarize, the parameters relevant for the lunar simulation are given in Table 6.1, along with likely values for these parameters.

Table 6.1 Parameter values for studies of the lunar collision history. Reasonable ranges for each parameter are given; these values will be constrained later by comparison with the meteorite data.

Parameter	Description	Value
α	$\Phi \propto D^{\alpha}$	2 – 4
β	$N(D) \propto D^{-\beta}$ (for < 100 m)	2 – 3
A_{ice}	retention age of ice sheet	0.03 – 0.1 Myr
D_{small}	smallest impactor bin	<100 m (maybe $\ll$?)
t_{peg}	Freq. D >1-km impactor hits Moon	4 Myr ($\pm$ factor of 3?)

6.2.5 Constraining the lunar parameters

Fig. 6.3 shows the baseline case; the top panel gives the 'age spectrum' and the bottom panel the 'launcher spectrum' (as defined above). The five relevant parameters are indicated (likely ranges for these parameters are given in Table 6.1). The notation $N(D) \propto D^{-2}, D^{-2}$ refers to the power laws for $D < 100$ m and $D > 100$ m, respectively; *i.e.,* the first number is β since the size exponent is always taken to be -2 above 100 m. The five parameter values given are in fact close to optimal for producing a good match with the data. I will vary the parameters away from this baseline case in order to demonstrate the various dependencies. For these purposes I temporarily will not allow the impactors to be randomly spaced, because this introduces variations in the spectra that obscure the systematic changes induced by altering the parameters. Random spacing will be reinstated in Sec. 6.2.5.5, but for now the impacts will occur spaced exactly by t_{space}; *i.e.,* if $t_{space} = 10^4$ yr, then the impacts are considered to occur 10^4, 2×10^4, 3×10^4 yrs, etc., ago. The properties of the size bins for the standard case are listed in Table 6.2.

Fig. 6.3 has several features of note. Two sets of meteorite data are shown, connected by dotted lines, and these agree above 250 kyr. The rightmost set of data uses only upper limits obtained from the available CRE data. The left set instead adopts the thermoluminescence (TL) 4π ages for those meteorites that have them (Table 2.1), and uses lower limits for all other quantities in order to calculate a minimum blast-off age. For Y-793274 and EET87521, which have no lower bound on t_{bo} available from either analysis, I have used a minimum t_{bo} of one-tenth the upper limit. It is likely that the left curve based on the TL data underestimates the actual transit ages; TL ages can be erroneously low due to heating of the meteoroid (see Benoit *et al.* 1996); the right curve serves as a definite upper bound. The correct spectrum is probably somewhere in the middle, like the computed spectrum in this case. I will continue to show both limits for the actual ages, and readers can judge for themselves.

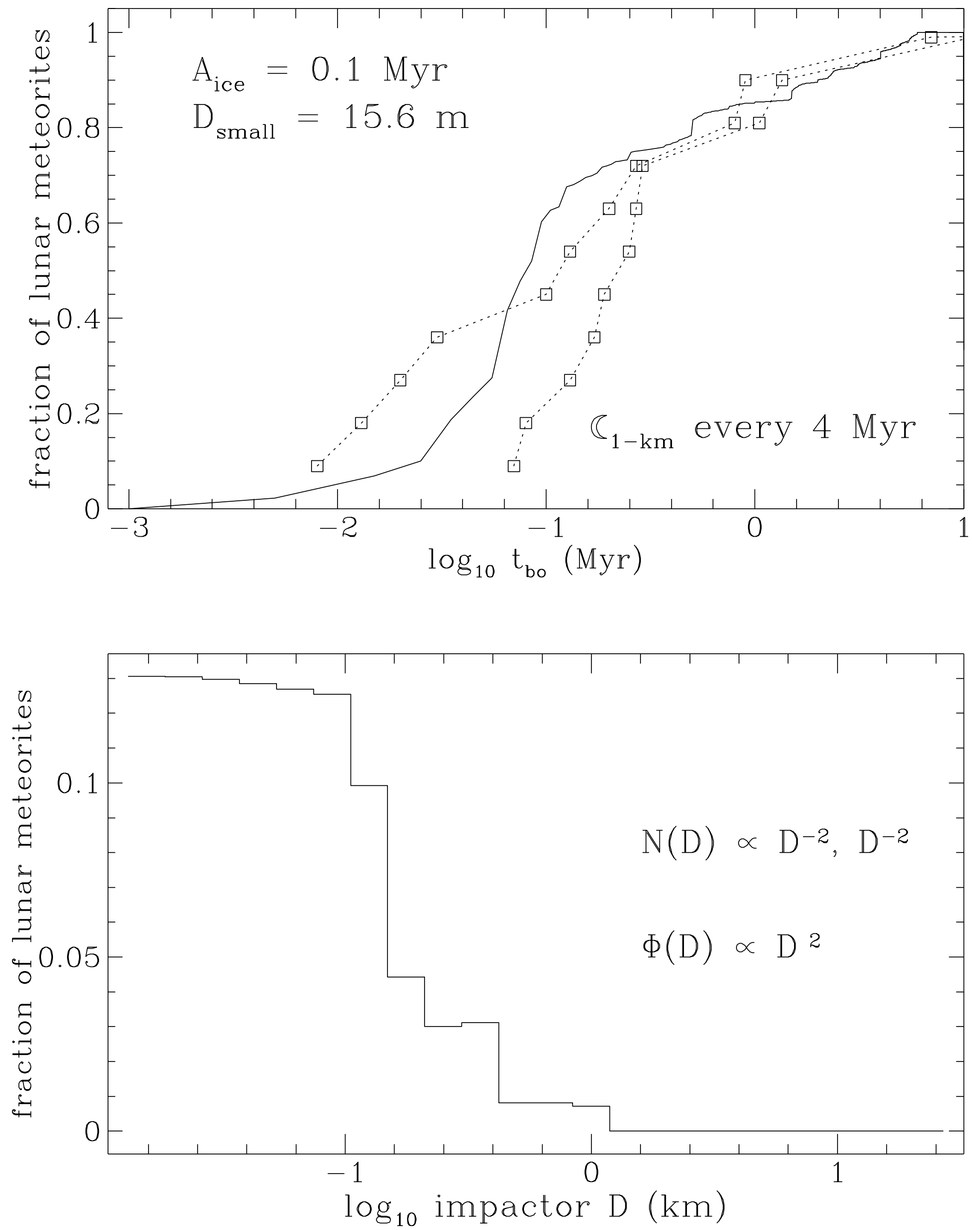

Figure 6.3 Upper panel: Age spectrum of simulated lunar deliveries (solid line) overlain with two sets of CRE data (points connected by dashed lines). The rightmost set of CRE data consists of upper limits from the cosmonuclide data; the left set is lower limits (see text). Lower panel: The launcher spectrum of the meteorites (the fraction of delivered meteorites launched by each size bin of impactors). In this case most of the meteorites in the ice sheet were launched by small ($D < 100$ m) impactors. The $N(D)$ notation indicates that a D^{-2} power law was used both above and below 100 m for the impactors. This calculation had the random timing of impactors turned off.

Table 6.2 Properties of the impactor bins for the lunar case. For each bin with lower bound $D_{\rm lower}$ (and upper bound $\sqrt{2}D_{\rm lower}$), the number of impactors X_{imp} relative to the $D_{\rm lower}$ =1-km bin is shown. The impactors of each bin hit the Moon on average t_{space} apart, and launch N_l meteoroids from the Moon above the escape velocity. The normalization for N_l was set at 10^6 meteoroids for a 100-m impactor, but the absolute value here has no effect on the spectra.

$D_{\rm lower}$ (m)	X_{imp}	t_{space} (Myr)	N_l
15.6	4.10×10^{03}	0.00098	2.44×10^{04}
22.1	2.05×10^{03}	0.00195	4.88×10^{04}
31.2	1.02×10^{03}	0.00391	9.77×10^{04}
44.2	5.12×10^{02}	0.00781	1.95×10^{05}
62.5	2.56×10^{02}	0.01563	3.91×10^{05}
88.4	1.28×10^{02}	0.03125	7.81×10^{05}
125.0	6.40×10^{01}	0.06250	1.56×10^{06}
176.8	3.20×10^{01}	0.12500	3.12×10^{06}
250.0	1.60×10^{01}	0.25000	6.25×10^{06}
353.6	8.00×10^{00}	0.50000	1.25×10^{07}
500.0	4.00×10^{00}	1.00000	2.50×10^{07}
707.1	2.00×10^{00}	2.00000	5.00×10^{07}
1000.0	1.000	4.00000	1.00×10^{08}
1414.2	5.00×10^{-01}	8.00000	2.00×10^{08}
2000.0	2.50×10^{-01}	16.00000	4.00×10^{08}
2828.4	1.25×10^{-01}	32.00000	8.00×10^{08}
4000.0	6.25×10^{-02}	64.00000	1.60×10^{09}
5656.9	3.12×10^{-02}	128.00000	3.20×10^{09}
8000.0	1.56×10^{-02}	256.00000	6.40×10^{09}
11313.7	7.81×10^{-03}	512.00000	1.28×10^{10}
16000.0	3.91×10^{-03}	1024.00000	2.56×10^{10}
22627.4	1.95×10^{-03}	2048.00000	5.12×10^{10}

A second interesting feature is that the launcher spectrum shows that even though large impacts that occurred in the past are included, almost all of the lunar meteorites now present on Earth were launched by impactors smaller than 1 km, and the majority by impactors <100 m. This lack of representation of large launchers is aided by, but not exclusively due to, α's value of 2 in this simulation (as discussed in Sec. 6.2.5.3 below) Notice a very important fact; even though more than half of the delivered meteorites from an impact arrive within 0.01 Myr of launch (Fig. 3.13) for the 2.4 km/s $\mathcal{F}(T)$ function we are using, the age spectrum in Fig. 6.3 predicts only $\simeq$5% of the simulated deliveries have blast-off ages this low. This rather obvious effect was not mentioned in Gladman *et al.* (1995); if the meteorites come from multiple impacts, only very recent (and therefore presumably smaller on average) impacts can deliver young samples to the ice sheet because meteorites that have landed in the last 50 kyr from impacts that occurred hundreds of kyr ago will not have short t_{bo} ages. This effect does not modify the argument (which is based solely on 4π ages) that the ejecta's velocity-spectrum must be steep (Sec. 6.2.3).

When judging the quality of matches to the data, we must keep in mind the small-number problem of the meteorite data. Accordingly, the most that should be required of the model is to reproduce the gross features of the problem to within a factor of 2 or 3. In the lunar case, these features are: (1) the age spectrum, with half of the meteorites arriving in less than 100,000 years; and (2) a lack of SCPs, indicated by having most of the meteorites launched by small impactors as opposed to a few large ones.

6.2.5.1 The smallest impactor $D_{\rm small}$

Fig. 6.3 showed the case where an impactor between 1 and $\sqrt{2}$ km hits the Moon every 4 Myr. Since the impactor size distribution varied as D^{-2} below 100 m, impactors between D=88 and 125 m hit the Moon roughly every 30 kyr (Table 6.2). As Warren (1994) points out, impactors capable of launching lunar meteorites must be smaller than this since we have had several launches in the last 50 kyr (barring a statistically unlikely barrage of recent impactors of this size range). This raises the question: how small an impactor can launch a D=2 cm, $\simeq$10 g lunar meteorite? This is a difficult question to answer beyond the trivial argument that the impactor would have to be at least of order the same diameter. Can we perhaps discover the answer from the meteorite record?

Fig. 6.4 shows how the expected meteorite 4π-age spectrum would change as a function of $D_{\rm small}$. The predictions are essentially identical for $D_{\rm small}$ <31 m, but above this the spectra begin to not agree with the data. This is because below $D_{\rm small}$ =63 m the smallest impactors, which deliver most of the meteorites, strike much more often than $A_{\rm ice}$ (see Table 6.2). Above $D_{\rm small} \simeq$ 63 m few, if any, impactors strike the Moon more recently than $A_{\rm ice}$, and therefore almost no meteorites with t_{bo} < 0.05 Myr are present. The (62.5,88.4) m impactor bin

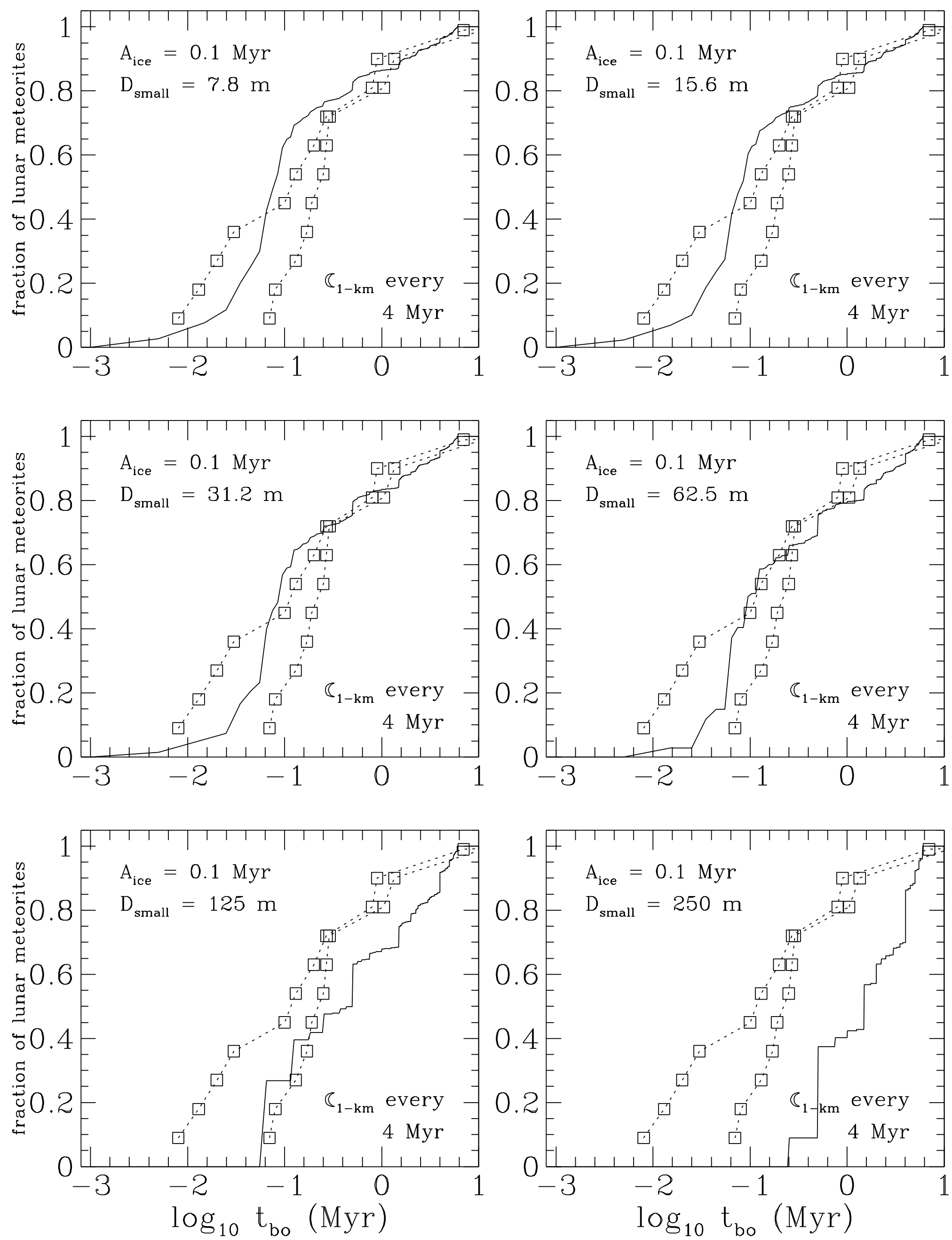

Figure 6.4 These panels show the expected age spectra as a function of the smallest diameter impactor that is allowed to launch lunar meteorites. The launcher spectra (not shown) each look similar to that of Fig. 6.3, in that the majority of the delivered meteorites are launched by impactors smaller than $D \simeq 300$ m.

delivers an impactor to the Moon every 16,000 years, so apparently the impactors capable of launching meteoroids must be striking at least this often in order to produce the observed age spectrum. Unfortunately, the age spectrum is not sensitive to a minimum value for D_{small}, so this remains unconstrained. However, below 63 m the value of D_{small} does not effect the results.

6.2.5.2 The age of the ice sheet A_{ice}

Varying the assumed average retention age of the ice sheet for meteorites results in the expected spectra changing as shown in Figs. 6.5 and 6.6. As A_{ice} increases, the fraction of young meteorites drops monotonically. The age spectrum can be seen to be fairly sensitive to the value of A_{ice}; an older ice sheet becomes more able to retain meteorites from larger, more ancient impacts. In fact, only in the range A_{ice}=0.08–0.16 Myr does the predicted age spectrum agree with the data (by 0.32 Myr the spectrum is too close to the upper limits of the CRE data to be considered a likely match). This age range for A_{ice} is entirely consistent with the discussion of 6.1.4.1, and so from now on I shall adopt A_{ice}=100 kyr, in agreement with the lifetime of Antarctic meteorites determined by radioactive dating (Sec. 6.1.4.1).

Fig. 6.6 is interesting because it clearly shows the effects of an unrealistically long retention age for the ice sheet. Even though it is still the case that almost all of the meteorites are launched by small impactors, only a tiny fraction of those meteorites will have blast-off ages <0.25 Myr due to the fact that there are so many more small impacts between 0.25 and 1.0 Myr that have delivered their meteorites to the long-lived ice sheet. Thus, the preponderance of short blast-off times in the lunar meteorite sample is due to two effects: the very high initial accretion rates due to low ejection velocities *and* the young ice sheet.

6.2.5.3 The launch exponent α

The value of α has a very large effect on the incoming meteorite flux. If $\Phi(D) \propto D^2$ (*i.e.,* α=2) the number of meteoroids launched per impact scales as the surface area of the crater since the crater diameter is roughly proportional to that of the impactor (Melosh 1989). This would be expected if the meteorites are being launched in a very thin surface layer of roughly constant thickness, as both the CRE evidence and the theoretical considerations of the spallation model would predict. On the other hand, $\alpha = 3$ might be expected if the number of meteoroids launched scales as the volume of the crater (Warren 1994), with a spall zone thickness $\propto D$. Fig. 6.7 shows that if we adopt this latter scaling, the arriving meteorite flux would be inconsistent with the data.

An important property of the $\Phi(D) \propto D^2$ scaling is that, if the impactor distribution scales as $N(D) \propto D^{-2}$, then each logarithmic bin will *launch* equal numbers of meteoroids. The arriving spectrum will thus be entirely controlled

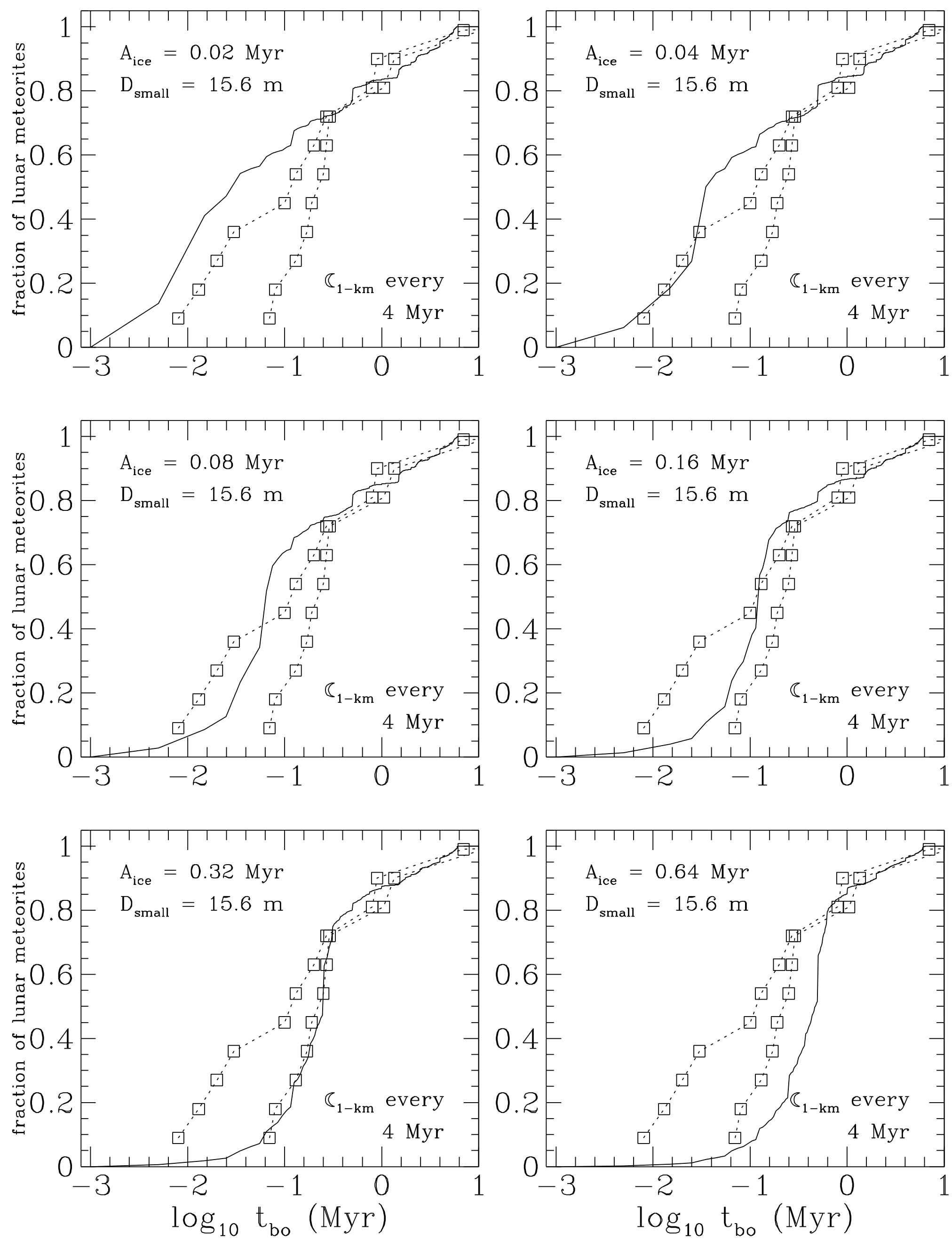

Figure 6.5 These panels show the expected age spectra as a function of the retention age of the ice sheet for lunar meteorites. The launcher spectra (not shown) again look similar to that of Fig. 6.3, in that the majority of the delivered meteorites are launched by impactors smaller than $D \simeq 100$ m.

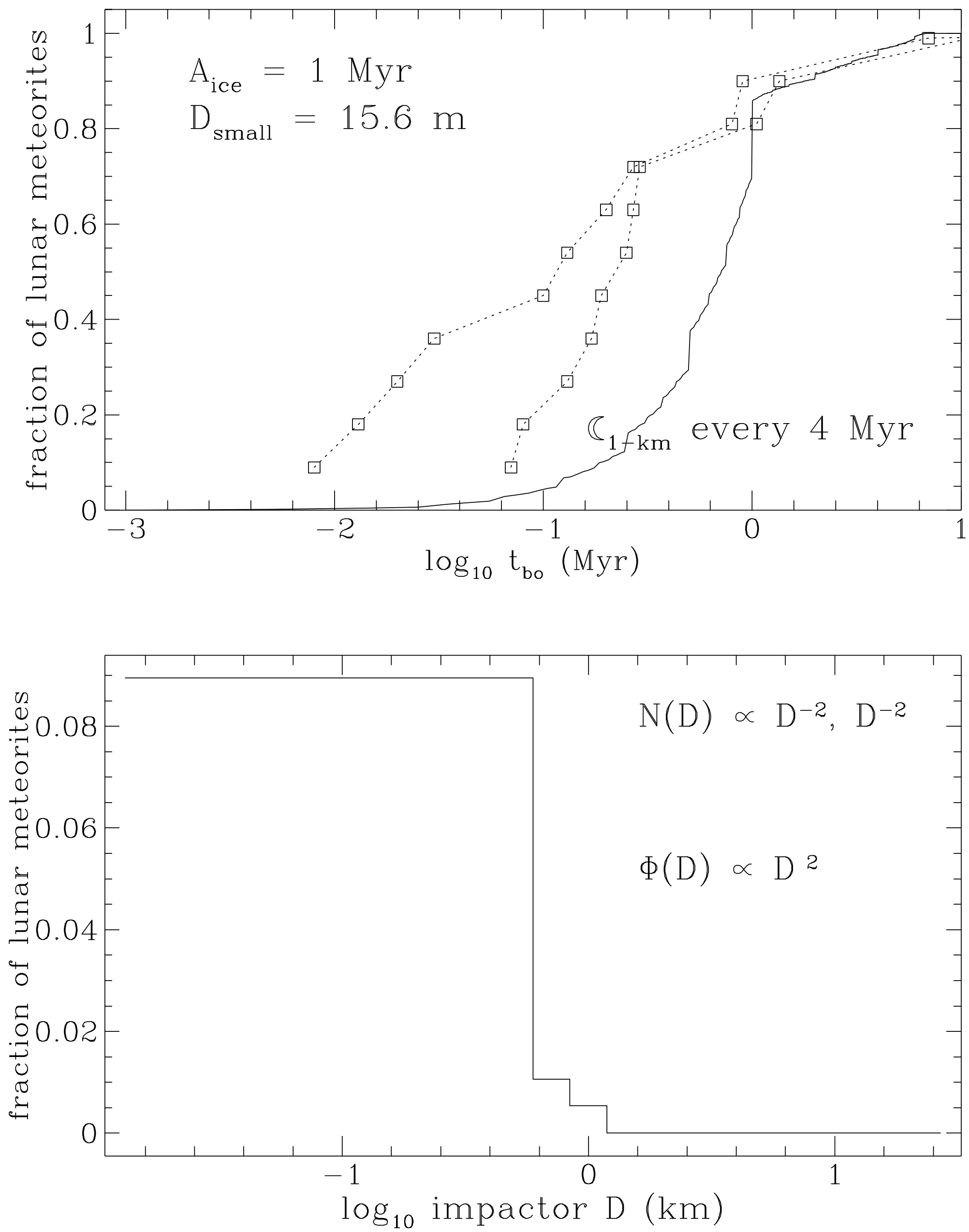

Figure 6.6 The age and launcher spectrum for the case of $A_{\rm ice}$=1 Myr, corresponding to an extremely old ice sheet. Using such an unrealistically long retention age results in almost all of the meteorites presently in the ice sheet coming from impacts that occurred more than 0.25 Myr ago; this is firmly ruled out by the CRE data.

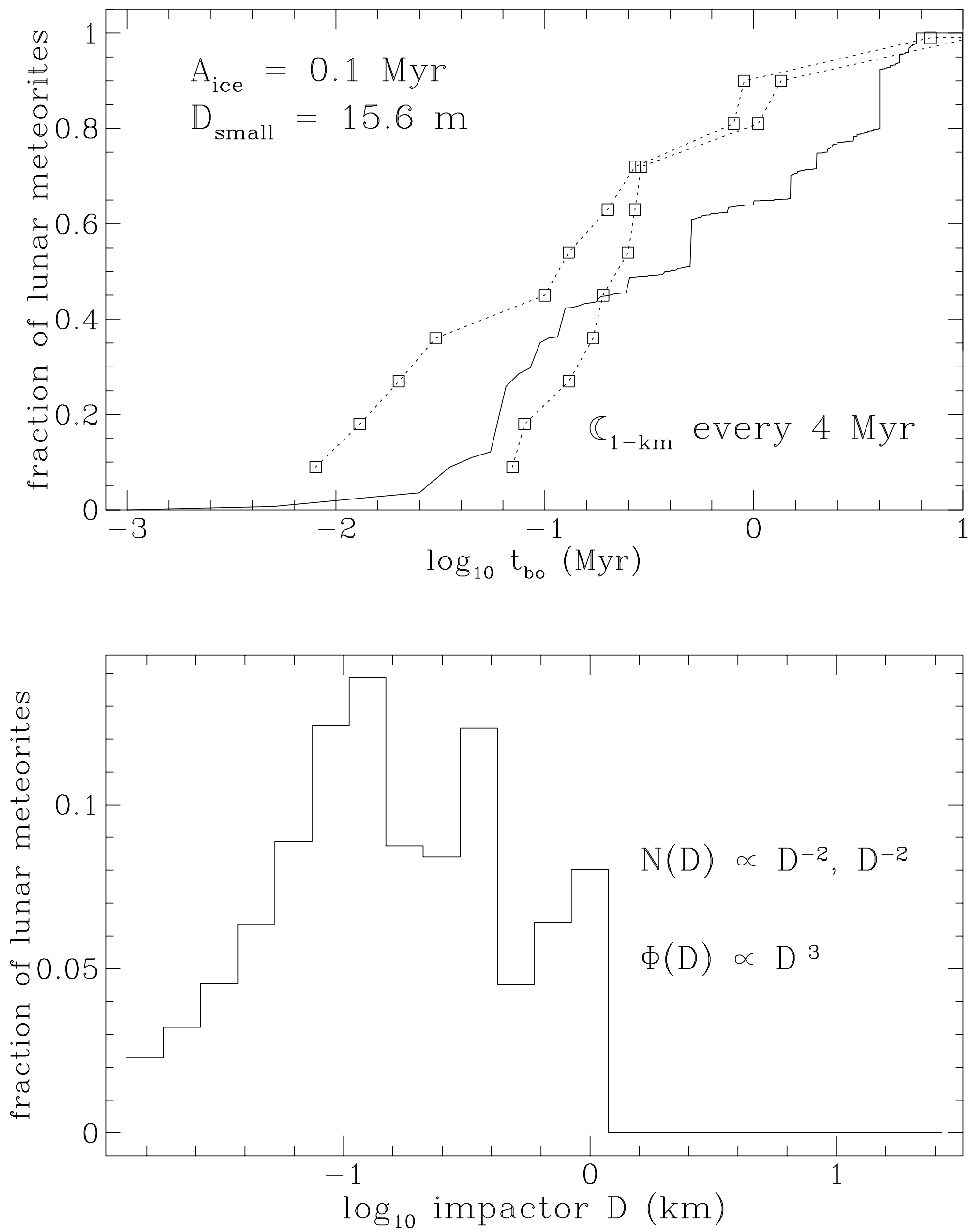

Figure 6.7 The age and launcher spectrum if the number of meteoroids launched per impact scales as the cube of the impactor diameter. Too many of the meteorites should then come from more than several hundred kyr ago, in disagreement with the data.

by the $\mathcal{F}(T)$ spectrum and the influence of the ice sheet. The drop-off in the launcher spectrum beginning at D ~100 m in the standard case of Fig. 6.3 is due to the fact that impactors larger than this are not hitting the Moon on a time scale less than $A_{\rm ice}$. The absolute cut-off at $D \simeq$1 km in that same figure results from no impactors larger than 1 km having hit the Moon in the ~10 Myr time scale over which lunar meteorite delivery takes place (*i.e.,* where $\mathcal{F}$ becomes close to 1). This reasoning is further clarified by a re-examination of Fig. 6.6, where all impactors that hit more often than the age of the ice sheet are equally represented, and the very dramatic cutoff still occurs at $D \simeq$1 km.

When α increases to 3, this behavior changes. Now the larger impactor bins launch more meteorites than the smaller ones, but these larger impactors occur less frequently, and thus on average longer ago. These two effects produce a launch spectrum as shown in Fig. 6.7, with most of the meteorites coming from impacts of objects a few hundred meters in diameter. The cut-off at 1 km is of course unaffected. If α were in fact 3, then not only would the age spectrum of meteorites be different, but we should probably expect a greater prevalence of more deeply launched meteorites since larger impactors should excavate to greater depths. It is notable that the three oldest lunar meteorites are also the ones that seem to have been launched from the greatest depths (Table 2.1, p. 16).

6.2.5.4 Steepening the size distribution $N(D)$

As long as α=2, steepening $N(D)$ below 100 m to be proportional to D^{-3} leaves the age spectrum virtually unaffected. This occurs because the majority of meteorites already come from small impactors spread evenly in time; thus adding additional smaller impactors occurring more often than $A_{\rm ice}$ only slightly modifies the age spectrum, producing a small enhancement in early deliveries (Fig. 6.8). The launcher spectrum is dramatically affected, however, since the extremely numerous impactors in the smallest size bins launch most of the meteorites. Since we have no direct evidence of what size impactors launched the lunar meteorites (although shallow launch depths probably imply smaller impactors), the lunar meteorite data cannot constrain the possibility that the impactor size distribution steepens for smaller bodies. However, neither do we have to worry about the possible steepening affecting the model either, for the age spectrum is insensitive to this change.

The absolute number of meteorites will depend rather strongly on this steepening. An $N(D) \propto D^{-2}$, $\Phi(D) \propto D^2$ distribution has the property that adding another size bin at the lower end increases the total number of launched meteorites only by a small amount since every bin contributes the same number of meteorites. On the other hand, if the size distribution steepens to D^{-3}, then each additional bin contributes more meteorites than the next larger one, explaining the skewing of the launcher spectrum towards smaller impactors.

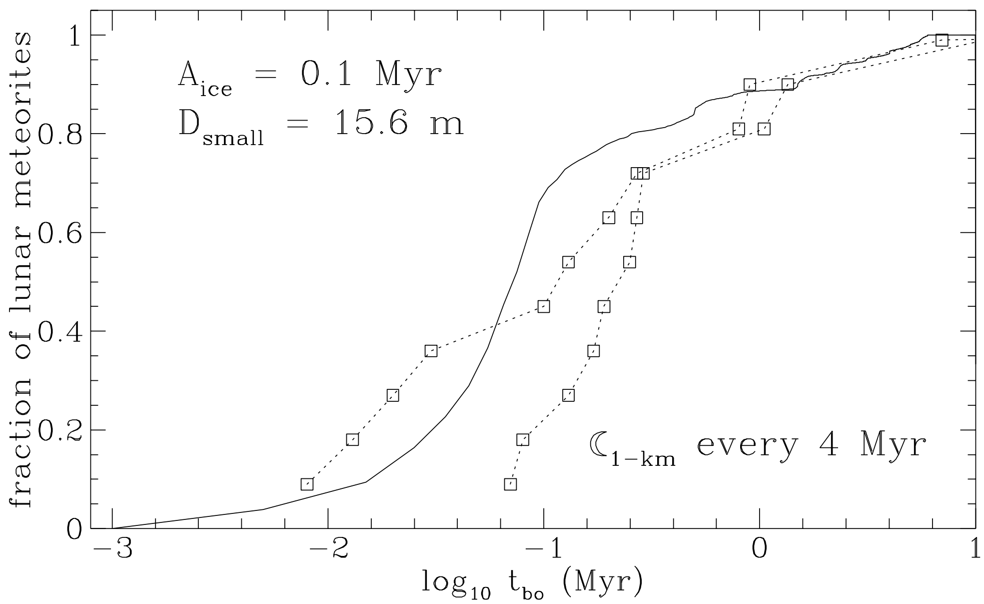

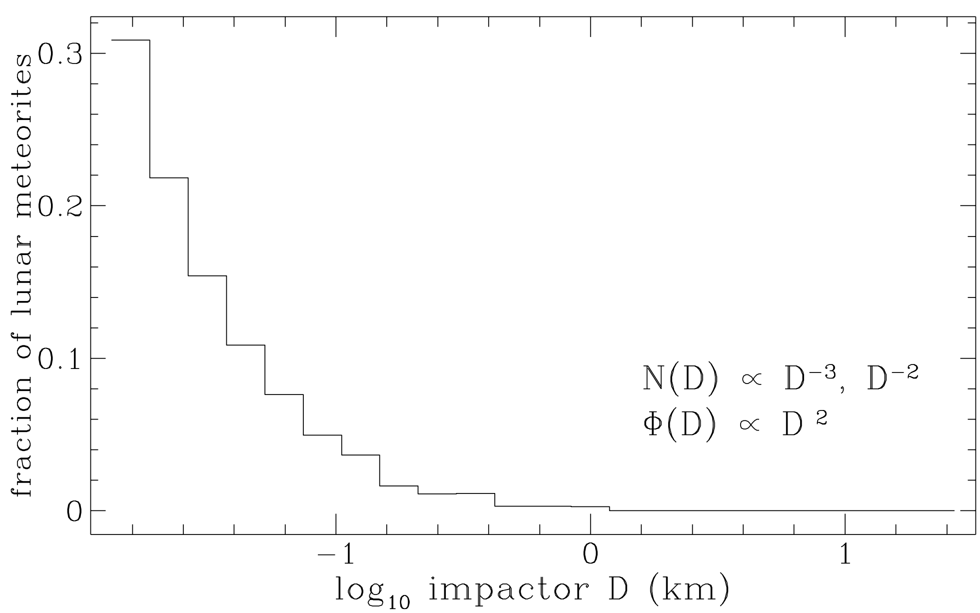

Figure 6.8 The age and launcher spectrum if the size distribution of the impactors steepens to $N(D) \propto D^{-3}$ below 100 m. The age distribution is skewed very slightly towards faster returns (compare to Fig. 6.3). The launcher spectrum changes more dramatically (see text).

6.2.5.5 Lunar source-crater pairings

One obvious way to produce an excess of younger meteorites (the chief constraint we have used to match the age spectrum) is to have a recent large impact. To illustrate this, now that we have explored the systematic effects of changing the other parameters, I have included the random spacing of the impactors (step 5 of the algorithm in Sec. 6.2.4), which allows larger impactors to have struck the Moon in the recent past. Fig. 6.9 shows such a case; a single 800-m impactor struck the Moon $\simeq$ 40,000 years ago. As can be seen from the launcher spectrum, this impact launches so many meteorites, and has such a high transfer efficiency, that about half of all the meteorites expected to be in the ice sheet are contributed by this single impact. However, all of these meteorites should have identical blast-off ages and similar petrologic characteristics (*i.e.,* they should be source-crater paired). Since Warren (1994) feels that few, if any, of the lunar meteorites are source-crater paired, we can rule out the occurrence of any large ($\gtrsim$300 m) impacts on the Moon in the last hundred thousand years. Note that the effect of these impactors would be more pronounced if we were to allow α=3, since the larger impactors would launch even more meteorites.

This example highlights the importance of the stochastic nature of the impact process. By performing about 30 such simulations I have observed that an impactor large enough to produce an unacceptable number of source-crater pairs occurs only in about one-third of the cases. Even if an impact larger than 500 m happened in the last 10 Myr, it can occur long enough ago that its initial peak of deliveries is prevented from 'contaminating' the age spectrum as illustrated by Fig. 6.10. I suggest that the source-crater pairing of Asuka-881757 and Y-793169 may be due to the occurrence of such a large impact $\simeq$1 Myr ago on the Moon; the deep provenance of these two meteorites supports such a hypothesis.

6.2.6 Lunar summary

In summary, of the five relevant parameters, only $A_{\rm ice}$ and the exponent α of $\Phi(D)$ dramatically affect the spectra (for plausible ranges of the parameters). Apparently α must be closer to 2 than 3, and thus the number of meteoroids launched per impact scales with the surface area of the crater rather than its volume; this conclusion was already reached by Warren (1994) on the basis of the number of recent launch events. The modelling suggests that the ice sheet is less than about 60 kyr old, which is perhaps somewhat younger than one might estimate (see Nishiizumi *et al.* 1989); however, recall that the relevant parameter $A_{\rm ice}$ is actually the mean survival time of lunar meteorites on the ice surfaces that have been searched so far. If we base our estimate of $A_{\rm ice}$ on the meteorite sample (Sec. 6.1.4.1), then 60 kyr is reasonable.

The diameter of the smallest impactors capable of launching lunar meteoroids, the mean impact rate of 1-km impactors, and a possible steepening of the size

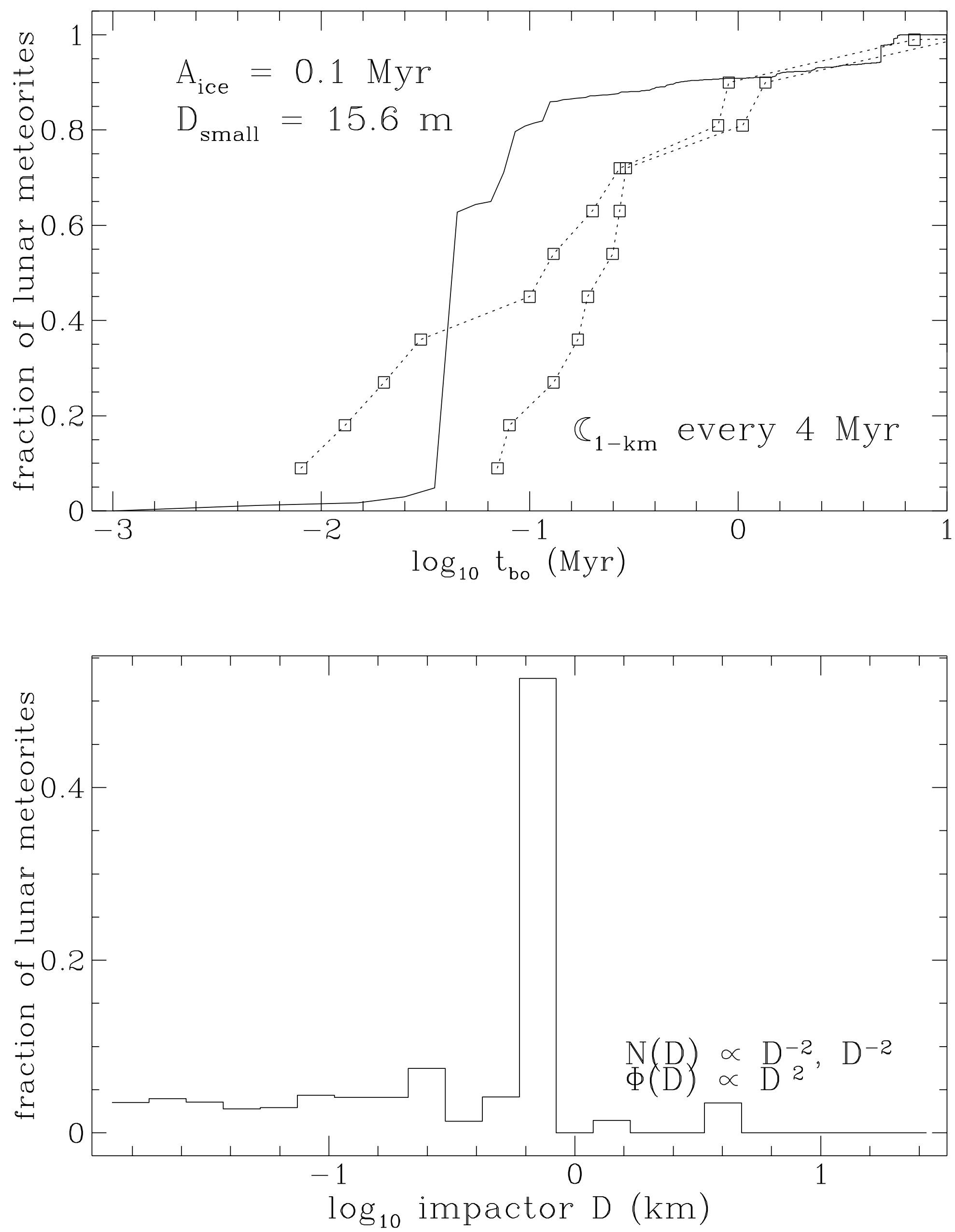

Figure 6.9 With random impact timing allowed, it is possible to have a large impactor hit the Moon recently. In the case shown, a single 800-m impactor striking the Moon 40,000 years ago would contribute about half of the lunar meteorites present in the ice sheet. The impact is indicated by the large spike in the launcher spectrum and the discontinuous jump in the age spectrum. This possibility is not supported by the meteorite data.

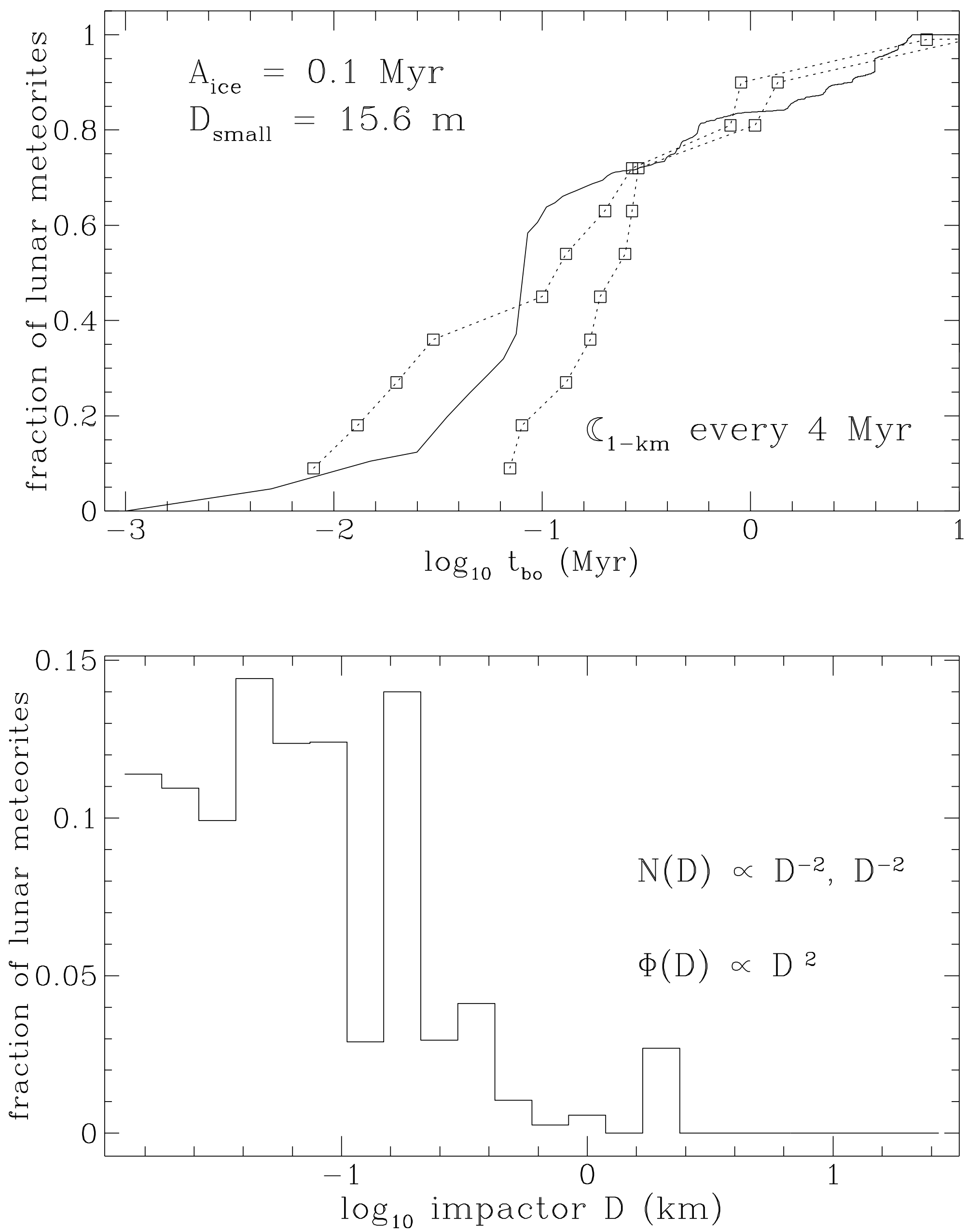

Figure 6.10 If a large impactor strikes the Moon more than several hundred thousand years ago, it delivers so little material to the ice sheet in the recent past that it produces only a minor effect in the age spectrum. In the case shown a 2 km impactor strikes the Moon $10^{0.6} = 4$ Myr ago (its presence is indicated by the small vertical jump of the age spectrum at this time). The peaks in the launcher histogram at large D are due to individual impacts, whereas at small D the meteorites are contributed by a myriad of small impacts.

distribution of the impactors below 100 m all have relatively small effects on the age spectrum.

6.3 Modelling martian launch

Our chief concern once we broaden our study to include the launch of martian material is to understand the circumstances under which the number of lunar to martian meteorites is roughly equal. This requires the inclusion of four additional parameters: (1) the relative flux of impactors hitting Mars as compared to the Moon; (2) the exponent p in the scaling of the number of launched meteoroids vs. ejection velocity in Eq. 6.12; (3) the energy exponent of $\Phi(D)$ for Mars; and (4) the fraction of the martian surface suitable for meteoroid ejection.

The flux of impactors onto Mars is not well constrained observationally. Theoretical models estimate that the space density of impactors near Mars should be comparable or slightly larger than that near the Moon. Wetherill (1989) calculates that the cratering rate *per unit area* on Mars is 1.94 times that of Earth. One might naively expect that the space density of impactors should be higher at Mars since it is nearer to the main asteroid belt, but the population of impactors in near-Mars and near-Earth space depends critically on the processes which inject asteroids and comets (the two classes of impactors) onto orbits inside the asteroid belt. However, there is no particular reason to assume that the *size* distribution of impactors in these classes should be any different at the Moon and Mars. Thus I assume that either asteroids or comets dominate at both targets, and that the flux of impactors $I_{\rm Mars}(D)$ near Mars is some fixed multiple of the lunar flux irrespective of size; that is,

$$I_{\rm Mars}(D) = F I_{\rm Moon}(D) \propto F D^{-2} \ . \tag{6.19}$$

If the space density of impactors were identical and gravitational focussing were ignored, then F would be simply the ratio of the martian to lunar surface area, which is four. The gravitational focussing of Mars is $\propto 1 + (v_{esc}/v_\infty)^2$ (Eq. 3.4). Most Earth-Moon impactors approach with v_∞ = 10–20 km/s (Wetherill 1969, Chyba *et al.* 1994, *cf.* p. 94) and, since we expect the martian values to be comparable, gravitational focussing likely results in an enhancement of a few tens of percent in the martian impactor flux.

I use F = 8, which combines focussing, Wetherill's estimate, and an order unity enhancement in the space density of impactors; F is likely to be accurate to a factor of two.

The assumption of a D^{-2} power-law over the entire impactor size range is probably even more valid for Mars since one would expect its higher escape velocity (of 5.03 km/s, more than twice that of the Moon) to result in a larger minimum impactor size for meteoroid launch. From Eq. 6.16, the minimum diameter for launching a meteoroid can be seen to scale as $v_{esc}^{(p-1)/\alpha}$, where p is the exponent of the velocity spectrum of the escaping particles. Since we concluded earlier that $p \geq 4$ (Sec. 6.2.3), martian launch requires impactors at least 3 times larger (and thus an order of magnitude less frequent) than lunar ones, assuming similar surface properties ($\alpha = 2$).

The exponent p is also very important for determining the relative number of launched meteorites. If surface properties were identical, Eq. 6.13 predicts that for *equal size impactors*,

$$\left.\frac{N_{Moon}}{N_{Mars}}\right|_{\text{launched}} = \left(\frac{v_{Mars}}{v_{Moon}}\right)^{p-1} \simeq 2^{p-1} \tag{6.20}$$

in terms of the ratio v_{Mars}/v_{Moon} of the escape speeds. The number of meteorites that arrive at Earth is influenced by the delivery efficiencies. If we adopt 40% for the lunar and 4% for the martian total delivery efficiency (Sec. 6.1.4), then the ratio of numbers that eventually reach the Earth from impactors of equal size is

$$\left.\frac{N_{Moon}}{N_{Mars}}\right|_{\oplus} = 10 \times \left(\frac{v_{Mars}}{v_{Moon}}\right)^{p-1} \sim 2^{p+2}\,. \tag{6.21}$$

Even if p is the probably minimal value of 4 from the lunar data, then the number ratio should be at least 60, as opposed to the observed value of $\simeq$1.

I will allow the exponent α of $\Phi(D)$ for Mars to be different from that of the Moon. This was done to permit the possibility of a general difference of surface properties between Mars and the Moon. Warren (1994) claims that the martian α must be closer to 3 than 2 in order to match the CRE evidence; I will explore the consequences of this. Lastly, I will also examine the effect of limiting the available area on Mars for meteoroid launch, in order to help reproduce the prevalence of young source terrains for the martian meteorites.

6.3.1 The baseline martian case

Fig. 6.11 shows the baseline case for the full simulation that considers both Mars and the Moon. The match here with the meteorite data is very good; large numbers of source-crater pairs are expected for the martian meteorites, and the ratio of lunar to martian meteorites R (indicated in the bottom left plot) is within a factor of 2 of unity. The exact timing of the large martian impact events need not precisely agree with the data of course; only the general spectral shape and prevalence of source-crater pairing need to be reproduced. The values of p, F, and the exponent of $\Phi(D)$ are also indicated on the martian panels. I shall again vary the parameters systematically to explore the model dependencies.

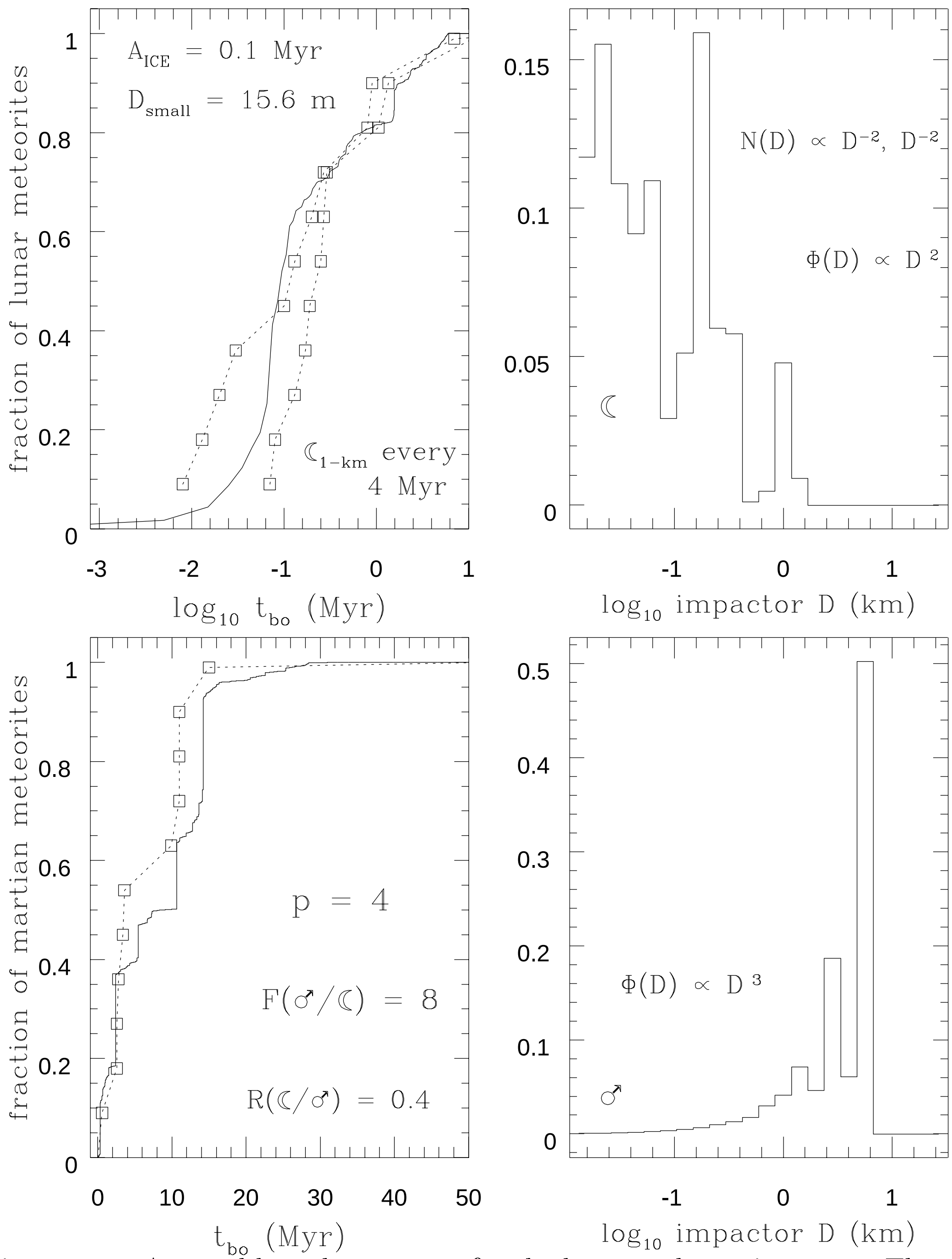

Figure 6.11 Age and launcher spectra for the lunar and martian cases. The two left panels show the age spectrum for the lunar (top) and martian (bottom) meteorites; note that the lunar panel uses a logarithmic time axis whereas the martian one is linear. The two right panels show the lunar (top) and martian (bottom) launcher spectra. *Random impact timing was included in this simulation.*

6.3.2 The velocity power law and impactor flux ratio

The only way in which the exponent p of the velocity power-law (Eq. 6.12) enters into the model calculation is when determining the ratio of the numbers of meteoroids launched in an impact of a given diameter (see Eq. 6.20). Thus, when p is increased by one, the lunar to martian meteorite ratio R goes up by a factor of about two (the ratio of the escape velocities). Thus changing p to 7 would not alter Fig. 6.11 at all except to change the meteorite number ratio to $\simeq 8 \times 0.4 = 3.2$.

Changes in the value of F produce an approximately linear change in the value of R since the flux of martian impactors in each bin is proportional to F. The model is basically incapable of distinguishing between variations in the parameters F and p, but I have kept both since they represent different physics.

6.3.3 The martian launch exponent

The martian spectrum depends critically on the value of α. In order to explore the effect of α's variation, I again temporarily turn-off the random spacing of the impactors (Fig. 6.12). As discussed in the context of the lunar case, if α=3 the larger impactor bins launch more material than the smaller ones, as shown in the martian launcher spectrum. Thus the largest impactor ($D \simeq 5$ km), which struck Mars $\simeq$16 Myr ago in this simulation, contributes the most meteorites (slightly more than 30%). All of the (source-crater paired) meteorites from this event would have the same blast-off age, as indicated by the discontinuity in the martian age spectrum. In this simulation the ratio R of lunar to martian meteorites is 0.6. A factor of two more martian meteorites have fallen during the age of the ice sheet, even though more lunar than martian meteorites have been delivered to Earth over all of history. This occurs because the current delivery rate from ancient lunar impacts is reduced to a relative trickle, whereas any martian impact delivers meteorites at almost a constant (but smaller) rate for $\approx$15–20 Myr (Fig.6.1). Since large impacts on Mars are more likely (due to the larger impactor flux), ancient martian impacts that launch large numbers of meteoroids are heavily represented in the meteorite record; this is doubly important because only when sampling these large impacts is there a reasonable chance of seeing source-crater pairs.

When α for Mars is changed to 2 (Fig. 6.13) the martian launcher spectrum is changed radically. Here, as in the lunar case, almost all the meteorites come from small impactors, because α=2 implies that each logarithmic bin launches the same number of meteoroids. Note from the expected martian age spectrum that although the distribution of transfer times is roughly correct, source-crater pairings are almost absent in the expected age spectrum. This disagrees with the meteorite data. Observe also that the lunar to martian meteorite ratio has risen by an order of magnitude.

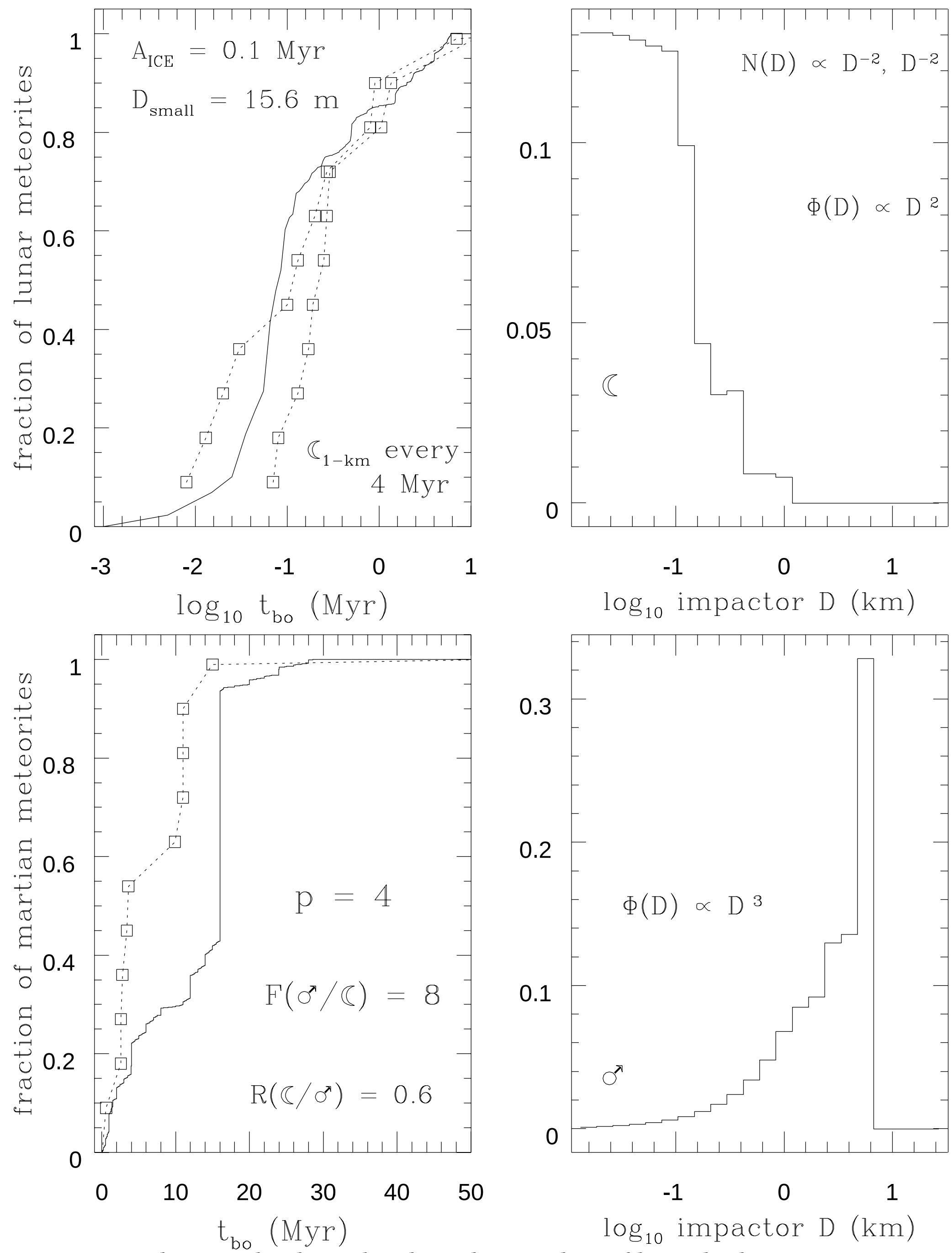

Figure 6.12 The standard result when the number of launched martian meteorites scales as the volume of the crater and random impacts are *not* allowed. The age spectrum of the martian materials is unrepresentatively skewed towards later launches. Note that the D^3 scaling of the launchers means that most of the martian meteorites are launched by the largest impactors that occur during the $\approx$20 Myr delivery horizon.

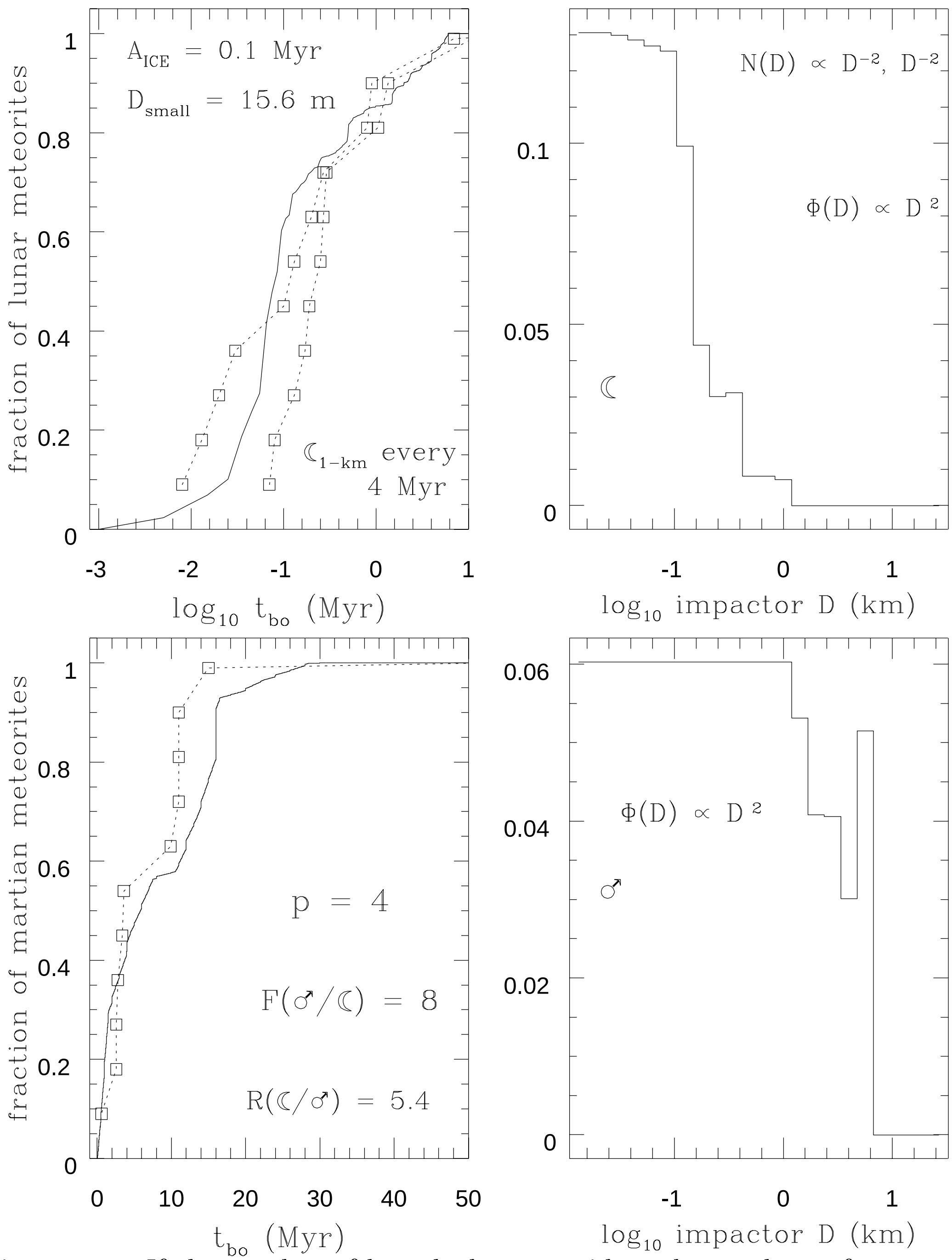

Figure 6.13 If the number of launched meteoroids scales as the surface area of the crater, then (1) the number of arriving martian meteorites drops by an order of magnitude (relative to the lunar flux), (2) almost all martian meteorites are launched by small impactors, and (3) SCPs become very rare. This scenario is not supported by the data.

6.3.3.1 Implications

These results suggest that there must be some process which discriminates against meteoroid production by smaller martian impactors, and yet still allows for large impactors to produce enough of a flux to keep $R \sim 1$. One can imagine several hypotheses to explain this.

(1) Perhaps the martian atmosphere appreciably modifies the size distribution of the impactors or launched meteoroids. It is unlikely that the 6 mbar atmosphere can prevent impactors from reaching the surface; even Earth's more massive atmosphere only stops silicate impactors below $D \sim 100$ m (Chyba 1993). The martian atmosphere will only stop yet smaller impactors, which probably would lack sufficient kinetic energy to liberate meteoroids in any case. On the other hand, the atmosphere may hinder small (up to tens of cm) launched meteoroids from escaping back out to space, since they have much smaller ratios of surface area to mass (the important parameter for drag). Therefore it is conceivable that smaller ejected particles are preferentially prevented from escaping the planet. This would help explain the larger average mass of the martian meteorites.

(2) An entirely different launch process may dominate on Mars. Perhaps the vaporization of subsurface ice could assist meteoroid launch. Any such proposed process must still satisfy all of the constraints (preferences for deep launch, young source terrains, and bigger impactors). The data do not yet seem to demand this extreme hypothesis.

(3) As shown above, if the number of meteoroids scales as the volume of the crater, this naturally resolves the problem. Volume scaling might occur in two ways.

(i) Perhaps the martian surface is not covered with a regolith layer having a sound speed as low as the lunar one, at least not in the young source terrains of most of the martian meteorites. This would result in the martian impactors mining down deeper than their lunar counterparts and launching more ejecta. However, in this case we might then expect many objects from small impactors and thus fewer source-crater pairs.

(ii) Alternately, perhaps the surface layers on the two parent bodies are identical. Then small martian impactors only excavate very shallow surface layers of little volume. But the transfer dynamics show that ancient (~1-10 Myr ago) large martian impacts are well represented in the impact record. Even *with* a 100 m/s sound speed, a 3-km impactor (not an uncommon occurrence on Mars over 10 Myr) will have a spall zone of depth $z \approx 30$ m (Eq. 6.7). Once down into bedrock, as such an impact would almost surely be, the sound speed would rise dramatically and thus the spall layer may be considerably deeper than 30 m. In this regime the amount of ejecta may become proportional to the volume of the projectile (Melosh 1985, Vickery and Melosh 1987) and almost all the meteorites will come from larger craters (*cf.* launcher spectrum in Fig. 6.12). The scenario has the advantage that it does not matter if the smaller impactors are being screened out or not. The larger masses of the martian meteorites may then be simply due to their being produced in larger impacts; on the other hand, atmospheric effects may still enhance this effect by selecting against smaller meteoroids. The deep provenance of the martian meteorites may be either (1) due to a lack of near-surface rocks suitable for ejection (Warren 1994), or (2) simply because only a very small fraction of the material spalled off in larger impacts is within $\approx$3 m of the surface when depths down to many tens of meters are excavated.

6.3.3.2 The fraction of young terrain

Since 11 of the 12 martian meteorites are from geologically young terrain which occupies a small portion of the surface, this strongly argues that these terrains are favored (perhaps almost exclusively) for launch. Conceivably, small number statistics could be to blame, but if six impact events are in fact represented (Eugster *et al.* 1996), then this hypothesis begins to stretch the bounds of credibility. I have explored including the effect of having limited source regions by simply randomly rejecting 80% of all martian impacts, hypothesizing that only 15% of the martian surface contains sufficiently young terrain (Tremain 1995a), and allowing 5% of the older terrain to be suitable (to allow for the existence of ALH84001). Although clearly ad hoc, this assumption does provide a mechanism for the selection of younger meteorites. It simultaneously increases the frequency of source-crater pairings, since the martian launch process becomes even more dependent on the stochastic nature of the largest impacts, which must now strike inside the 15 Myr 'delivery window', but also into young terrain. Even the baseline case seems to have too little source-crater pairing in the expected spectrum (Fig. 6.11). After reinstating random impactor-timing, allowing only 20% of the martian surface to launch meteorites produces expected spectra such as the example of Fig. 6.14. Here, three large impactors hitting Mars in the last 6 Myr have produced 90% of the martian meteorites; so many meteoroids were in fact produced that just as many martian meteorites were delivered to the ice sheet as lunar ones. Such an outcome is not commonplace however. In most simulations that use the parameters of Fig. 6.14 lunar meteorites are favored by a factor of 3–6; this discrepancy could be easily rectified by minor changes in the relative flux or power law exponent. Of course, it need not be rectified at all; Fig. 6.14 shows that the observed spectra can be reproduced with this set of parameters.

A possibility worthy of mention is that the martian atmosphere is in large part responsible for the selection of young terrains. This could occur because the young volcanic terrains on Mars (specifically in the Tharsis region) are at higher altitudes than the older terrains. If the martian atmosphere does effectively hinder meteoroid launch, as discussed in the previous section, then the higher altitude regions could be favored since considerably less atmospheric mass will

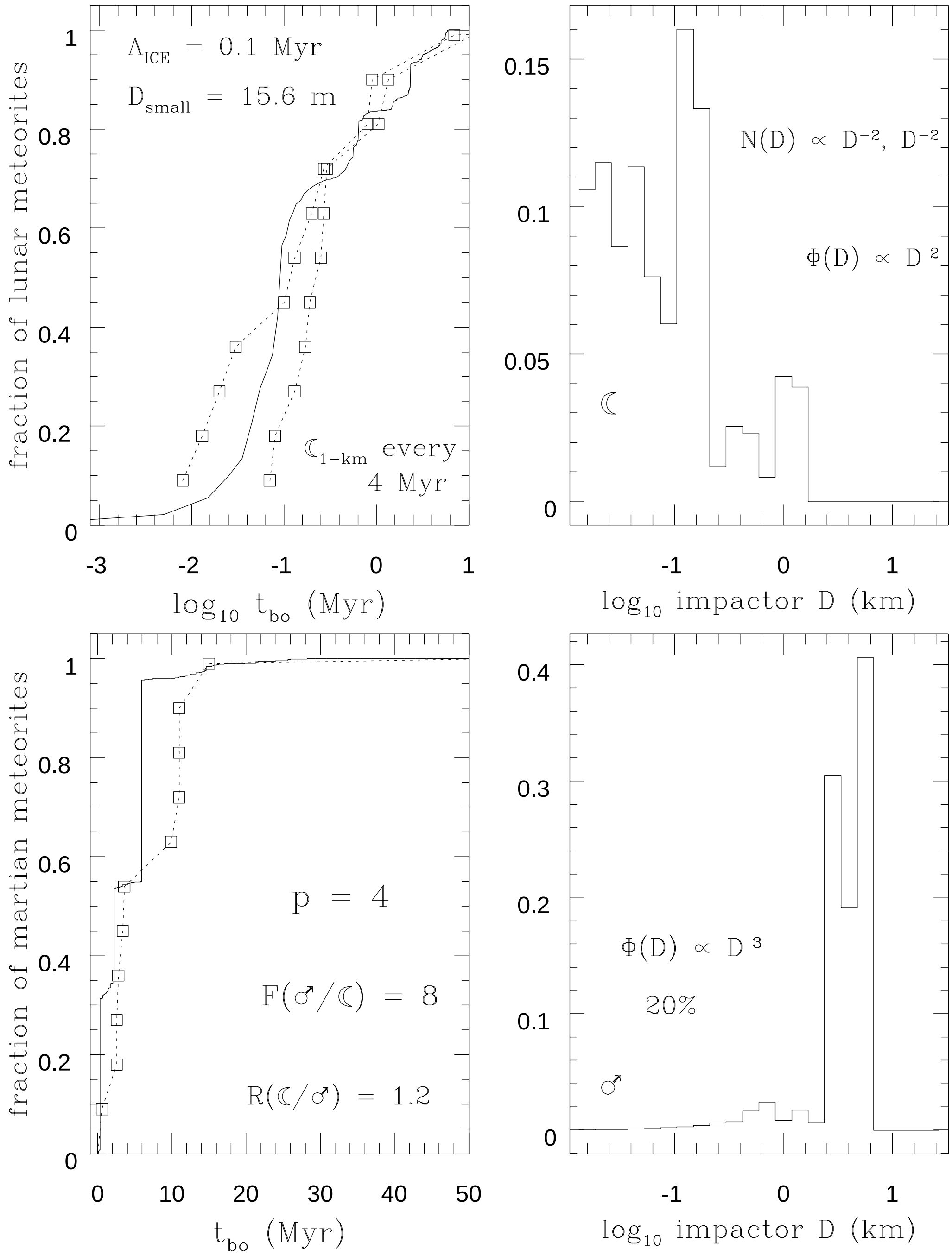

Figure 6.14 Limiting the fraction of Martian terrain results in a greater tendency for source-crater pairing. Although this on average would be expected to decrease the number of launched martian meteoroids, large impacts into young terrain can still produce more than enough meteorites, as in this example where just as many martian as lunar meteorites are present in the ice sheet. The exact form of the martian age spectrum clearly depends on the timing of these impacts.

need to to penetrated by the ejecta. At the 6 mbar level (the zero-altitude reference level on Mars), the amount of atmospheric mass per unit area above the surface is $\sigma = P_\circ/g \simeq 16$ g/cm^2, where $P_\circ$ is the surface pressure and $g =$ 371 cm/s^2 the gravitational acceleration. Meteorite launch would be hindered if the ejected meteoroid needs to traverse roughly its own mass in atmosphere (Chyba 1993). At 0-km altitude, only very large meteoroids ($r \gtrsim 15$ cm, $m \gtrsim$ 30 kg) have ratios of mass-to-surface area larger than necessary. In contrast, at elevations above one martian scale-height (≈ 11 km), 5-cm meteoroids ($m \sim 1$ kg) could escape. The ancient northern highlands have an average elevation of about 4 km (Esposito *et al.* 1992), so only the very highest terrains will be above a scale-height, and thus favored by this atmospheric effect. While this scenario clearly favors launch from the very young volcanic terrains, it further restricts the available portions of the martian surface. In fact, only the flanks of the four largest Tharsis volcanos are above 11 km altitude; Jeffrey E. Moersch (1996, private communication) estimates this represents only $\sim$ 0.3% of the martian surface area.

6.3.3.3 Stochastic variability

The example of Fig. 6.14 illustrates that the stochastic nature of the martian (and sometimes lunar) impacts could be crucial to understanding features in the data. For this reason, to provide the reader with some sense of how much random variation occurs, I show the results of several simulations. Figs. 6.15–6.23, along with Fig. 6.14, present the outcomes of ten sequential simulations, all with the same parameters. The differences in these plots are entirely due to the random-impact timing and the limited viable martian launch area. These figures demonstrate that: (1) the exact nature of the martian age spectrum in regards to source-crater pairings depends heavily on the timing of the largest impacts, and (2) a lunar-to-martian meteorite number ratio $R \sim 1$ is not in fact uncommon; the ratio is usually within a factor of 6 of this.

Fig. 6.15 is an especially interesting case, because it illustrates the consequences of a large, recent lunar impact. 100 Kyr after the event, the ice sheet is still so dominated by this 2-km impactor's ejecta that almost all lunar meteorites come from the impact and these meteorites outnumber the martin ones by a factor of 100. Only after the hail of meteorites from this impact ceases (after a few hundred kyr at most), and are destroyed in the ice sheet, does R return to order 1–6, as it is most of the time.

6.3.4 Musings on martian source-crater pairings

An unresolved issue in the previous discussion is the extent of source-crater pairing (SCP) in the martian meteorites. As discussed in Sec. 4.4, it is almost inconceivable in light of the constraints that all of the martian meteorites were

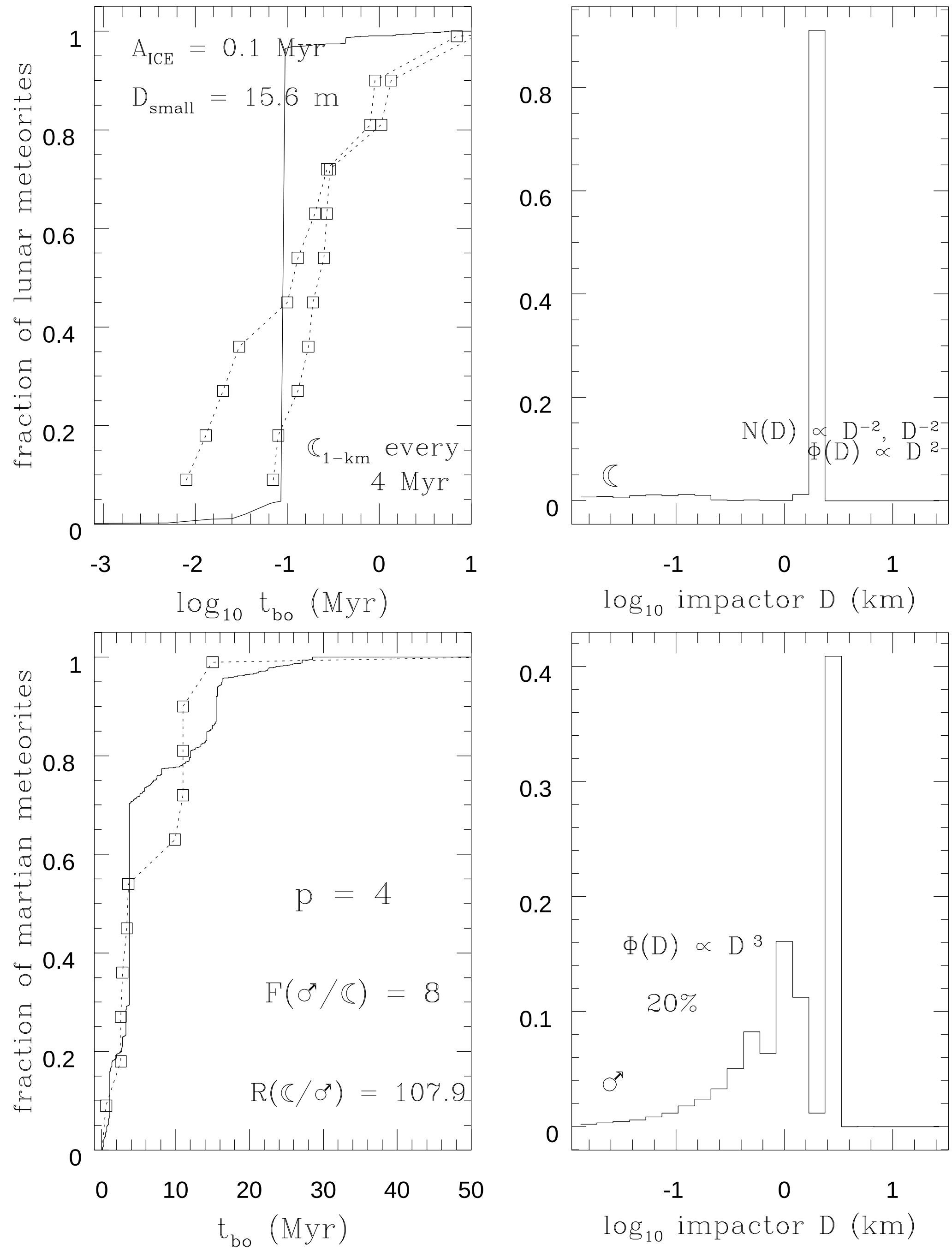

Figure 6.15 A sample delivery history for lunar and martian meteorites. This is part of a series of ten simulations (Figs. 6.14–6.23), all of which use the same parameters, intended to illustrate the importance of large stochastic impacts on the Moon and Mars. These simulations use randomly timed impacts and limited martian source area.

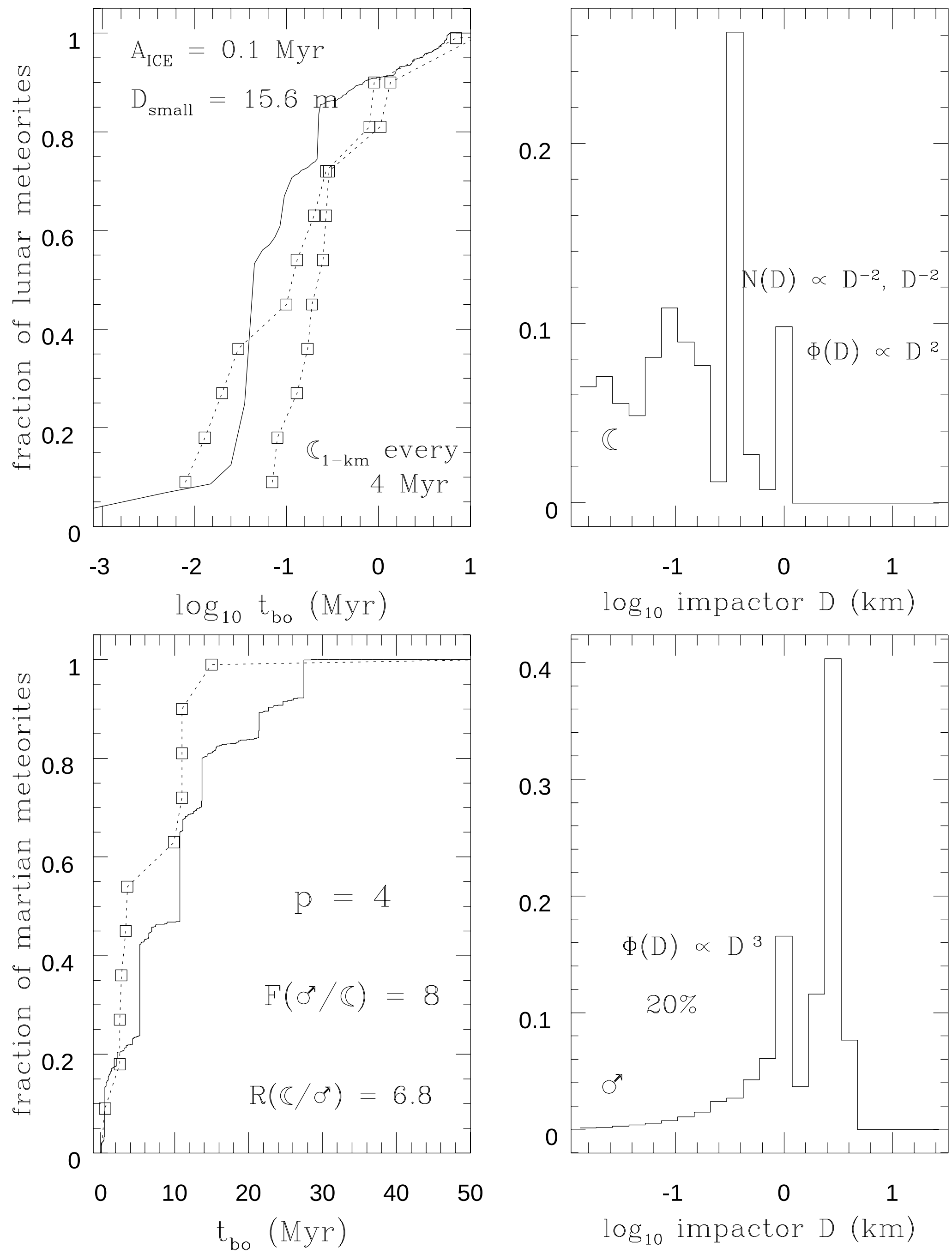

Figure 6.16 A sample delivery history for lunar and martian meteorites. This is part of a series of ten simulations (Figs. 6.14–6.23), all of which use the same parameters, intended to illustrate the importance of large stochastic impacts on the Moon and Mars. These simulations use randomly timed impacts and limited martian source area.

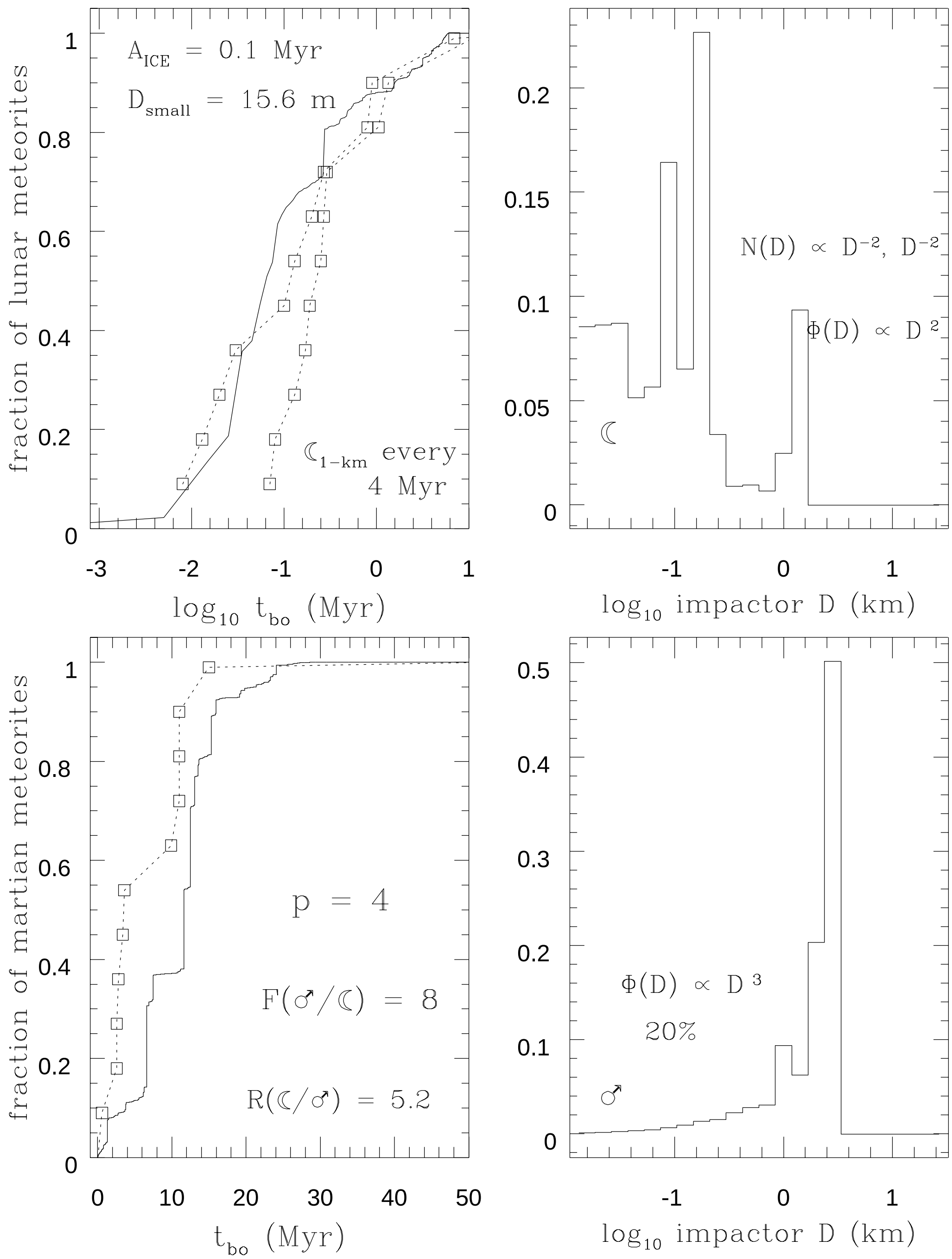

Figure 6.17 A sample delivery history for lunar and martian meteorites. This is part of a series of ten simulations (Figs. 6.14–6.23), all of which use the same parameters, intended to illustrate the importance of large stochastic impacts on the Moon and Mars. These simulations use randomly timed impacts and limited martian source area.

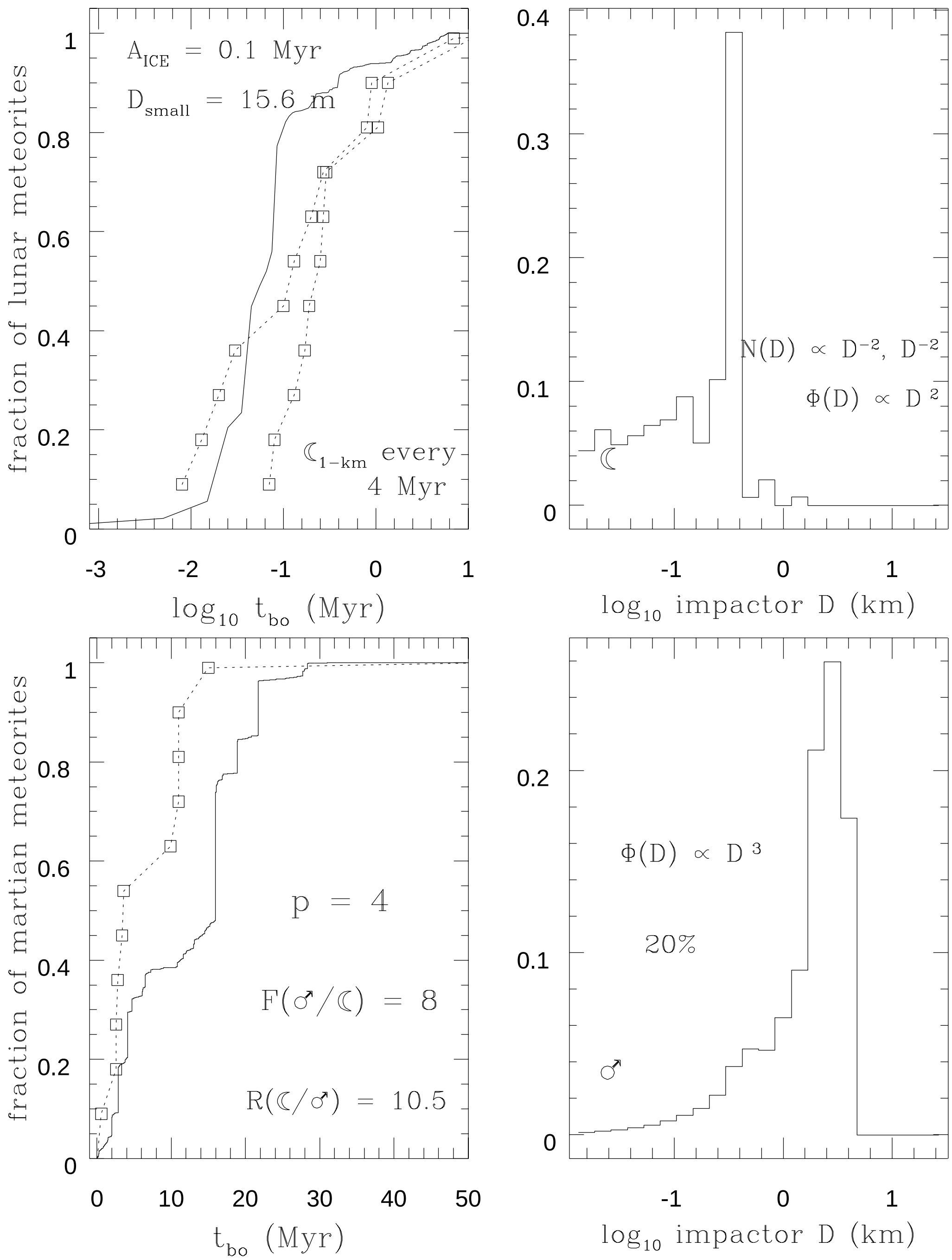

Figure 6.18 A sample delivery history for lunar and martian meteorites. This is part of a series of ten simulations (Figs. 6.14–6.23), all of which use the same parameters, intended to illustrate the importance of large stochastic impacts on the Moon and Mars. These simulations use randomly timed impacts and limited martian source area.

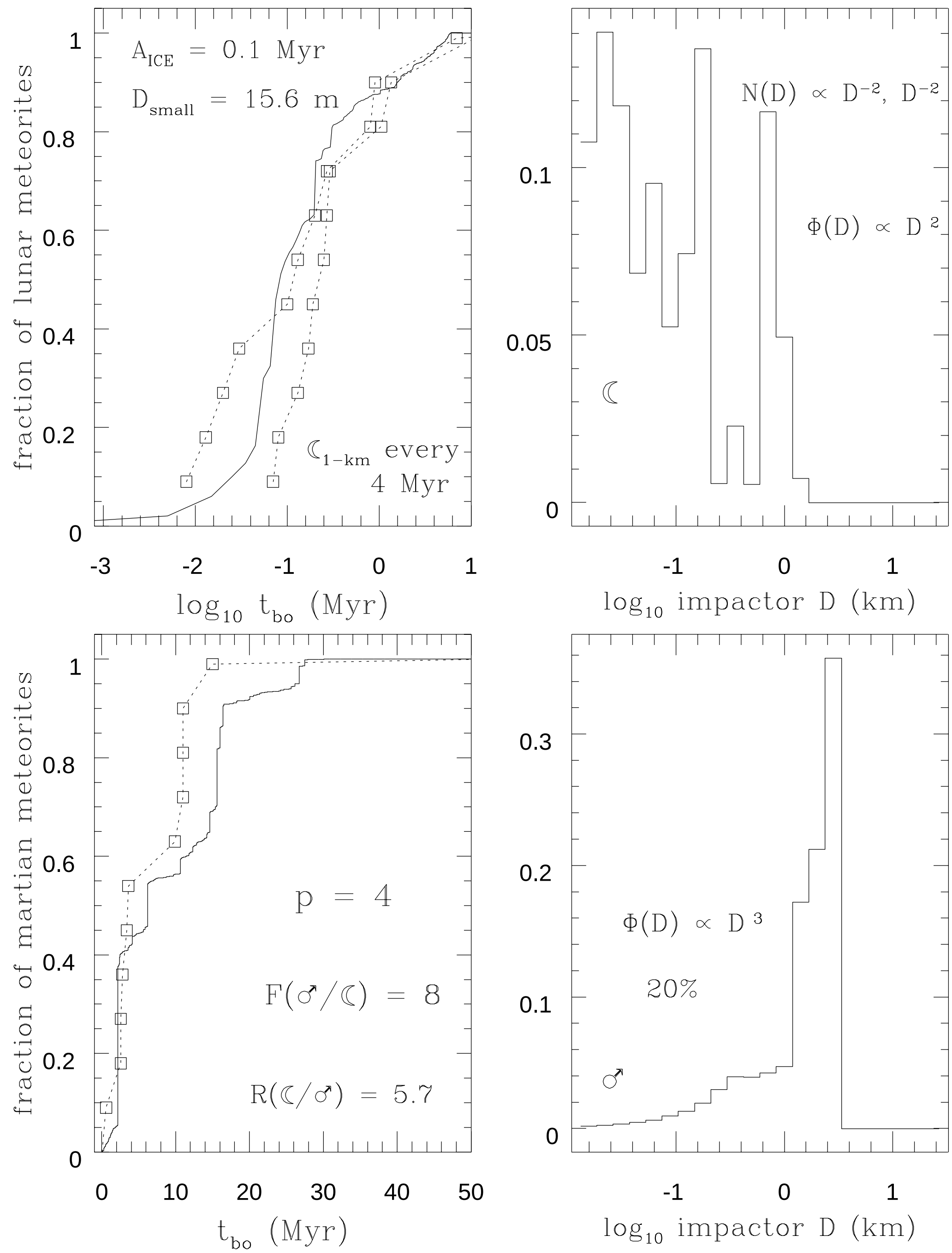

Figure 6.19 A sample delivery history for lunar and martian meteorites. This is part of a series of ten simulations (Figs. 6.14–6.23), all of which use the same parameters, intended to illustrate the importance of large stochastic impacts on the Moon and Mars. These simulations use randomly timed impacts and limited martian source area.

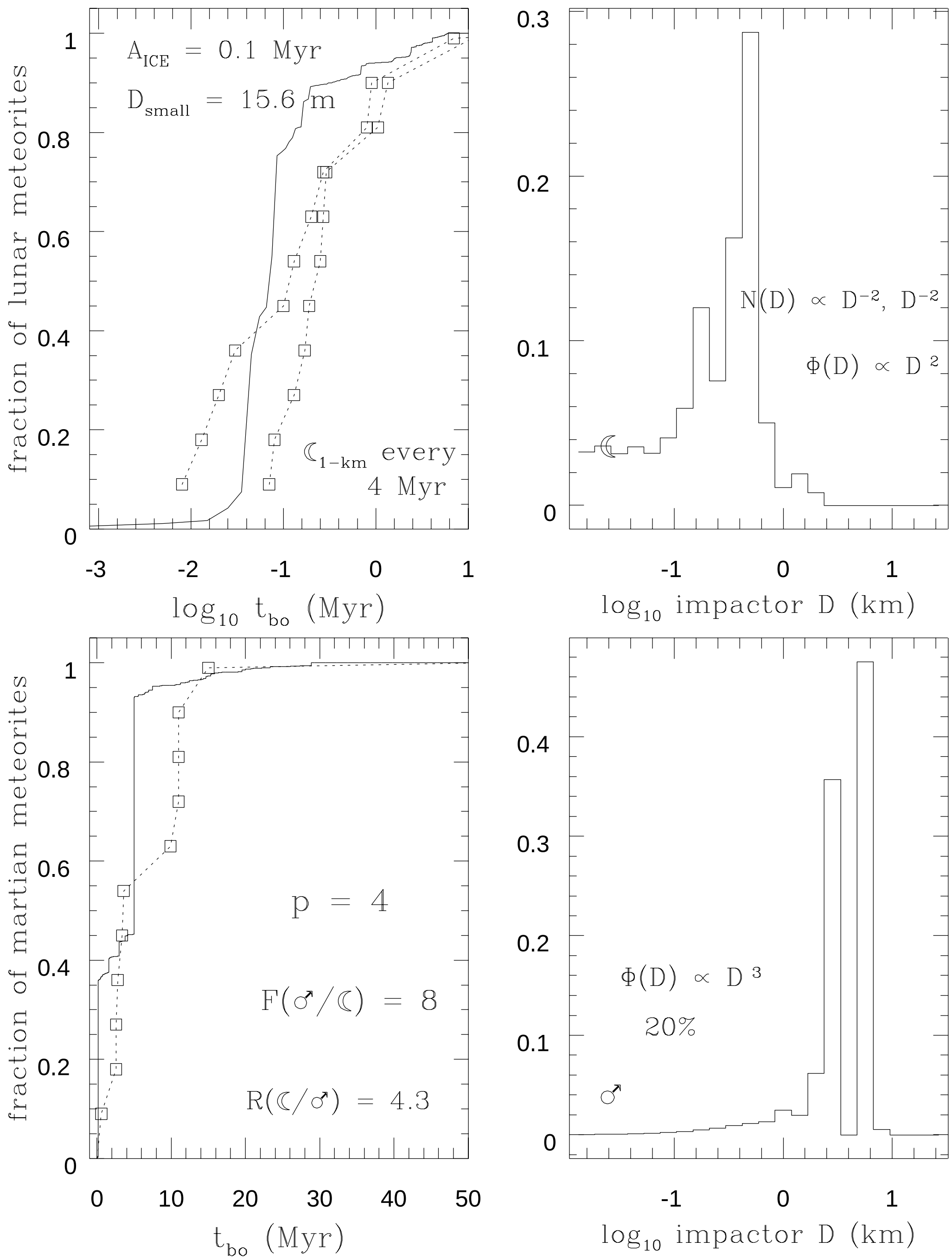

Figure 6.20 A sample delivery history for lunar and martian meteorites. This is part of a series of ten simulations (Figs. 6.14–6.23), all of which use the same parameters, intended to illustrate the importance of large stochastic impacts on the Moon and Mars. These simulations use randomly timed impacts and limited martian source area.

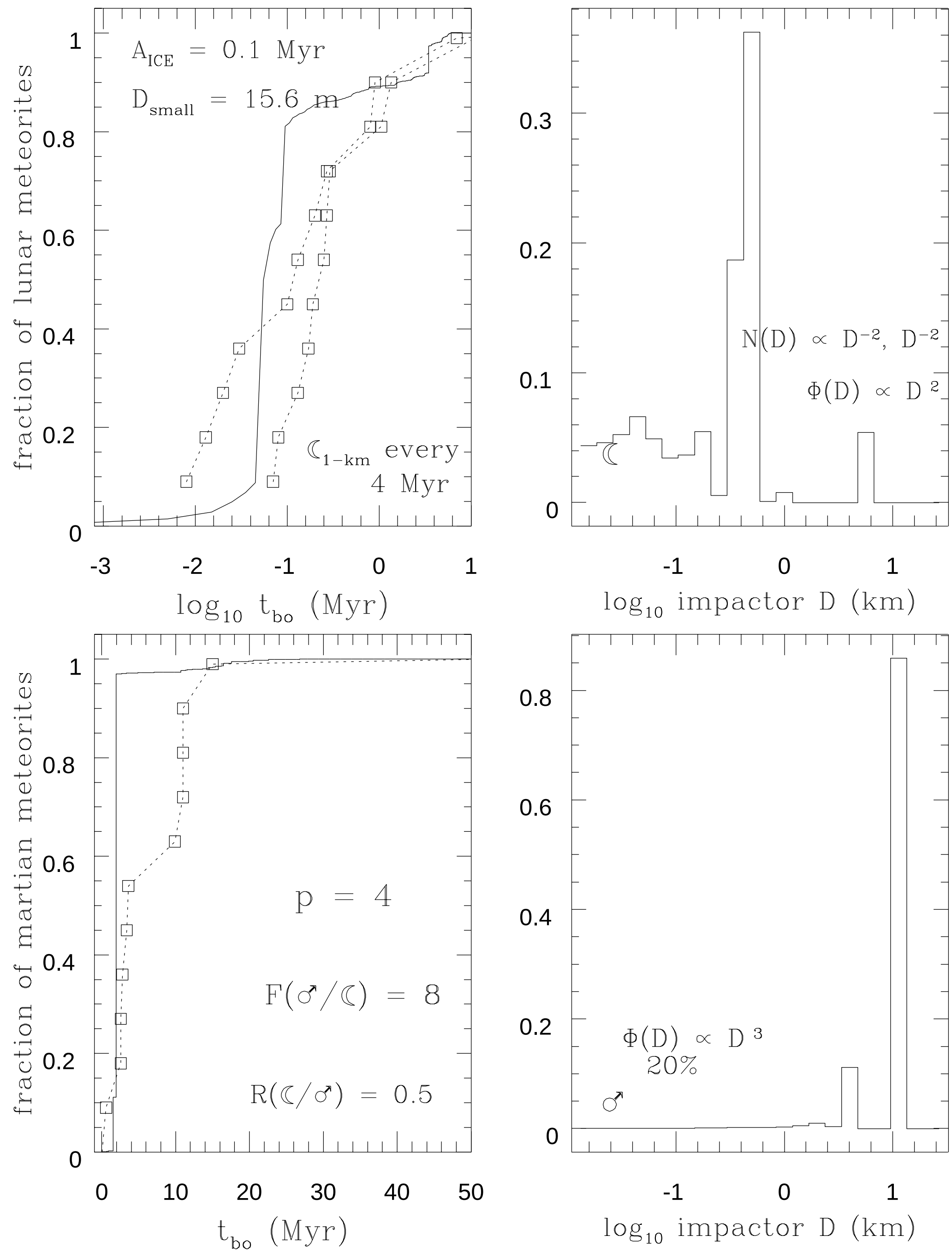

Figure 6.21 A sample delivery history for lunar and martian meteorites. This is part of a series of ten simulations (Figs. 6.14–6.23), all of which use the same parameters, intended to illustrate the importance of large stochastic impacts on the Moon and Mars. These simulations use randomly timed impacts and limited martian source area.

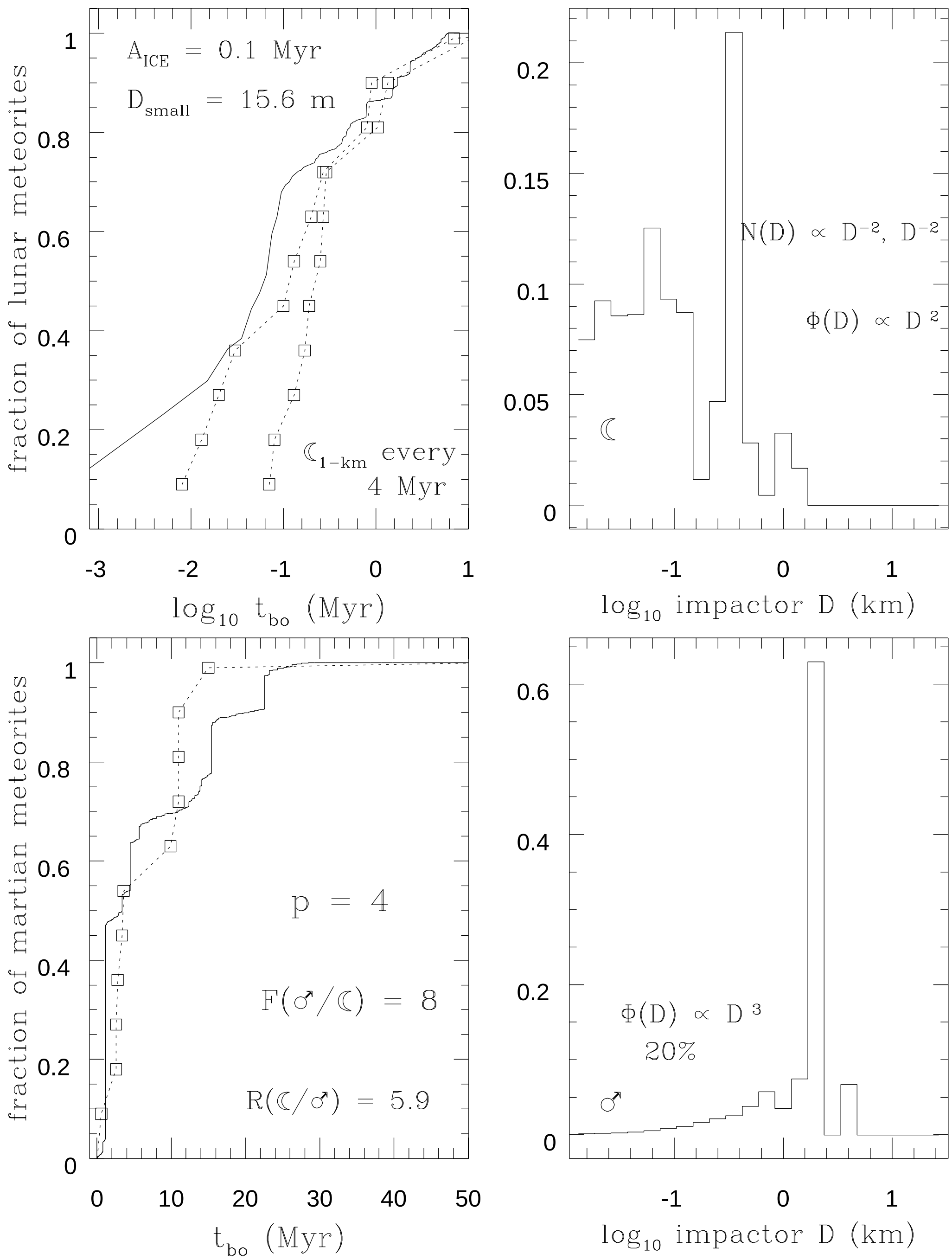

Figure 6.22 A sample delivery history for lunar and martian meteorites. This is part of a series of ten simulations (Figs. 6.14–6.23), all of which use the same parameters, intended to illustrate the importance of large stochastic impacts on the Moon and Mars. These simulations use randomly timed impacts and limited martian source area.

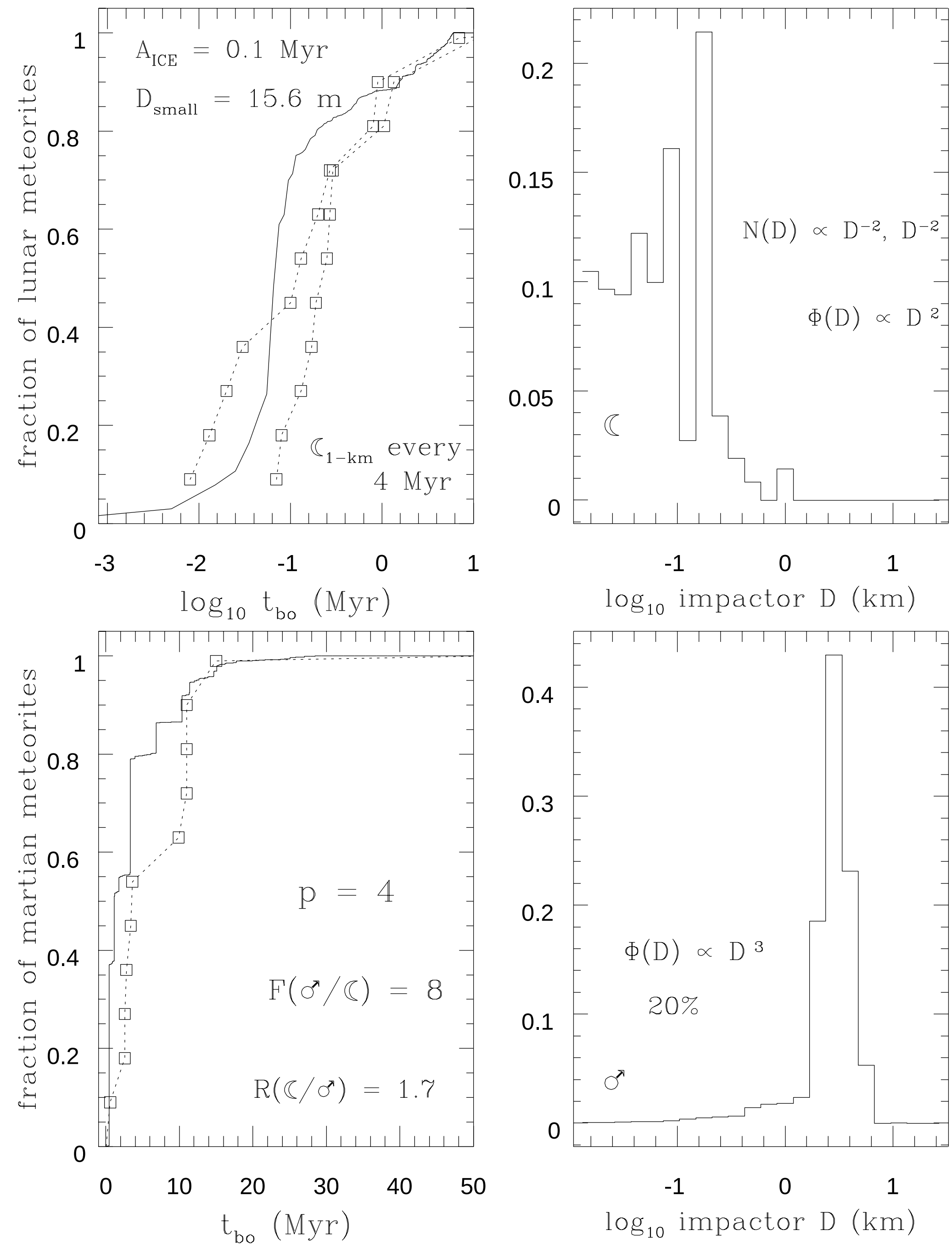

Figure 6.23 A sample delivery history for lunar and martian meteorites. This is part of a series of ten simulations (Figs. 6.14–6.23), all of which use the same parameters, intended to illustrate the importance of large stochastic impacts on the Moon and Mars. These simulations use randomly timed impacts and limited martian source area.

launched in a single impact. However, one could attempt to make a case for only three impacts being represented: ALH84001 15 Myr ago, the NCs about 10 Myr ago, and all the shergottites about 3 Myr ago. This scenario would require the 10-Myr impact to overlap both N and C source terrains. It would also require the 3-Myr impact to launch both lherzolitic and basaltic lithologies *and* to produce very large meteoroids in order to shield at least EET79001 for 2 Myr (and perhaps the basaltic shergottites for $\approx$1 Myr). Such a hypothesis eases the problem involving the young source terrains, for then only 2 of 3 impacts are into the young regions instead of needing 5 of 6 to be so. This hypothesis thus demands a very large 3-Myr impact, which is plausible as indicated by the variety of possible histories seen in Figs. 6.14–6.23.

The model presented in this chapter is unable, given the amount of data, to distinguish between the likelihood of having 3 versus 6 martian impacts represented, although I prefer the latter option. It is unlikely that EET79001 is a shielded collisional fragment from a 2.5-Myr event *and* that the lherzolitic shergottites are from a separate impact event; I believe it to be all or nothing (*i.e.,* all the shergottites were launched in a single event with partial shielding, or three events occurred).

These questions are likely unanswerable at present. In fact, it may be fair to say that they may never be answered.

6.4 The big picture

I now summarize the general theory, and put forward a hypothesis that resolves the puzzles presented in the introduction regarding the lunar and martian meteorites. The data are not yet plentiful enough to constrain these conjectures with certainty; the following general picture does explain the available facts, but perhaps not uniquely.

The lunar and martian surfaces are bombarded by a set of impactors whose diameters fall off as D^{-2}. These impactors launch meteoroids by stress-wave interference, from a spall zone of depth $z \sim Dc_L/U$. In the Moon's surface layers the sound speed $c_L \simeq$100 m/s so that impactors of tens to hundreds of meters in diameter (striking with $U \sim$10 km/s), can only loft into space a thin spall layer of a few meters depth. Impactors large enough to tunnel below the lunar regolith do not tend to strike often enough be represented in the present-day meteorite sample. In contrast, such large impactors ($D \gtrsim 1$ km) do hit Mars on time scales less than 10 Myr, where these impactors launch ejecta in greater quantity and from greater depth.

Once ejected into space, 40$\pm$15% of lunar meteoroids find their way to Earth, whereas 4$\pm$2% of martian meteoroids do. The lunar meteorites mostly fall in a fairly brief burst immediately after launch; the majority arrive in 100,000 years, with only a relatively slow trickle continuing after a million years. In contrast, the martian meteorites are delivered in an almost steady stream over about 10–20 Myr, where the upper limit is caused by a combination of collisional destruction and orbital loss. On this basis alone we expect the large impacts either represented in the ice sheet or recovered as falls to be solely martian. A slightly oversimplified statement would be that the lunar meteorites we have are launched by 10–300 m impactors that strike the Moon every tens of thousands to few hundred thousand years, while the martian meteorites we have were launched by 1–10 km impactors that are striking Mars every 1–10 Myr.

I propose the following resolution of the 5 puzzles listed on p. 7, which I present in the reverse of the order given there.

(5) The martian age spectrum terminates at $\approx$15 Myr because Sun-grazing and collisional destruction eliminate the meteoroid population in space on this time scale.

(4) The prevalence of geologically young rocks amongst the martian meteorites is either a statistical fluke, due to pervasive weathering which makes the older regions of Mars unsuitable for meteorite launch (as suggested by Warren 1994), or caused by martian atmospheric effects. This is probably the most important unresolved puzzle.

(3) The lack of shallow-provenance martian meteorites comes about simply because the upper 3 m of surface material comprises a tiny fraction of the very thick spall layers thrown off in the large impacts that are responsible for launching martian meteoroids.

(2) The martian meteorites have larger mean masses because they are produced by larger impactors. The martian atmosphere may play some role in preventing smaller meteoroids from escaping.

(1) The equal numbers of lunar and martian meteorites is a consequence of the finite age of the ice sheet combined with transfer dynamics that today deliver few meteorites from ancient lunar impacts, but a reasonable flux from larger ancient martian impacts.

Appendix A

Lunar Gravity Assists

This appendix discusses gravity assists in the context of a restricted three-body problem (Earth-Moon-test particle), and explores an interesting phenomenon of possibly great utility to astrodynamics. I will not rigorously explore the phenomenon, but instead will describe it and present some simple arguments which provide some intuitive insight. This appendix assumes that the reader is familiar with the material presented in Sec. 3.2.1.

A.1 Motivation

At the start of the heliocentric stage of the lunar simulations with $v_{ej} = 2.4$ km/s, a small clump of particles (see Fig. 3.6) with common orbital elements ($a \simeq 1.05$ AU, $e \simeq 0.045$) was noticed. Such a clump is surprising since particles are typically liberated from the Earth-Moon system via gravitational scatterings by the Moon; random encounter geometries occurring at random times should evenly scatter particles both interior and exterior to the Earth's orbit. The particles in this clump were identified and their orbital histories tracked. Very surprisingly, these particles did not complete a single geocentric orbit, but escaped directly to heliocentric orbit even though they were launched only barely faster than the lunar escape velocity! What is happening here?

A.2 Energy arguments

Consider a small object launched from an isolated massive body. Based on elementary principles, the escape velocity $v_{\rm esc}$ from a body of mass M and surface radius R_s is

$$v_{\rm esc} = \sqrt{\frac{2GM}{R_s}}\ , \tag{A.1}$$

where G is the gravitational constant. For the Moon, $v_{\rm esc} = 2.38$ km/s. A body launched with velocity $v_l < v_{\rm esc}$ will only reach a height $R_{\rm max}$ which satisfies

$$\frac{1}{R_s} - \frac{1}{R_{\rm max}} = \frac{v_l^2}{2GM} , \tag{A.2}$$

before falling back to the surface.

The Moon is, of course, not isolated. Once a particle recedes a sufficient distance it is clear that the gravitational pull of the Earth will become more important than that of the Moon. There are various estimates of this distance (Greenberg *et al.* 1991); I adopt that of the Hill sphere

$$R_H = a_{\rm orb} \left(\frac{\mu}{3}\right)^{1/3} \simeq 35 R_s \simeq 9.6 R_\oplus , \tag{A.3}$$

where $a_{\rm orb}$ is the Moon's orbital radius ($\simeq 60 R_\oplus$), and $\mu \simeq 1/81$ is the ratio of the Moon's mass to that of the Earth. Therefore a quantity of greater interest than the Moon's 'escape' velocity is the launch speed v_* necessary for a particle to reach the lunar Hill sphere. Since, due to the $1/r$ potential, most of the gravitational work is done near the Moon, v_* is only slightly smaller than $v_{\rm esc}$; in fact $v_* = 2.35$ km/s. This is confirmed in an additional set of launch simulations (Table A.1) identical to those performed in Sec. 3.2.1, except that the launch velocities were all near the lunar escape speed. For $v_l < v_*$, all the particles fall back to the lunar surface without escaping to geocentric orbit. Above v_*, an increasing fraction of particles escape the Moon's gravitational pull, although many of these subsequently re-impact the parent object. Eventually more than 80% of the particles escape to heliocentric orbit (in concordance with the earlier results of Chap. 3), mostly via repeated gravity assists by the Moon.

A.3 Gravity assists

This section will develop the background of gravity-assist trajectories in the context of a patched-conic approach. I will use one of the computed trajectories from the simulations just discussed for illustrative purposes.

Fig. A.1 shows the orbital path taken by the particle escaping to the Earth's Hill sphere in the shortest time (about 8 months) from the 2.35 km/s simulation. The particle follows the lunar orbit closely for the first month. Close approaches appear as cusps in the trajectory. In fact, the particle is in a temporary capture orbit around the Moon, as shown in Fig. A.2. Almost exactly one month after launch (*i.e.,* near the same geocentric coordinates where the launch took place) a close encounter occurs which ejects the particle from lunar orbit and alters the path to one with orbital semi-major axis considerably smaller than the Moon's, which the particle follows for seven revolutions (Fig. A.1). The Moon then draws

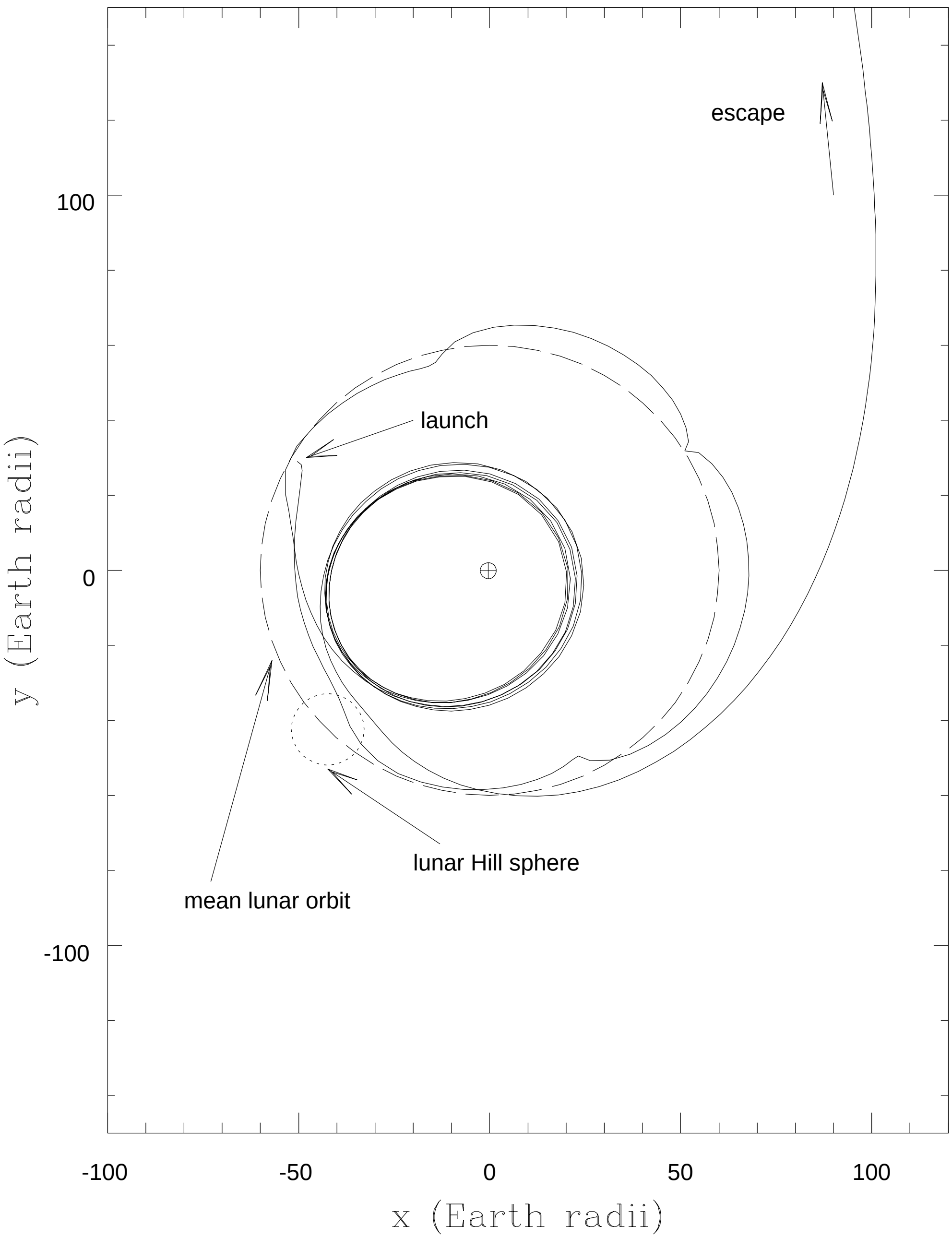

Figure A.1 The path taken by a particle escaping the Earth-Moon system via a series of gravity assists. The relative geocentric position is shown, in an non-rotating frame centered on the planet and projected onto the ecliptic plane. The dashed line shows the mean lunar orbit (at $60R_\oplus$). Recall that the Moon's Hill sphere (shown) is $\approx$10 $R_\oplus$. The launch does not occur at the distance of the mean lunar orbit due to the Moon's eccentricity. See text for description.

Table A.1 For each geocentric-stage simulation the table lists the total number N of particles launched (18 particles per impact site), the percentage Esc of particles that escape to heliocentric space, and the percentages that impact the Earth ($\oplus$) and Moon (M), as a function of the lunar launch speed v_l. To reach the lunar Hill sphere requires v_l=2.35 km/s.

Geocentric Stage Results				
v_l (km/s)	N	% Esc	% $\oplus$	% M
2.33	360	0.0	0.0	100.0
2.34	360	0.0	0.0	100.0
2.35	360	2.8	0.0	97.2
2.36	360	31.7	1.9	66.4
2.37	360	65.8	2.2	32.0
2.38	360	81.9	2.5	15.6
2.39	360	84.7	3.1	12.2

the particle off this orbit and flings it away at sufficient speed that it escapes the Earth-Moon system entirely. This second encounter is also seen in Fig. A.2 (marked 'second entry' and 'second escape').

It is clear that the route to escape in this case is that discussed in Sec. 3.2.1, namely, during close approaches to the Moon, the particle's geocentric velocity vector is modified. The most common way to conceptualize this is by a 'patched conic' approach (see D'Amario *et al.* 1992 for example). This method views the orbits before and after the encounter as unperturbed Kepler orbits about the Earth, and during the encounter as a hyperbolic orbit past the Moon. However, *this is an idealization*: Fig. A.2 illustrates that, during its second entry into the lunar Hill sphere, the particle's orbit never seems to be particularly well represented by a lunocentric hyperbola. This is because the particle is never much closer to the Moon than $R_H/2$ and therefore a two-body problem centered on the Moon is not a particularly good representation of the dynamics. However, we can still use the usual patched-conic vector-addition picture (Fig. A.3) to understand how the final close encounter resulted in a gravity-assist that produced escape velocity. From Figs. A.1 and A.2, it can be seen that the Moon catches up to the test particle just before the particle enters the lunar Hill sphere (the Moon is moving in the positive x direction during the fly-by). Therefore, as shown schematically in Fig. A.3, while inbound to the encounter the particle's geocentric velocity is smaller than the Moon's, and in the lunar frame $\vec{\boldsymbol{v}}_{\boldsymbol{in}}$ is moving opposite to the apex of the lunar motion. The close encounter reverses the relative velocity vector to $\vec{\boldsymbol{v}}_{\boldsymbol{out}}$ and so, when the vector addition is performed, the particle has rather substantially increased the magnitude of its geocentric speed (from $\vec{\boldsymbol{V}}_{\boldsymbol{in}}$ to

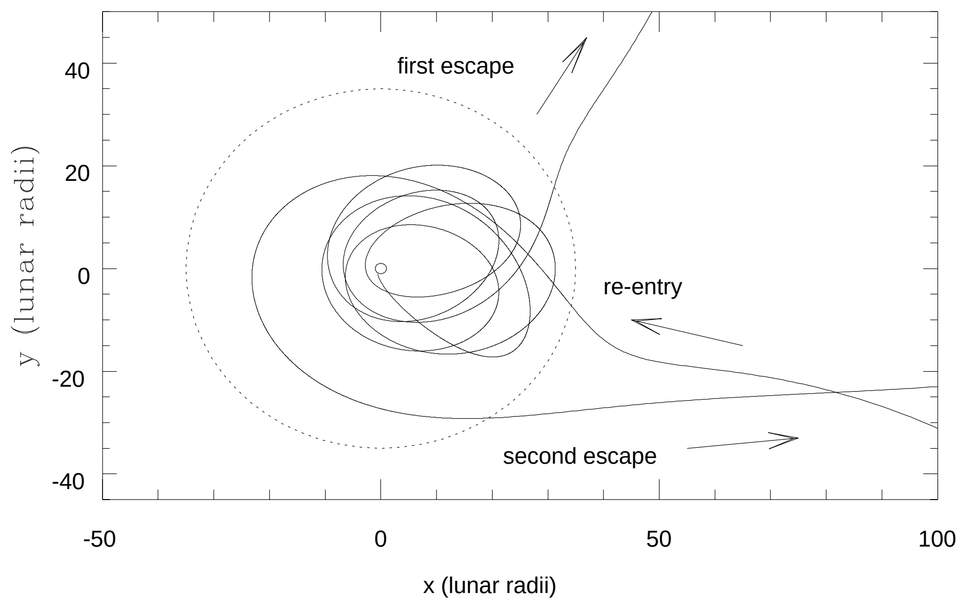

Figure A.2 The lunocentric trajectory of the particle shown in Fig. A.1, in the same non-rotating frame projected onto the ecliptic plane. The Moon (to scale) is indicated, as well as the approximate location of its Hill sphere (dotted circle). After launch the particle remains in temporary orbit until escape. It returns later for a hyperbolic encounter which ejects it from the geocentric orbit. See text for discussion.

$\vec{V}_{out}$). In this case the magnitude of the increase is enough to make the particle unbound with respect to the Earth.

A.4 The three- and four-body problems

The type of gravity assist just discussed was the picture in the author's mind of how all escapes from the Earth-Moon system occur, at least when particles are launched off the Moon with a residual velocity (Fig. 3.3) below geocentric escape speed. That is, after escaping the Moon the particle's geocentric orbit will be modified repeatedly by close approaches until one of these fortuitously flings the particle 'off to infinity'. (It turns out that the example just discussed is extremely atypical in that only a single re-encounter with the Moon was necessary; this particle was selected as being the fastest escaping meteoroid.) However, it turns out that a gravity assist is *not* the method of escape that produces the group of particles that make up the above-mentioned clump in Fig. 3.6 in the original $v_l = 2.4$ km/s simulation.

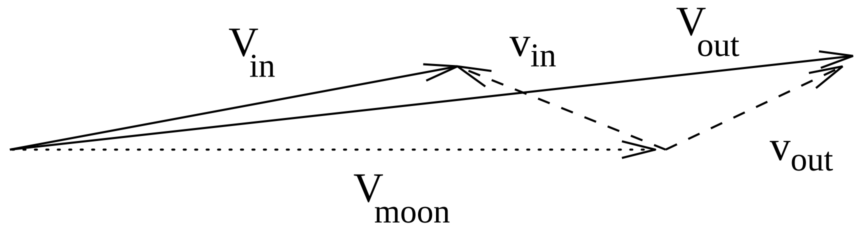

Figure A.3 A vector-addition diagram representing a patched-conic gravity-assist. This is a schematic representation of the final encounter pictured in Figs. A.1 and A.2. Geocentric velocities are indicated by uppercase letters and lunocentric velocities by lower case letters.

Snapshots of the full geocentric simulation over the first 3 months of time are shown in Figs. A.4 and A.5. Since the simulation consists of 20 launch events ejecting 18 particles each in a cone, the Moon appears to eject particles in an expanding shell (all launch directions being equally likely). After a few days this shell acquires a noticeable asymmetry, which becomes more pronounced after 0.2 months. This asymmetry occurs because some particles have had their orbital energies reduced by the Moon's gravity; thus they have smaller semimajor axes and correspondingly shorter orbital periods. Such particles therefore lead the Moon. Many of these same particles have acquired substantial geocentric eccentricities, producing perigees of $\simeq$20 $R_\oplus$, as seen in Fig. A.4c and d. In contrast, other particles have gained orbital energy from the Moon, acquiring larger semimajor axes, and therefore lag the Moon in longitude. However, the most interesting aspect of these figures is the devlopment of a 'lobe' or 'petal' of these lagging particles (containing about 10–15% of the total), seen clearly in the lower right quadrant of panels (e)–(h), which simply expands away from the Earth, never to return. This cluster becomes the clump of Fig. 3.6; all of these particles exit the Earth's heliocentric Hill sphere (of about 230 $R_\oplus$) in short order (about a month). The remaining particles circle the planet, continuing in Earth orbit until they hit a primary or are ejected by subsequent lunar gravity assists.

In the remainder of this appendix I will attempt to develop an intuitive understanding of the dynamics in terms of simple energy arguments and 2-body reasoning. These discussions will not be rigorously correct, because the real dynamics are closer to 4-body problem (or at least, two sequential restricted 3-body problems). A complete understading of this phenomenon is probably equivalent to another thesis.

Let us examine two of these quickly escaping trajectories more carefully (Fig. A.6). The particles simply leave the Moon on hyperbolic trajectories, and continue smoothly out to the Earth's Hill sphere, with no temporary capture

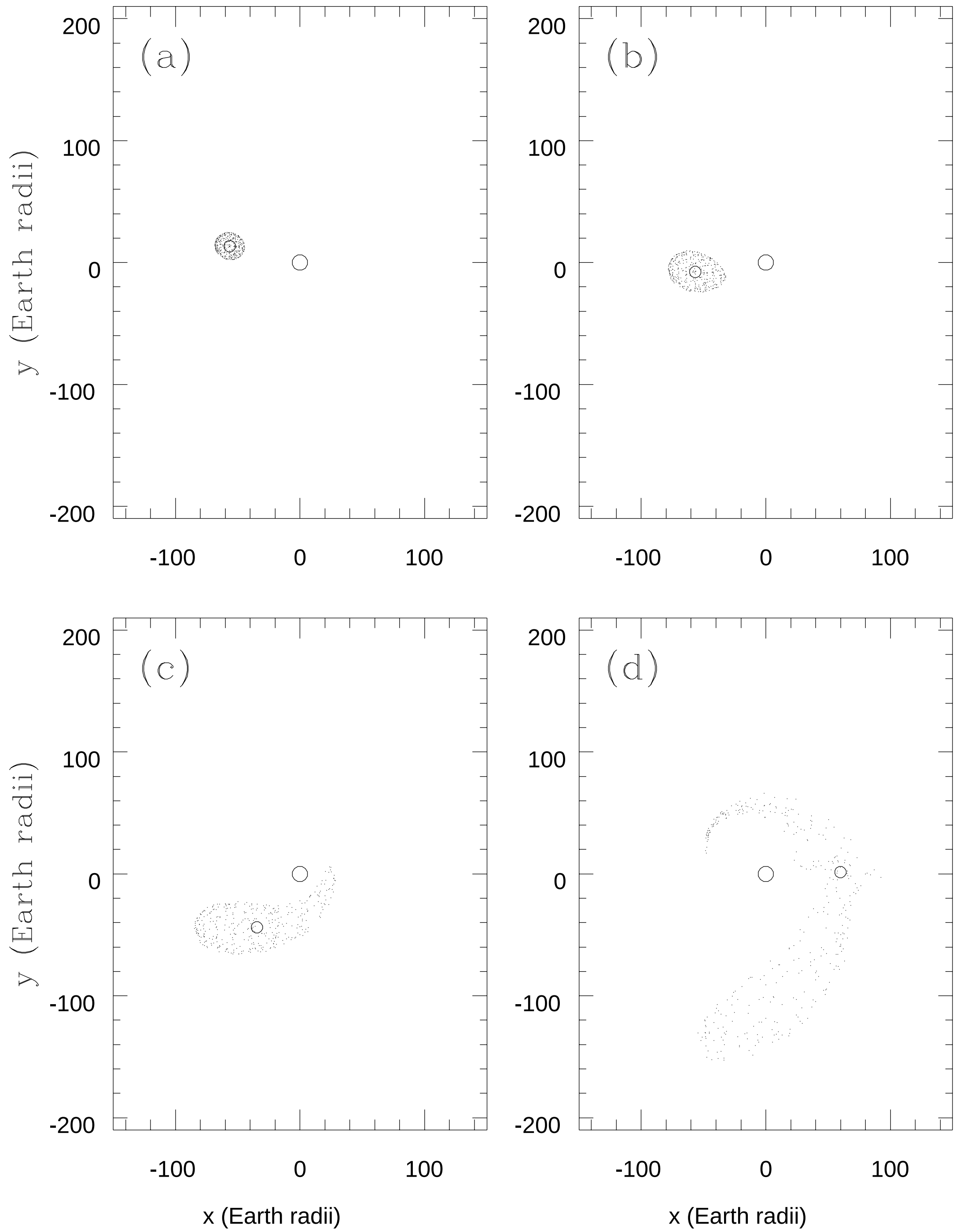

Figure A.4 Geocentric snapshots of the evolution of the swarm of lunar ejecta in a v_l=2.4 km/s simulation. The positions of all surviving test particles are projected onto the non-rotating ecliptic plane. The Earth (at 0,0) and Moon are indicated by the open circles (not to scale). The snapshots are taken at elapsed times of approximately (a) 0.05 months, (b) 0.1 months, (c) 0.2 months, and (d) 0.5 months.

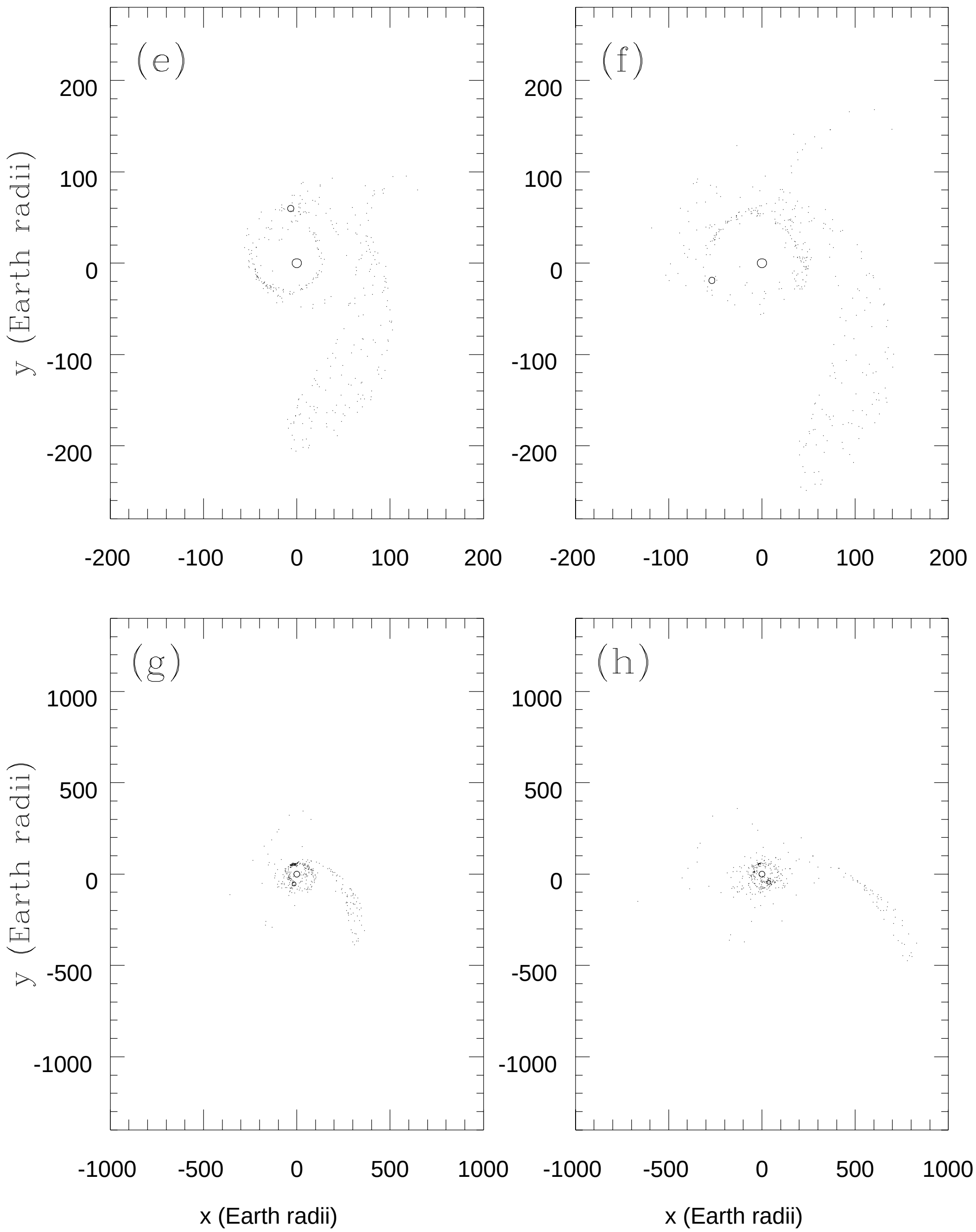

Figure A.5 Geocentric snapshots of the evolution of the swarm of lunar ejecta in a v_l=2.4 km/s simulation. The positions of all surviving test particles are projected onto the ecliptic plane. The Earth (at 0,0) and Moon are indicated by the open circles (not to scale). Note the scale of the figures change. The snapshots are shown at elapsed times of approximately (e) 0.75 months, (f) 1 months, (g) 2 months, and (h) 3 months.

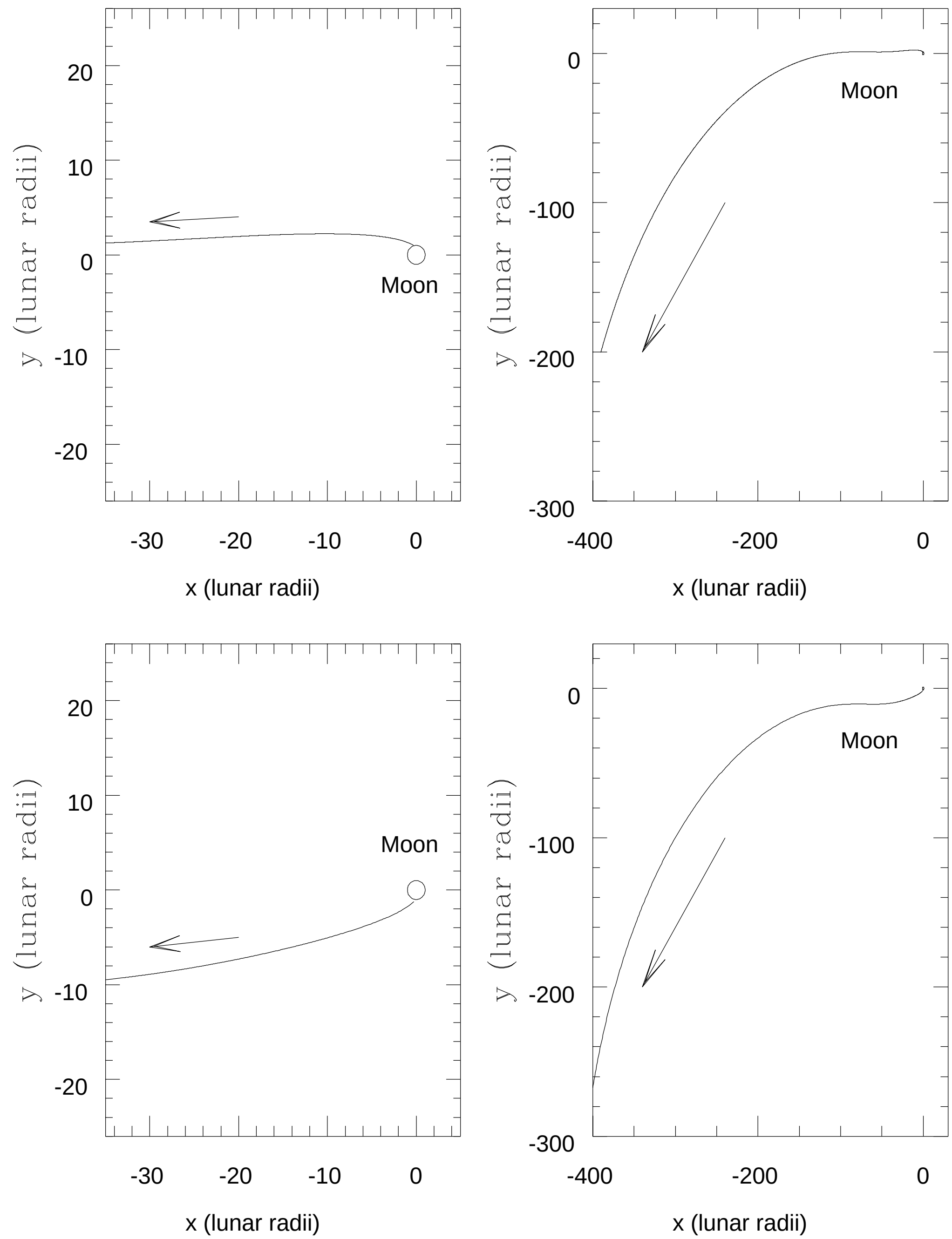

Figure A.6 The escape trajectories of two fast escapers, in lunocentric coordinates (non-rotating frame). The Moon is shown (to scale) in each case. Left panels: the hyperbolic ejection out to the lunar Hill sphere (requiring about a day). Right panels: The trajectory out to about one-half of the Earth's Hill sphere.

or second lunar encounter involved. In terms of a patched-conic picture of the dynamics, the motion could be explained as follows. In the lunar frame, the particle's specific orbital energy (*i.e.,* per unit mass) is

$$E_L = \frac{1}{2}v_L^2 - \frac{GM_m}{r_L} \tag{A.4}$$

where the L subscripts indicate quantities referred to the Moon, and so r_L is the lunar distance of the particle. If the particle is launched at v_l=2.4 km/s, then by the time the particle reaches the lunar Hill sphere (at $\simeq$ 35 lunar radii), its residual speed should be

$$\begin{aligned} v_r^2 &= v_l^2 + 2\frac{GM_m}{R_m}(\frac{1}{35} - 1) \\ &\simeq 500\text{m/s} . \end{aligned}$$

If this residual velocity were fortuitously added to the lunar velocity vector ($V_m \simeq$ 1 km/s) as discussed in conjunction with Fig. 3.3), then temporarily the particle would have the escape speed necessary to depart geocentric orbit (*i.e.,* about $\sqrt{2} \times 1$ km/s at the lunar distance). However, just reaching the lunar Hill sphere is really not sufficient since the particle will still have to do work against the Moon's gravitational field to get to 'infinity'. At infinity the residual velocity is only $\simeq$300 m/s (Eq. 3.2), and thus the particle should not have enough energy to escape geocentric orbit.

The discussion just presented is wrong because the physics cannot be represented as a superposition of two 2-body problems (*i.e.,* escape from the Moon followed by escape from Earth). Instead, we need to consider a 4-body problem. Since there is no relevant theory for the dynamics of these particles a 4-body context, I shall continue in the previous vein.

A better way to discuss the problem is to examine a particle's orbital energy in the *geocentric* frame, viewing the Moon and Sun as objects which do work on the particle. That is, in order to be on a hyperbolic geocentric orbit, the particle must reach a positive specific orbital energy in the expression

$$E_g = \frac{1}{2}v_g^2 - \frac{GM_\oplus}{R_g} , \tag{A.5}$$

where the g subscripts refer to geocentric quantities. Of course, this is still using 2-body reasoning, but it should be valid within the Earth's Hill sphere as long as the object is more than several lunar Hill-sphere radii from the Moon (so that the latter's influence on the particle's geocentric velocity is negligible). Expression (A.5) allows us to easily calculate that the Moon has a specific orbital energy of -0.538 MJ/kg (bound orbits have $E_g < 0$). Thus this much work per unit masss must be performed in the geocentric frame on an escaping particle in order to unbind it from Earth orbit.

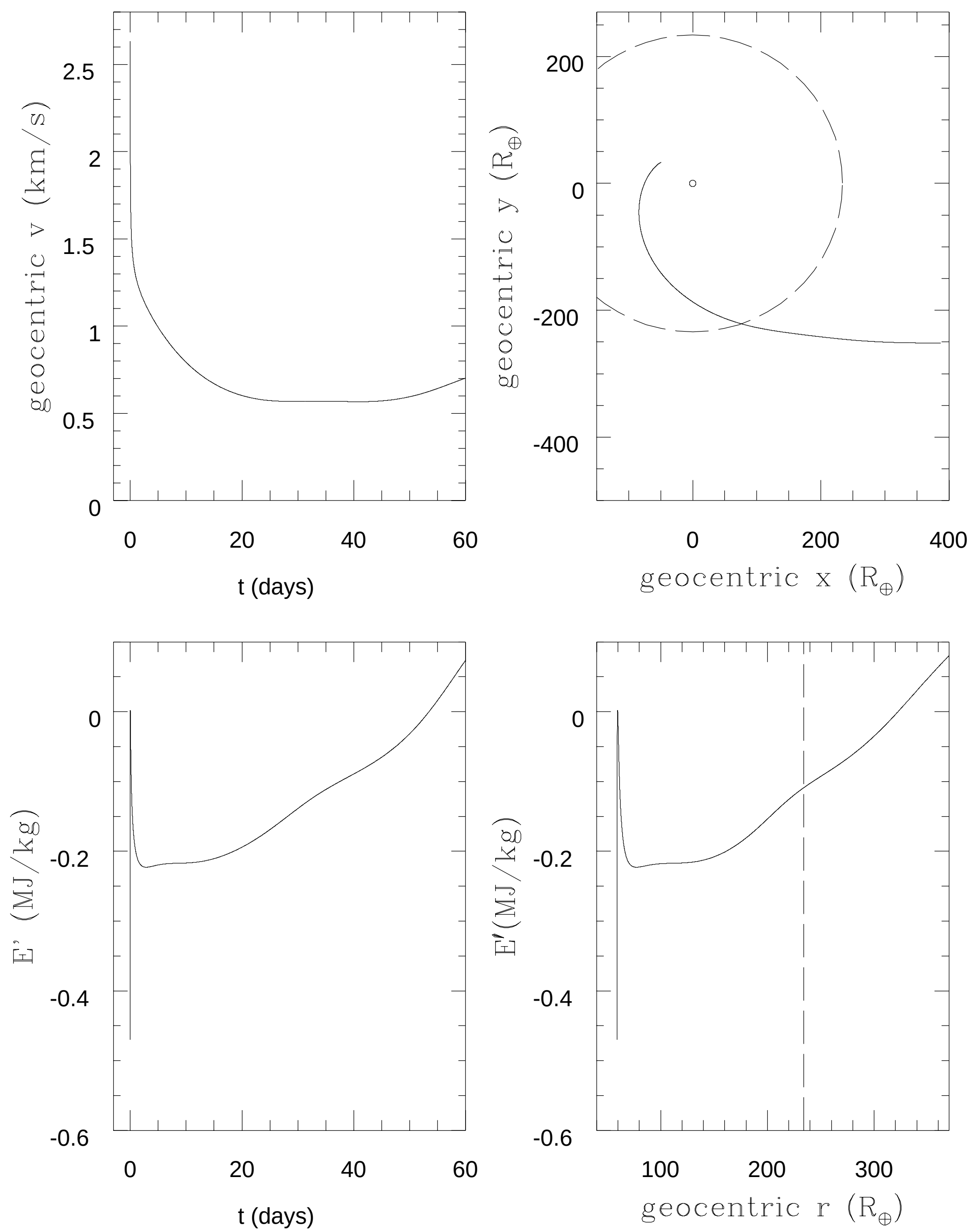

Figure A.7 The history of a fast escaper. The dashed lines mark the Earth's Hill sphere. In the upper right panel the orbit is shown projected onto a non-rotating coordinate system in the ecliptic plane with the Earth at the origin; during this particular escape the Sun occupies a point near the positive y-axis (at $y \simeq 23,000 R_{\oplus}$). See the text for discussion.

The energy history for one of the rapidly escaping particles is shown in Fig. A.7, where instead of plotting E_g, I have shown

$$E' = \frac{1}{2}v_g^2 - \frac{GM_\oplus}{R_g} - \frac{GM_m}{R_l} \; . \tag{A.6}$$

E' is more meaningful since, at the instant of launch, the geocentric velocity is very large; this is because $v_l = 2.4$ km/s, which translates into a geocentric velocity of $v_g \simeq 2.6$ km/s for this particle (upper left panel). The particle would thus be immediately unbound if the Moon had no mass. Of course, most of this kinetic energy is lost escaping the Moon's gravity-well; this is heuristically corrected for by the presence of the lunar term in Eq. A.6. Far from the Moon $E' \to E_g$.

The lower left panel of Fig. A.7 shows the energy history. In the few days it takes the particle to leave the Moon's vicinity, E' first increases rapidly, and then drops again. The peak, where the particle appears temporarily unbound ($E' > 0$), occurs near the lunar Hill sphere. However, by the time the particle escapes to a few lunar Hill-sphere radii the Moon's influence is negligible, and the geocentric energy levels off to a constant (bound) value of $\simeq -0.2$ MJ/kg. The apogee of this Keplerian orbit would be at $\simeq 313R_\oplus$, which is outside the Earth's Hill sphere of $\simeq 234R_\oplus$. Unsurprisingly, as this particle approaches the Earth's Hill sphere (upper right plot), the Sun's influence manifests itself; orbital energy increases starting at 2/3 R_H. After leaving the Earth's Hill sphere, the Sun's continuing influence unbinds the particle from Earth orbit, and the particle escapes to an independent heliocentric orbit.

A.5 Implications

The conclusion that can be drawn from this study is rather dramatic: a judiciously chosen launch at the lunar escape velocity can not only escape the Moon, but geocentric orbit as well! This can be done in a single stage; no second lunar encounter is necessary to take advantage of a gravity assist. Escape to the Earth's Hill sphere required approximately one month.

This method is more energy efficient and faster than might be expected. Using 2-body reasoning, one might think that enough fuel is needed to apply a Δv of 2.38 km/s to escape the lunar gravity field, and then another $(\sqrt{2}-1)$ times the lunar orbital velocity (400 m/s) to achieve the transition from a circular geocentric orbit to a hyperbolic escape trajectory. In fact, the extra 400 m/s of Δv is not necessary. The trajectory is also the fastest, since escape cannot occur in less than a month if a second lunar close encounter is required to obtain a gravity assist.

The dynamics discussed here is similar to the 4-body dynamics described by Belbruno and Miller (1993), who constructed energy-optimal transfer trajectories.

I have not attempted to discover how to specify the initial conditions which belong to the escaping set; I suspect that this will be a complex problem. Such a calculation would be of interest since it would provide a low-fuel method to launch spacecraft to heliocentric space from the lunar surface.

Appendix B

The Numerical Method

The heliocentric simulations of this thesis were carried out with a Regularized Mixed Variable Symplectic (RMVS) algorithm. This method allows for the efficient numerical integration of a large number of test particles that suffer recurring close approaches with planets. The code was not written as part of this thesis research, although some minor modifications were made and the code was rigorously tested. The RMVS algorithm was developed as part of a software package called SWIFT (Levison and Duncan 1994) that implements and improves the mixed-variable symplectic method of Wisdom and Holman (1991).

B.1 Mixed-variable symplectic (MVS) integrators

These codes are outgrowths of the intense work that has gone into the study of efficient methods for integrating the equations of motion of Hamiltonian systems in the last two decades (Ruth 1983, Forest and Ruth 1990, Channell and Scovel 1990, Yoshida 1993). The differential equations of motion derived for a Hamiltonian system have special properties. The goal is to take advantage of this 'symplectic' structure in the phase space of these systems; for example, as particles move they must remain on a hypersurface of constant energy. Most numerical integration algorithms (*e.g.,* Runge-Kutta) do not make allowances for this special structure, and thus the trajectories drift away from surfaces representing integrals of the motion (for example, the energy or angular momenta may change). Symplectic integrators are designed to conserve these invariants; much more complete discussions are given in Gladman *et al.* (1991) and Yoshida (1993).

The basic algorithm is to break the problem into exactly soluble pieces, and then to solve them alternately in such a fashion as to match as closely as possible the original system. Until 1991 the two pieces of the Hamiltonian used were the kinetic and potential energy functions, either of which by itself describes a trivially integrable system (see Gladman *et al.* 1991).

A further improvement was provided by Wisdom and Holman (1991), who created a symplectic integrator that took explicit advantage of the fact that the Kepler problem is exactly soluble. These authors alternate between solving the Kepler problem and the interaction Hamiltonian of the system. That is, each test particle moves along a Kepler ellipse, which is then perturbed by the remaining, non-Keplerian forces. The Kepler problem is solved efficiently and exactly by using the Gauss f and g functions (Danby 1988). The interaction Hamiltonian contains the forces from all the interactions between the particles (excepting the Sun), and is trivially integrable if expressed in the Jacobi coordinates for the N-body problem (Wisdom and Holman 1991). Because two sets of coordinates are simultaneously used in the solution, the method is referred to as 'Mixed-Variable Symplectic' (MVS).

The code is structured in two pieces. The N_p planets are integrated in an N-body fashion; that is, each planet feels the gravitional perturbations of all the others. The number of force calculations necessary per time step scales as N_p^2. Simultaneously, the forces exerted by these planets on a large number of test particles is calculated and the test particle orbits are also evolved. The n test particles do not interact with each other or with the planets, and thus the number of force calculations scales only linearly with n. Therefore the CPU time t required to perform a simulation for a simulated duration T scales as $t \propto T N_p^2 n$.

In this algorithm the non-Keplerian forces must be small in order for the integrator to remain efficient. If the test particles were to undergo a close approach to a planet, the truncation error of the algorithm will increase. Decreasing the time step of a numerical integrator is a common way of dealing with such a problem. Unfortunately, changing the time step in a symplectic integrator degrades the integral conservation properties (Gladman *et al.* 1991), and thus the MVS algorithm is best applied to systems that do not undergo close approaches (*e.g.*, studies of dynamical stability for orbits that are not planet-crossing).

B.2 The regularized MVS (RMVS) integrator

Since many interesting problems involve planet-crossing orbits, it was important to attempt to extend the MVS algorithm to allow for test particles to have repeated close encounters. RMVS (Levison and Duncan 1994) uses an adaptive Hamiltonian that in some sense 'regularizes' close approaches (producing the 'R' in the acronym). The idea is simple: when a particle approaches a planet, instead of treating the problem as a Kepler orbit about the Sun perturbed by the planet, the orbit is considered to be around the planet and perturbed by the Sun. In the intermediate regime (near the planetary Hill-sphere) the time step is simply lowered. Although this destroys the exact symplectic nature of the algorithm in a rigorous sense, extensive testing has shown (Levison and Duncan 1994, Michel and Valsecchi 1996) that the statistical results of code are correct.

The term 'regularized' should be applied to this integrator only in an intuitive sense. Regularization is a mathematical process that removes a singularity from a differential equation. Regularizing the Kepler problem (or the N-body problem) has been a method of dealing with the force singularity at $r = 0$ (see Stiefel and Schiefele 1971). In this process the Kepler problem is turned into the harmonic oscillator by coordinate transformations; the singularity is thus eliminated from the equations. In the RMVS algorithm, the singularity is effectively removed from the problem by switching to a Kepler problem centered on the planet. Using the exact solution to the problem provided by the Gauss f and g functions then allows arbitrarily-close approaches to be computed efficiently.

The RMVS code is thus able to deal with large numbers of test particles moving in a system with multiple planets. Objects not close to a planet are integrated with the MVS algorithm. Particles within 3 Hill-sphere radii of a planet are temporarily treated differently than the rest of the bodies; after their close encounter is over they are returned to the swarm of other test particles. Only particles that enter a planetary Hill-sphere have their Hamiltonian recast so that the planet is the central object. Upon emerging from the Hill sphere, the particles are carefully re-synchronized with the rest of the integration.

This algorithm is more efficient computationally (by an order of magnitude) than all other methods that this author is aware of. Several hundred planet-crossing particles can be integrated in the field of 7 planets at a rate of order 500,000 years per day of CPU time on a very fast dedicated workstation. All told, the lunar simulations required about 5 months of actual computer time on a Hewlett Packard 715 with a 75 MHz clock speed. The martian simulations required somewhat more time, and were performed on a variety of computer platforms.

References

Arnold, J.R. 1965. The origin of meteorites as small bodies: II. The model. *Ap. J.* **141**, 1536-1547.

Ash, R.D., S.F. Knott, and G. Turner 1996. A 4-Gyr shock age for a martian meteorite and implications for the cratering history of Mars. *Nature* **380**, 57-59.

Bailey, M.E., J.E. Chambers, and G. Hahn 1992. Origin of sungrazers: A frequent cometary end-state. *Astron. Astrophys.* **257**, 315-322.

Bandermann, L.W., and S.F. Singer. 1973. Calculation of meteoroid impacts on Moon and Earth. *Icarus* **19**, 108-113.

Barnes, V.E. 1990. Tektite research 1936-1990. *Meteoritics* **25**, 149-159.

Belbruno, E.A. and J.K. Miller 1993. Sun-perturbed Earth-to-Moon transfers with ballistic capture. *J. Guidance, Control, and Dynamics* **16**, 770–775.

Benoit, P.H., S. Symes, and D. Sears 1996. The irradiation and recent thermal history of QUE94281 and other lunar antarctic meteorites; Evidence for short transit times. *LPSC XXVII*, 101-102.

Bhandari, N., J.N. Goswami, R. Jha, D. Sengupta, and P.N. Shukla 1988. Cosmogenic effects in shergottites. *Geochim. Cosm. Acta* **50**, 1023-1030.

Bogard, D.D. 1995. Exposure age initiating events for martian meteorites: Three or four? *Lunar Planet. Sci. XXVI*, 143-144.

Bottke, W.F., M.C. Nolan, R. Greenberg, and R.A. Kolvoord 1994. Collisional lifetimes and impact statistics of near-Earth asteroids. In *Hazards Due to Comets & Asteroids* (T. Gehrels, ed.) University of Arizona Press: Tucson, pp. 337-357.

Bottke, W.F., M.C. Nolan, H.J. Melosh, A.M. Vickery, and R. Greenberg 1996. Origin of the Spacewatch small Earth-approaching asteroids. *Icarus*, in press.

Brouwer D., and G.M. Clemence 1961. *Methods of Celestial Mechanics.* Academic Press: New York.

Burke, J.G. 1986. *Cosmic Debris.* Univ. of California Press: Berekely.

Burns, J.A., P.L. Lamy, and S. Soter 1979. Radiation forces on small particles in the solar system. *Icarus* **40**, 1-48.

Burns, J.A., M.R. Showalter, and G.E. Morfill 1984. The ethereal rings of Jupiter and Saturn. In *Planetary Rings* (R. Greenberg and A. Brahic, eds.) Univ. of Arizona Press: Tucson, 200-272.

Caffee, M.W., J.N. Goswami, C.M. Hohenberg, and T.D. Swindle 1988. Irradiation records in meteorites. In *Meteorites and the Early Solar System* (J.F. Kerridge and M.S. Matthews, eds.) Univ. of Arizona Press: Tucson, 205–245.

Carrier, W.D. III, G.R. Olhoeft, and W. Mendell 1991. Physical properties of the lunar surface. In *Lunar Sourcebook, a User's Guide to the Moon.* (G.H. Heiken, D.T. Vaniman, and B.M. French, eds.) Cambridge Univ. Press, Cambridge, 475–594.

Cassidy, W.M., and L.A. Rancitelli 1982. Antarctic Meteorites. *Amer. Scientist* **70**, 156–64.

Cassidy, W.A., and I.M. Whillans 1990. *Workshop on Antarctic Meteorite Stranding Surfaces.* LPI Tech. Rpt. 90-03. Lunar and Planetary Institute, Houston. 103 pp.

Cassidy, W.M., R. Harvey, J. Schutt, G. Delisle, and K. Yanai 1992. The meteorite collection sites of Antarctica. *Meteoritics* **27**, 490-525.

Channell, P.J. and C. Scovel 1990. Symplectic integration of Hamiltonian systems. *Nonlinearity* **3**, 231–259.

Christensen, P.R., and H.J. Moore 1992. The martian surface layer. In *Mars* (H.H. Kieffer, B.M. Jakosky, C.W. Snyder, and M.S. Matthews, eds.) University of Arizona Press: Tucson, pp. 686-729.

Chyba, C. 1993. Explosions of small Spacewatch objects in the Earth's atmosphere. *Nature* **363**, 701-3.

Chyba, C.F., T.C. Owen, and W.-H. Ip 1994. Impact delivery of volatiles and organic molecules to Earth. In *Hazards Due to Comets & Asteroids* (T. Gehrels, ed.) University of Arizona Press: Tucson, pp. 9-58.

D'Amario, L.A., L.E. Bright, and A.A. Wolf 1992. Galileo trajectory design. In *The Galileo Mission* (C.T. Russell, ed.) Kluwer Academic: Boston, pp.23-78.

Danby, J.M.A. 1988 *Fundamentals of Celestial Mechanics (2nd Ed.)*, Willmann-Bell: Richmond.

Dermott, S.F., and C.D. Murray 1981. The dynamics of tadpole and horseshoe orbits. *Icarus* **48**, 1–11.

Dobrovolskis, A.R., and J.A. Burns 1980. Life near the Roche limit: Behavior of ejecta from satellites close to planets. *Icarus* **42**, 422–441.

Dohnanyi, J.S. 1977. Groups of micrometeoroids in the Earth-Moon system. *COSPAR Space Research XVII*, 623-626.

Dones, L., H. Levison, and M. Duncan 1996a. On the dynamical lifetimes of planet-crossing objects. In *Completing the Inventory of the Solar System* (T. W. Rettig, Ed.), Astronomical Society of the Pacific Conference Series: San Francisco, in press.

Dones, L., M. Duncan, B. Gladman, H. Levison, H.J. Melosh, and W. Tonks 1996b. A comparison of the results of Öpik-Arnold algorithms with direct numerical integrations. *Icarus*, submitted.

Englert, P., and W. Herr 1980. On the depth-dependent production of long-lived spallogenic ^{53}Mn in the St. Severin chondrite. *Earth Planet Sci. Lett.* **47**, 361–369.

Esposito, P.B. and 7 co-authors 1992. Gravity and topography. In *Mars* (H.H. Kieffer, B.M. Jakosky, C.W. Snyder, and M.S. Matthews, eds.) University of Arizona Press: Tucson, pp. 209–248.

Eugster, O. 1989. History of meteorites from the Moon collected in Antarctica. *Science* **245**, 1197–1202.

Eugster, O., and S. Niedermann 1988. Noble gases in lunar meteorites Yamato-82192 and -82193 and history of the meteorites from the Moon. *Earth Planet Sci. Lett.* **89**, 15–27.

Eugster, O., A. Weigel, and E. Poinau 1996. Two different ejection events for basaltic shergottites QUE94201, Zagami and Shergotty (2.6 Ma ago) and lherzolitic shergottites LLEW88516 and ALH77005 (3.5 Ma ago). *LPSC XXVII*, 345–346.

Farinella, P., Ch. Froeschlé, Cl. Froeschlé, R. Gonczi, G. Hahn, A. Morbidelli, and G.B. Valsecchi 1994. Asteroids falling into the Sun. *Nature* **371**, 314–317.

Forest, E. and R.D. Ruth 1990. Fourth-order symplectic integration. *Physica D* **43**, 105–117.

Frisch, W. 1992. Hypervelocity impact experiments with water ice targets. In *Proc. of the Workshop on Hypervelocity Impacts in Space* (J.A.M. McDonnell, ed.) Canterbury, UK, pp. 7–14.

Froeschlé, Ch., and A. Morbidelli 1994. The secular resonances in the solar system. In *Asteroids, Comets, and Meteors, 1993* (A. Milani, M. Di Martino, A. Cellino, Eds.) Kluwer: Boston, 189–204.

Gault, D.E. 1983. The terrestrial accretion of lunar material. *LPSC XIV*, 8–9.

Gault, D.E., E.M. Shoemaker, and H.J. Moore 1963. Spray ejected from the lunar surface by meteoroid impact. *NASA TND-1767*, 39 pp.

Gladman, B., M. Duncan, and J. Candy 1991. Symplectic integrators for long-term integrations in celestial mechanics. *Celest. Mech.* **52**, 221–240.

Gladman, B., J.A. Burns, M. Duncan, and H. Levison 1995. The Dynamical Evolution of Lunar Impact Ejecta. *Icarus* **118**, 302–321.

Gladman, B., J.A. Burns, M. Duncan, P. Lee, and H. Levison 1996. The Exchange of Impact Ejecta Between Terrestrial Planets. *Science* **271**, 1387–1392.

Golombek, M., and D. Rapp 1996. Size-frequency distributions of rocks on Mars and Earth analog sites: Implications for future landed missions. *JGR, Planets*, submitted.

Graf, J.C. 1993. Lunar soils grain size catalog. *NASA RF-1265*, 466pp.

Gratz, A.J. 1993. Observations of high-velocity, weakly shocked ejecta from experimental impacts. *Nature* **363**, 522–524.

Greenberg, R., W.F. Bottke, A. Carusi, and G.B. Valsecchi 1991. Planetary accretion rates: Analytical derivation. *Icarus* **94**, 98–111.

Greenberg, R., and M.C. Nolan 1993. Dynamical relationships of near-Earth asteroids to main-belt asteroids. In *Resources of Near-Earth Space* (J. Lewis, M.S. Matthews, and M.L. Guerrieri, eds.) University of Arizona Press: Tucson, pp. 473–492.

Grün, E., H.A. Zook, H. Fechtig, and R.H. Giese 1985. Collisional balance of the meteoritic complex. *Icarus* **62**, 244–272.

Halliday I., and A.A. Griffen 1982. A study of the relative rates of meteorite falls on the Earth's surface. *Meteoritics* **17**, 31–46.

Halliday I., A.T. Blackwell, and A.A. Griffen 1984. The frequency of meteorite falls on the Earth. *Science* **223**, 1405–1407.

Halliday I., A.T. Blackwell, and A.A. Griffen 1989. The flux of meteorites on the Earth's surface. *Meteoritics* **24**, 173–178.

Halliday I., A.T. Blackwell, and A.A. Griffen 1991. The frequency of meteorite falls: Comments on two conflicting solutions to the problem. *Meteoritics* **26**, 243–249.

Halliday I., A.T. Blackwell, and A.A. Griffen 1996. Detailed data for 259 fireballs from the Canadian camera network and inferences concerning the influx of large meteoroids. *Meteoritics* **31**, 185–217.

Hartmann, W.K. 1995. Planetary cratering 1. The question of multiple impactor populations: Lunar evidence. *Meteoritics* **30**, 451–467.

Hill, D.H., W.V. Boynton, and R.A. Haag 1991. A lunar meteorite found outside the Antarctic. *Nature* **352**, 614–617.

Holman, M., and J. Wisdom 1993. Dynamical stability in the outer solar system and the delivery of short period comets. *Astron. J.* **105**, 1987-1999.

Holsapple, K.A., and K.Y. Choe 1988. Surface spall in large impact events. *LPSC XIX*, 501–502.

Huss, G.R. 1990. Meteorite infall as a function of mass: Implications for the accumulation of meteorites on Antarctic ice. *Meteoritics* **25**, 41–56.

Jagoutz, E., A. Sorowka, J.D. Vogel, and H. Wänke 1994. ALH84001: Alien or progenitor of the SNC family? *Meteoritics* **29**, 478–479.

Kato, M., Y. Iijima, M. Arakawa, Y. Okimura, A. Fujimura, N. Maeno, and H. Mizutani 1995. Ice-on-ice impact experiments. *Icarus* **113**, 423–441.

Kirsten, T. 1978. Time and the solar system. In *The Origin of the Solar System* (S. Dermott, ed.) John Wiley and Sons: New York, 267-346.

Koeberl, C. 1986. Geochemistry of tektites and impact glasses. *Ann. Rev. Earth Planet. Sci.* **14**, 323–350.

Koeberl, C., and W. Cassidy, eds. (1990). *Workshop on Differences Between Antarctic and Non-Antarctic Meteorites.* LPI Tech. Rpt. 90-01. Lunar and Planetary Institute, Houston. 102 pp.

Laul, J.C. 1991 The Shergotty consortium and SNC meteorites: An overview. *Geochim. Cosm. Acta* **50**, 875–887.

Levison, H., and M. Duncan 1994. The long-term behavior of short-period comets. *Icarus* **108**, 18–36.

Lindstrom, M.M., A.H. Treiman, and D.W. Mittlefehdt 1994. Pigeonholing planetary meteorites: The lesson of misclassification of EET87521 and ALH84001. *Lunar Planet. Sci. XXV*, 797–798.

Love, S.G., and K. Keil 1995. Recognizing mercurian meteorites. *Meteoritics* **30**, 269–278.

McKay, D.S., and 7 co-authors 1991. The lunar regolith. In *Lunar Sourcebook, a User's Guide to the Moon.* (G.H. Heiken, D.T. Vaniman, and B.M. French, Eds.) Cambridge Univ. Press: Cambridge, 285–356.

McSween, H.Y. and 8 co-authors 1979. Petrogenetic relationship between Allan Hills 77005 and other achondrites. *Earth Planet. Sci. Lett.* **45**, 275–284.

McSween, H.Y. 1995. What we have learned about Mars from SNC meteorites. *Meteoritics* **29**, 757–779.

Melosh, H.J. 1984. Impact ejection, spallation and the origin of meteorites. *Icarus* **59**, 234–260.

Melosh, H.J. 1985. Ejection of rock fragments from planetary bodies. *Geology* **13**, 144–148.

Melosh, H.J. 1988. The rocky road to panspermia. *Nature* **332**, 687–688.

Melosh, H.J. 1989. *Impact Cratering.* Oxford University Press: New York.

Melosh, H.J., and W.B. Tonks 1993. Swapping rocks: Ejection and exchange of surface material among the terrestrial planets. *Meteoritics* **28**, 398.

Michel, P., and F. Thomas 1996. The Kozai resonance for Near-Earth Asteroids with semimajor axes smaller than 2 AU. *Astron. Astrophys.* **307**, 310–318.

Michel, P., and G. Valsecchi 1996. Numerical experiments on the efficiency of second-order mixed-variable symplectic integrators for N-body problems. *Celest. Mech.*, submitted.

Mikkola, S. and K. Innanen 1992. A numerical exploration of the evolution of Trojan-type asteroidal orbits. *Astron. J.* **104**, 1641–1649.

Milani, A., M. Carpino, G. Hahn, and A.M. Nobili 1989. Dynamics of planet-crossing asteroids: Classes of orbital behavior: Project SPACEGUARD. *Icarus* **78**, 212–269.

Milani, A., M. Carpino, and F. Marzari 1990. Statistics of close approaches between asteroids and planets: Project SPACEGUARD. *Icarus* **88**, 292–335.

Mittlefehldt, D.W. 1994. ALH84001, a cumulate orthopyroxenite member of the martian meteorite clan. *Meteoritics* **29**, 214–21.

Moore, J.M., and A.S. McEwen 1996. The abundance of large, Copernican-age craters on the Moon. *LPSC XXVII*, 899–900.

Murchie, S., and S. Erard 1996. Spectral properties and heterogeity of Phobos from measurements by Phobos 2. *Icarus*, in press.

Neukum, G., and B.A. Ivanov 1994. Crater size distributions and impact probabilities on Earth from lunar, terrestrial-planet, and asteroid cratering data. In *Hazards Due to Comets & Asteroids* (T. Gehrels, ed.) University of Arizona Press: Tucson, pp. 359–416.

Nishiizumi, K. 1986. Terrestrial and exposure histories of Antarctic meteorites. *Int. Work. on Antarctic Meteorites, LPI TR No. 86-01*, 71–73.

Nishiizumi, K., D. Elmore, and P.W. Kubik 1989. Update on terrestrial ages of Antarctic meteorites. *Earth Planet. Sci. Lett.* **93**, 299–313.

Nishiizumi, K., J.R. Arnold, J. Klein, D. Fink, R. Middleton, P.W. Kubik, P. Sharma, D. Elmore, and R.C. Reedy. 1991 Exposure histories of lunar meteorites ALH81005, MAC88104/5, and Y79117. *Geochim. Cosm. Acta* **55**, 3149–3155.

Nishiizumi, K., M.W. Caffee, R.C. Finkel, and R.C. Reedy. 1995. Exposure history of lunar meteorite QUE93069. *Lunar Planet. Sci. XXVI*, 1051–1052.

Nishiizumi, K., and M. Caffee 1996a. Exposure histories of lunar meteorites QUE94281 and 94269. *LPSC XXVII*, 959–960.

Nishiizumi, K., and M. Caffee 1996b. Exposure history of shergottite QUE94201. *LPSC XXVII*, 961–962.

Nyquist L.E., 1983. Do oblique impacts produce martian meteorites? *Proc. 13th Lunar and Plan. Sci. Conf.*, A785–798.

Nyquist L.E., D.D. Bogard, J.L. Wooden, H. Wiesmann, C.-Y. Shih, B.M. Bansal, and G.A. McKay 1979. Early differentiation, late magnatism, and recent bombardment of the shergottite parent planet. *Meteoritics*, 502.

Nyquist L.E., B.M. Bansal, H. Wiesmann, and C.-Y. Shih 1983. Martians young and old: Zagami and ALH84001. *Lunar Planet. Sci. XXVI*, 1065–1066.

O'Keefe, J.A. 1976. *Tektites and Their Origin*. Elsevier Press: New York.

O'Keefe, J.D., and T.J. Ahrens 1977. Meteorite impact ejecta: Dependence of mass and energy lost on planetary escape velocity. *Science* **198**, 1249–1251.

O'Keefe, J.D., and T.J. Ahrens 1986. Oblique impact: A process for obtaining meteorite samples from other planets. *Science* **234**, 346–349.

Opik, E.J. 1976. *Interplanetary Encounters*. Elsevier Press: New York.

Ott, U. 1988. Noble gases in SNC meteorites: Shergotty, Nakhla, Chassigny. *Geochim. Cosm. Acta* **52**, 1937–1948.

Pal, D.K., C. Tuniz, R.K. Moniot, W. Savin, T. Kruse, and G.F. Herzog 1986. Beryllium-10 contents of shergottites, nakhlites, and Chassigny. *Geochim. Cosm. Acta.* **50**, 2405–2409.

Rabinowitz, D.L. 1993. Evidence for a near-Earth asteroid belt. *Nature* **363**, 704–706.

Rabinowitz, D.L. 1994. The size and shape of the near-Earth asteroid belt. *Icarus* **111**, 364–377.

Rabinowitz, D.L. 1996. Observations constraining the origins of Earth-approaching asteroids. In *Completing the Inventory of the Solar System* (T. W. Rettig, Ed.), Astronomical Society of the Pacific Conference Series: San Francisco, in press.

Rabinowitz, D., E. Bowell, E. Shoemaker, and K. Muinonen. 1994. The population of Earth-crossing asteroids. In *Hazards due to Comets and Asteroids* (T. Gehrels, ed.) University of Arizona Press: Tucson, 285–312.

Reedy, R.C., J.R. Arnold, and D. Lal 1983. Cosmic-ray record in solar system matter. *Science* **219**, 127–135.

ReVelle, D.O. 1979. A quasi-simple ablation model for large meteorite entry: Theory vs. observations. *J. Atmos. Terrest. Phys.* **41**, 453–473.

Ruth, R.D. 1983. A canonical integration technique. *IEEE Trans. Nucl. Sci.* **30**, 2669–2671.

Schaber, G.G., and 9 co-authors 1992. Geology and distribution of impact craters on Venus: What are they telling us? *J. G. R.* **97**, 13257–13301.

Sears, D., and R.T. Dodd 1988. Overview and classification of meteorites. In *Meteorites and the Early Solar System* (J.F. Kerridge and M.S. Matthews, Eds.) Univ. of Arizona Press: Tucson, 3–31.

Shoemaker, E.M. 1962. Interpretation of lunar craters. In *Physics and Astronomy of the Moon* (Z. Kopal, ed.) Academic Press, New York, pp. 283–359.

Shoemaker, E.M. 1983. Asteroid and comet bombardment of the Earth. *Ann. Rev. Earth Planet. Sci.*, 461–494.

Shoemaker, E.M, and 7 co-authors 1969. Television observations from Surveyor. In *Surveryor Program Results, NASA SP-184*, pp. 19–129.

Shoemaker, E., P. Weissman, and C.S. Shoemaker 1994. The flux of periodic comets near Earth. In *Hazards due to Comets and Asteroids* (T. Gehrels, ed.) University of Arizona Press: Tucson, 313–336.

Stiefel, E.L, and G. Schiefele 1971. *Linear and Regular Celestial Mechanics.* Springer Verlag: New York.

Svedhem, H., H. Iglseder, and R. Münzenmayer. 1994. In-situ measurements of cosmic dust by the Hiten spacecraft. *BAAS* **26**, 1178.

Swindle, T.D., B. Li, and D.A. Kring 1996. Noble gases in martian meteorite QUE94201. *LPSC XXVII*, 1297–1298.

Swindle, T.D., M.K. Burkland, and J.A. Grier 1995. Noble gases in the lunar meteorites Calcalong Creek and QUE 93069. *Meteoritics* **30**, 584–585.

Taylor, G.J., and 5 co-authors 1991. Lunar Rocks. In *Lunar Sourcebook, a User's Guide to the Moon.* (G.H. Heiken, D.T. Vaniman, and B.M. French, eds.) Cambridge Univ. Press, Cambridge, 183–284.

Thalmann, Ch., and O. Eugster. 1995. Lunar meteorite Queen Alexandra Range 93069: History derived from cosmic-ray-produced and trapped noble gases. *Meteoritics* **30**, 585–586.

Thalmann, Ch., O. Eugster, G.F. Herzog, J. Klein, U. Krähenbühl, S. Vogt, and S. Xue. 1996. History of lunar meteorites Queen Alexandra Range 93069, Auska-881757, and Yamato-793169 based on noble gas isotopic abundances, radionuclide concentrations, and chemical composition. *Meteoritics*, in press.

Thomas, P., J. Veverka, J. Bell, J. Lunine, and D. Cruikshank 1992. Satellites of Mars: Geologic history. In *Mars* (H.H. Kieffer, B.M. Jakosky, C.W. Snyder, and M.S. Matthews, eds.) University of Arizona Press: Tucson, pp. 1257–1282.

Treiman, A.H. 1995a. S≠NC: Multiple source areas for martian meteorites. *JGR* **100**, 5329–5340.

Treiman, A.H. 1995b. A petrographic history of martian meteorite ALH84001: Two shocks and an ancient age. *Meteoritics* **30**, 294–302.

Treiman, A.H. and 8 co-authors 1994. Comparison of the LEW88516 and ALHA77005 martian meteorites: Similar but distinct. *Meteoritics* **29**, 581–592.

Urey, H.C. 1965. Meteorites and the Moon. *Science* **147**, 1262–1265.

Vickery, A.M. 1987. Variation in ejecta size with ejection velocity. *Geophys. Res. Letters* **14**, 726–729.

Vickery, A.M., and H.J. Melosh 1987. The large crater origin of SNC meteorites. *Science* **237**, 738–743.

Vogt, S., G.F. Herzog, and R.C. Reedy 1990. Cosmogenic nuclides in extraterrestrial materials. *Revs. Geophys.* **39**, 253–275.

Walker, D., E.M. Stolper, and J.F. Hays 1979. Basaltic volcanism: The importance of planet size. *Proc. 10th Lunar and Plan. Sci. Conf.*, 1995–2015.

Ward, W. 1981. Orbital inclination of Iapetus and the rotation of the Laplacian plane. *Icarus* **46**, 97–107.

Warren, P. 1994. Lunar and Martian meteorite delivery services. *Icarus* **111**, 338–363.

Warren, P., and G.W. Kallemeyn 1993. Geochemical investigation of two lunar mare meteorites: Yamoto-793169 and Asuka-881757. *Proc. NIPR Symp. Antarct. Meteorites*, **6** 35–57.

Wasson, J.T. 1985. *Meteorites.* W.H. Freeman and Company: New York.

Wasson, J.T., and G. Wetherill 1979. Dynamical, chemical and isotopic evidence regarding the formation locations of asteroids and meteorites. In *Asteroids* (T. Gehrels, ed.) University of Arizona Press: Tucson, 926–74.

Wetherill, G. 1968. Stone meteorites: Time of fall and origin. *Science* **159**, 79–82..

Wetherill, G. 1969. Relationships between orbits and sources of chondritic meteorites. In *Meteorite Research* (P. Millman, ed.) Reidel: Dordrecht, 573–589.

Wetherill, G. 1980. Multiple Cosmic-ray exposure ages of meteorites. *Meteoritics* **15**, 386–387.

Wetherill, G. 1984. Orbital evolution of impact ejecta from Mars. *Meteoritics* **19**, 1–12.

Wetherill, G. 1988. Where do the Apollo objects come from? *Icarus* **76**, 1–18.

Wetherill, G. 1989. Cratering of the terrestrial planets by Apollo objects. *Meteoritics*, **24**, 15–22.

Whipple, A., and P. Shelus 1994. The long-term dynamical evolution of the minor planet (4179) Toutatis. *Icarus* **105**, 408–419.

Wisdom, J., and M. Holman 1991. Symplectic maps for the N-body problem. *Astron. J.* **102**, 1528–1538.

Wood, J. 1961. Stony meteorite orbits. *MNRAS* **122**, 79–88.

Yau, K., P. Weissman, and D. Yeomans 1994. Meteorite falls in China and some related human casualty events. *Meteoritics* **29**, 864-871.

Yoshida, H. 1993. Recent progress in the theory and applications of symplectic integrators. *Celest. Mech.* **56**, 27–43.

Zellner, B., and E. Wells 1996. Spectrophotometry of the martian satellites with the Hubble Space Telescope. *LPSC XXV*, 1541-1542.

Zel'dovich, Y.B., and Y.P. Raizer 1967. *The Physics of Shock Waves and High-temperature Hydrodynamic Phenomena.* Academic Press: New York.